Validation of Multi-Dimensional Stirling Engine Design Codes: Measurements in the 90-Degree Turn Test Section

Terrence W. Simon and David Adolfson
University of Minnesota, Minneapolis, Minnesota

NASA STI Program . . . in Profile

Since its founding, NASA has been dedicated to the advancement of aeronautics and space science. The NASA Scientific and Technical Information (STI) program plays a key part in helping NASA maintain this important role.

The NASA STI Program operates under the auspices of the Agency Chief Information Officer. It collects, organizes, provides for archiving, and disseminates NASA's STI. The NASA STI program provides access to the NASA Aeronautics and Space Database and its public interface, the NASA Technical Reports Server, thus providing one of the largest collections of aeronautical and space science STI in the world. Results are published in both non-NASA channels and by NASA in the NASA STI Report Series, which includes the following report types:

- TECHNICAL PUBLICATION. Reports of completed research or a major significant phase of research that present the results of NASA programs and include extensive data or theoretical analysis. Includes compilations of significant scientific and technical data and information deemed to be of continuing reference value. NASA counterpart of peer-reviewed formal professional papers but has less stringent limitations on manuscript length and extent of graphic presentations.

- TECHNICAL MEMORANDUM. Scientific and technical findings that are preliminary or of specialized interest, e.g., quick release reports, working papers, and bibliographies that contain minimal annotation. Does not contain extensive analysis.

- CONTRACTOR REPORT. Scientific and technical findings by NASA-sponsored contractors and grantees.

- CONFERENCE PUBLICATION. Collected papers from scientific and technical conferences, symposia, seminars, or other meetings sponsored or cosponsored by NASA.

- SPECIAL PUBLICATION. Scientific, technical, or historical information from NASA programs, projects, and missions, often concerned with subjects having substantial public interest.

- TECHNICAL TRANSLATION. English-language translations of foreign scientific and technical material pertinent to NASA's mission.

Specialized services also include creating custom thesauri, building customized databases, organizing and publishing research results.

For more information about the NASA STI program, see the following:

- Access the NASA STI program home page at *http://www.sti.nasa.gov*

- E-mail your question via the Internet to *help@sti.nasa.gov*

- Fax your question to the NASA STI Help Desk at 301–621–0134

- Telephone the NASA STI Help Desk at 301–621–0390

- Write to:
  NASA STI Help Desk
  NASA Center for AeroSpace Information
  7121 Standard Drive
  Hanover, MD 21076–1320
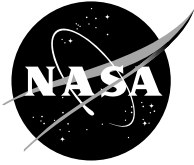
Validation of Multi-Dimensional Stirling Engine Design Codes: Measurements in the 90-Degree Turn Test Section

Terrence W. Simon and David Adolfson
University of Minnesota, Minneapolis, Minnesota

National Aeronautics and
Space Administration

Glenn Research Center
Cleveland, Ohio 44135

May 2006

Acknowledgments

Level of Review: This material has been technically reviewed by NASA technical management.

Available from

NASA Center for Aerospace Information	National Technical Information Service
7121 Standard Drive	5285 Port Royal Road
Hanover, MD 21076–1320	Springfield, VA 22161

Available electronically at http://gltrs.grc.nasa.gov

Contents

List of Figures and Tables

Validation of Multi-Dimensional Stirling Engine Design Codes: Measurements in the 90-Degree Turn Test Section

Terrence W. Simon and David Adolfson
University of Minnesota
Minneapolis, Minnesota 55455

Abstract

The work to be presented herein was motivated largely by a desire to improve the understanding of oscillatory fluid mechanics inside a Stirling engine. To this end, a CFD project was undertaken at Cleveland State University with the goal of accurately predicting the fluid dynamics within an engine or engine component. Along with the CFD efforts, a code validation project was undertaken at the University of Minnesota. The material covered herein consists of four main parts. In section 1, an experimental investigation of a small aspect ratio impinging jet is discussed. Included in this discussion is a description of the test facilities and instrumentation. A presentation of the collected data is given and comments are made. Next, in section 2, a parallel experimental investigation is presented in which the same geometry as that of section 1 is used, but the flow conditions are changed from steady unidirectional flow to sinusoidally oscillating flow. In section Two, collected data are presented and comments are made. In section 3, a comparison is made between the results of sections 1 and 2, namely, sinusoidally oscillating flow results are compared to steady, unidirectional flow results from the same geometry. Finally, in section 4, a comparison is made between experimentally collected data (the main subject of this work) and CFD generated results. Furthermore, in appendix A, an *introductory* description of the primary measurement tool used in the experimental process—the hot wire anemometer—is given for the unfamiliar. The anemometer calibration procedure is described in appendix B. A portfolio of data reduction and data processing codes is provided in appendix C and lastly, a DVD and a roadmap of its contents is provided in an appendix D.

1.0 Unidirectional Flow Investigations

1.1 Introduction

This unidirectional experimental program was undertaken to complement an oscillatory flow investigation conducted at the University of Minnesota. The oscillatory investigation is discussed thoroughly in section 2. We defer the description of the motivation behind these experiments until the introduction of section 2. The work that is discussed in this thesis began (chronologically) with oscillatory flow visualization experiments. It was decided that it would be valuable and important to investigate the flow under unidirectional conditions in the same geometry as that of the oscillatory experiments. The thought was that the unidirectional case would be less complicated to model with a CFD program (a moving boundary would be replaced with a steady state boundary condition). Thus, a series of unidirectional experiments were carried out to capture the important features of the flow within the test section. The purpose of these experiments was to provide a data set for comparison to CFD generated velocity fields. Hot-wire anemometry data were taken and flow visualization was conducted as a standard for code validation. The flow geometry was simple, such that it could be easily gridded in a CFD program. However, the geometry provided separation and transition zones, shear layers and recirculation zones. These characteristics made the flow complex and challenging for CFD computation.

We comment that the order of experiments that produced this report is as follows: experimental flow visualization under oscillatory flow conditions was carried out; this was followed by unidirectional flow visualization and hot wire anemometry; finally, oscillatory hot wire anemometry was conducted. We present the results out of chronological order for the following reason: the unidirectional results are easier

to understand. We sacrifice order for clarity. In the presentation of unidirectional results that follow, the reader will become familiarized with the general flow characteristics within the test section. This familiarity will make the presentation of oscillatory results easier to understand and more concise. One thing to keep in mind while reading the unidirectional presentation is that the operating points of the experiment (under unidirectional flow) were chosen to match the oscillatory case. Also, a large portion of the experimental set-up for the unidirectional case is similar, but not identical to, the oscillatory flow case, hence, exercise caution when reading section 2.

Below, the unidirectional experimental process will be outlined and the data collection process will be presented. Representative results will be discussed and a summary of all collected data will be given. The experimental results will be compared to theoretical predictions and trends will be discussed.

1.2 Nomenclature

Symbol	Description	Units
a	A constant	[1/s]
D	Tube diameter	[m]
$f(t)$	Generalized function of time	[various units]
$F(\omega)$	Fourier transform of $f(t)$	[various units]
$\vec{F}(\omega_N)$	Discrete analogue of $F(\omega)$	[various units]
Fo	The $N \times N$ Fourier matrix	[dimensionless]
$g(z)$	A trial function in z	[m/s]
i	Square root of -1	[dimensionless]
N	An integer	[dimensionless]
p	Pressure	[N/m^2]
r	Radial test section coordinate	[m]
R	Tube radius	[m]
Re	Reynolds number	[dimensionless]
S	Disc spacing	[m]
t	Time variable	[s]
TI	Turbulence intensity	[dimensionless]
u	Instantaneous velocity	[m/s]
U	Inviscid velocity	[m/s]
u_{cl}	Tube centerline velocity	[m/s]
u_j	Instantaneous velocity	[m/s]
$\bar{u}$	Ensemble averaged velocity	[m/s]
w	Boundary layer velocity	[m/s]
W	Invicid velocity	[m/s]
x	Axial test section coordinate	[m]
$\vec{X}$	Generalized discrete function of time	[various units]
z	Axial analysis variable	[m]
ε	Error quantity	[dimensionless]
$\phi(\zeta)$	Similarity transform function	[dimensionless]
μ	Dynamic viscosity	[N s/m^2]
ν	Kinematic viscosity	[m^2/s]
ρ	Density	[kg/m^3]
τ	Shear stress	[N/m^2]
ω	Frequency variable	[1/s]
ω_n	Discrete Frequency variable	[1/s]
ζ	Similarity variable	[dimensionless]

1.3 Experimental Set-Up

The test hardware consists of the following; a large fan, flexible ductwork, two large plywood flow-conditioning boxes, a Laminar Flow Element (LFE), a baffle plate, "polarfleece" quieting sheets, a bellmouth and a test section (see fig. 1.1). In figure 1.1, atmospheric air enters the fan (not shown) and is pumped through flexible tubing into the first flow conditioning box. This flow conditioning box serves to "spread the flow out" and provide an even distribution to the LFE. The LFE kills any large scale eddies that may have been caused by the fan. Upon leaving the LFE, the air enters the second flow conditioning box and immediately impinges on a baffle plate. This baffle plate destroys the air jet exiting the LFE. The flow then passes through the first of two felt-like quieting sheets. Both quieting sheets serve to eliminate any eddies that may have remained in the flow. Finally, the flow passes through the second flow conditioning box and exits through a bellmouth into the test section. In figure 1.1, two dimensions of interest, S and D, are identified. The spacing between the two discs, S, is a variable. The delivery tube diameter (or "tube" for short) is denoted by D and is a constant and equal to 216 mm (8.5 in.). For future reference, the area inside the tube will be called the tube space and the area between the two discs will be called the disc space. It is also to be noted that the flow conditioning boxes are parallelepipeds, whereas the laminar flow element and the test section are bodies of revolution (and hence axisymmetric).

Within the test section, the flow travels through the tube and impinges on the "target" disc (see figure 1.2). The flow stagnates, turns radially outward, and exits the test section. An approximate time-average picture of the flow inside the test section is presented in figure 1.2. Flow entering the test section (i.e., in the tube) looks generally like a developing pipe flow and is shown in figures 1.33 through 1.36. For reference, the walls of the test section are made of Plexiglas to allow optical access. Figure 1.3 is introduced to give the reader a sense of perspective and size.

1.4 Data Collection

Quantitative velocity data are collected with a hot-wire anemometer and probe. The anemometer is a model 1053A constant-temperature anemometer made by TSI, Inc. The probe is a TSI model 1210 end flow hot-wire sensor (see fig. 1.4). The signal from the anemometer is monitored in one of two ways: for low-frequency sampling, the signal is sent directly to an IOTech ADC488 analog-to-digital converter; for high frequency sampling, the signal, prior to going to the A/D converter, is run through a D-C offsetting device and a Stanford Systems Inc. Dual Channel Filter. Both arrangements are shown in figure 1.5. The A/D converter is controlled with C code and is interfaced to a PC via an IEEE 488 bus. The sampling stations are shown in figure 1.6. At each sampling station (each radial position), two different types of data are collected; a collection of low-sampling-frequency, long-time points and a single, high-sampling-frequency point. The collection of low frequency points is used to build an average velocity profile (i.e., u vs. x at a fixed r) as the probe is traversed away from the wall in the x-direction (co-ordinate directions are shown in figure 1.6). The low-frequency points are collected in a random order (in the x co-ordinate) such that any potential temporal variations do not appear as trends associated with x-position. The low-frequency sampling rate is 20 Hz, with a sample duration of five minutes. This sampling frequency (i.e., 20 Hz) was chosen after looking at the results of a high-frequency (2000 Hz) sample. It was observed that the Fast Fourier Transform (FFT) of the high-frequency sample shows no significant power contribution beyond 20 Hz (shown in figs. 1.13 through 1.32). The concepts of the FFT and "power" are explained below.

For each high sampling frequency point, the wire is approximately 1 mm (0.040 in.) off of the target impingement plate. The sampling frequency is 2000 Hz. The choice of frequency says something about the expected bandwidth of the signal. The sampling frequency is chosen in accordance with the following logic. The flow in the test section has a certain velocity associated with it and, hence, a small packet of fluid is convected downstream at this "characteristic" velocity. The packet of fluid (henceforth called an eddy) has a certain rotational velocity and spatial size associated with it. Thus, as an eddy flows past the anemometer probe, a certain velocity fluctuation will be seen (where the velocity fluctuation can be

interpreted as a frequency—that is, the change in velocity due to the eddy looks like a little wave propagating past the probe). We choose the sampling frequency to capture the smallest eddies of interest traveling at the characteristic fluid velocity. We shall see during the discussion of power-spectra plots that this choice of sampling frequency is quite reasonable. The duration of the high frequency sample is 32.768 seconds. The sampling frequency-time combination gives a total of $65536 = 2^{16}$ data points which, by virtue of the "power of 2" size of the sample, optimizes the Fourier transform (to be discussed shortly).

Flow visualization equipment consists of a Nikon FE2 35 mm camera with a Tamaron SP 1:2.5 by 90 mm lens. A schematic of the set up is shown in figure 1.7. In all cases, there is a red filter screwed on the lens; the filter serves to cut all non-red light from the photographs. The camera is loaded with Tri-X ASA 125 black and white film and mounted on a tripod with the camera shutter release set to "bulb." Bulb is a setting that holds the camera shutter open as long as the shutter trigger is depressed. The camera is aligned normally with the *x*-axis of the test section and is focused such that the *x*-axis is in the focal plane. The focal plane is illuminated with a LASER sheet. The LASER source is a Melles-Griot He-Ne LASER that emits red light at a frequency of 632.8 nm. A glass rod is placed in the path of the beam to create the sheet. Particles are introduced into the flow with a Sage Action Inc. Model 33 Multi Head Bubble Generator. This device combines compressed air, helium and a soap solution to make neutrally-buoyant, variable-sized bubbles. The bubble size is in general about 0.8 mm (1/32 in.). The bubbles, which are injected just downstream of the second quieting screen (see fig. 1.1), travel with the flow into the test section. When the bubbles arrive in the disc space, some of them are illuminated in the laser sheet. The product is a real-time, two-dimensional view of the flow. To capture a picture of the flow, the camera is set-up as described above and the shutter is opened for five minutes. This method of photography produces a *time average* picture (shown in figs. 1.8 through 1.11) of the flow. As a note, due to the long duration of the photo, all of this work is carried out in a blackened room.

The cases of interest are as follows:
1. Re = 7600, *S* = 127 mm (5 in.)
2. Re = 7600, *S* = 54 mm (2.125 in.)
3. Re = 17700, *S* = 127 mm (5 in.)
4. Re = 17700, *S* = 54 mm (2.125 in.)

where the Reynolds number is based on tube diameter, *D*, and tube core exit velocity.

1.5 Results

1.5.1 Flow Visualization

The flow visualization scheme produced several photographs. Scanned versions are shown in figures 1.8 through 1.11. The photographs give a rough idea of where transition to turbulence along the target wall takes place. To locate transition zones, one looks at the flow adjacent to the target plate. While moving the eye radially outward along the near-wall flow, one observes that the streaks start to wiggle. The presence of "wigglyness" implies that the flow has begun to transition. The location of the onset of transition, as revealed by the flow visualization, is pointed out with white arrows in figures 1.8 through 1.11 and is summarized below. As a note, in figures 1.8 through 1.11, two sets of arrows appear. The green (or gray if printed in black and white) arrows will be discussed below.

Re = 17700, *S* = 127 mm (5 in.)
Figure 1.8
Normalized Radial Transition Location (*r/D*) = 1

Re = 7600, *S* = 127 mm (5 in.)
Figure 1.9
Normalized Radial Transition Location (*r/D*) ~ 1

Re = 17700, S = 54 mm (2.125 in.)
Figure 1.10
Normalized Radial Transition Location (r/D) = 0.8

Re = 7600, S = 54 mm (2.125 in.)
Figure 1.11
Normalized Radial Transition Location (r/D) ~ 1

One thing that the reader may note about the flow visualization pictures it that in some cases (figs. 1.8 and 1.10) the "top" of the photo is more heavily laden with bubbles, whereas in figures 1.9 and 1.11 the bottom is more bubble-dense. This is because the bubbles are not *exactly* neutrally buoyant. The photos were taken on different days, and, as such, the bubble machine was turned off and on. It is difficult to exactly control the buoyancy of the bubbles; hence, sometimes they are slightly heavy and fall towards the floor in the plenum upstream of the test section where the velocities are very low. On other days they rise. The net result is the phenomenon that appears in the photographs.

1.5.2 Fourier Analysis and Spectral Techniques

As was mentioned in the data collection section, a high-sampling rate point was taken at each radial location for all four cases. We use these signals to help determine the location of transition to turbulence in the boundary layer.

To begin, the Fourier transform of a continuous signal, and its implications, will be described. The discrete case, which is inherent to data collection, is discussed thereafter.

The Fourier transform of a continuous signal can be defined as:

$$F(\omega) = \int_{-\infty}^{\infty} f(t)e^{i\omega t}dt$$

where $f(t)$ is a real-time signal (i.e., a continuous and bounded function). Integration against a complex exponential takes the time signal to "frequency space." The idea is that at a fixed frequency, ω, the product of the time signal and the complex exponential will "pick out" the oscillations of the time signal that correspond to the given frequency, ω. In short, we now have a function that describes the frequency content of our original time signal.

The description of how this "picking out" process works is mathematically deep and the curious reader is directed to Pinsky[2] (or your favorite text on Fourier analysis). This integration process produces a (usually) continuous function in "frequency space." The new function is (almost always) complex, and, as such, requires some kind of processing. To this end, the function $F(\omega)$ is pointwise squared (i.e., we take the product $F(\omega) \times F(\omega)$ at each ω). We define this new function $F^2(\omega)$ as "power" or "energy." As a note, $F(\omega)$ carries the units (in the present discussion) of length/frequency. Thus, the square of this combination of units produces a quantity that is similar in *form* to the idea of kinetic energy, hence the name "energy" or "power."

Data collection is inherently discrete, hence the continuous signal $f(t)$ is sampled at some frequency ω. Suppose N points are collected. Then the data set can be represented as a column vector called $\vec{X}$, where $\vec{X}$ has a length of N.

$$X = \begin{pmatrix} f_1 \\ f_2 \\ ... \\ f_{N-1} \\ f_N \end{pmatrix}$$

The definition of the continuous Fourier transform makes little sense as integration is no longer possible. We turn to linear algebra. We define the $N \times N$ Fourier matrix as:

$$Fo = \frac{1}{\sqrt{N}} \begin{pmatrix} 1 & 1 & ... & 1 & 1 \\ 1 & \psi & ... & \psi^{N-2} & \psi^{N-1} \\ . & . & . & . & . \\ . & . & . & . & . \\ 1 & \psi^{N-1} & . & \psi^{(N-2)(N-1)} & \psi^{(N-1)^2} \end{pmatrix}$$

where the ψ's are defined as the N roots of $\psi^N = 1$. The Discrete Fourier Transform (DFT) and the power associated with it are defined now:

$$\vec{F}(\omega_N) = Fo\vec{X}$$

and

$$\vec{F}^2(\omega_N) = F(\omega_N)F^H(\omega_N)$$

We note that there are optimization algorithms associated with the above definition of the DFT. We do not care to elaborate on the details but rather refer the reader to the references (Hayes,[1] Strang[4]). We note further that these algorithms take the DFT to the Fast Fourier Transform (FFT). The FFT depends on samples (vectors) of length 2^j (recall that our sample length, N, was chosen to meet this requirement).

Figures 1.13 through 1.32 present two plots each; one is the actual time signal, $\vec{X}$, and the second is the "power," $\vec{F}^2(\omega_N)$. We use spectral (i.e., high-frequency Fourier transformed) data to determine the location of transition onset. The general method is as follows: one observes the frequency domain velocity signals (i.e., power) at the radial sampling positions $r/D = 0.118, 0.471, 0.588, 0.824,$ and 0.941. One can see that as r/D increases, the power signal first flattens, then develops a "hump" in the neighborhood of 2 Hz $< \omega <$ 20 Hz (figs. 1.13 through 1.32). The range of frequencies associated with transition is shown in figure 1.12. We associate transition with a power rise in the vicinity of these frequencies. The logic is that a fluctuation power increase over a certain frequency range corresponds to (in the physical situation) the emergence of coherent waves being carried past the probe. The presence of coherent waves implies the onset of turbulence.

This process was carried out for all four cases of different Reynolds numbers and disc spacings. It was found that there was general agreement with the flow visualization results, with one exception; the transition points were generally at a slightly smaller upstream radial position than the transition onset locations that the flow visualization data indicated. In other words, the hot-wire revealed the development of turbulence to a higher level of sensitivity than that of the flow visualization. The insight that the spectral technique provides is shown with green arrows (or gray if printed in black and white) in contrast to the flow visualization in figures 1.8 through 1.11 and is given quantitatively below.

Re = 17700, S = 54 mm (2.125 in.)
Figures 1.13 to 1.17 and 1.10
Normalized Radial Pre-Transition Location (r/D) = 0.588
Normalized Radial Post-Transition Location (r/D) = 0.824
(On fig. 1.10, transition is identified as r/D = 0.7 for the sake of comparison to flow visualization data, we can only say that it is between 0.588 and 0.824.)

Re = 17700, S = 127 mm (5 in.)
Figures 1.18 to 1.22 and 1.8
Normalized Radial Transition Location (r/D) = 0.941

Re = 7600, S = 54 mm (2.125 in.)
Figures 1.23 to 1.27 and 1.11
Normalized Radial Transition Location (r/D) = 0.941

Re = 7600, S = 127 mm (5 in.)
Figures 1.28 to 1.32 and 1.9
Normalized Radial Transition Location (r/D) = 0.824

1.5.3 Ensemble Averaged Velocity and Turbulence Intensity Profiles

Velocity and turbulence intensity profiles were generated using long-time, low-frequency sampling. In the disc space, these data offer the primary test of code validation. To seed the computations, tube velocity and turbulence intensity profiles are used as a boundary condition for CFD calculations.
Turbulence intensity is defined in this case as:

$$TI = \frac{1}{\bar{u}} \sqrt{\frac{\sum_{j=1}^{N} \left(u_j - \bar{u} \right)^2}{N-1}}$$

Where N is the number of sampled points, $\bar{u}$ is the local velocity averaged over all of the sampled data points and u_j is the instantaneous velocity of the jth point.

The boundary data are (i.e., tube velocity and TI profiles) shown in figures 1.33 through 1.40. The quantity being measured is $\bar{u}$, the average velocity in the axial direction (the assumption is that in the tube space, the main component if the velocity is in the axial direction). The axial location of the probe in the tube is (as is shown in fig. 1.6) 127 mm downstream of the test section entrance. There is apparently a slight skewing of the flow which approaches the bellmouth entrance to the test section. The reader might notice that the profile shapes are not exactly symmetric (in terms of velocity and TI). One other thing to note is that there are considerably more data points taken in the radial range $0 < r/D < 0.5$ than over the range $-0.5 < r/D < 0$. Emphasis was given to one side because the team at CSU used only one half of the measured domain for boundary conditions. (They made the assumption that the flow is axisymmetric, hence it is two-dimensional. Thus, assuming that the flow is two-dimensional, they reduced the computation domain to cover one-half of the tube). The sparse data on the other side are given to document symmetry.

Turbulence intensity profiles in the disc space are presented in figures 1.41 through 1.44. These turbulence intensity profiles are useful in the sense that they indicate where the hot-wire is collecting "reasonable" data. In other words, in figures 1.41 through 1.44, regions exist where TI values exceed 25%. Measured values of velocity rise above actual values and measured values of TI drop below actual values as TI rises above 25%.

Average velocity profiles are presented in figures 1.45 through 1.48. Using the *TI* data, one can divide the velocity profiles into two regions; a region where average velocities may be considered valid for code validation purposes and a second region where the profiles are not accurate. In figures 1.45 through 1.48, entire average velocity profiles are presented. In regions of large *TI* the points along the profile are colored black.

Using the data from the average velocity and *TI* profiles, we are able to distinguish between the near-wall impinging-jet-type flow and the reverse flow far off the target plate and identify the shear layer that separates the two. We defer further discussion of this topic to section 1.7.

1.6 Average Velocity profiles and a Description of the Shear Layer

Of interest was the documentation of the shear layer (or recirculation zone) shape (see fig. 1.52). To accomplish this task, the peak velocity at each normalized radial location was observed. This peak velocity corresponds with a particular normalized distance from the target wall. For a clarification of this process, we refer the reader to figure 1.49. The data for figure 1.49 came from figure 1.48. In figures 1.45 through 1.48 ensemble averaged velocity profiles as a function of normalized distance (*x/S*) from the target wall are presented. Figures 1.45 through 1.48 present five profiles, where the profiles correspond to the normalized radial positions (*r/D*) 0.118, 0.471, 0.588, 0.824, and 0.941. At each operating point (as functions on RE and S), the velocity profiles corresponding to *r/D* = 0.588, 0.824, and 0.941 were inspected. From each of these cases, (12 in all) the maximum value of velocity was chosen. This collection of maximum velocities was then plotted and is shown in figure 1.50.

Figure 1.50 reveals that the shape of the shear layer seems to be independent of Reynolds number. However, one can see that curves of equal disc spacing seem to follow each other. This implies that the shape of the shear layer with radial location, *r/D*, depends primarily on dimensionless disc spacing, S/D.

1.7 Experimentally Collected Data vs. Theoretical Results

1.7.1 An "Exact" Solution of the Navier-Stokes Equations

As a matter of curiosity, the time-averaged velocity profiles collected via low sampling rate anemometry are compared to an "exact" solution of the Navier-Stokes equations. The method of comparison is given below. In the viscous region, a theoretical boundary layer analysis is compared to experimentally measured shear stresses.

Before we begin, we make a comment; we note that in figures 1.33 through 1.36, the delivery tube centerline velocities, u_{cl}, are, respectively, 1.23, 1.15, 0.50, and 0.52 m/s. With the definition:

$$\mathrm{Re} = \frac{\rho u_{cl} D}{\mu}$$

and air at Standard Temperature and Pressure (STP), we find that these centerline velocities correspond to Reynolds numbers of, respectively, 16422, 15354, 6676, and 6943. Thus, the previously referenced Reynolds numbers of 17700 and 7600 were only approximate. This difference is ineffectual in the sense that code validation was based on the velocity profiles which yielded the correct Reynolds numbers rather than the nominal values. In the analysis that follows, the value of the Reynolds number at the tube centerline *is* important, so we make the following formal statement: the cases of interest are changed to:

Case 1. Re = 16422, *S* = 54 mm (2.125 in.) (corresponding to fig. 1.33)
Case 2. Re = 15354, *S* = 127 mm (5 in.) (corresponding to fig. 1.34)
Case 3. Re = 6676, *S* = 54 mm (2.125 in.) (corresponding to fig. 1.35)
Case 4. Re = 6943, *S* = 127 mm (5 in.) (corresponding to fig. 1.36)

The laminar solution of the Navier-Stokes equations in an axisymmetric stagnation flow is well known and is presented in sources such as "Boundary Layer Theory" by Schlichting.[3] In the inviscid region (see fig. 1.51), potential flow theory yields the following equations for the U and W velocities:

$$U = ar \qquad (1)$$

$$W = -2az \qquad (2)$$

where a is a constant and is related to the "strength" of the jet. Close to the impingement target surface there will be viscous effects. In that region, the following form of the Navier-Stokes equations govern the fluid dynamics:

$$u\frac{\partial u}{\partial r} + w\frac{\partial u}{\partial z} = -\frac{1}{\rho}\frac{\partial p}{\partial r} + \nu\left(\frac{\partial^2 u}{\partial r^2} + \frac{1}{r}\frac{\partial u}{\partial r} - \frac{u}{r^2} + \frac{\partial^2 u}{\partial z^2}\right)$$

$$u\frac{\partial w}{\partial r} + w\frac{\partial w}{\partial z} = -\frac{1}{\rho}\frac{\partial p}{\partial z} + \nu\left(\frac{\partial^2 w}{\partial r^2} + \frac{1}{r}\frac{\partial u}{\partial r} + \frac{\partial^2 w}{\partial z^2}\right) \qquad (3a)$$

$$\frac{\partial u}{\partial r} + \frac{u}{r} + \frac{\partial w}{\partial z} = 0$$

With the boundary conditions:

$$u(r,0) = w(r,0) = 0$$
$$u(r,z \to \infty) = U \qquad (3b)$$

Introducing the transformations (with primes denoting differentiation with respect to z):

$$u = rg'(z)$$
$$w = -2g(z)$$

into (3a) and (3b) yields:

$$g'^2 - 2gg' = a^2 + \nu g''' \qquad (4a)$$

and

$$g(0) = g'(0) = 0$$
$$g'(z \to \infty) = a \qquad (4b)$$

Now a similarity transformation is introduced:

$$\zeta = z\sqrt{\frac{a}{\nu}} \qquad (5a)$$

$$g(z) = \phi(\zeta)\sqrt{a\nu} \qquad (5b)$$

Putting this transformation into (4a) and (4b) gives:

$$\phi''' + 2\phi\phi'' - \phi'^2 + 1 = 0 \tag{6a}$$

$$\phi(0) = \phi'(0) = 0 \tag{6b}$$

$$\phi'(\zeta \to \infty) = 1 \tag{6c}$$

(Here, primes denote differentiation with respect to ζ.)

The solution to equation (6a) subject to ((6b) and (6c)) is presented in Schlichting,[3] pp. 90-91.

We now find an exact solution for wall shear stress. Regarding equation (5a), we form the differential and write:

$$\frac{\partial}{\partial \zeta} = \frac{\partial}{\partial z} \sqrt{\frac{\nu}{a}} \tag{7}$$

From the algebra required to go from equations (4) to equations (6), we know that:

$$\phi' = \frac{u}{U} \tag{8}$$

Combining equations (1), (7) and (8) and introducing viscosity yields:

$$\tau(z) = \left[\mu \sqrt{\frac{a^3}{\nu}} \phi''(\zeta) \right] r$$

If we are interested in the shear stress at the wall, we have:

$$\tau_w = \left[\mu \sqrt{\frac{a^3}{\nu}} \phi''(0) \right] r \tag{9}$$

We now pause to review. So far we have developed a relationship for wall shear stress as a function of radial position along the target plate. We also state that this solution is *exactly* valid for the geometry of figure 1.51.

The method of comparison is as follows; assume that in the neighborhood of the stagnation point (see fig. 1.52) the exact solution closely models the experimental set-up. Thus, we can use (9) to predict wall shear stress close to the tube centerline (we suspect that away from the centerline, the flow, and specifically the boundary layer, will feel the influence of the shear layer and recirculation bubble above it). The next assumption is about the inviscid flow region. We assume that the tube exit velocity at the centerline u_{cl}, can be specified at a distance S from the target plate. With these thoughts in mind, we turn to equation (2):

$$W = -2az \tag{2}$$

Inserting our assumptions we have:

$$u_{cl} = -2aS \Rightarrow |a| = \frac{u_{cl}}{2S} = \frac{\mathrm{Re}_D \nu}{2SD} \tag{10}$$

Where the Reynolds number is based on tube diameter, D and the tube centerline exit velocity u_{cl}. Putting (9) and the result of (10) together gives:

$$\tau_w = \left[\frac{\mu^2 \phi''(0)}{8\rho R^{3/2}} \sqrt{\frac{Re_D^3}{S^3}} \right] r \tag{11}$$

where R is the tube radius. The known numerical values are:

$$R = 0.10759 \, m \; (4.25 \; in.)$$

$$\rho = 1.1614 \, kg/m^3$$

$$\mu = 184.6 \times 10^{-7} \, N \cdot s/m^2$$

$$\phi''(0) = 1.3120 \, [\text{dimensionless}]$$

This gives (as an approximation):

$$\tau_w = \left[1.364 \times 10^{-9} \sqrt{\frac{Re_D^3}{S^3}} \right] r \tag{12}$$

Near the stagnation point we expect that the above equation will be in close agreement with measured shear stress results. We hope that reasonable agreement will extend from the stagnation point to a radial location equal to the radius of the tube.

We compare shear stress data at radial locations $r = 102$ mm (4 in. or $r/D = 0.473$) and $r = 127$ mm (5 in. or $r/D = 0.588$). We presume that in this region, and for smaller values of r, the effect of the difference in geometry between that of figure 1.51 and the actual geometry of figure 1.52 will be minimal. We note that the data-collection process was not originally intended for shear stress measurements in that we did not focus on near-wall measurements. As such, some of the data give a reasonable approximation of the gradient (and consequently the wall shear stress) whereas, others do not. One can get a sense of the accuracy of the shear stress by looking at the near wall velocity gradients in figures 1.45 through 1.48. Only the "good" data will be presented. Finally, we note that these data represent only the lower bounds to the actual values of wall shear stress. (The closest data point was 1 mm from the target wall, thus, the gradient at 1 mm was assumed to extend all the way to the wall.)

Regarding figure 1.53, one can see that the experimental values are in agreement with the theoretical values and the trends with S and Re_D (actually u_{cl}) are captured reasonably well.

1.8 Conclusions

The flow field in a semi-constrained, steady, impinging jet was investigated. The flow was documented with flow visualization and hot wire anemometry. The flow visualization results served to provide a qualitative characterization of the flow field. From it, the general shapes of the shear layer and wall jet could be identified. Moreover, from the flow visualization results, approximate transition points in the wall jet could be identified. With the knowledge gained from the flow visualization, we turned to hot wire anemometry coupled with Fourier theory to identify wall jet transition zones. Low frequency hot wire samples allowed for the generation of average velocity and *TI* plots that are useful for code validation purposes. From the low frequency hot wire data, plots of the shear layer shape were made. It was found that the shear layer is more or less independent of Reynolds number and strongly dependant on

disc spacing. Finally, approximate values of wall shear stress were computed. These results, by themselves, are useful for code validation; however, it was found that when compared to analytical predictions of shear stress, the results were very favorable; a much more general and useful result.

1.9 Error Analysis

A hot wire calibration error analysis was conducted and is described in detail in appendix B. It revealed that the hot wire anemometer has a variable uncertainty associated with it. The uncertainty in hotwire measurements is presented in appendix B, figure B.5. This figure shows that as fluid velocities drop below 20 cm/s there is a marked increase in error. We note, however, that even at low velocities (sub 20 cm/s) the measurement is very repeatable; thus, we do not expect a large stochastic error. For a detailed explanation the curious reader is referred to appendix B.

Outside of anemometer errors, there are errors associated with the positioning of the hot wire probe. The probe saw the flow in two different regions of the test section; the "tube" and the "disc space." Within the tube, the probe was allowed to move only radially. However, in the disc space, the probe was moved both radially and axially. Each of these positioning schemes has its associated errors, which we now state.

Within the tube, for any radial position, there is a normalized error (error/tube diameter) of:

$$\varepsilon_{tube} = \pm 0.00094$$

In other words, for any radial position within the tube (e.g., figs. 1.33 through 1.40), the plotted or stated values may have the above deviation in radial position.

Within the disc space, for any axial location (i.e., normalized distance from the wall) there is normalized error (error/disc spacing) of:

$$\varepsilon_{disc,axi,2.125"} = \pm 0.0047 \qquad \text{(for the 54 mm (2.125 in.) case)}$$

$$\varepsilon_{disc,axi,5"} = \pm 0.002 \qquad \text{(for the 127 mm (5 in.) case)}$$

In other words, for any axial position within the disc space (e.g., fig. 1.47), the plotted or stated values may have the above deviation in axial position.

Finally, the probe was moved radially within the disc space. The normalized error (error/tube diameter) associated with radial position within the disc space is stated as:

$$\varepsilon_{disc,radial} = \pm 0.012$$

This type of error may appear in statements such as $r/D = 0.941$.

For completeness, all of the above error statements are based on a 95% confidence interval.

1.11 Figures
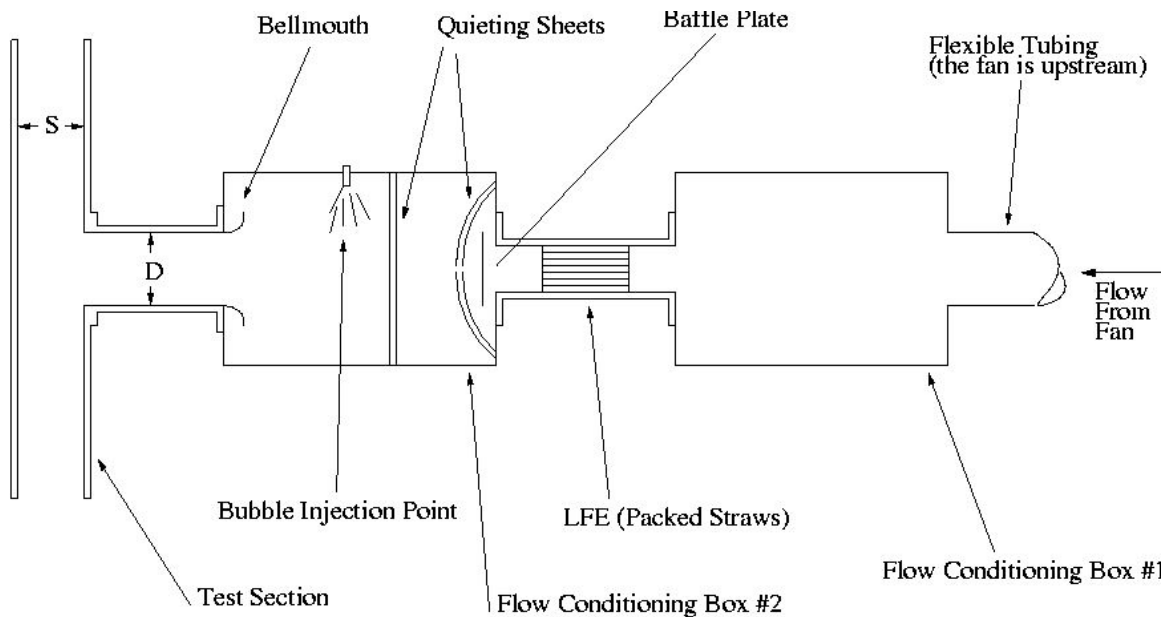
Figure 1.1.—A schematic of the experimental set-up. Flow enters on the right and passes through the various flow conditioning elements. As a note, the flow conditioning boxes are parallelepipeds, whereas the laminar flow element and the test section are bodies of revolution (and hence axisymmetric).
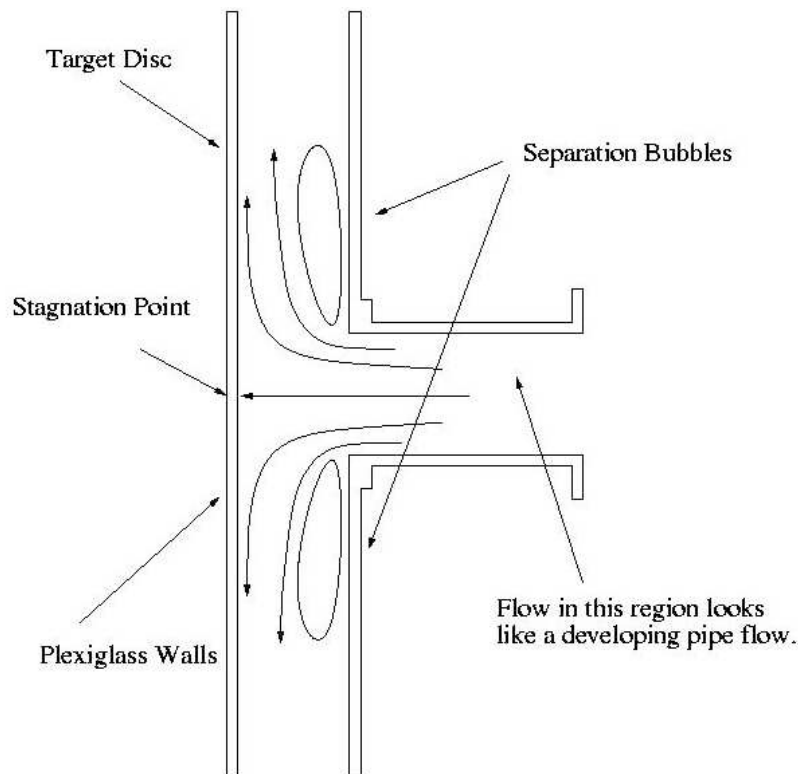
Figure 1. 2.—An approximate picture of the flow within the test section.

Disc major diameter = 1.22m

Tube inner diameter,
D = 216 mm (8.5")

Delivery tube length = 254mm
(10")
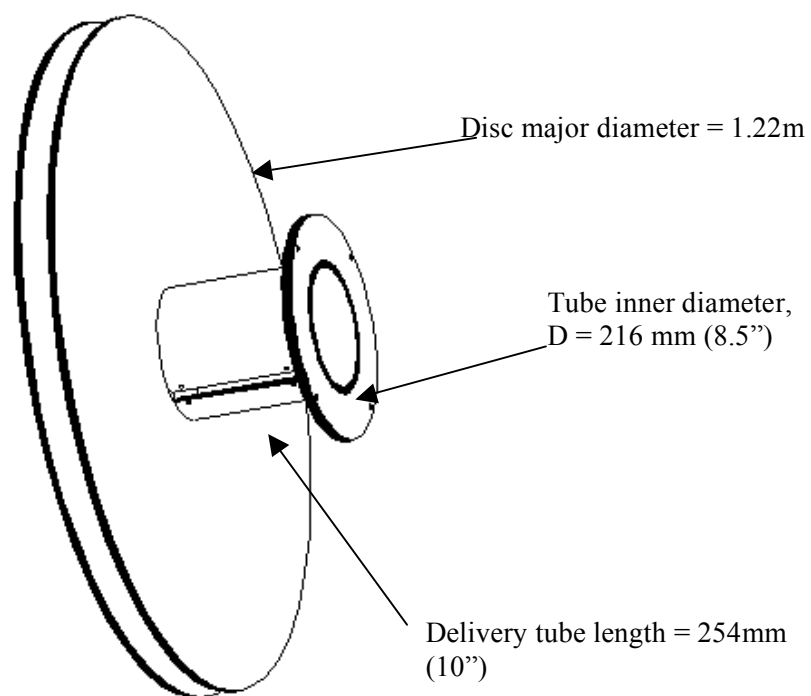
Figure 1.3.—A stylized version of the test section.

12.7 mm (.50) Hot Film
9.5 mm (.38) Hot Wire

38 mm (1.50)

3.2 mm (.125) Dia.   4.6 mm (.18) Dia.
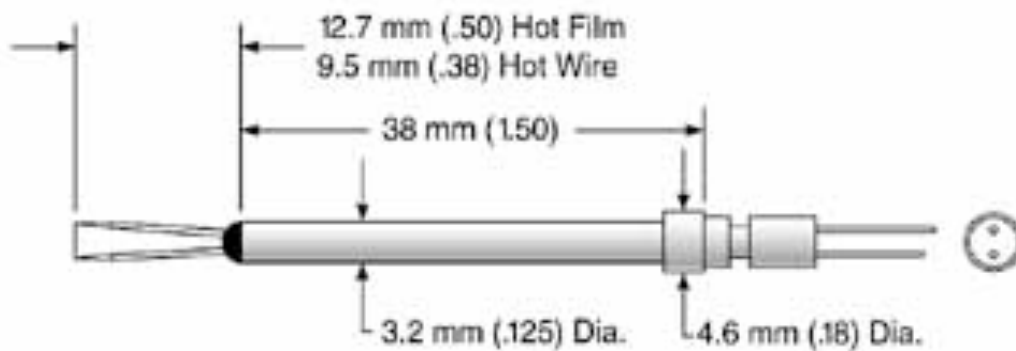
Figure 1.4.—A TSI model 1210 hot-wire probe.
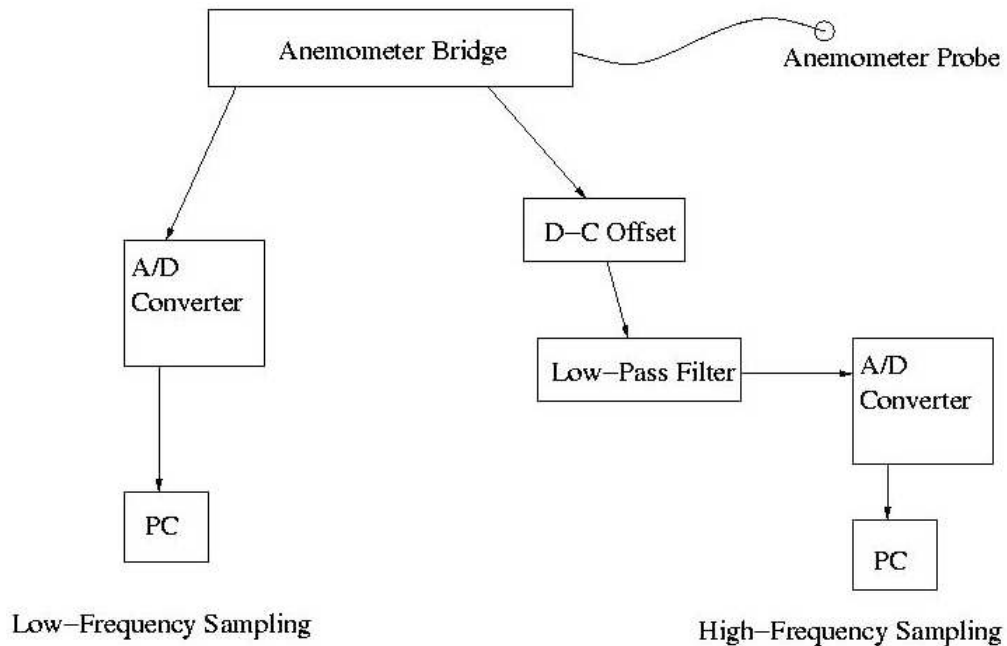
Figure 1.5.—A schematic of the data collection hardware.
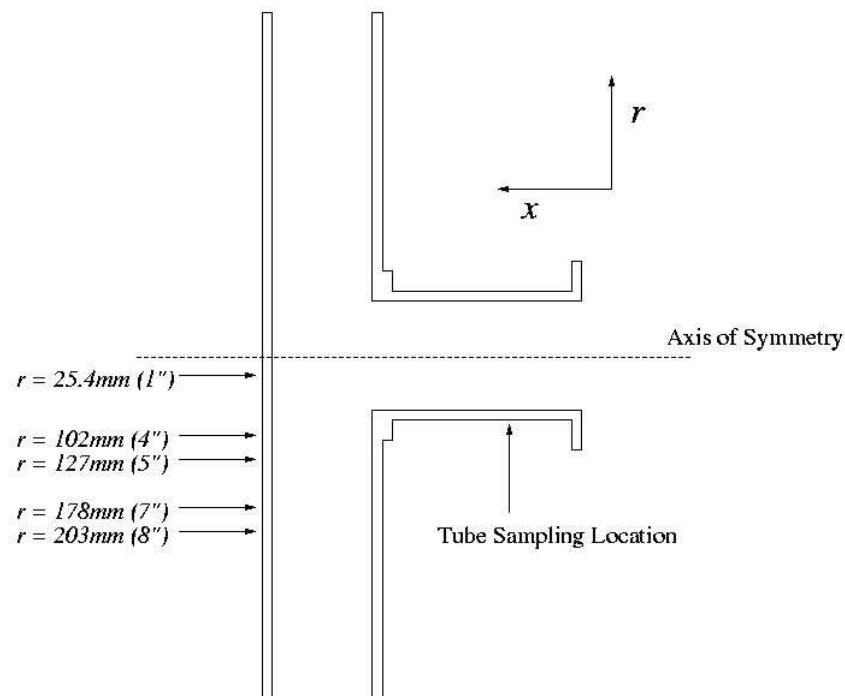
Figure 1.6.—A cross-section of the test section. Sampling stations are indicated with arrows. The "tube traverse location" was 127 mm (5 in.) downstream of the test section entrance. The tube traverse was in the "r" direction. All of the traverses in the disc space were in the "x" direction. This is also the view that the camera sees in flow visualization experiments. Essentially, the x-axis is in focus (i.e., $r = 0$).
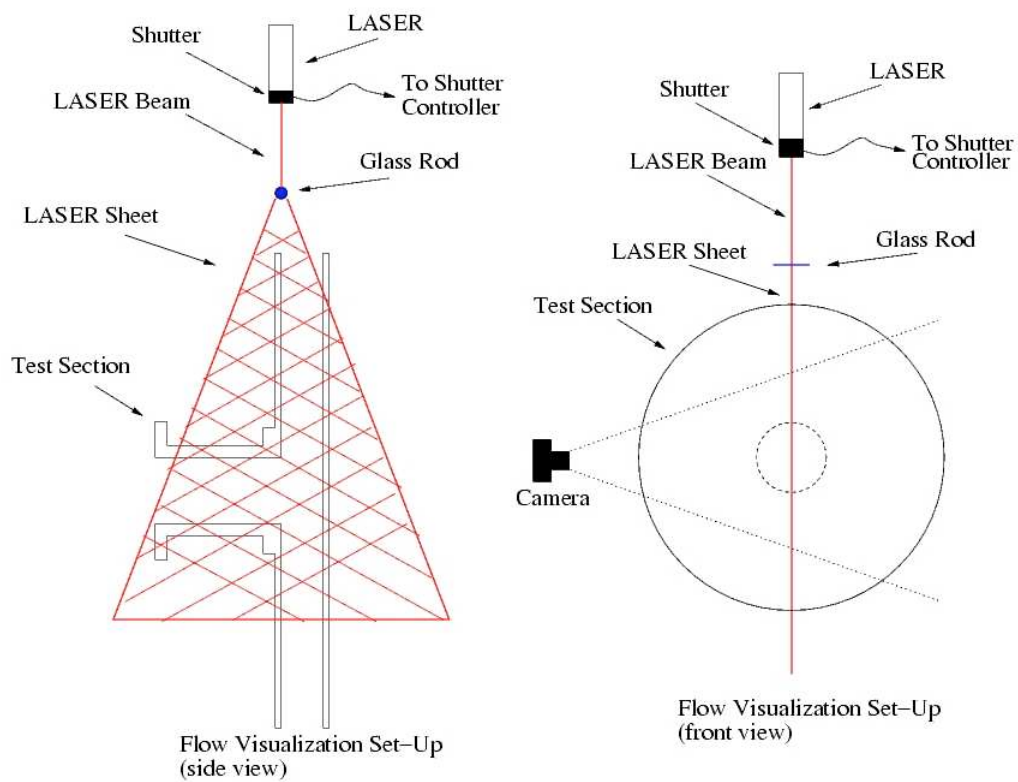
Figure 1.7.—Flow visualization hardware set up schematic.
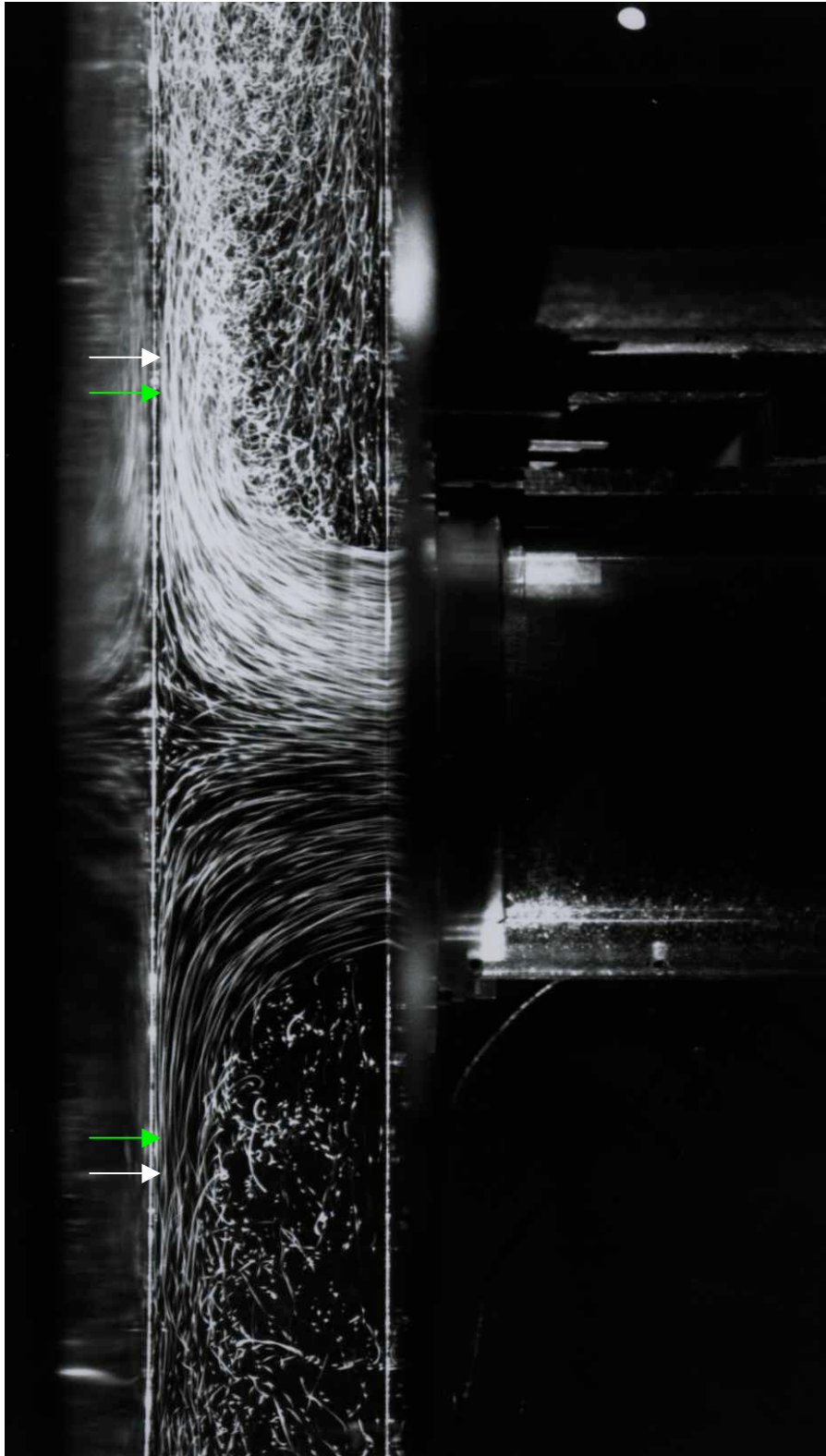
Figure 1.8.—Re = 17700, *S* = 127 mm (5 in.). Flow visualization indicates that transition occurs at approximately *r*/*D* = 1 (labeled with white arrows). Spectral data indicate that transition occurs at approximately *r*/*D* = 0.941 (labeled with green arrows, or gray if printed in black and white).
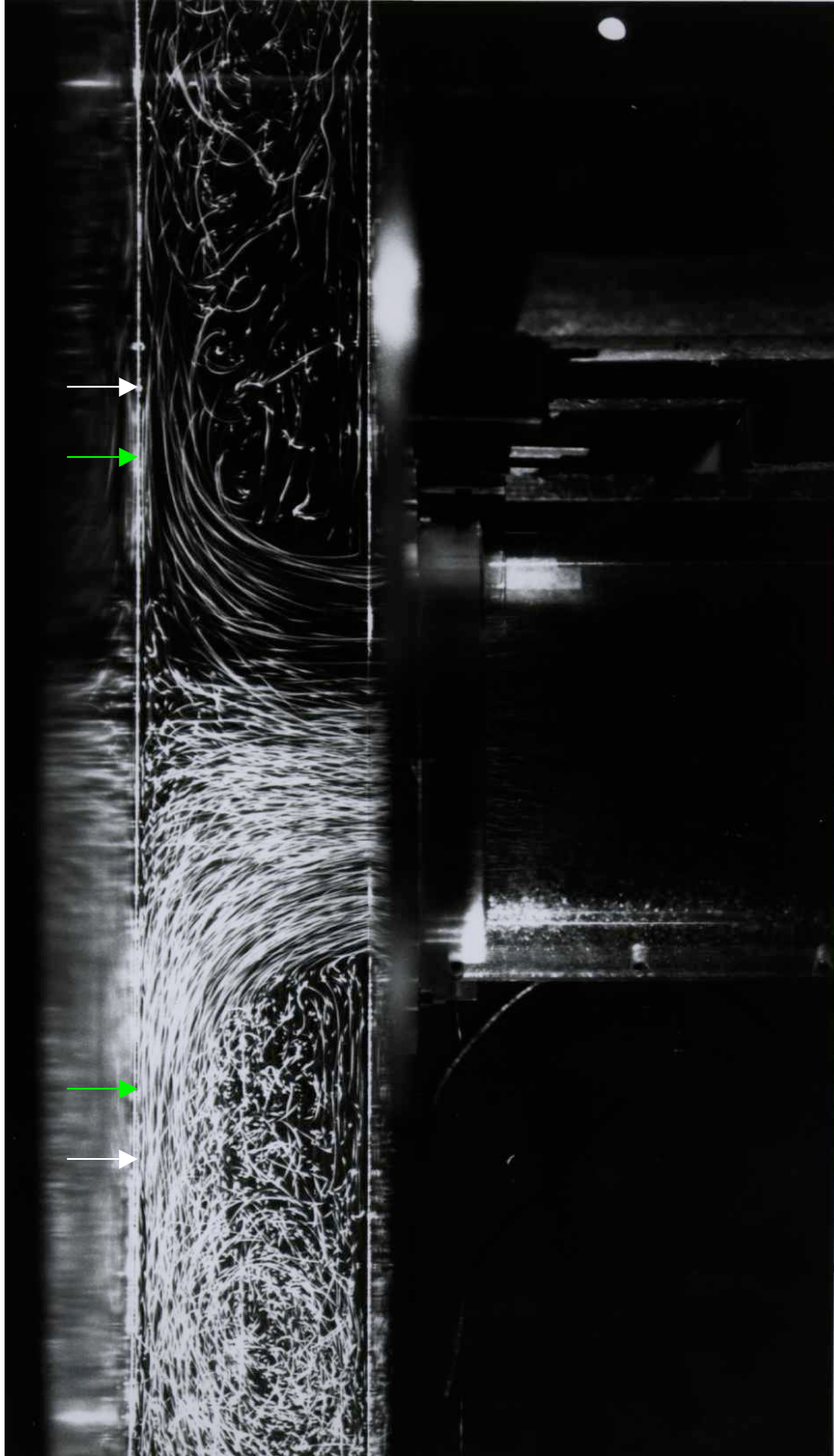
Figure 1.9.—Re = 7600, S = 127 mm (5 in.). Flow visualization indicates that transition occurs at approximately $r/D = 1$ (labeled with white arrows). Spectral data indicate that transition occurs at approximately $r/D = 0.824$ (labeled with green arrows, or gray if printed in black and white).
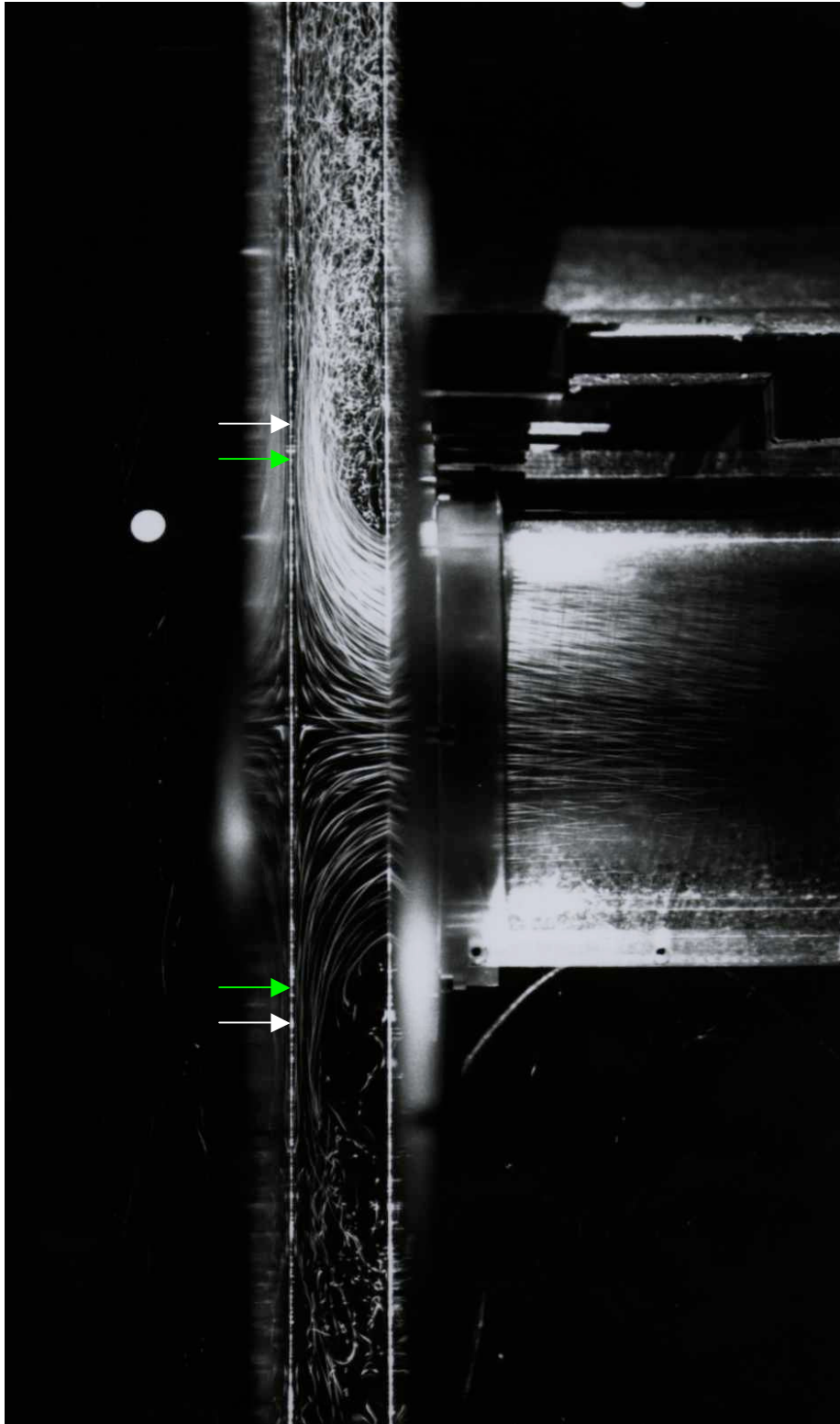
Figure 1.10.—Re = 17700, *S* = 54 mm (2.125 in.). Flow visualization indicates that transition occurs at approximately *r*/*D* = 0.8 (labeled with white arrows). Spectral data indicate that transition occurs at approximately *r*/*D* = 0.706 (labeled with green arrows, or gray if printed in black and white).
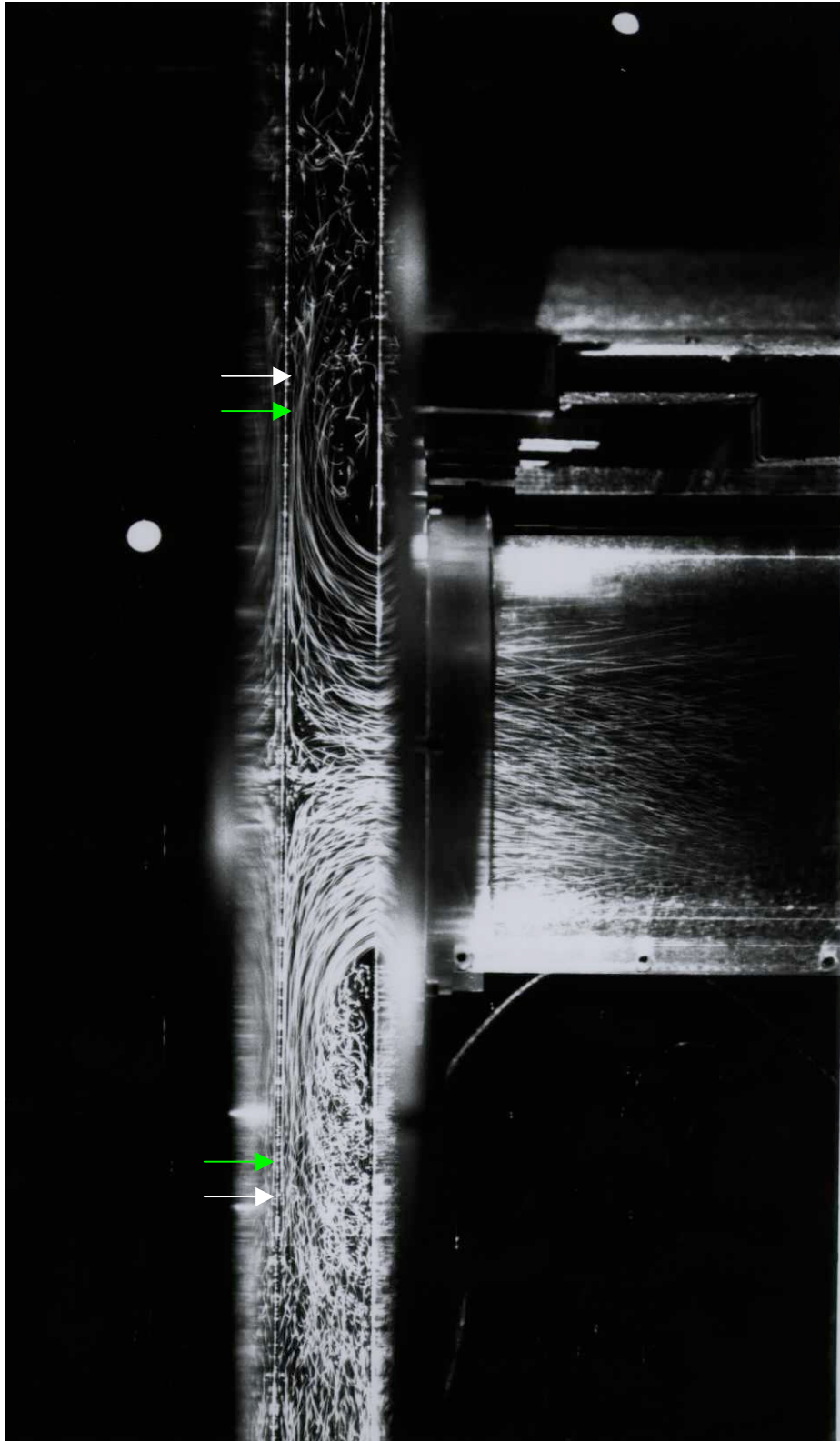
Figure 1.11.—Re = 7600, *S* = 54 mm (2.125 in.). Flow visualization indicates that transition occurs at approximately *r/D* = 1 (labeled with white arrows). Spectral data indicate that transition occurs at approximately *r/D* = 0.941 (labeled with green arrows, or gray if printed in black and white).
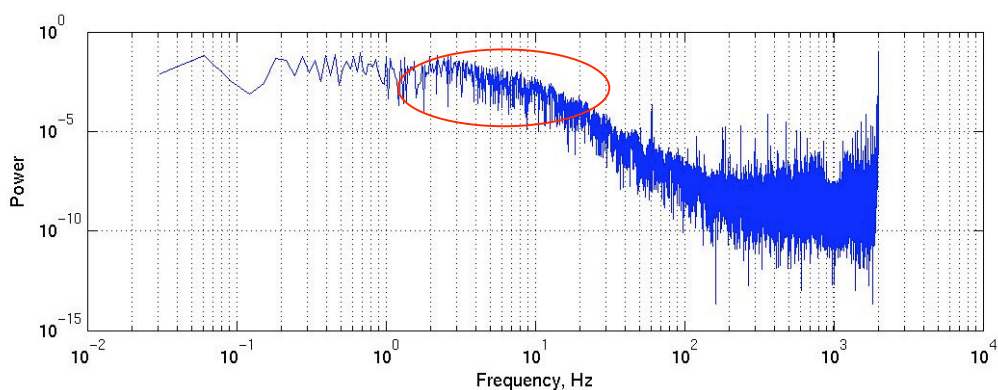
Figure 1.12.—A typical FFT of a velocity-time signal. The "power" and the corresponding frequencies in the oval are associated with transition to turbulence.
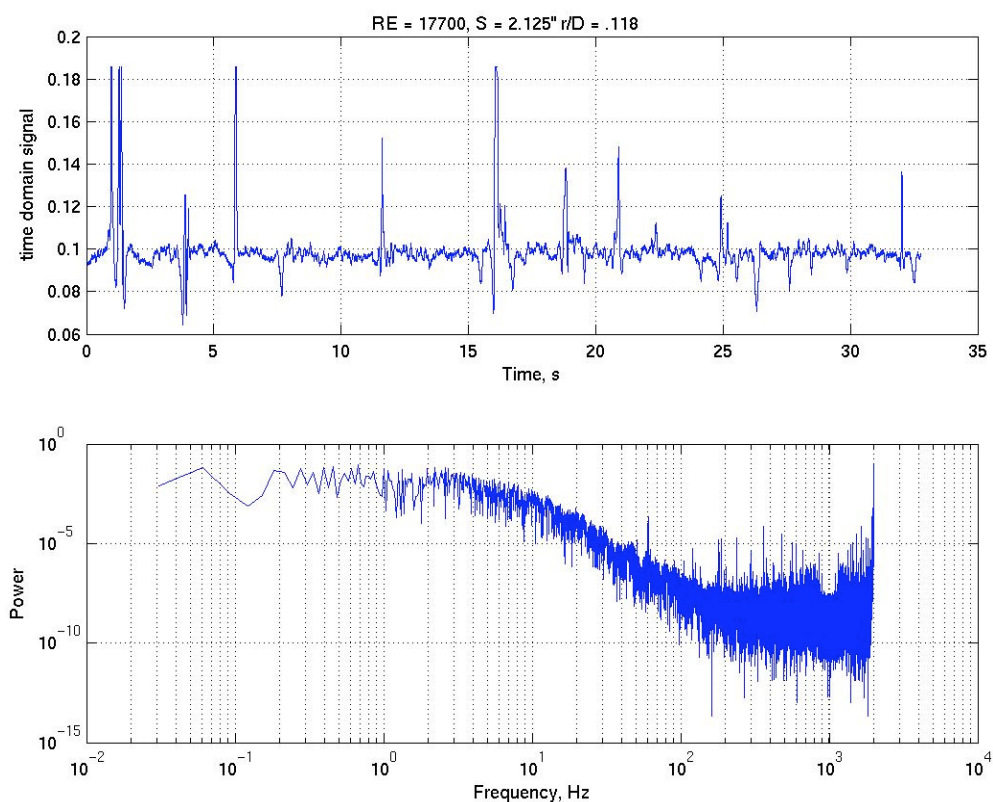
Figure 1.13.—A picture of the velocity-time and velocity-FFT signals for the case RE = 17700, S = 54 mm (2.125 in.), r/D = 0.118. The distance from the impingement target plate = 1 mm (0.040 in.). Sampling frequency = 2000 Hz. Cutoff frequency = 750 Hz.
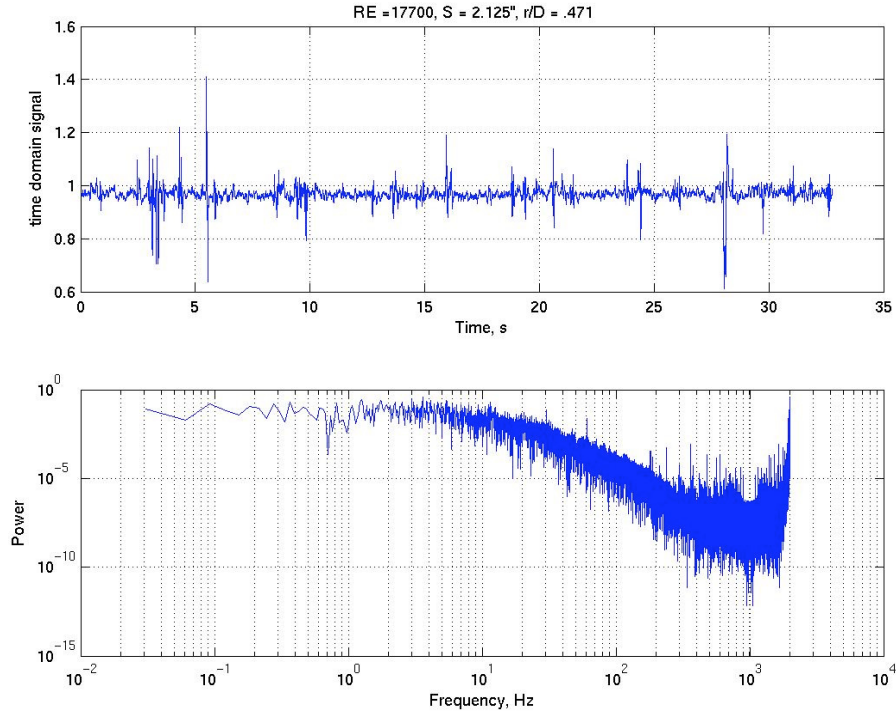
Figure 1.14.—A picture of the velocity-time and velocity-FFT signals for the case RE = 17700, S = 54 mm (2.125 in.), r/D = 0.471. The distance from the impingement target plate = 1 mm (0.040 in.). Sampling frequency = 2000 Hz. Cutoff frequency = 750 Hz.
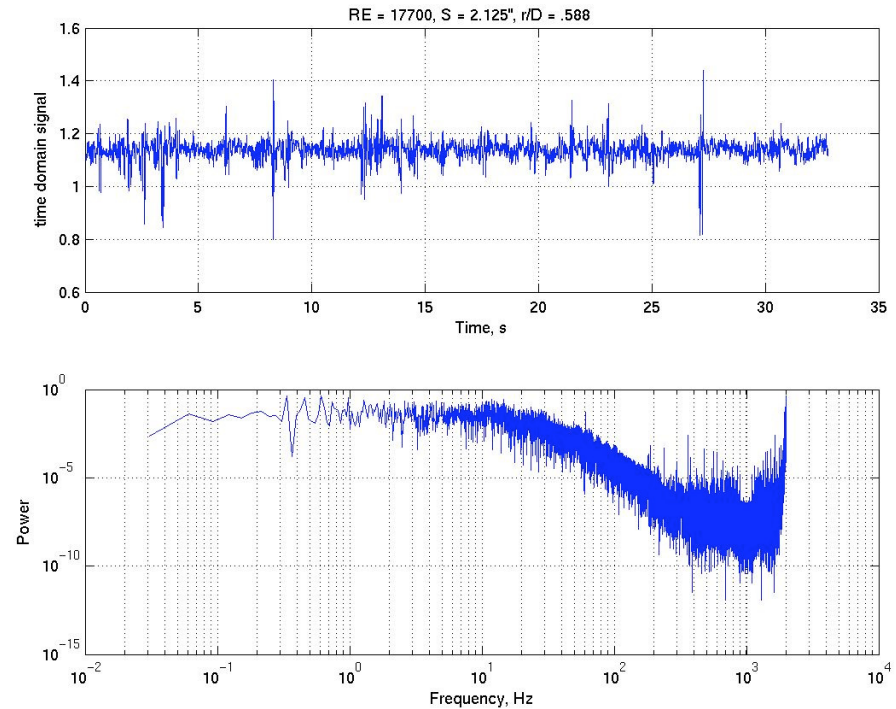
Figure 1.15.—A picture of the velocity-time and velocity-FFT signals for the case RE = 17700, S = 54 mm (2.125 in.), r/D = 0.588. The distance from the impingement target plate =1 mm (0.040 in.). Sampling frequency = 2000 Hz. Cutoff frequency = 750 Hz.
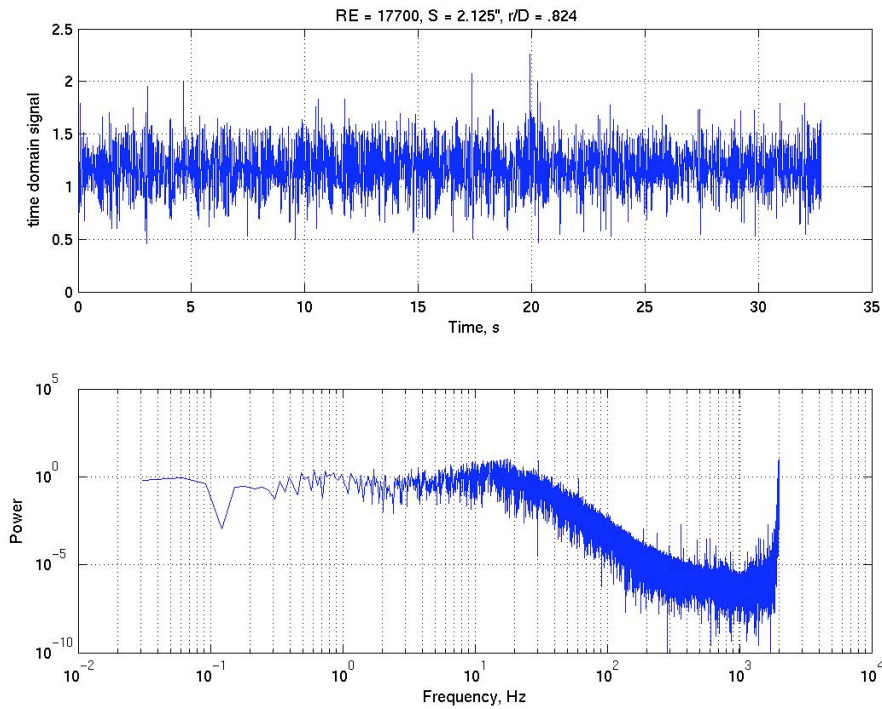
Figure 1.16.—A picture of the velocity-time and velocity-FFT signals for the case RE = 17700, S = 54 mm (2.125 in.), r/D = 0.824. The distance from the impingement target plate =1 mm (0.040 in.). Sampling frequency = 2000 Hz. Cutoff frequency = 750 Hz.
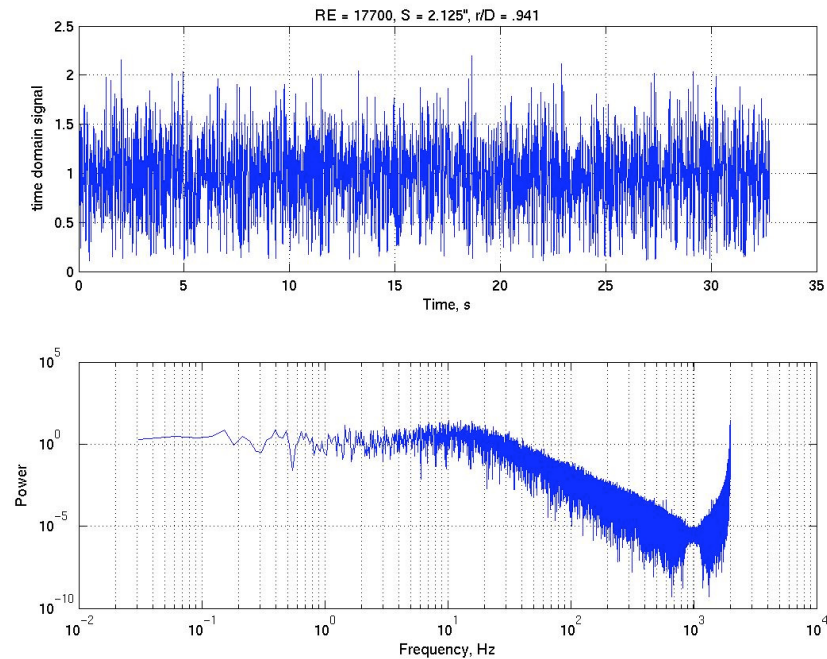
Figure 1.17.—A picture of the velocity-time and velocity-FFT signals for the case RE = 17700, S = 54 mm (2.125 in.), r/D = 0.941. The distance from the impingement target plate = 1 mm (0.040 in.). Sampling frequency = 2000 Hz. Cutoff frequency = 750 Hz.
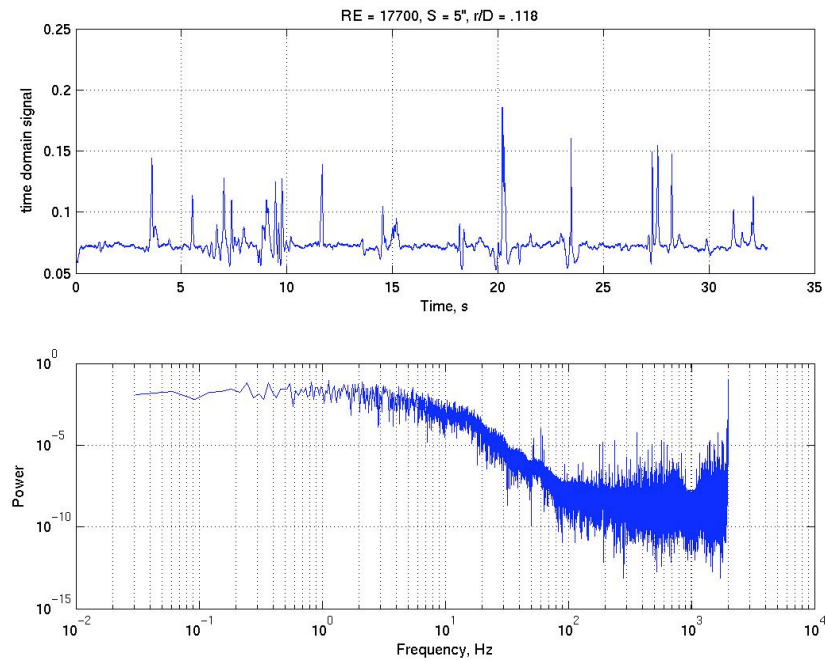
Figure 1.18.—A picture of the velocity-time and velocity-FFT signals for the case RE = 17700, S = 127 mm (5 in.), r/D = 0.118. The distance from the impingement target plate = 1 mm (0.040 in.). Sampling frequency = 2000 Hz. Cutoff frequency = 750 Hz.
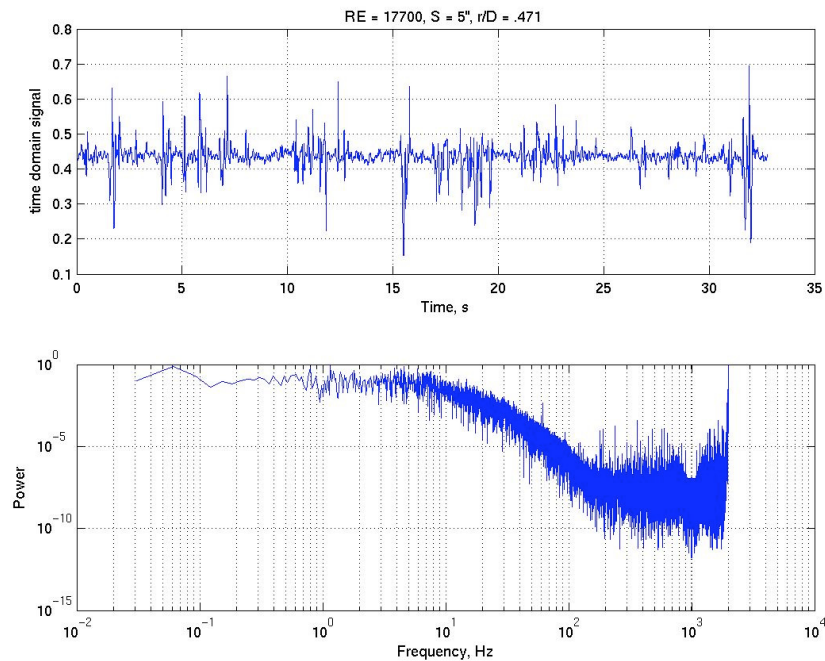
Figure 1.19.—A picture of the velocity-time and velocity-FFT signals for the case RE = 17700, S = 127 mm (5 in.), r/D = 0.471. The distance from the impingement target plate = 1 mm (0.040 in.). Sampling frequency = 2000 Hz. Cutoff frequency = 750 Hz.
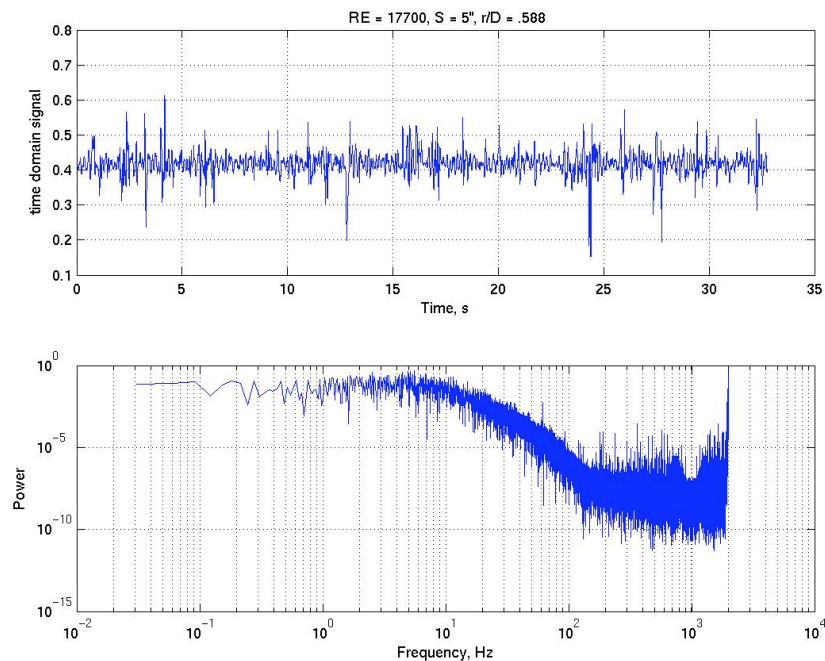
Figure 1.20.—A picture of the velocity-time and velocity-FFT signals for the case RE = 17700, S = 127 mm (5 in.), r/D = 0.588. The distance from the impingement target plate = 1 mm (0.040 in.). Sampling frequency = 2000 Hz. Cutoff frequency = 750 Hz.
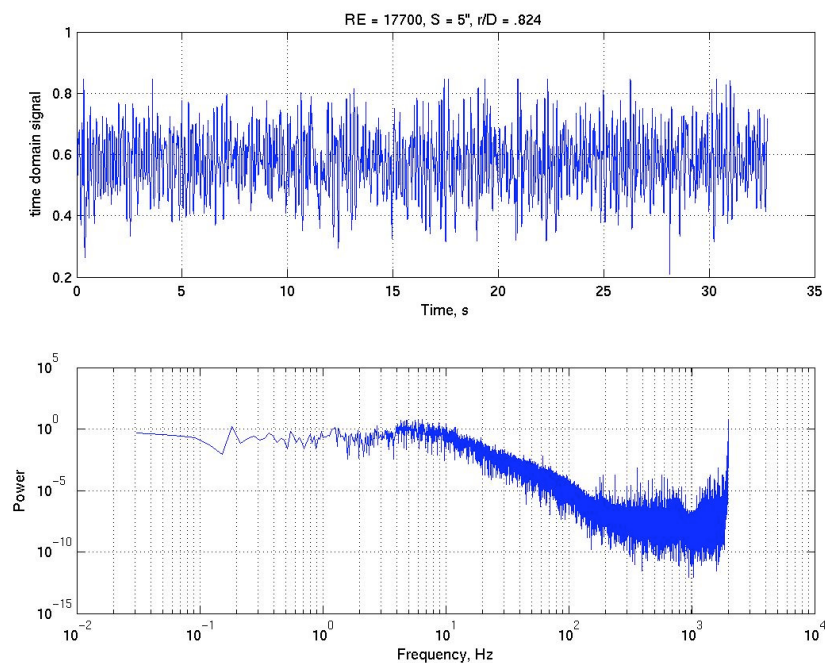
Figure 1.21.—A picture of the velocity-time and velocity-FFT signals for the case RE = 17700, S = 127 mm (5 in.), r/D = 0.824. The distance from the impingement target plate = 1 mm (0.040 in.). Sampling frequency = 2000 Hz. Cutoff frequency = 750 Hz.
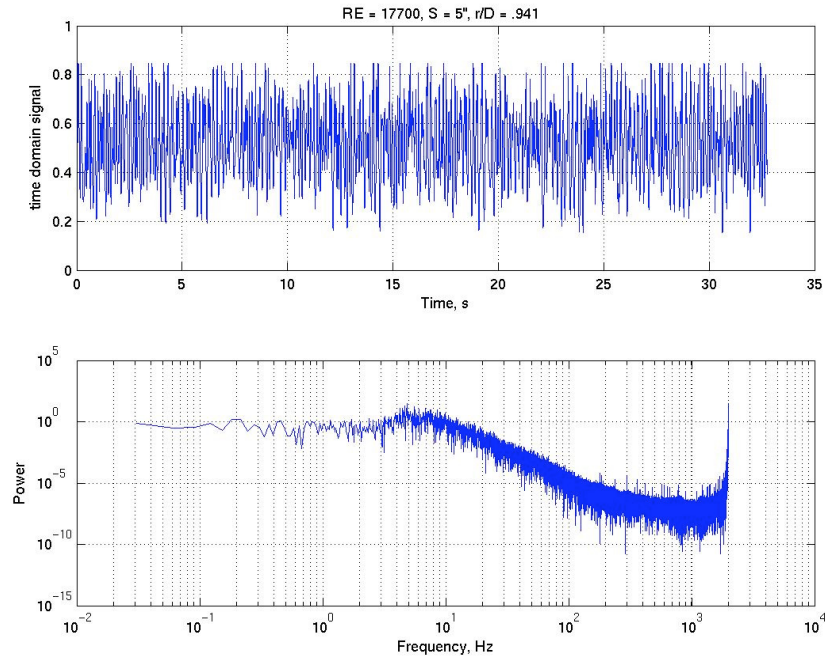
Figure 1.22.—A picture of the velocity-time and velocity-FFT signals for the case RE = 17700, *S* = 127 mm (5 in.), *r/D* = 0.941. The distance from the impingement target plate = 1 mm (0.040 in.). Sampling frequency = 2000 Hz. Cutoff frequency = 750 Hz.
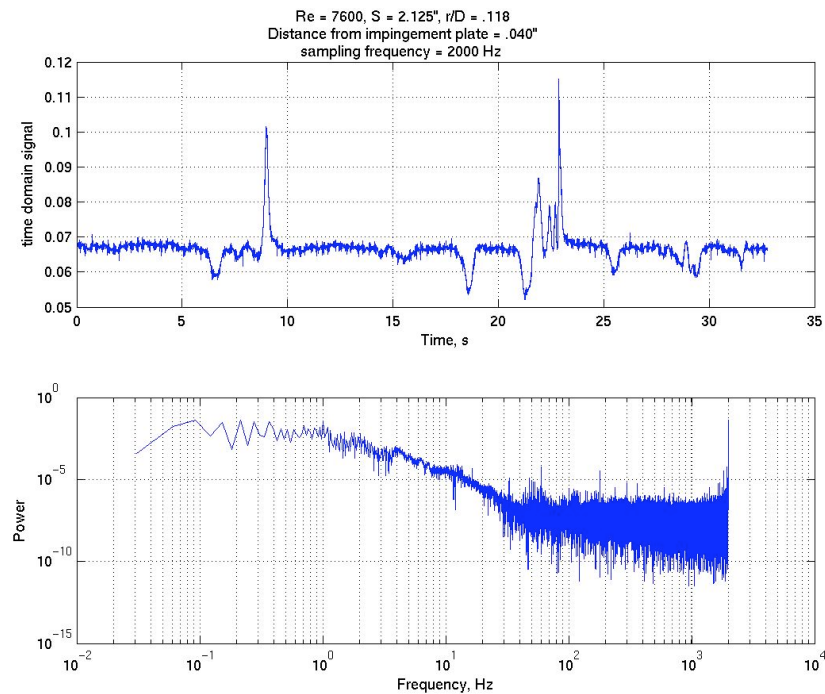
Figure 1.23.—A picture of the velocity-time and velocity-FFT signals for the case RE = 7600, *S* = 54 mm (2.125 in.), *r/D* = 0.118. The distance from the impingement target plate = 1 mm (0.040 in.). Sampling frequency = 2000 Hz. Cutoff frequency = 750 Hz.
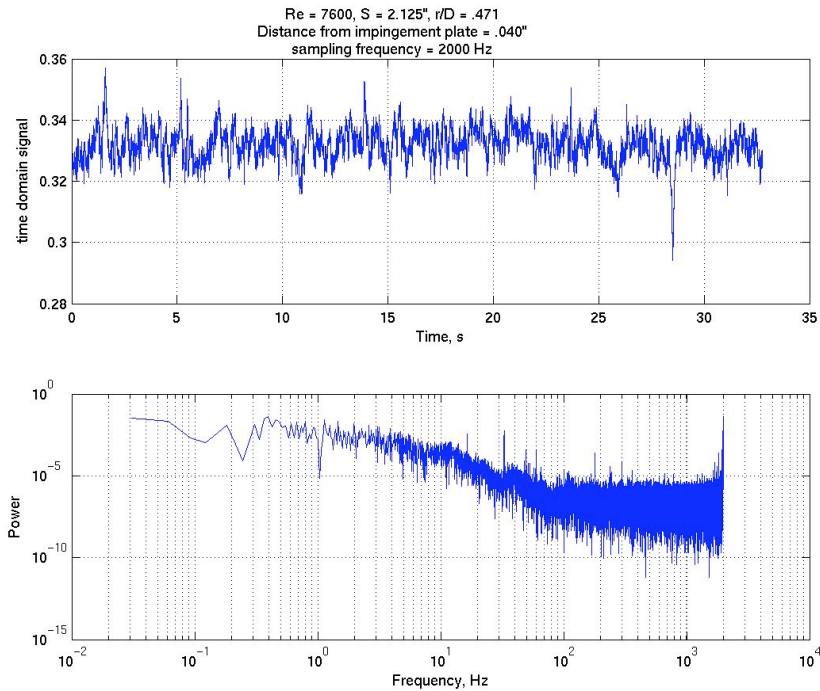
Figure 1.24.—A picture of the velocity-time and velocity-FFT signals for the case RE = 7600, *S* = 54 mm (2.125 in.), *r/D* = 0.471. The distance from the impingement target plate = 1 mm (0.040 in.). Sampling frequency = 2000 Hz. Cutoff frequency = 750 Hz.
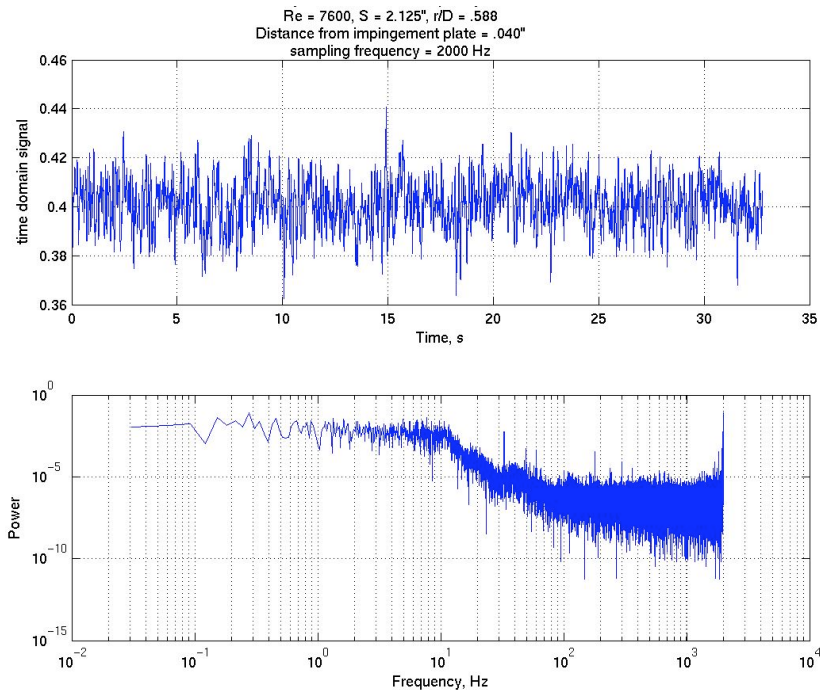
Figure 1.25.—A picture of the velocity-time and velocity-FFT signals for the case RE = 7600, *S* = 54 mm (2.125 in.), *r/D* = 0.588. The distance from the impingement target plate = 1 mm (0.040 in.). Sampling frequency = 2000 Hz. Cutoff frequency = 750 Hz.
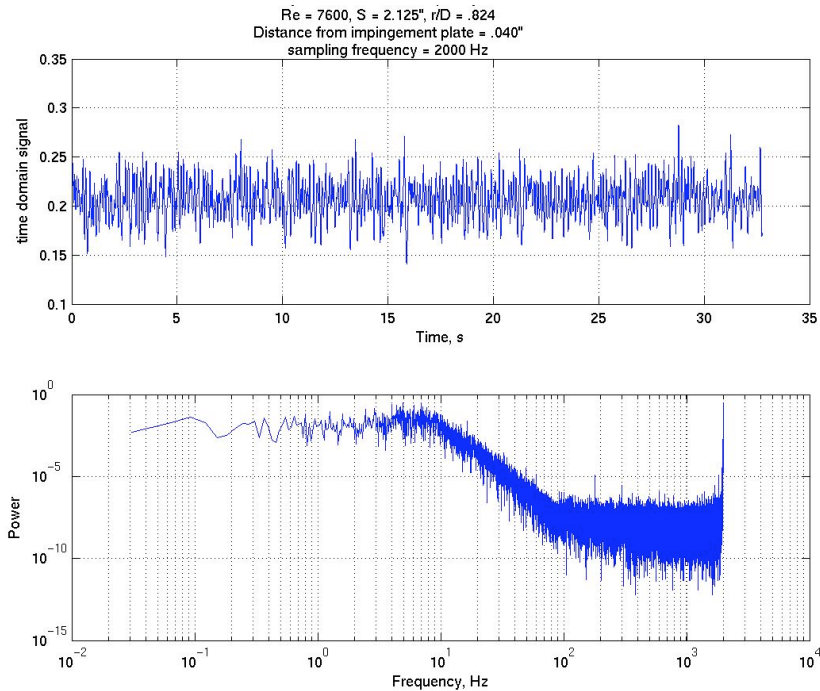
Figure 1.26.—A picture of the velocity-time and velocity-FFT signals for the case RE = 7600, S = 54 mm (2.125 in.), r/D = 0.824. The distance from the impingement target plate = 1 mm (0.040 in.). Sampling frequency = 2000 Hz. Cutoff frequency = 750 Hz.
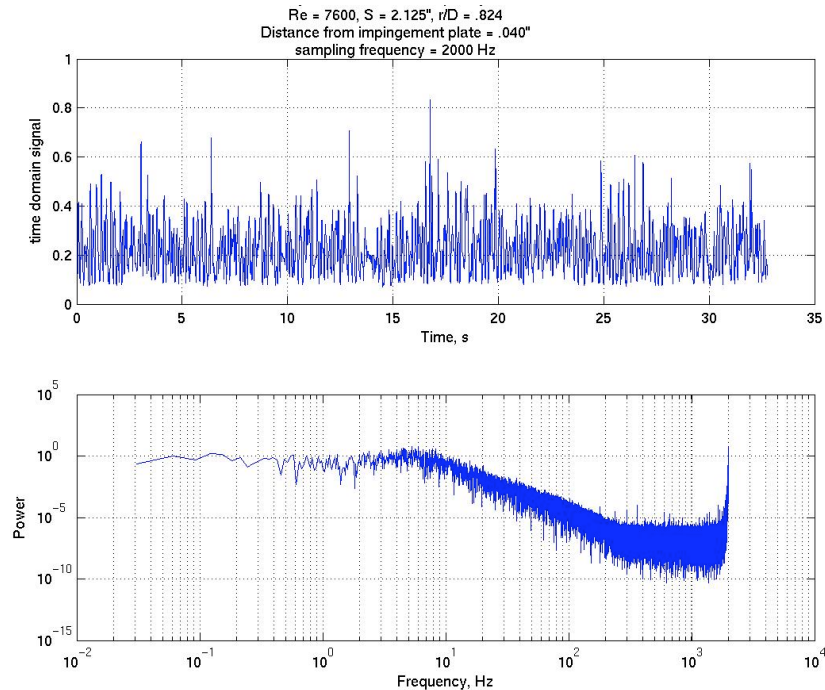
Figure 1.27.—A picture of the velocity-time and velocity-FFT signals for the case RE = 7600, S = 54 mm (2.125 in.), r/D = 0.941. The distance from the impingement target plate = 1 mm (0.040 in.). Sampling frequency = 2000 Hz. Cutoff frequency = 750 Hz.
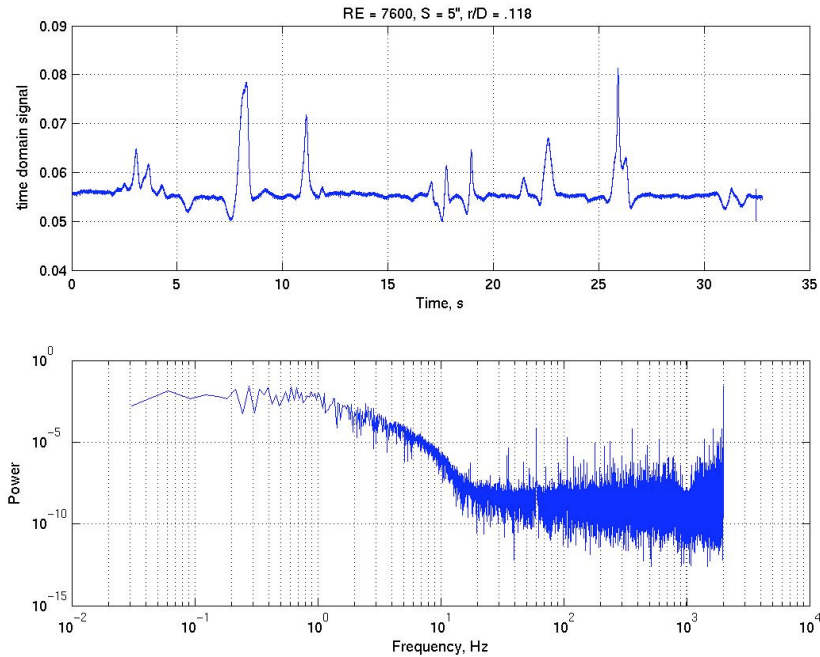
Figure 1.28.—A picture of the velocity-time and velocity-FFT signals for the case RE = 7600, *S* = 127 mm (5 in.), *r/D* = 0.118. The distance from the impingement target plate = 1 mm (0.040 in.). Sampling frequency = 2000 Hz. Cutoff frequency = 750 Hz.
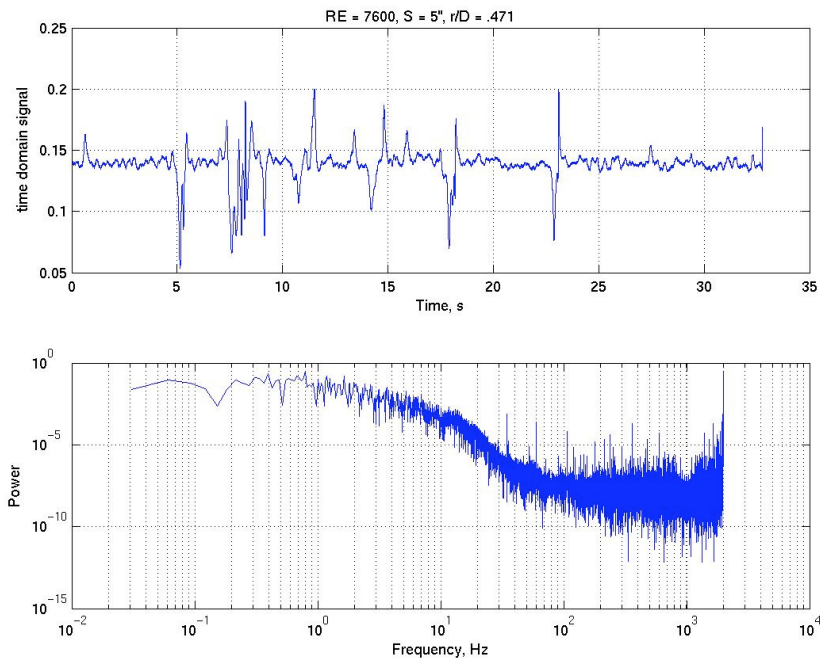
Figure 1.29.—A picture of the velocity-time and velocity-FFT signals for the case RE = 7600, *S* = 127 mm (5 in.), *r/D* = 0.471. The distance from the impingement target plate = 1 mm (0.040 in.). Sampling frequency = 2000 Hz. Cutoff frequency = 750 Hz.
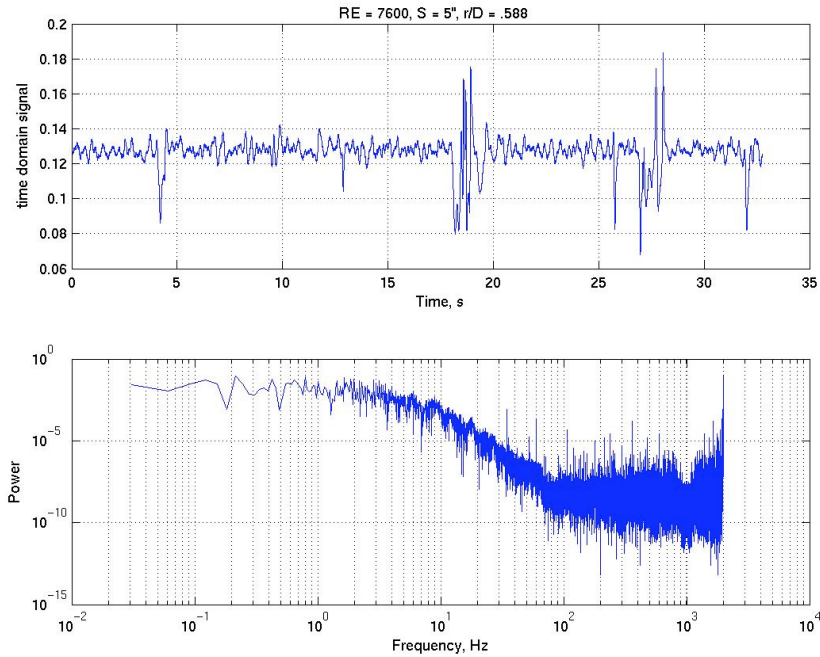
Figure 1.30.—A picture of the velocity-time and velocity-FFT signals for the case RE = 7600, S = 127 mm (5 in.), r/D = 0.588. The distance from the impingement target plate = 1 mm (0.040 in.). Sampling frequency = 2000 Hz. Cutoff frequency = 750 Hz.
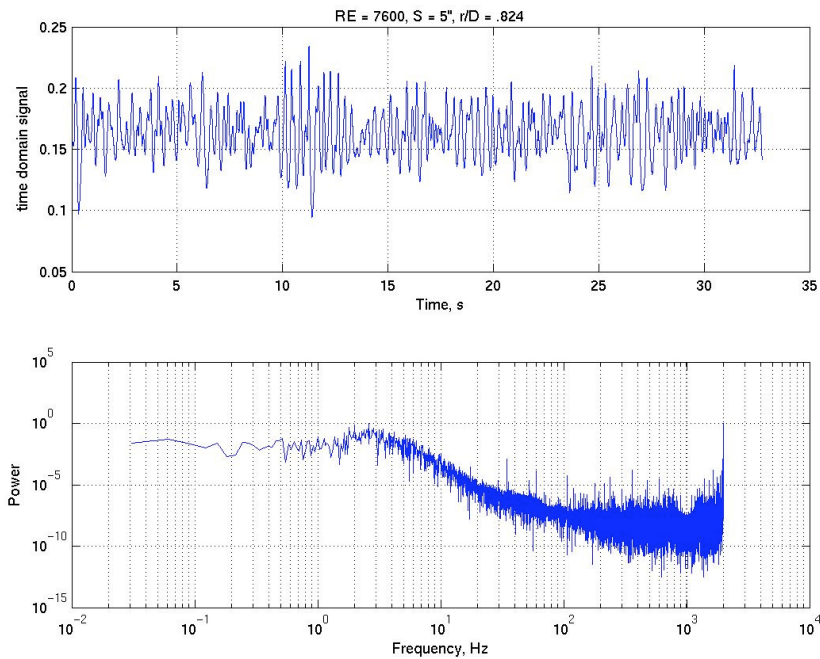
Figure 1.31.—A picture of the velocity-time and velocity-FFT signals for the case RE = 7600, S = 127 mm (5 in.), r/D = 0.824. The distance from the impingement target plate = 1 mm (0.040 in.). Sampling frequency = 2000 Hz. Cutoff frequency = 750 Hz.
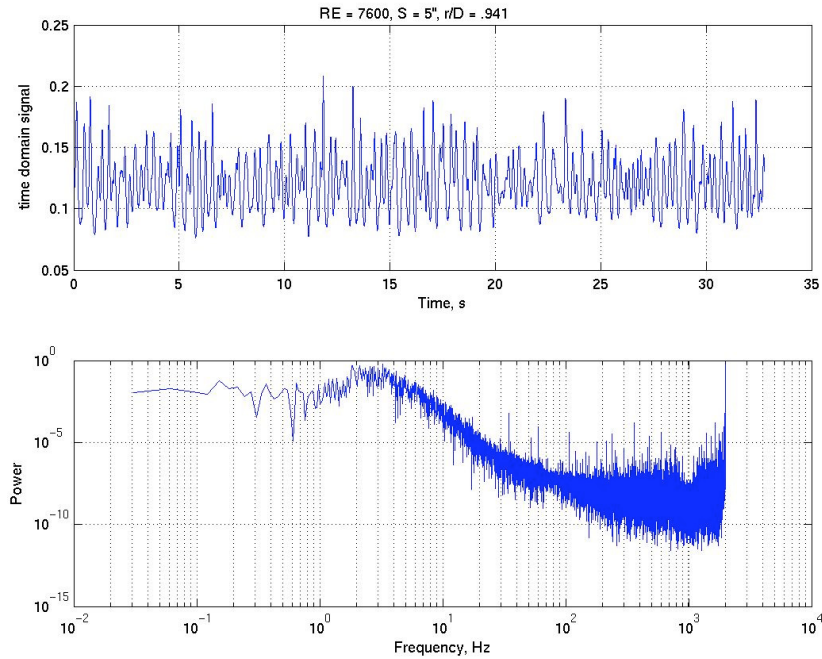
Figure 1.32.—A picture of the velocity-time and velocity-FFT signals for the case RE = 7600, *S* = 127 mm (5 in.), *r/D* = 0.941. The distance from the impingement target plate = 1 mm (0.040 in.). Sampling frequency = 2000 Hz. Cutoff frequency = 750 Hz.
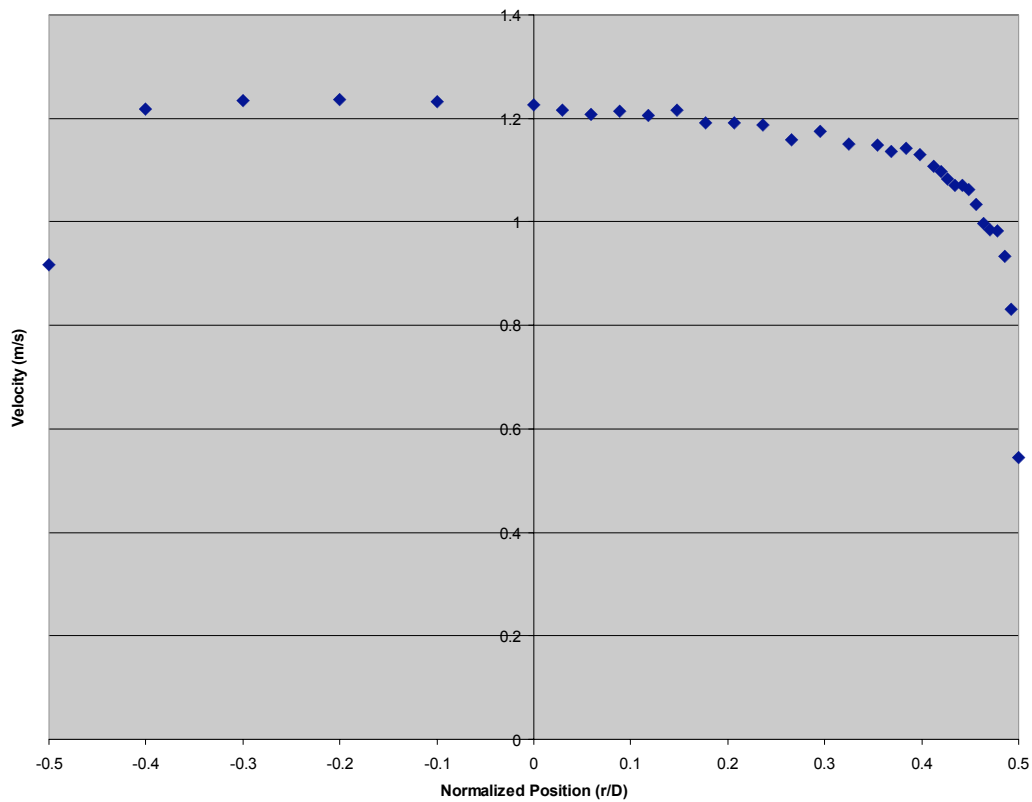
Figure 1.33.—Average velocity profile in the tube space for the case Re = 17700, S = 54 mm (2.125 in.).
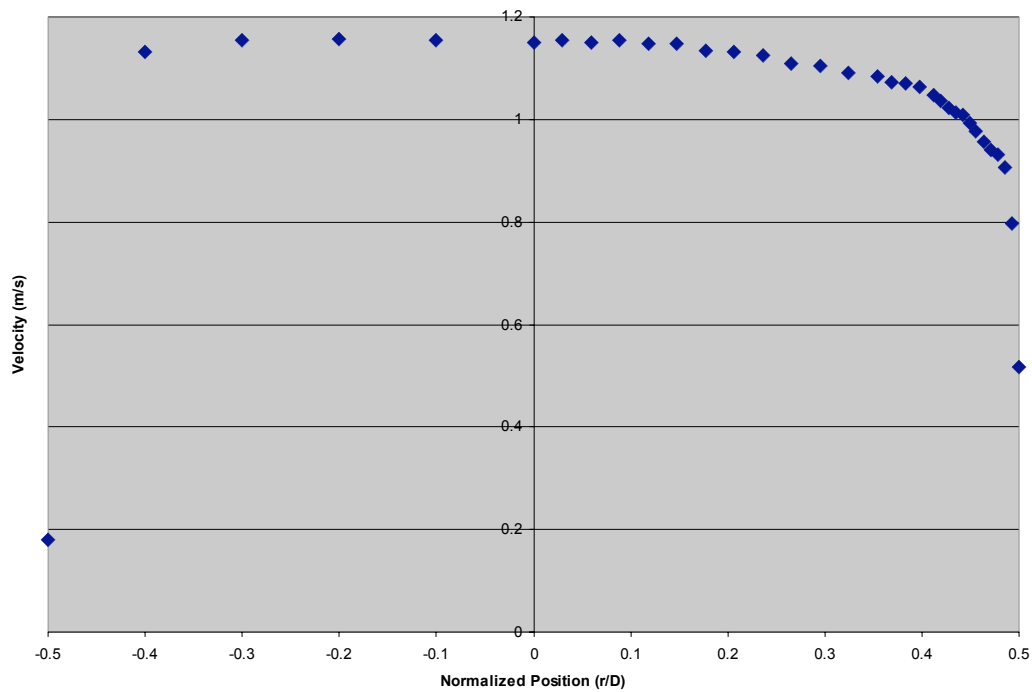
Figure 1.34.—Average velocity profile in the tube space for the case Re = 17700, S = 127 mm (5 in.).
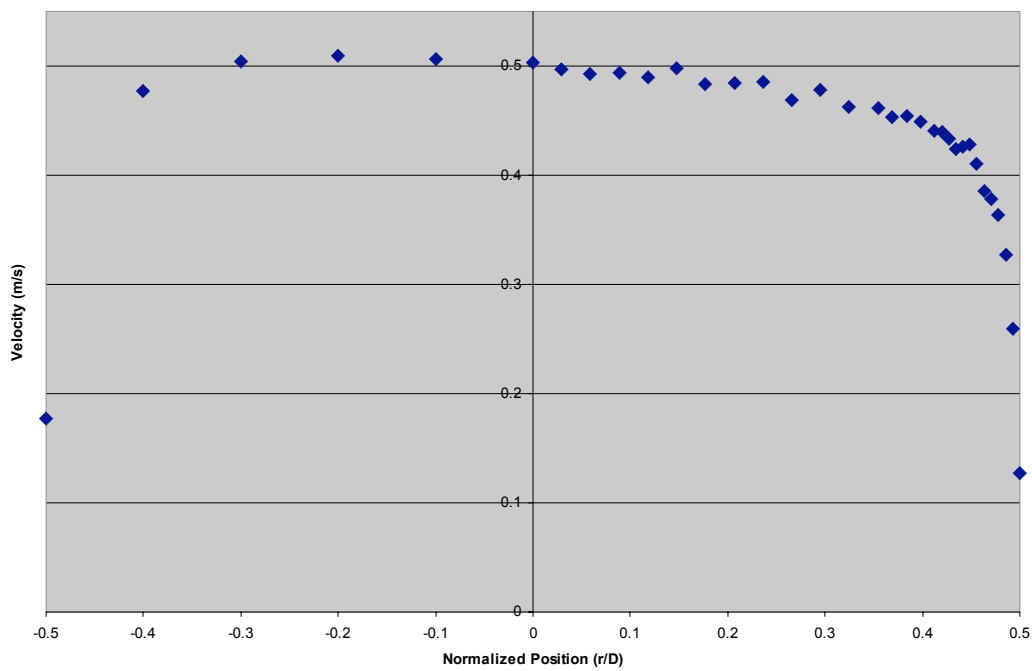
Figure 1.35.—Average velocity profile in the tube space for the case Re = 7600, S = 54 mm (2.125 in.).
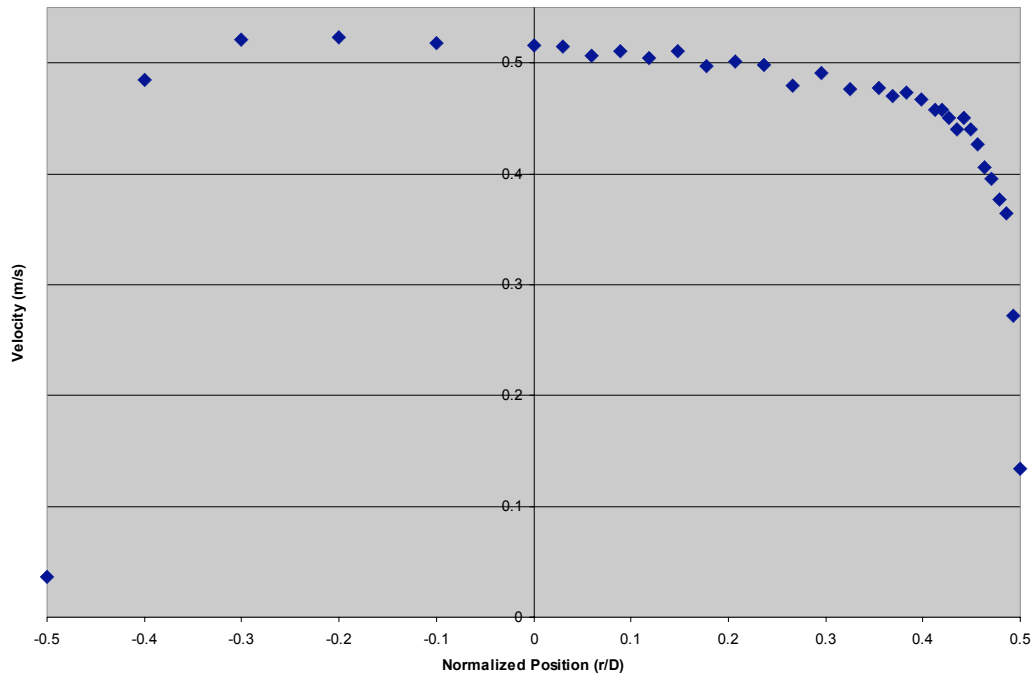
Figure 1.36.—Average velocity profile in the tube space for the case Re = 7600,
  S = 127 mm (5 in.).
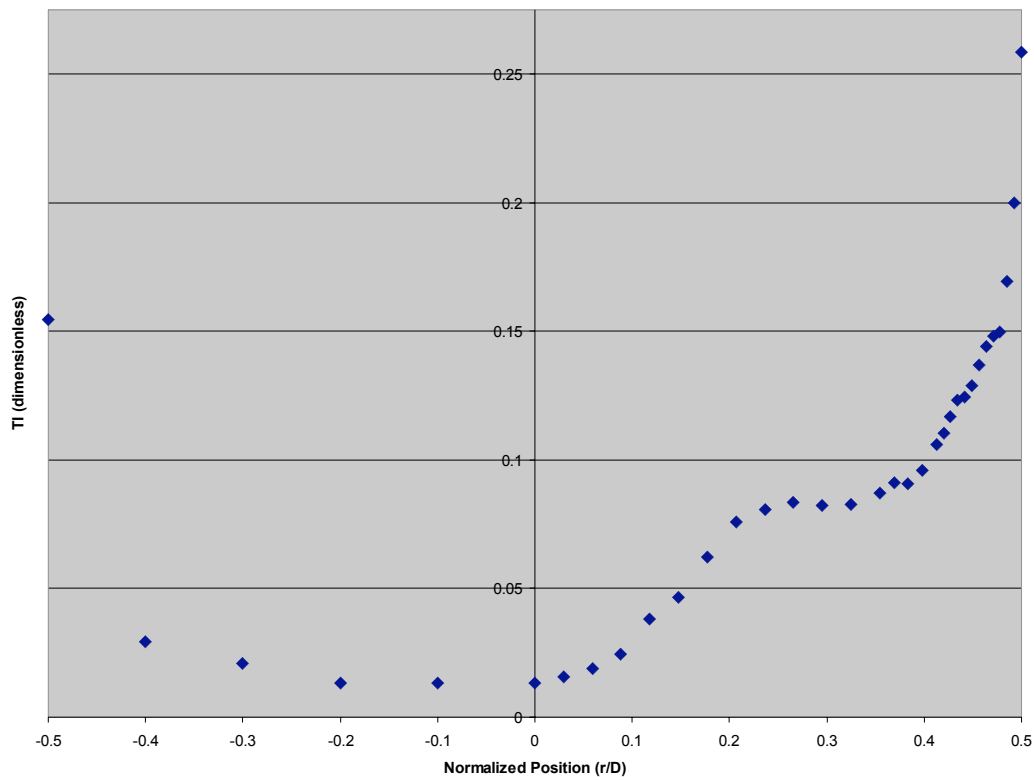
Figure 1.37.—Turbulence intensity in the tube space for the case Re = 17700,
  S = 54 mm (2.125 in.).
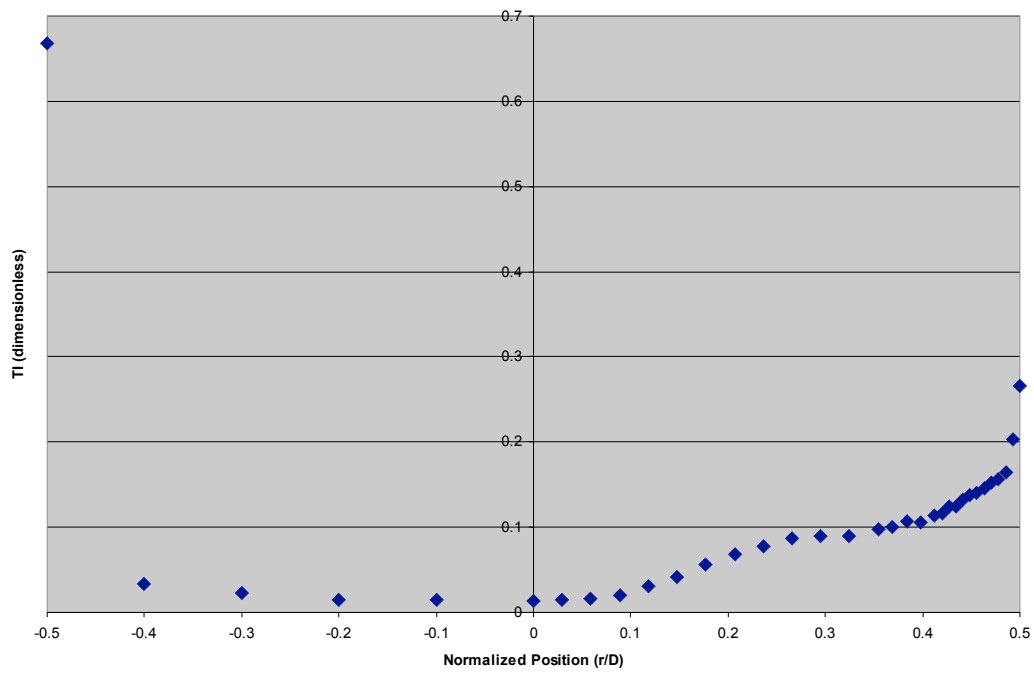
Figure 1.38.—Turbulence intensity in the tube space for the case Re = 17700,
  S = 127 mm (5 in.).
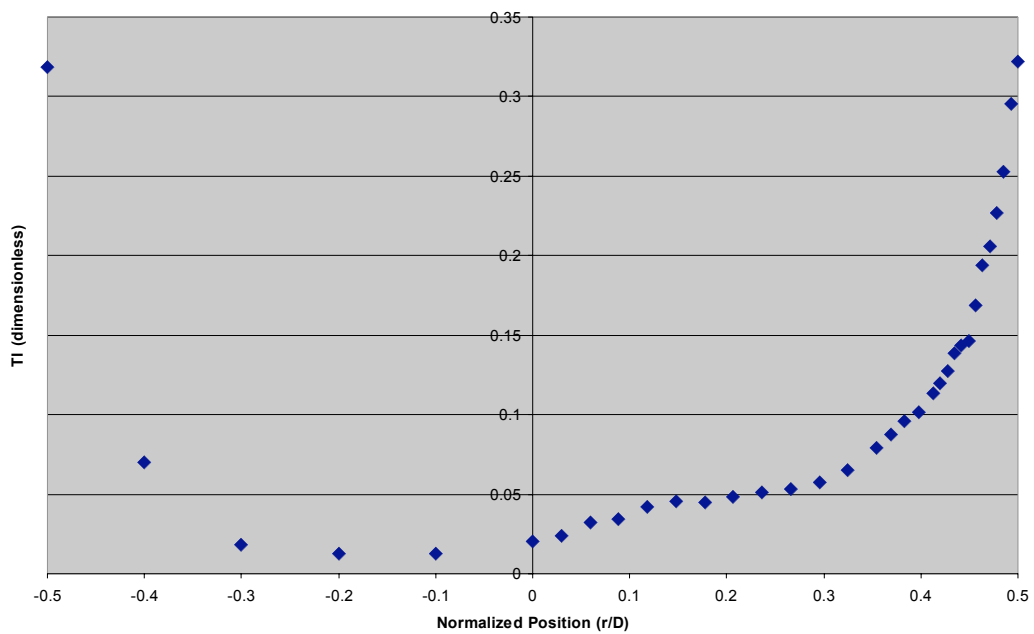
Figure 1.39.—Turbulence intensity in the tube space for the case Re = 7600,
  S = 54 mm (2.125 in.).
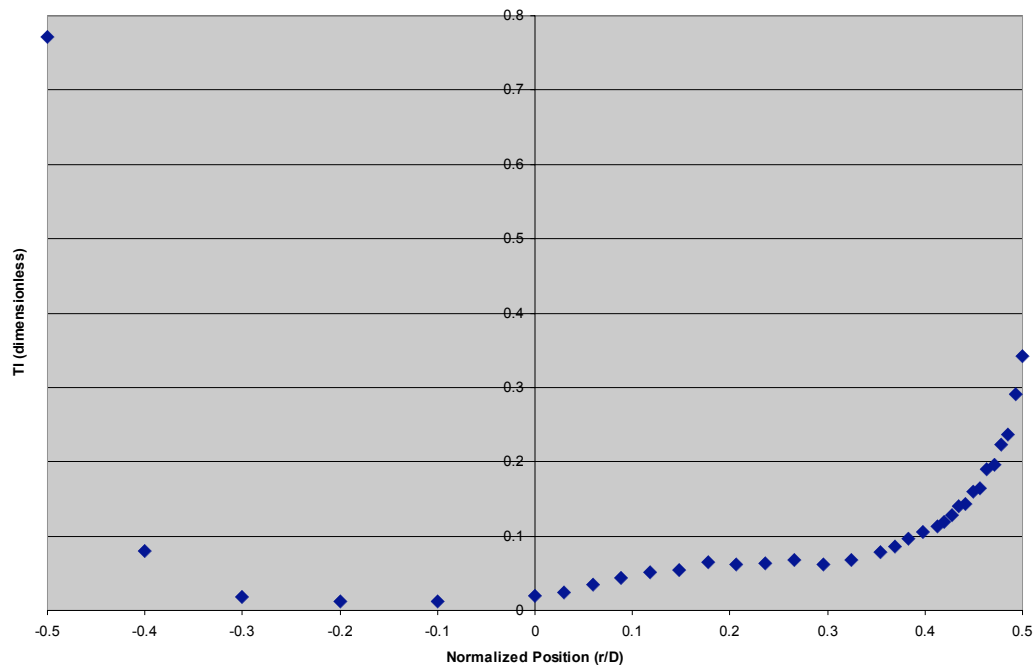
Figure 1.40.—Turbulence intensity in the tube space for the case Re = 7600, S = 127 mm (5 in.).
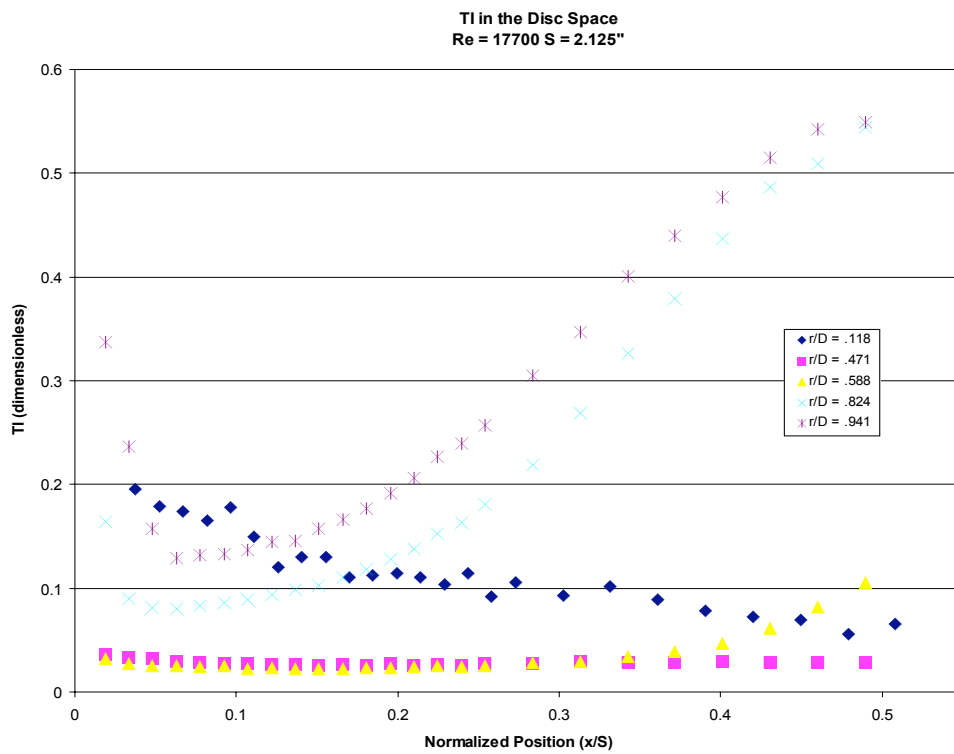
Figure 1.41.—Turbulence intensities in the disc space for the case Re = 17700, S = 54 mm (2.125 in.).
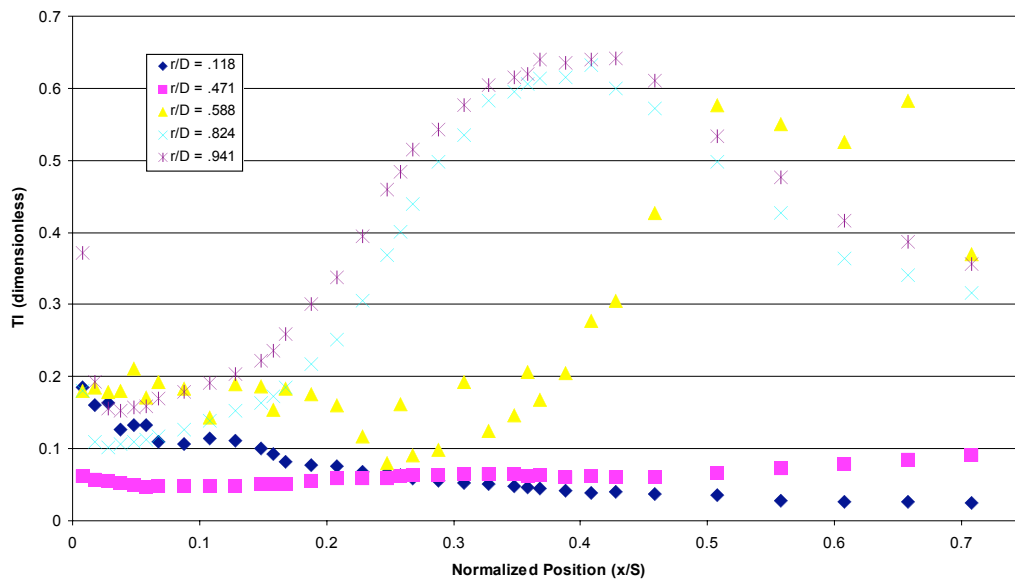
Figure 1.42.—Turbulence intensities in the disc space for the case Re = 17700,
 S = 127 mm (5 in.).
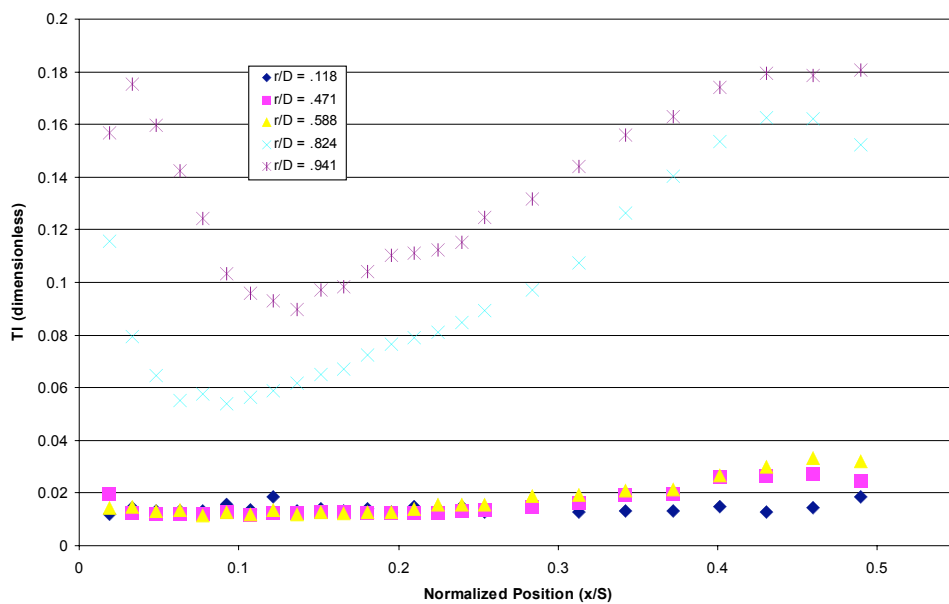
Figure 1.43.—Turbulence intensities in the disc space for the case Re = 7600,
 S = 54 mm (2.125 in.).
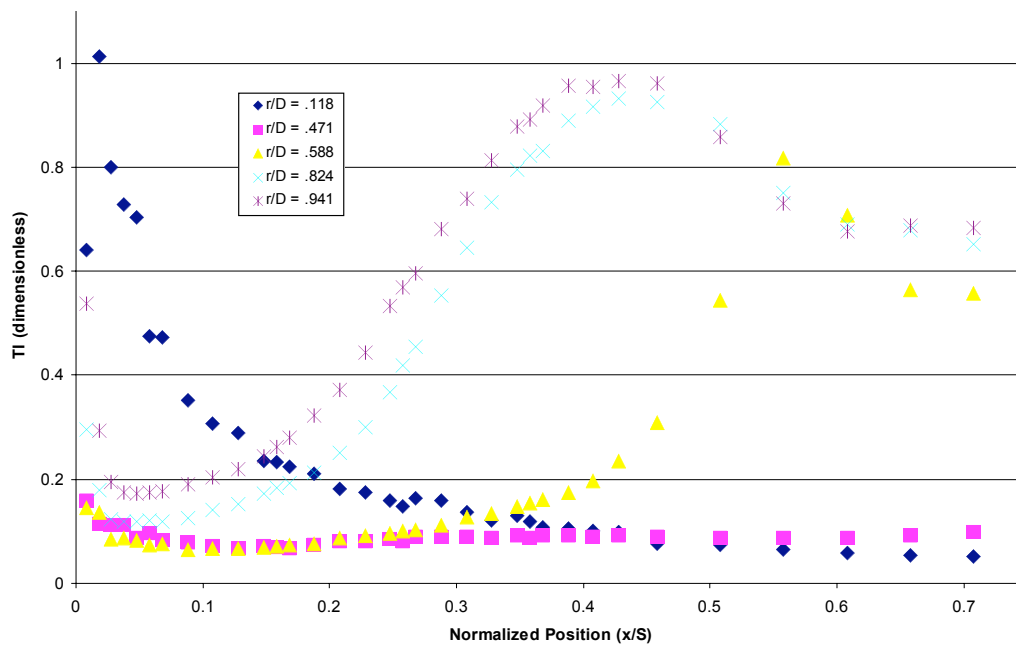
Figure 1.44.—Turbulence intensities in the disc space for the case Re = 7600, *S* = 127 mm (5 in.).
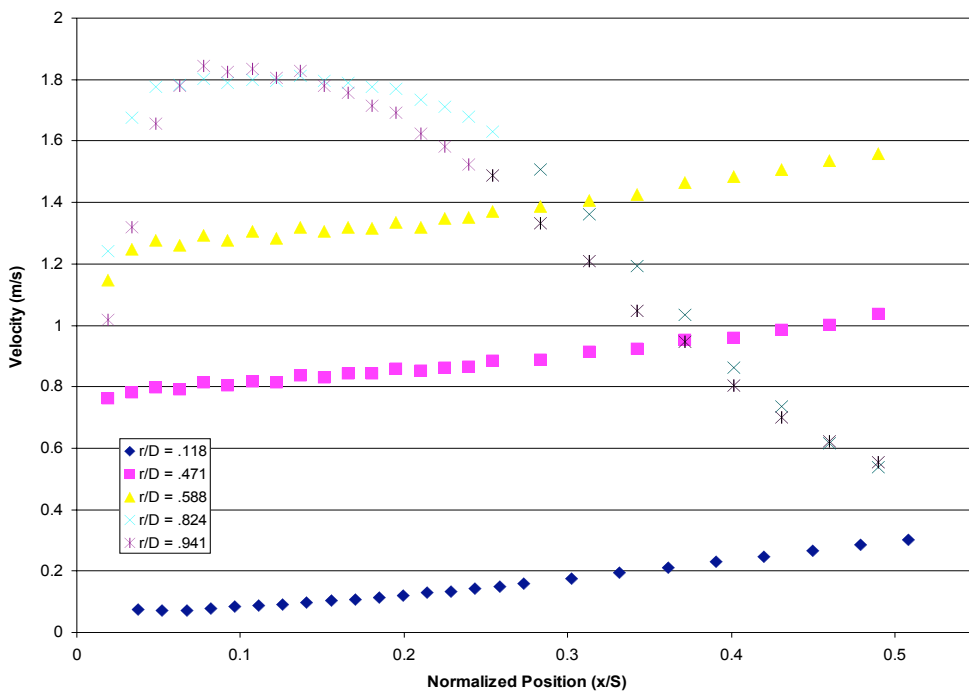
Figure 1.45.—Average velocities in the disc space for the case Re = 17700, *S* = 54 mm (2.125 in.). Portions of the velocity profiles in regions of high turbulence intensity are colored black.
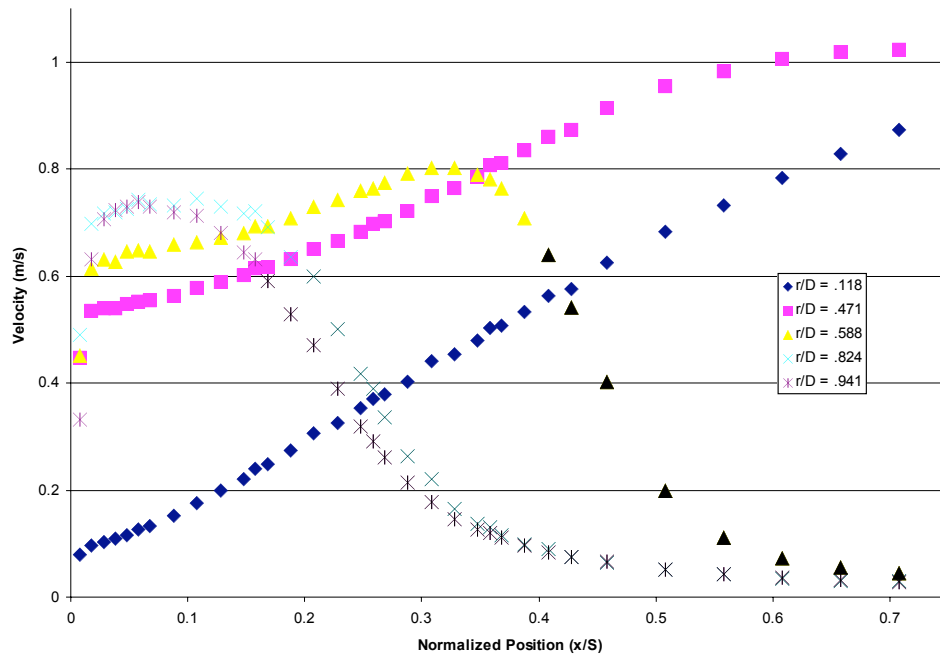
Figure 1.46.—Average velocity in the disc space for the case Re = 17700, S = 127 mm (5 in.). Portions of the velocity profiles in regions of high turbulence intensity are colored black.
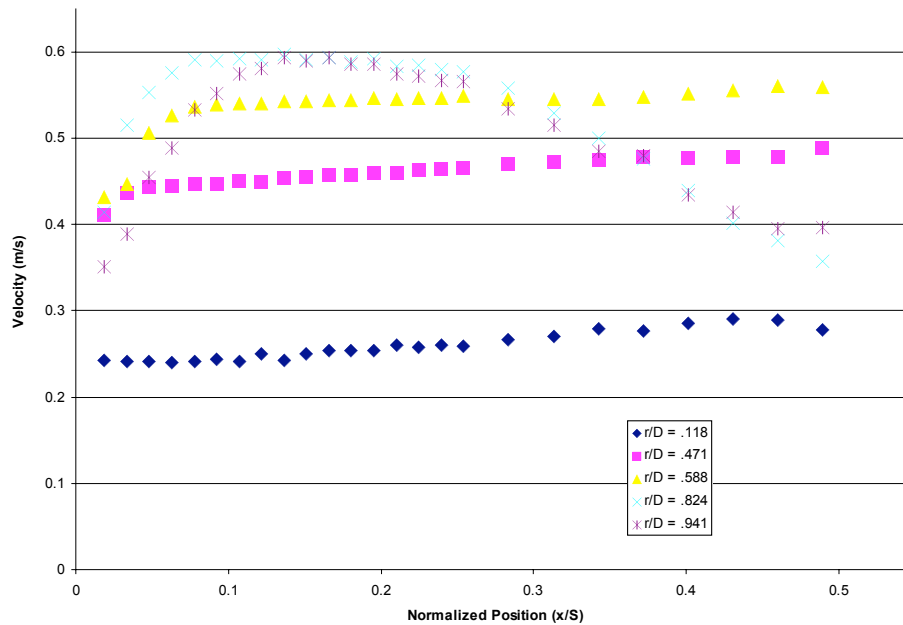
Figure 1.47.—Average velocity in the disc space for the case Re = 7600, S = 54 mm (2.125 in.). Turbulence intensity never exceeds 25% in these profiles.
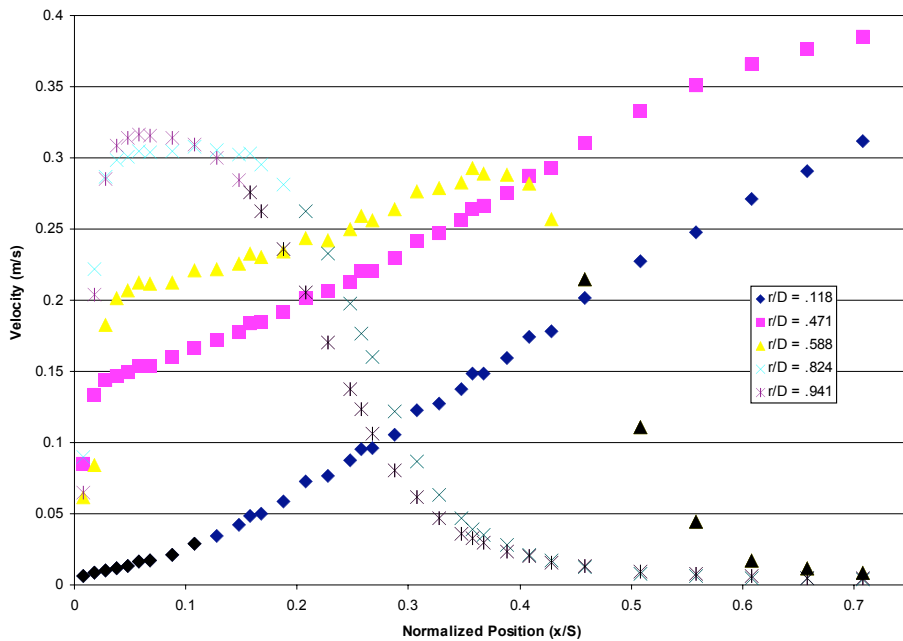
Figure 1.48.—Average velocity in the disc space for the case Re = 7600, *S* = 127 mm (5 in.). Portions of the velocity profiles in regions of high turbulence intensity are colored black.
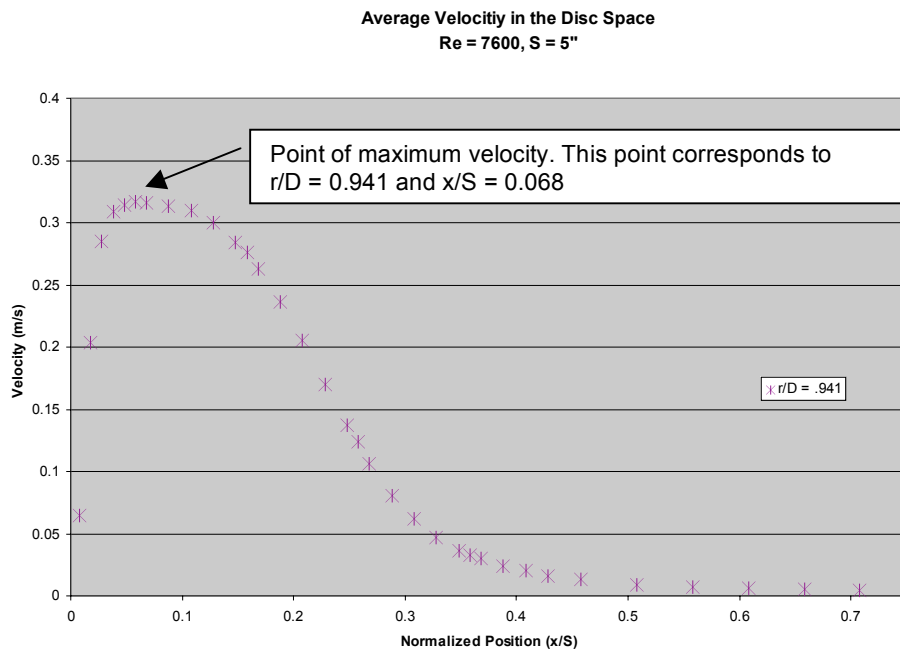
Figure 1.49.—The figure above illustrates the method of determining wall jet thickness.
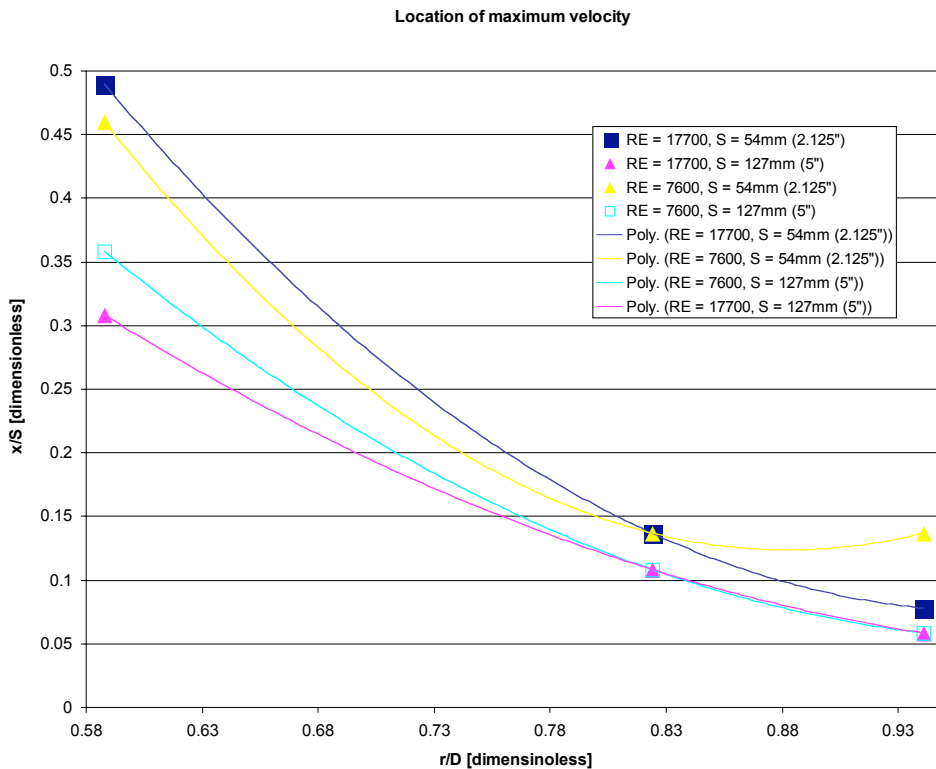
Figure 1.50.—The figure above shows the development of the shear layer for the Reynolds number – disc spacing cases of interest.
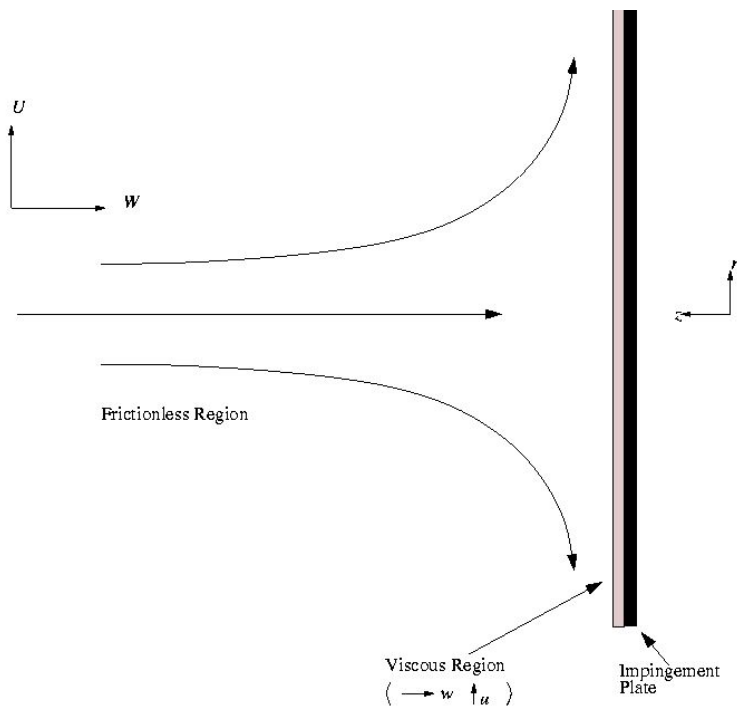
Figure 1.51.—This is the geometry that is applicable to the analysis covered in Schlichting. The impingement plate should extend to infinity.
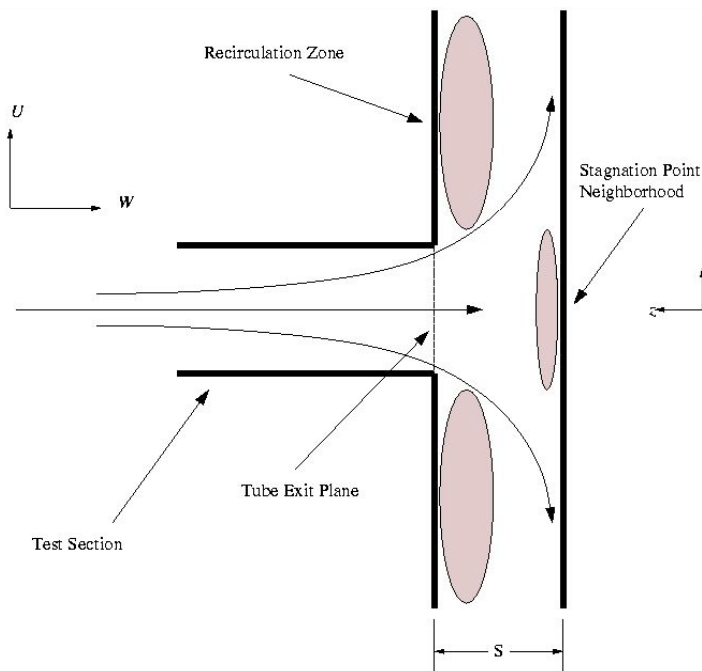
Figure 1.52.—The test section geometry at the University of Minnesota. We expect that equation (12) applies in the neighborhood of the stagnation point. The recirculation zones have been observed via flow visualization and are included to give the reader a better understanding of the flow field.
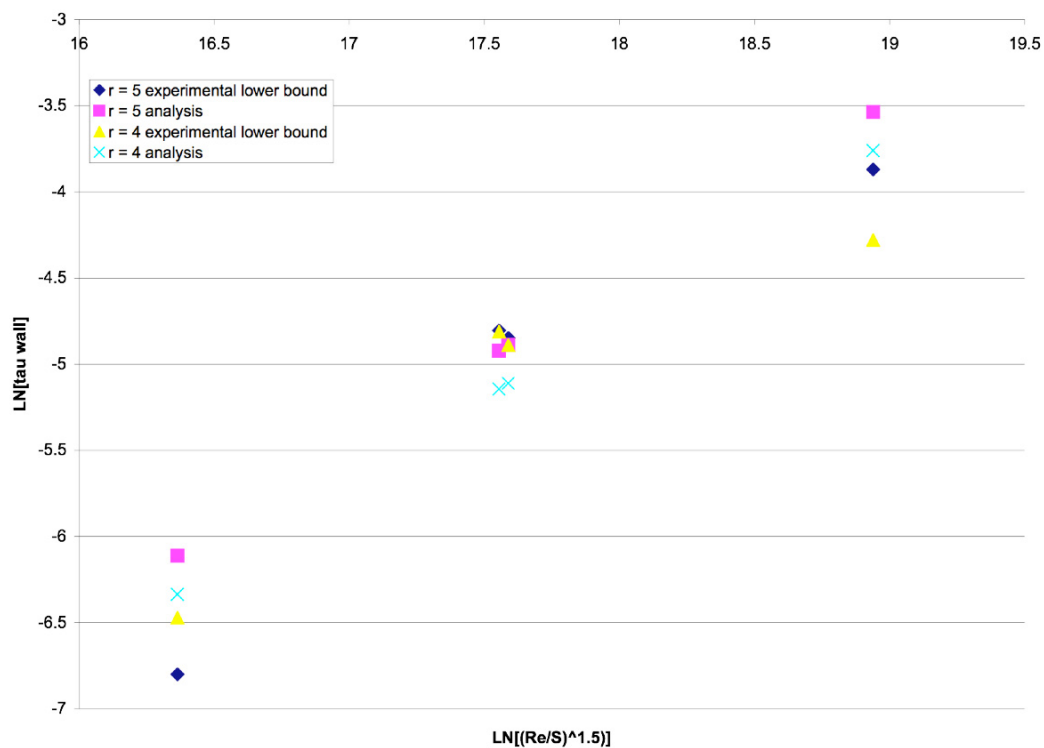
Figure 1.53.—Experimentally gathered shear stress values vs. theoretical predictions.

1.12 References

1. Hayes, M. "Digital Signal Processing," Schaum's Outline Series, McGraw-Hill Book Company.
2. Pinsky, M. "Partial Differential Equations and Boundary-Value Problems with Applications," 3rd edition, McGraw-Hill Book Company.
3. Schlichting, H. "Boundary Layer Theory," 6th edition McGraw-Hill Book Company.
4. Strang, G. "Introduction to Linear Algebra," 2nd edition, Wellesley-Cambridge Press.

2. Oscillatory Flow Investigations

2.1 Introduction

This study addresses the need for validation of multi-dimensional, oscillatory flow techniques that can be employed in codes used for Stirling engine design. There is concern about the accuracy of modeling certain regions, such as the compression space, of a Stirling engine. This is addressed by isolating an important region of the engine (e.g., the compression space) and identifying the important features of the flow there. Once an area of interest is chosen, experiments are conducted to characterize the flow, compute the flow in those experiments, identify weaknesses in the computation and modify the models to improve their ability to simulate the experiments. The result is that Stirling engine design models are one step better in their simulation of the entire engine and the designer can use them with more confidence. After discussing with engineers at Stirling Technologies Co. (now Infinia, our teaming partner and one of several companies with which we communicate), we chose to focus on the flow exiting the heater channels and entering the expansion space, as it turns radially inward, then reverses.

This work provides a complete description of oscillatory flow in a geometry that is representative of a Stirling engine expansion space. Secondarily, these investigations generated a data set that could be used as a standard for Stirling engine CFD simulations. It is a fact that oscillatory fluid dynamics data of this nature are generally lacking and hence there is a need for this type of investigation. An exception is an MIT study by Kornhauser[4] that presents wall heat flux measurements in a heat exchanger/two-space experiment. Further exceptions include work carried out at the University of Minnesota in the past by Seume and Simon,[9,11,12] Seume et al.,[10] Friedman and Simon,[2] Seume et al.[13] and Qiu and Simon.[7,8] The most recent work was, and is currently being carried out by Niu et al.[5,6] and Simon et al.[14] This work focuses on heat transfer in a Stirling engine regenerator.

To this end, this section presents hot-wire anemometry and flow visualization data from an experiment that replicates important features of oscillatory flows in Stirling engines. These features include impinging and sink flows, large-scale separation zones, recirculation bubbles, unsteady shear layers and temporally varying transition and relaminarization zones. The test operating conditions (see below) were chosen to match representative Reynolds and Valensi numbers by scaling the test section up and the oscillation frequency down.

2.2 Nomenclature

Symbol	Description	Units
BDC	Bottom dead center	[no units]
CAD	Crank angle degrees	[degrees]
f	Data sampling frequency	[1/s]
r	Radial variable	[m]
Re_{max}	Maximum Reynolds number	[dimensionless]
RTD	Resistance temperature detector	[no units]
RPM	Crankshaft revolutions per minute	[1/min]
TDC	Top dead center	[no units]
D	Disc diameter	[m]
S	Disc spacing	[m]
TI	Turbulence intensity	[dimensionless]
$\|u\|$	Velocity magnitude	[m/s]
$\bar{u}$	Vector velocity	[m/s]
Va	Valenci number	[dimensionless]
x	Axial variable	[m]
θ	Crank angle	[degrees]
ω	Crankshaft rotational speed	[1/min]

2.3 Experimental Set-Up

The test facility is shown schematically in fig. 2.1. A Scotch yoke drive is used to develop sinusoidal piston motion of a constant rotational speed, ω, where ω is variable from 4 to 120 revolutions per minute (rpm). Attached to the drive are a top dead center (TDC) indicator, a shaft angle encoder and a tachometer. The test section shown in fig. 2.1 is enlarged in fig. 2.2. The delivery tube inner diameter, *D*, matches the test rig cylinder bore. The two large discs have a major diameter of 1.22 m. The disc diameter is large to minimize the flow of momentum in and out of the test section. The delivery tube attached to the right disc in fig. 2.2 is 0.25 m in length. When the drive is at TDC, (the closest that the piston comes to the test section) the piston face is flush with the tube inlet plane (as shown in fig. 2.1). The piston stroke is 0.36 m (14 in.). The distance between the two large discs, *S*, is fixed for each case, but variable from 0.025 m (1 in.) to 0.127 m (5 in.).

2.4 Data Collection

2.4.1 Flow Visualization

Pictures of the flow are captured with a 35 mm camera. The flow is seeded with particles, which, in turn, are illuminated with a laser light sheet. Particles are introduced into the flow with a Sage Action Model 33 Multi-Head Bubble Generator. This device combines compressed air, helium and a soap solution to produce nearly neutrally buoyant bubbles. The bubble size is adjustable from 6 mm to less than 1 mm. The bubbles used in the experiments are generally on the order of 3 mm. The bubbles follow the flow and give a 3-D, real-time view of the fluid motion. To illuminate a 2-D slice of the test section, a Melles Griot, He-Ne laser was used in conjunction with a cylindrical glass rod. When the beam passes through the rod, it spreads into a sheet of light, which, when appropriately placed, can illuminate any plane of interest within the test section. Attached to the end of the laser is an electronically controlled shutter which receives signals from the TDC indicator and the shaft angle encoder. The bubbles within the sheet are photographed with a Nikon FE2 35 mm camera loaded with ASA 400 or ASA 125 black and white film.

The experimental procedure commences by selecting a disc spacing and an rpm. A crank angle during which flow is visualized is chosen, e.g., 15° to 30° (where 0° corresponds to TDC, $0° < \theta < 180°$ corresponds to the intake stroke, 180° corresponds to bottom dead center (BDC) and $180° < \theta < 360°$ corresponds to the blowing or exhaust stroke). The shutter controller is programmed to open the shutter at 15° and close it at 30° (in the 15° to 30° example). This gives a 15° window in which the flowing particles within the sheet of light are illuminated. The shutter controller is programmed to open (and close) the shutter 100 times over this interval. The room is then blackened and the camera is set up to view the light sheet continuously (most manual cameras have a setting called 'bulb' which holds the camera shutter open for as long as desired). After 100 cycles, the camera shutter is closed and the result is an ensemble-averaged photograph of a 15° segment of crank angle duration. The process is repeated for other intervals in the cycle until the entire cycle is characterized. The flow visualization field of view is shown in fig. 2.3. Three different rpm and disc spacing operating points are documented, as summarized in table 2.1.

TABLE 2.1.—CASES TESTED

Case	rpm	Re$_{max}$	S (mm)	Va	Location	*S/D*
I.a	30	7600	54	2300	Tube	0.251
I.b	30	7600	54	2300	Channel	0.251
II.a	30	7600	127	2300	Tube	0.591
II.b	30	7600	127	2300	Channel	0.591
III.a	70	17700	54	5400	Tube	0.251
III.b	70	17700	54	5400	Channel	0.251

2.4.2 Hot-Wire Anemometry

A TSI model 1053 hot-wire anemometer bridge was used for velocity measurements. The signal from the anemometer was sent to an IOTech A/D converter and then directed to a PC for recording. The angular position of the drive (from which piston position is calculated) was determined with an optically-triggered TDC indicator and a tachometer. Barometric pressure was recorded with an in-house pressure sensor. Ambient temperature was monitored with an RTD. The position of the anemometer probe was controlled with a Velmex stepper motor and an integrated slide unit. All data collection, probe positioning and data reduction were carried out with C code.

Velocity and turbulence intensity (*TI*) profiles were documented by traversing the probe within the test section. A single traverse was taken within the delivery tube and several traverses were taken within the disc space (see fig. 2.4)

Disc space traverses are (following the convention of fig. 2.4) in the *x*-direction. The single traverse in the tube space was in the *r*-direction. The coordinate origin is taken on the tube centerline (the "Axis of Symmetry") at the target (left in fig. 2.4) disc. For reference, the disc on the right in figure 2.4 will be named the 'back' disc. The sequence of spatial points in a given traverse was randomized to prevent any temporal changes from being interpreted as spatial trends.

At any given point, the analog signals from the anemometer and the TDC indicator were sampled at a frequency, *f*, of 500 Hz. Given *f*, ω and the signal from the TDC indicator, it was possible to determine the location of the crank and piston. The raw data were ensemble averaged over 100 cycles to produce velocity and *TI* values resolved in time within the cycle at each measurement station. For example, in the 30 rpm case, the total run time for a single point was 200 seconds (100 cycles). Thus the total number of samples was 10,000. These 10,000 points were then separated by crank angle (the resolution was 1/2 CAD) and the result was averaged over the 100 cycles. The probe was then moved to a new station and the process was repeated until an entire profile was completed. The cases investigated are shown in table 2.1.

2.5 Results

Unlike section 1 of this work, under oscillatory flow, it isn't so simple to compartmentalize results into different subheadings (i.e., flow visualization, average velocity profiles, etc.) and discuss each separately. For example, flow visualization results give qualitative insight into the fluid behavior within the test section. Of course, little is revealed in terms of velocity magnitude aside from whether the flow is 'fast' or 'slow.' This information is retrieved with hot wire velocity data. A compilation of hotwire data produces velocity and *TI* plots. However, as we will shortly see, there are regions where *TI* values not only exceed 30% but sometimes are as high as 100% or more (The magnitude of *TI* values and their implications will be discussed shortly). We then turn to visualization and say; "of course, the wire is in a separation zone, and in these regions there is no reason to believe that an average velocity as indicated by a hot wire reflects anything about a typical flow condition." Thus, in this section we present and discuss the results as a collection of flow visualization data, ensemble averaged velocity data and turbulence intensity data.

The three cases of table 2.1, each with a sub-case which presents data in the tube and a sub-case in the disc space, were conducted. All six of the entries in table 2.1 will be described below.

To the reader: you may find the following discussion conspicuously scant of flow visualization *results*. This is intentional; 144 pictures were taken to cover the three cases. A complete presentation would necessarily be lengthy and verbose. Thus, we present summary figures (sketches of the major features) of the results. However, we wouldn't want to disappoint; to this end, we present a subset of the flow visualization photos in section 4 – Comparisons Between Experimentally Gathered Results and CFD Generated Data. We feel that, when viewed in light of CFD results, the flow visualization results 'speak for themselves.'

Please note that a hot wire is unable to resolve flow direction, hence the quantity

$$\| u \| = \left(\vec{u} \bullet \vec{u} \right)^{1/2} = \sqrt{u^2 + v^2 + w^2}$$

appears in velocity plots (where u, v and w are the vector velocity components). Suppose that the wire is in a flow and the flow is moving with some vector velocity $\vec{u}$. Suppose some time later the flow reverses and has a vector velocity $\vec{U}$ that is anti-parallel to $\vec{u}$ with the same vector magnitude. The anemometer will report *identical* velocities. The point is that to a hot wire, which essentially measures the rate of cooling of a small cylinder, positive and negative velocities look the same. Thus, to get a grasp of the flow direction, one must look at the corresponding crank angle.

We wish to acquaint the reader with the type of hot wire data to be presented. First of all, we are investigating average velocities, $\| u \|$, or turbulence intensities, TI,

$$TI = \frac{1}{\| u \|} \sqrt{\frac{\displaystyle\sum_{j=1}^{N} \left(u_j - \| u \| \right)^2}{N-1}}$$

as a function of both crank angle, θ, normalized axial location x/S and normalized radial location, r/D. In this light, we could present a collection of two-dimensional slices of the data set with comments about the connection between each of the slices. Owing to the fact that crank angle resolution is 1/2 of a degree, this method would lead to an excessive number of figures.

In this light, we choose to present three-dimensional plots with the independent variables presented as functions of two of the three independent variables, with the third independent variable held fixed. We begin by referring the reader to figure 2.5: this is the 3-D view that Matlab produces when it is fed a 3-D data set; $\|u\|$ vs. x/S with r/D held constant in this case. Figures 2.6 and 2.7 are pictures of the same data set from different angles. The point is that, although a complete picture is presented in one figure, the reader has to imagine how it may look from different angles.

Another note; the variable θ appears in the discussion below. The reader should be aware that $0° < \theta < 180°$ corresponds to the "suction" stroke, i.e., the piston is drawing fluid into the test section. On the other hand, $180° < \theta < 360°$ corresponds to the blowing half-cycle. In the following, we use the words blowing, blowing half-cycle, suction, suction stroke, etc. to represent the above stated crank angle regimes. Finally, we give the crank angle $\theta = 0° = 360°$ the special name 'Top Dead Center' or TDC, and the angle $\theta = 180°$ the name 'Bottom Dead Center' or BDC.

One further note about average velocities $\| u \|$ and turbulence intensities TI; without exception, in the *TI* profiles that will be presented shortly, there are regions where TI exceeds 30%. According to the literature, (Smits,[15] Hinze[3]), when *TI* values exceed 30% there is instantaneous flow reversal across the hot wire. Recall that the wire acts as a rectifier, thus, the net effect is that in zones of high values of *TI measured average velocity values are too high and measured TI values are too low*. For example, suppose that two velocities were taken and the *actual* value of velocity was 3.1 m/s and -3 m/s. The *actual* average velocity over these two points is 0.05 m/s and the *actual TI* over these two points is 8630% (this ridiculous *TI* value is strictly for demonstration purposes). The anemometer will report velocity values of 3.1 and 3 m/s. Therefore, the average velocity $\| u \|$, according to the anemometer, is 3.05 m/s and according to the anemometer, the *TI* is 2.3%.

According to Smits,[15] for measured *TI* values of 30%, the error associated with *TI* measurements is 10%, and the error associated with average velocity measurements is 10%. For measured *TI* values greater than 30%, the average velocity measurement error grows strongly with *TI* whereas for *TI* less than 30%, the errors in *TI* and average velocity measurements are small.

Case Ia—Tube flow, Va = 2300, *S*/*D* = 0.245

We begin the explanation with a presentation of ensemble average velocity and *TI* data. Shown in figure 2.8 is average velocity plotted against crank angle and normalized radial location. One sees that the flow in the tube follows the sinusoidal motion of the piston. The changing boundary layer thickness can be observed near $r/D = -0.5$ and some streaking of the flow is seen near the centerline ($r/D \sim 0$) during the exhaust stroke (180 to 360 CAD). Presented in figure 2.9 is a *TI* plot. With the exception of BDC (and the surrounding θ values) *TI* values are low (*TI* < 0.3) and we may assume that velocity measurements are accurate.

Turning to flow visualization, we present a summary report of crank angles near TDC on the intake stroke in figure 2.10. In the early portion of the cycle, the flow has little momentum, and is reversing. As the cycle proceeds, flow is drawn into the cylinder in an apparently laminar manner. One curious and noteworthy flow feature during this portion of the cycle is that visualization reveals no growth or presence of separation bubbles (fig. 2.11) for this portion of the cycle. At 45 CAD, separation bubbles appear in the visualization results and at about 80 CAD, the flow seems to trip to turbulence (see fig. 2.12). An interesting feature of the flow is that for $45° < θ < 105°$ there is a separation bubble that does not grow with increasing crank angle (i.e., stronger suction or pressure gradient). For illustrations of these features (see figs. 2.12 and 2.13). As the suction stroke proceeds, the flow remains turbulent and the separation bubbles begin to grow (fig. 2.14). At BDC, the piston achieves zero velocity and consequently, the flow in the tube becomes full of small-scale turbulence. Upon reversal, the flow begins as a turbulent slug, and is blown out of the cylinder (fig. 2.15). Following in the wake of the turbulence is a laminar-like flow. The turbulence has apparently been dissipated by the walls and the strong temporal acceleration. As the piston continues the exhaust stroke, all of the turbulent flow is driven out and a laminar-like regime is maintained almost until TDC, as shown in figure 2.16.

Case Ib—Disc space flow, Va = 2300, *S*/*D* = 0.245

This is a collection of measured velocity and *TI* profiles and flow visualization results in the disc space. We begin with a presentation of flow visualization results. As a first comment, we note that during the blowing stroke, close to both TDC and BDC, the flow is more or less quiet in nature (i.e., lacks any perceptible momentum). However, for intermediate crank angles, the flow is drawn radially inward in a more or less uniform fashion. This idea is presented pictorially in figure 2.17. The blowing stroke is different in nature; the flow feels the effect of the piston-driven pressure gradient almost immediately. A jet quickly forms on the target wall and with it comes a separation/recirculation bubble at the sharp edge of the tube exit (see fig. 2.18). The jet undergoes transition and radially outward of the transition point is a turbulent zone. The jet loses it's coherent nature at a normalized radial location of approximately $r/D = 1.2$. These comments are illustrated in figure 2.18.

Turning to anemometry results, velocity profiles are presented at normalized radial locations, r/D, of 0.68, 0.81, 0.93, 1.05, 1.17, and 1.30 in figures 2.19 through 2.24. One can see that for smaller values of r/D, during the blowing portion of the cycle, there is a coherent jet along the target wall (i.e., for $x/S < 0.4$). As one moves radially outward, the jet thickness first decreases, then begins to increase. For r/D greater than 1.17, it appears that the jet spreads out to fill the entire channel (see figs. 2.23 and 2.24).

Looking at *TI* profiles (figs. 2.25 through 2.30) we see that, indeed, there is a region of low turbulence in the wall jet region until $r/D = 0.93$. For r/D greater than 1.05, the turbulence intensity during the blowing cycle is approximately uniform across the center of the channel. However, the *TI* near the walls is much larger. This suggests a thick boundary layer as a result of the strong temporal deceleration of the flow. The *TI* levels indicate a region of energized, turbulent flow.

During the suction stroke (see figs. 2.19 through 2.30), the velocity profiles exhibit a uniform sink flow appearance. Moreover, for all radial locations, except $r/D = 0.93$, we have the fortunate condition that away from TDC (perhaps at 75 CAD or so) *TI* levels are of a reasonable value. It is likely that in the late portion of the blowing stroke, a fair amount of residual turbulence is deposited in the disc space, which remains during the initial phase of the intake stroke. As the stroke proceeds, perhaps the turbulent

residuals from the previous half-cycle are re-ingested in the tube, and, as the flow accelerates, it stabilizes (i.e., becomes laminar-like). In any case, the combination of flow visualization and low *TI* values seems to suggest that velocity profiles in this regime are trustworthy.

Case IIa—Tube flow, Va = 2300, *S*/*D* = 0.577

Figure 2.31 shows that during the early part of the intake portion of the cycle, $0 < \theta < 180$, the velocity near the tube walls is of a higher absolute value than the core flow velocity. This suggests that the higher momentum fluid in the core flow (see values for $\theta < 270°$) is slower to respond to change in pressure gradient imposed by the piston. Viscous forces near the wall reduce the momentum of the near-wall fluid and allow it to respond more quickly to the change in pressure field.

The exhaust portion of the cycle $180 < \theta < 360$ is somewhat different. Here, the flow is being driven out of the tube by the piston. It seems that for this case, the flow behaves like a developing pipe flow, with the core flow velocity being flat and following the piston velocity. Boundary layer growth can be seen, particularly for the deceleration portion of the cycle.

Figure 2.32 presents a plot of turbulence intensity in the tube space. Periods of strong acceleration (e.g., $0° < \theta < 45°$) show dissipation of turbulence, whereas periods of deceleration (e.g., $90° < \theta < 135°$) show large production of turbulence. One may also notice that, excluding $160° < \theta < 210°$, the absolute value of *TI* is low; hence we may consider average velocity data outside of this range to be reliable.

We now turn to flow visualization. Figure 2.33 shows that near TDC on the intake stroke, the flow has a low over-all momentum and is locally and instantaneously reversing. As the cycle proceeds, flow is drawn into the cylinder and, in the early portion of the cycle, seems to exhibit a 'alternating' behavior, perhaps from cycle to cycle, with respect to the tube centerline. This is to say that on some strokes the flow seems to be drawn from the top of the disc space whereas on other strokes it seems to come from the bottom. Also noteworthy is the presence and growth of separation bubbles at the sharp-edged tube entrance. These phenomena are sketched in figure 2.34. As the cycle proceeds, the alternating behavior seems to disappear. In the degree range $60° < \theta < 90°$, the flow seems to be axisymmetric, with a laminar core and growing separation bubbles (fig. 2.35). After 90 CAD (maximum intake piston speed) the flow appears to rapidly trip to turbulence. Again, separation bubble growth is present, but the core flow is turbulent in nature (fig. 2.36). As the intake stroke proceeds to completion, the flow decelerates with the piston, and reverses. The early part of the blowing stroke shows that the bulk flow is fully turbulent (fig. 2.37) and remains so until 240 CAD. After 240 CAD, the flow seems to 'laminarize' and it remains stable as shown in figure 2.38. This is perhaps due to the sustained exposure to temporal acceleration and dampening by the tube and piston walls. At the end of the blowing stroke (not shown), flow deceleration causes turbulent structures to form in the tube flow which persist into the next cycle.

Case IIb—Disc space flow, Va = 2300, *S*/*D* = 0.577

The area of concern is the disc space (see figs. 2.3 and 2.4). Flow visualization reveals that during the blowing stroke and a portion of the suction stroke, there is a large standing vortex (or eddy) between the discs. The blowing stroke energizes the eddy; the suction stroke simply moves the eddy slightly. The motion of the eddy, along with other pertinent flow features is sketched in figures 2.39 and 2.40. Figure 2.39 shows that during the blowing stroke there is a strong and coherent wall jet. This jet generates an eddy, which initially forms at the sharp edge of the tube exit and, as crank angle increases, its center follows the dashed red line upwards. The region in the wake of the eddy and to the left of it is more or less dead (motionless) flow. Figure 2.40 is a summary of flow visualization results for the suction stroke. The eddy from the blowing stroke is pulled downwards in the general direction of the bulk flow but rapidly loses its momentum and becomes very weak after about 30 degrees of crank angle. The main flow which fills the volume that is opened is pulled from the back wall where the momentum from the previous half-cycle is low, with velocity seeming to decrease as one moves rightwards.

Turning to anemometry data, we present a collection of profiles in the disc space at normalized radial locations, *r*/*D*, of 0.68, 0.81, 0.93, 1.05, 1.17, and 1.30. As a first comment, for all profiles with *r*/*D* >

0.81, *TI never* drops below 30% (with the exception of some regions at the radial location r/D = 1.30). In short, we must look on ensemble-average velocity profiles with a somewhat skeptical eye. Turning to figure 2.41 we present a velocity profile at r/D of 1.30. At this radial location, there is some remnant of the wall jet at θ = 0° and x/S ~ 0.10, but more or less, velocities are low, turbulence intensity is high (see fig. 2.42), and for all practical purposes measurements of velocity in this flow are too high in absolute value. We move radially inward, and present velocity and *TI* profiles at r/D of 1.17 (figs. 2.43 and 2.44). Again, we see a similar behavior; remnants of a wall jet are present, and again *TI* is high and velocities are low. Next we present profiles at r/D of 1.05 (figs. 2.45 and 2.46). Here we have the fortunate condition of having flow visualization results to aid in the discussion. As is the case for larger radial locations, we still have the condition that *TI* is too high for accurate anemometry; the recorded velocities are too high and the *TI* values are too low. However, the anemometry data show the presence of a wall jet. The jet thickness is approximately 30 to 40% of the channel width. Looking at figure 2.47, we see that there is, in fact, a wall jet. We can expect that it is as thick as the hot wire data says. Turning back to our summary figures (figs. 2.39 and 2.40) we may expect a wall jet throughout the blowing stroke and a relatively weak sink flow on the intake stroke in the vicinity of the back wall (i.e., for large values of x/S). In figure 2.45, the jet is visible. It even seems to maintain some of its momentum throughout the first 30 degrees of the suction stroke. Turning now to the idea of a sink flow in the vicinity of x/S =1, there exists a region of high velocity fluid in this area, which suggests that this flow may be present. We continue inward now and present profiles for r/D of 0.93 in figures 2.48 and 2.49. Again, the same behavior is observed as for the larger radius cases. Moving inward again, we present profiles at r/D = 0.81 in figures 2.50 and 2.51. For the first time, we see that *TI* levels drop below 20%. This happens near x/S = 1 and x/S = 0, during periods of high flow momentum (see the top left and bottom right portions of fig. 2.51). For these data the hot wire values are accurate. Moving in again, we present profiles for r/D = 0.68 in figures 2.52 and 2.53. We also present flow visualization results in figure 2.54. We see a coherent (thicker, approximately 60% of the channel width) wall jet and a definite sink flow near x/S = 1.

Case IIIa—Tube flow, Va = 5400, S/D = 0.245

The field of view is the tube portion of the test section (see fig. 2.3). At the beginning of the cycle ~0° → 18° after TDC the piston is drawing fluid into the field of view from the right. In this degree range, it is observed that the fluid acceleration is spatially non-uniform (see fig. 2.55). After this degree range, from ~18° → 72° after TDC, a low-turbulence flow forms in the core of the pipe and separation bubbles grow downstream of the sharp inlet. Figure 2.56 shows a sketch of the separation zone on the right and how it grows in this degree range. Continuing through the cycle, a different behavior is observed from ~72° → 126° after TDC. The flow turbulence remains low and the separation bubbles continue to grow, but an alternating flow behavior is observed. To clarify, it appears in the photos that on some cycles, flow is drawn from the upper part of the disc space whereas on other cycles it is drawn from the lower part. This leads to a correspondingly variable separation zone from cycle to cycle. A sketch of the general features observed in this degree range is shown in figure 2.57. At this point, it is noted that for all values of crank angle between 90°→ *BDC*, the flow is decelerating. The deceleration destabilizes the flow and produces large-scale turbulence. At ~126°, large scale and strongly turbulent activity becomes prominent. With this, the growth of the separation bubbles changes. The growth rate in the streamwise direction of the bubbles on both top and bottom surfaces remains relatively constant. However, the bubble on the upper surface grows rapidly in the cross-stream direction (see fig. 2.58). The bubbles grow until BDC is reached. At BDC, the tube is entirely filled with eddys of multiple scales and the bulk convection is very low. After BDC, the drive pushes the piston and expels fluid from the cylinder to the disc space. The pictures of the exhaust stroke, e.g., *BDC* → *TDC*, show a "wave" propagating from left to right (fig. 2.59). This process may be understood if one assumes that there are two "slugs" of fluid within the test section during the exhaust stroke. First, there is a low-turbulence slug of fluid that is close to the piston face. This low-turbulence slug is trapped within the tube and simply shuttles back and forth.

Second, there is a slug of fluid that escapes into the area between the two discs and is shuttled between this space and the cylinder. The above idea is illustrated in figure 2.59. The second slug experiences flow separation and is highly turbulent in nature. Apparently, the turbulence in this slug is not effective in agitating the near-piston slug. No separation bubbles form within the cylinder during this part of the cycle. A perplexing flow feature is observed during the exhaust stroke at the very end of the stroke. From ~162° $ABCD \rightarrow TDC°$ there is a non-uniform velocity profile within the tube. In the upper left-hand side of the tube, the flow has a higher velocity. This corresponds to the entry flow at the beginning of the next cycle. This is sketched in figure 2.60.

A velocity profile is presented in figure 2.61. We see the flow follows the piston in a sinusoidal fashion. One immediately notices that the profiles on the intake and exhaust strokes have different shapes; the profile on the exhaust stroke is 'flat' whereas the profile on the intake stroke is convex. One may attribute the difference in shape to the fact that on the intake stroke, separation bubbles form at the tube entrance; hence the flow must accelerate around them. On the exhaust stroke there is no separation bubble influence, hence the flow assumes a flat profile and follows the piston. Figure 2.62 is a plot of turbulence intensity; as one may expect, periods of strong acceleration (25° – 90° and 200° – 270°) laminarize the flow. The careful reader may notice that on the intake stroke, turbulence quantities begin to increase around 120 CAD, whereas, on the exhaust stroke, a similar behavior is not seen until 350 CAD. In other words, *TI* values do not follow a sinusoid. This may be attributed to the fact that on the intake stroke, fluid is being drawn in from the disc space, which is an inherently turbulent flow.

Case IIIb—Disc space flow, Va = 5400, *S*/*D* = 0.245

We begin with flow visualization results. In the early portion of the suction stroke (0° < θ < 18°) the flow in the disc space seems to lack any coherent pattern; it is more or less a field of small-scale turbulent eddies (see fig. 2.63). As the piston continues the suction stroke, fluid begins to move radially inward. For small crank angles, fluid near the sharp-edged tube entrance begins to flow towards the tube (as shown in fig. 2.63). One can see that as crank angle increases, the pressure gradient is felt quickly in the cross-stream direction (blue arrows for small crank angles and red and blue arrows for larger ones). A picture of larger crank angles is shown in figure 2.64. Somewhere between 60 and 70 CAD, the sink flow reaches the target wall. In this region, as far as can be told, the velocity profile is more or less uniform. At the same time, the effects of the pressure gradient are being felt at larger radial locations. By the time maximum piston speed is achieved (i.e., 90 CAD), the flow is approximately uniform across the channel and covering the entire span of the flow visualization field of view (fig. 2.65). For the duration of the suction stroke, the flow remains uniform throughout the channel with flow velocity and piston velocities decreasing.

At BDC, the flow is, as is reasonable, devoid of momentum. As the piston begins to blow fluid out of the cylinder, a wall jet and separation bubble rapidly form. These features, and their development, are shown in figure 2.66. Everywhere adjacent to the separation bubble and near the target wall, the fluid has a remarkably high momentum as it streaks radially outward. The bubble, at its thinnest cross-stream dimension, occupies one-half of the disc space; at its thickest point, it occupies approximately seven-eighths of the channel. Figure 2.66 shows the very end of the separation bubble growth, (i.e., θ ~ 310°). At smaller crank angles of the 190° < θ < 310° range, the bubble is smaller, and the 'streaks' in the channel near the target wall are at a smaller radial location. For crank angles greater than 310°, the flow destabilizes, and except very near the tube exit, the channel fills with turbulence (fig. 2.67).

We now turn to anemometry data, and as the reader may have remarked while looking at the flow visualization summary diagrams, all of the hot wire sampling stations are within the flow visualization field of view. We begin the presentation of anemometry results by discussing a velocity profile at *r*/*D* = 0.68 (fig. 2.68). We see that during the suction stroke, as the flow visualization indicated, the flow responds quickly near the tube exit (near *x*/*S* = 1). Shortly thereafter, the flow takes on a uniform sink pattern. The flow follows the piston motion and slows in the vicinity of 180° and, then, during the blowing stroke, a strong wall jet forms and lasts for the rest of the cycle. Turning to *TI* data (fig. 2.69), we

see that there are two regions where *TI* values are at or below 30%. These regions correspond to the wall jet, shortly after the piston has reached its maximum exhaust velocity and the channel-spanning sink flow shortly after the piston has achieved its maximum intake velocity. This corresponds nicely with figures 2.65 and 2.66.

Moving radially outward, we present a velocity plot at *r/D* of 0.81 in figure 2.70. We observe a similar behavior to the smaller radial location; there is an excess of momentum in the degree range 270° < θ < 360° and 0° < θ < 100° near the back wall (*x/S* ~ 1). One might suspect that the separation bubble that forms on the back wall is influencing the hot wire signal, and, though the signal indicates a relatively high velocity, it may be due to large turbulent eddy transport. To clarify this idea we turn to figure 2.71. We see that the *TI* values in these regions are relatively high (30 to 40%); however, this does not clarify weather there is a high-energy eddy present there or if the flow is in fact streaking along the back wall.

Another step out lands us at *r/D* = 0.93. A velocity profile is presented in figure 2.72. Again, a wall jet and uniform sink flow are present. Also present is the region of high indicated velocity near the back wall. Turning to figure 2.73, we find uniform and high levels of *TI* across the channel at θ = 300°. The flow visualization does not indicate the presence of a strong flow in these regions. It indicates the presence of a separation bubble (or perhaps its remnants). Hence, we attribute these high-indicated velocities to a recirculating flow at this time; outward near the target wall, and inward near the back wall.

The same trends that were discussed above persist as one continues radially outwards. The results are presented in figures 2.74 through 2.79. One thing to notice in these figures is that at larger radial locations, the flow is more turbulent in nature. In general, the regions that are suitable for hot wire anemometry remain stationary (i.e., in the same crank angle and spatial location) but decrease in size with larger radii. One anomaly is present in the larger radial location plots; in the vicinity of 240° for 0.93 < *r/D* < 1.03, a low-turbulence region forms near the target wall and, with an increase in radius, grows towards the back wall. This is during the blowing stroke as the piston is approaching its maximum velocity. It corresponds to a 'ridge' forming on the velocity profiles (e.g., see fig. 2.74). Perhaps this 'ridge' corresponds to the flow accelerating around the separation bubble.

2.6 Wall Shear Stress as a Function of Crank Angle

Of interest was the determination of wall shear stress as a function of crank angle. This information is useful in the sense that it is the next level of complexity in code validation. In this section, we present wall shear stress measurements, as derived from the ensemble average velocity profiles presented above, as a function of crank angle. We will also outline the difficulties in measuring shear stress with a hot-wire, and the errors associated with the measurement.

To begin, we refer the reader to figures 2.99 and 2.100. These figures show that there is an effect on the hot-wire as the probe approaches the wall. This is unfortunate in the sense that wall shear is described as:

$$\tau_{wall} = \mu \frac{\partial u}{\partial x}\bigg|_{wall}.$$

Thus, to directly evaluate wall shear stress, one needs to know the gradient at the wall, which is influenced by the wall effect. To circumvent this somewhat inconvenient problem, we turn to theory. According to Burmeister,[1] in a turbulent flow, near a solid boundary, the following equation (a.k.a. the law of the wall) holds:

$$u^+ = x^+$$

where

$$u^+ \equiv \frac{\|u\|}{v^*}$$

and

$$x^+ \equiv \frac{xv^*}{v}$$

and

$$v^* \equiv \left(\frac{\tau_{wall}}{\rho}\right)^{1/2}.$$

Thus, when wall shear stress is *known*, and the velocity profile near the wall is cast in these non-dimensional variables, the velocity profile near the wall is *linear* with an intercept at the origin. Since we want to determine wall shear stress, this presents a small problem. To this end, we guess a value of wall shear stress and then check this guessed value against the collected data. We now present the algorithm used to accomplish this feat and refer the reader to appendix C for the Matlab code used to carry out the computations.

2.6.1 An Algorithm Capable of Determining Wall Shear Stress from Corrupted Experimental Data

Step 1. Truncate each velocity profile (at each crank angle) to eliminate far-wall velocity data. The truncation is made at $x/S = 0.1$ for all cases and crank angles. We feel that at larger axial locations (larger x/S) the "law of the wall" as described by Burmeister,[1] does not hold.

Step 2. With the remaining data, $0 < x/S < 0.1$, locate where the wall influence on the hot-wire disappears as one traverses away from the wall. With reference to figure 2.100 one can see that the profiles in the near-wall region ($x/S < 0.008$ or so) are corrupted regardless of crank angle. The simplest way to remove the wall effect is to look for the minimum value of velocity at each crank angle in the profile and remove all points inbord of this velocity minimum.

Step 3. Having now eliminated far-wall data and near wall effects, we are ready to guess a slope and hence a wall shear stress. This is achieved by first assigning a fixed point at the origin. We let velocity equal zero at $x = x/S = 0$. Next we take the minimum value of velocity (as identified in step 2) and the next five points outboard from the minimum. We then take their average in both velocity and position. The result is a single point in space and velocity corresponding to the average value of the near-wall profile.

Step 4. Fit a line through the origin and the average value determined in step 3. Multiply the slope of this line by viscosity to get shear stress.

We now have to identify any errors associated with the truncation and averaging of the profiles to determine shear stress.

Step 5. Now that shear stress is known from Step 4, we take the minimum value of velocity, and the 5 nearest points outboard of it (from Step 3), and convert them to u^+, x^+ coordinates.

Step 6. For each matched u^+, x^+ we define the quantity:

$$RSS = \sqrt{\frac{\displaystyle\sum_{i=1}^{5}(u_i^+ - x_i^+)}{4}}$$

and use this as an error bound on the slope (and hence wall shear stress) derived in Step 4.

2.6.2 Wall Shear Stress for Case IIb (Re$_{max}$ = 7600, Va = 2300, S = 127 mm, S/D = 0.591)

Given average velocity data for Case IIb and the algorithm above, we present the results in figures 2.80 through 2.85. For r/D = 0.68 (fig. 2.80), we see that the wall shear stress is low for a large portion of the intake stroke (0 < θ < 180). The large stresses in the early portion of the intake stroke are likely due to the fact that in this case, there is a strong remnant of the wall jet present from the previous half-cycle. During the blowing stroke, (180 < θ < 360), there is a more or less steady rise in shear until about 310 CAD. At this point the shear increases dramatically and might indicate a transition to turbulent flow. Figure 2.52 shows a rapid change in the wall layer velocity profile at θ = 300°. We see that for this particular radial location the error, as defined above, is generally in the neighborhood of 4-9%. Moving radially outward, in the next figure (fig. 2.81), we see a somewhat similar behavior at the radial location r/D = 0.81. Though difficult to know precisely, transition may be taking place when θ = 300°. Figure 2.50 shows a much thicker near wall layer at this radial position but a rapid change in shape at θ = 300°. Another step out takes us to r/D = 0.93 (fig. 2.82). There are two things to note about this particular profile; first, there may be an indication of a short-lived transition at about 300 CAD. Second, the magnitude of the maximum shear stress has dropped by about a factor of three. Figure 2.48 shows that the velocities are lower at this radial position and, though there is a change in shape at θ = 300°, the effect is weak. The next profile out (r/D = 1.05, fig. 2.83) is somewhat remarkable in terms of its 'smoothness' and that the shear stress values are quite low compared to the previous stations' values. The flow has slowed considerably at this radial location. Figure 2.45 shows very low velocities and a thick near-wall layer. The next radial location (r/D = 1.17, fig. 2.84) again becomes jagged and transition is difficult to detect. Figure 2.43 shows a very low and flat near-wall velocity profile around θ = 180°. The shear stress at this time may have been corrupted by occasional reverse flow. The last profile at r/D = 1.30 (fig. 2.85) is somewhat bizarre in its own right, and little can be said about it except that the value of shear stress is quite low. The oddity of the profile is not entirely unexpected, considering the nature of the average velocity profile at this point (fig. 2.41). Average velocities are quite low.

2.6.3 Wall Shear Stress for Case Ib (Re$_{max}$ = 7600, Va = 2300, S = 54 mm, S/D = 0.251)

Using the algorithm described above, plots were made for the radial locations r/D = 0.68, 0.81, 0.93, 1.05, 1.17, and 1.30 and are presented in figures 2.86 through 2.91. One thing to notice for the smallest radial locations (figs. 2.86 through 2.88), is that there is a distinct difference between the blowing and suction strokes. Namely, during the blowing stroke, 180 < θ < 360, there is a considerably higher shear stress than on the suction stroke. This is in line with the hot wire and flow visualization results presented earlier. For these small radial locations (r/D = 0.68, 0.81, and 0.93), there is a strong wall jet during the blowing stroke, and on the intake stroke, flow is drawn from the entire channel, but more strongly from the area near the back wall. Thus, the shear stress is actually reversing during the cycle, though the hot wire measurements cannot resolve it. These characteristics would suggest shear stress plots like the ones presented in figures 2.86 through 2.88. One thing to note about these profiles (figs. 2.86 through 2.88) is that, with the exception of r/D = 0.93, the error is somewhat high on the blowing stroke. Hence, it is likely that general trends are being correctly described whereas numerical values of stress might be incorrect. For the larger radial locations (r/D = 1.05, 1.17, and 1.30, figs. 2.89 through 2.91) the behavior is somewhat different. The magnitude of shear stress is approximately equal on the blowing and suction strokes. This is reasonable in light of the flow visualization and anemometry results discussed above; the best example is figure 2.24. One can see that the velocity profile is similar on both the intake and exhaust strokes – there isn't a strong wall jet present on the blowing stroke. In these larger radius profiles, the error is quite low and we expect that the values of shear stress are correspondingly accurate.

2.6.4 Wall Shear Stress for Case IIIb (Re$_{max}$ = 17700, Va = 5400, S = 54 mm, S/D = 0.251)

Presented in figures 2.92 through 2.97 are walls shear stress profiles at the radial locations r/D = 0.68, 0.81, 0.93, 1.05, 1.17, and 1.30. These profiles are somewhat similar to those presented above for Case Ia.

The value of shear stress is higher on the blowing stroke than it is on the suction for the closest four radial locations (figs. 2.92 through 2.95). However, these plots are somewhat fraught with error. More than likely it is the case that the increase in wall jet velocities has thinned the boundary layer and made accurate shear stress measurements difficult or impossible. For the last two profiles this is not the case (figs. 2.96 and 2.97, $r/D = 1.17$ and $r/D = 1.30$), the error drops, presumably the boundary layer thickens and the values of shear stress are more reasonable. For these cases, the velocity profiles in figures 2.68 through 2.79 can be referred to for further clarification of the near-wall flow. In this case, as in the last, the near-wall flow and the shear stress are reversing during the cycle.

2.7 Conclusions

A data set that is useful for CFD code validation has been generated. The geometry under investigation is spatially simple, yet it generates flow complex enough to challenge current available routines. The code developer will find the above ensemble average velocity data, *TI* quantities, and wall shear stresses indispensable in proving that the code "works." Moreover, from the design point of view, it has been observed that tube flows are generally sinusoidal in nature and relatively independent of engine parameters. It has been observed that flows in the disc space (which approximately models a heater head) generally show the presence of a wall jet (on the blowing stroke) and a sink flow (during suction). These features depend strongly on engine geometry (disc spacing) and Valensi number.

In light of sections 1 and 2, the reader may ask what is the connection? Section 3 – A Comparison Between Oscillatory Flow and Unidirectional Flow serves to answer this. The main subject of concern is to determine whether or not it is reasonable to expect similar fluid dynamic behavior from steady unidirectional flow and oscillatory flow in the same geometry. The impetus is the fact that there is a large body of work available for impinging jets, whereas, there are few data for oscillatory flows in Stirling engines. This knowledge is useful for both the engine designer and code developer alike.

A comment is in order regarding CFD development; the data provided above provide insight into what type of modeling may be necessary in different engine regions. For example, in the tube flow it was observed that by and large the flow was axisymmetric and sinusoidal. This type of flow could be well described with one-dimensional design codes given the proper choice of parameters (i.e., Reynolds number, Valensi number, etc.). Likewise, in the wall jet, given proper normalization and averaging procedure, one could accurately describe bulk fluid behavior. (Some sort of jet thickness as a function of engine parameters should be developed, which, in the authors' opinion, there is insufficient data available for this purpose.) Regarding multi-dimensional modeling, one can expect that large-scale flow features could be well described with RANS type modeling. However, development of proper turbulence models will be necessary. With the wrong turbulence model, one cannot reasonably expect accurate calculations of wall shear stress values, turbulence quantities, shear layer shape, etc. This will be discussed in further detail in section 4 – Comparisons Between Experimentally Gathered Results and CFD Generated Data.

2.8 Error Analysis

As a first comment, hot wires have a certain calibration error associated with them. This source of error is handled in detail in appendix B. Outside of specific calibration errors, there are errors associated with measurements of the above-described flow. We now present the errors that we noticed.

One potential error associated with anemometry in an oscillating flow is as follows; the probe introduces a disturbance to the flow. We introduce figure 2.98 to clarify our meaning. With reference to the 'Side View' in figure 2.98, one must imagine that during some portions of the oscillation cycle, flow is moving from left to right (as drawn) whereas at other times it is moving from right to left. The point is that the wake the probe creates will eventually be blown back over the probe and wire. Thus, the introduction of the probe into the flow might lead to higher *TI* measurements than actually present in the undisturbed flow. Moreover, shortly after reversal, as the wake is passing over the probe, velocity measurements may be perturbed in that the wake will 'shield' the probe from the bulk flow velocity.

Unfortunately, we have no direct way to quantify the effect of these errors, we can only state that they may exist. One could get a feel for the magnitude of the error by conducting a flow visualization experiment with the probe in the flow. This is difficult in the sense that hot wire probes are remarkably fragile and introducing particles into the flow would for visualization purposes invariably break the probe.

A second source of error arises when taking near-wall measurements. As the active part of the probe (the wire) is moved towards a solid boundary, conduction effects seem to become important (see fig. 2.99). In general, within a critical distance, 'A,' the wire thermally communicates with the wall via conduction through the air. The net result is that as more heat is removed from the wire (due to the presence of the wall) the measurement of apparent velocity increases. Of course, the flow must obey a no-slip boundary condition at the wall; hence velocity should go to zero as the probe approaches the wall. A sample data set is presented in figure 2.100. Figure 2.100 is a *particular* (i.e., A in fig. 2.99 varies with rpm) example of what one observes that near the wall (x/S is near zero). Regardless of crank angle all of the curves 'follow' this trend. At about $x/S = 0.008$, the curves begin to deviate, and, for larger axial positions, the curves are not correlated in any special way. Thus, we assume that the correlated portion of the curves is characteristic of wall conduction effects. To 'correct' this problem, we simply discard the points in the correlated region. Thus, we take A (as mentioned above), in this case as 0.008 and discard all points that are closer to the wall than A. In general, A ~ 0.008 for the 30 rpm cases and A ~ 0.004 for the 70 rpm case. As a note, this correction has been made to all of the velocity and *TI* plots presented in this report.

A third source of error concerning the hot wire corresponds to pulling the probe out of the flow. Again, a picture speaks better than words, so we reference the reader to figure 2.101. The type of error illustrated in figure 2.101 happens only near $x/S = 1$. At $x/S = 1$, the wire is essentially at the lip of the access hole. Looking at raw data (fig. 2.102), one sees that the velocity near this axial location is too high (almost like a jump discontinuity), hence, data points near to $x/S = 1$ are treated as erroneous and not presented in the plots above.

Outside of anemometry measurement errors, there are errors associated with probe positioning. We state them now.

In the disc space for $S = 54$ mm, the error an the axial direction, x, can be described as:

$$x/S = x/S \pm \delta x/S$$

where

$$\delta x/S = 0.002.$$

In the radial direction, r/D, the associated positioning error can be described as:

$$r/D = r/D \pm \delta r/D$$

where

$$\delta r/D = 0.005.$$

In the disc space for $S = 127$ mm, the error an the axial direction, x, can be described as:

$$x/S = x/S \pm \delta x/S$$

where

$$\delta x/S = 0.001.$$

In the radial direction, r/D, the associated positioning error can be described as:

$$r/D = r/D \pm \delta r/D$$

where

$$\delta r/D = 0.005 .$$

Finally, in the tube space the error in the radial direction, r, can be described as:

$$r/D = r/D \pm \delta r/D$$

where

$$\delta r/D = 0.0006 .$$

2.9 Figures
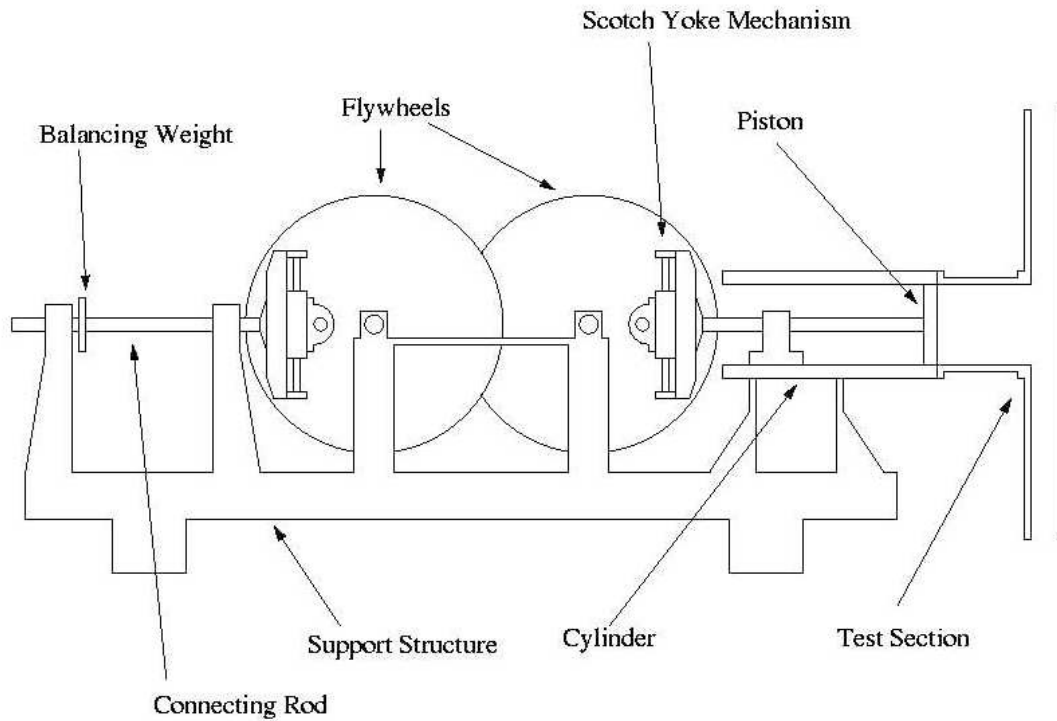
Figure 2.1.—The University of Minnesota Scotch Yoke Drive Facility and Test Section.
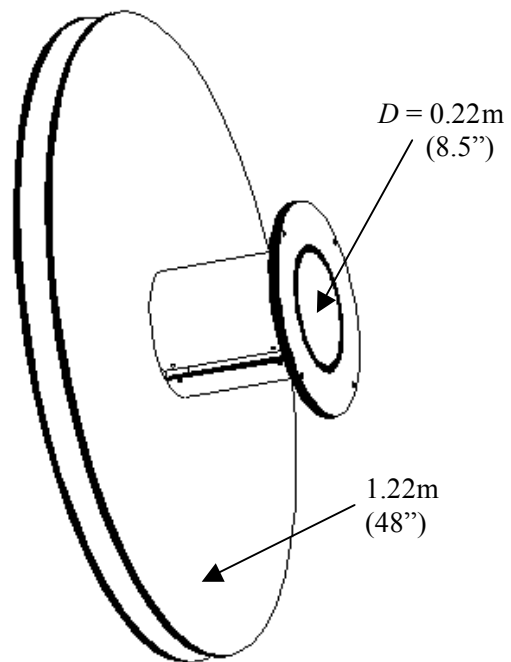
Figure 2.2.—The test section.
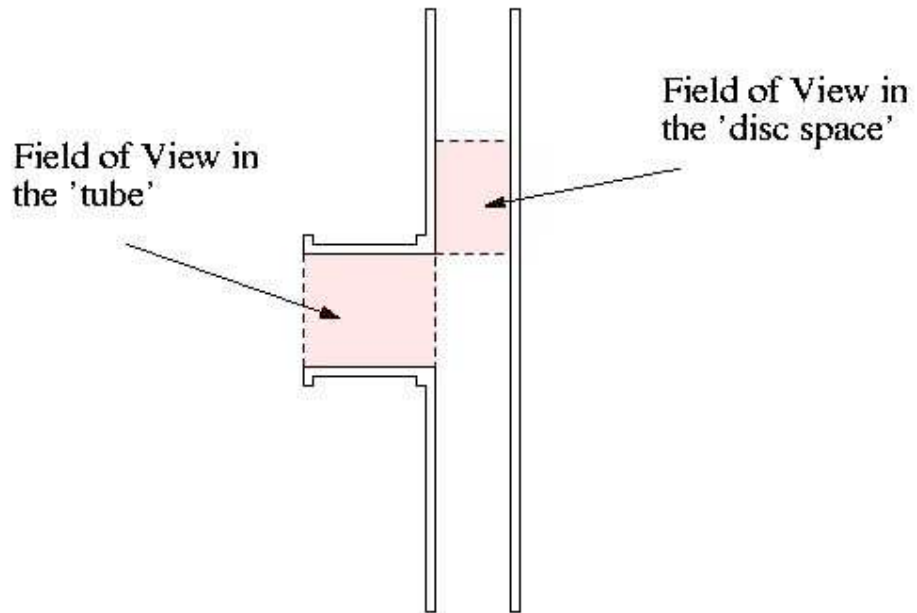
Figure 2.3.—Flow visualization fields of view.
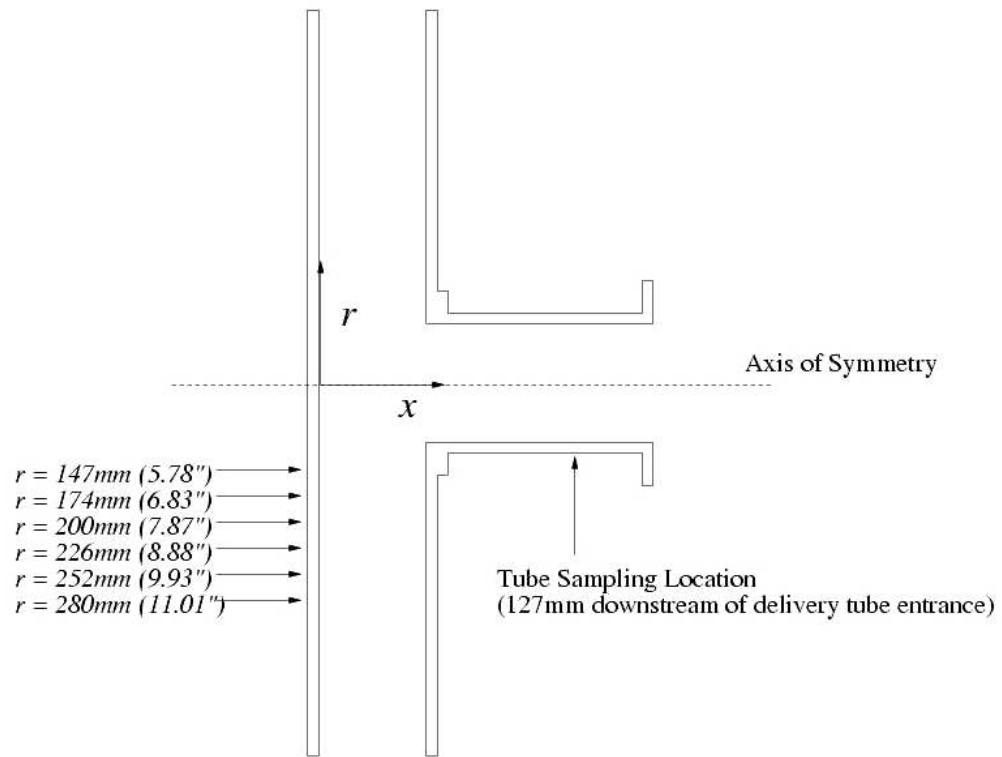
Figure 2.4.—Sampling locations and coordinate conventions.
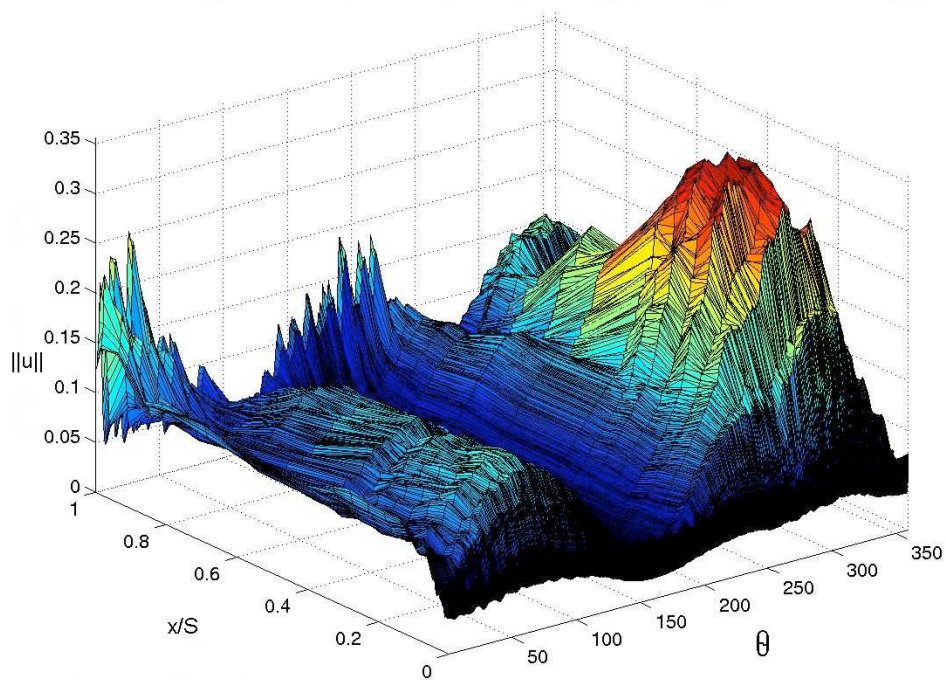
Figure 2.5.—A sample data set – the best view of small values of x/S.
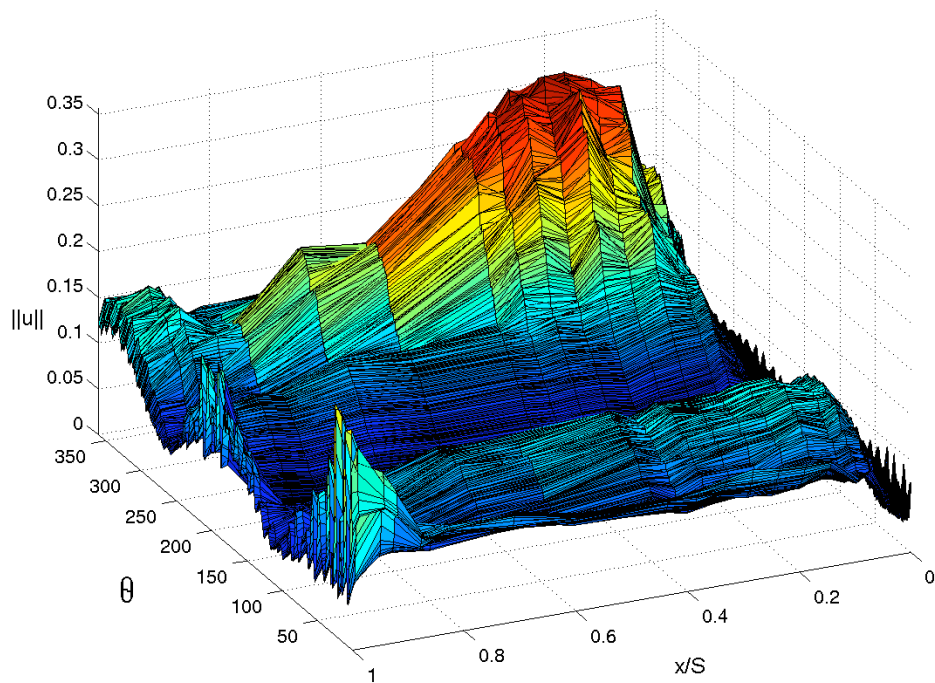
Figure 2.6.—The same data set as figure 2.5 but viewed from a different angle – the best view of the effect of crank angle.
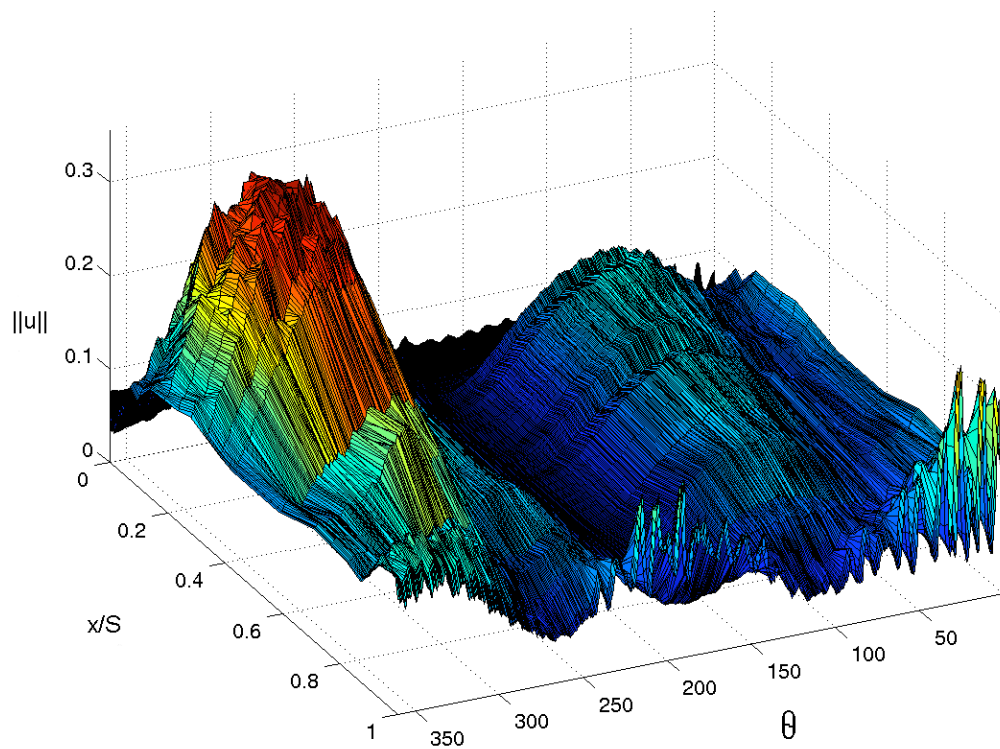
Figure 2.7.—The same data set as figure 2.5 but viewed from yet another angle – the best view of the region near $x/S = 1$.
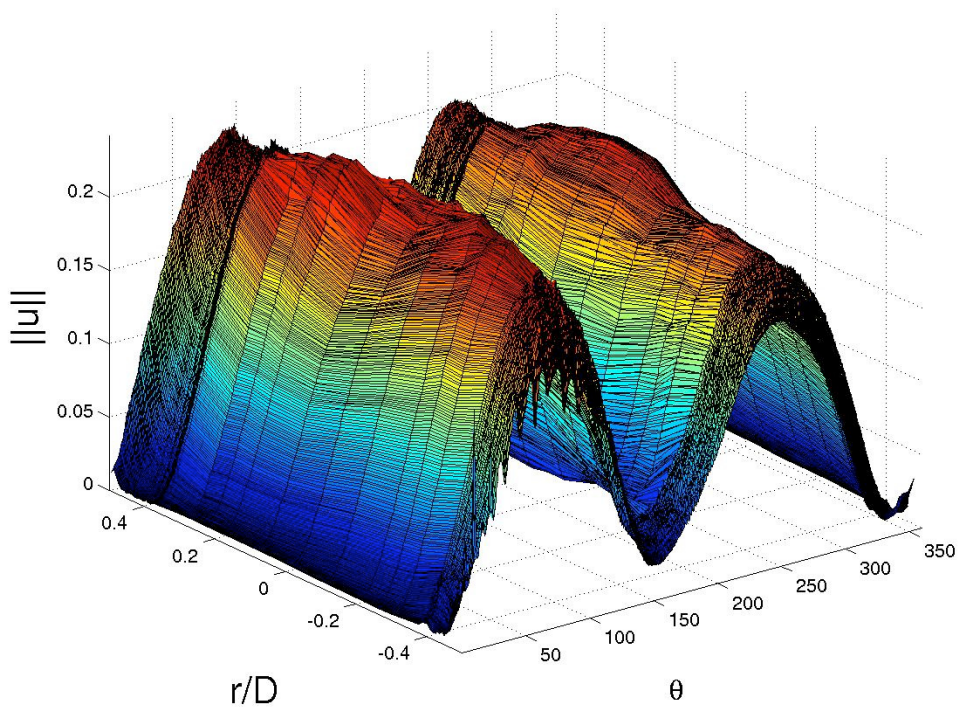
Figure 2.8.—Ensemble averaged velocity profile for Case Ia (tube space flow, Va = 2300, *S*/*D* = 0.251).
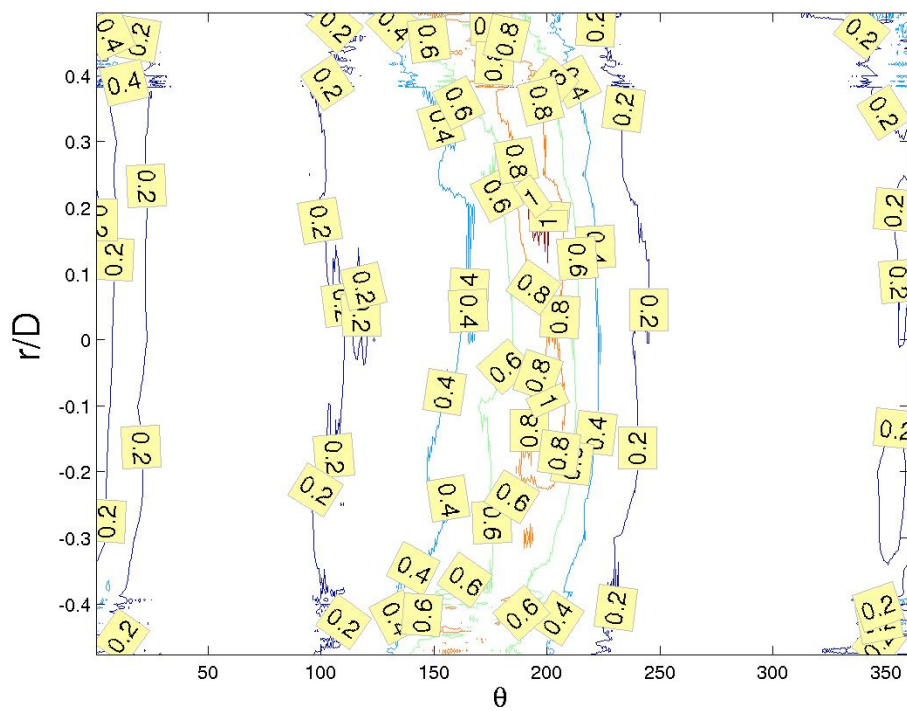
Figure 2.9.—*TI* contour map for Case Ia (tube space flow, Va = 2300, *S*/*D* = 0.251).
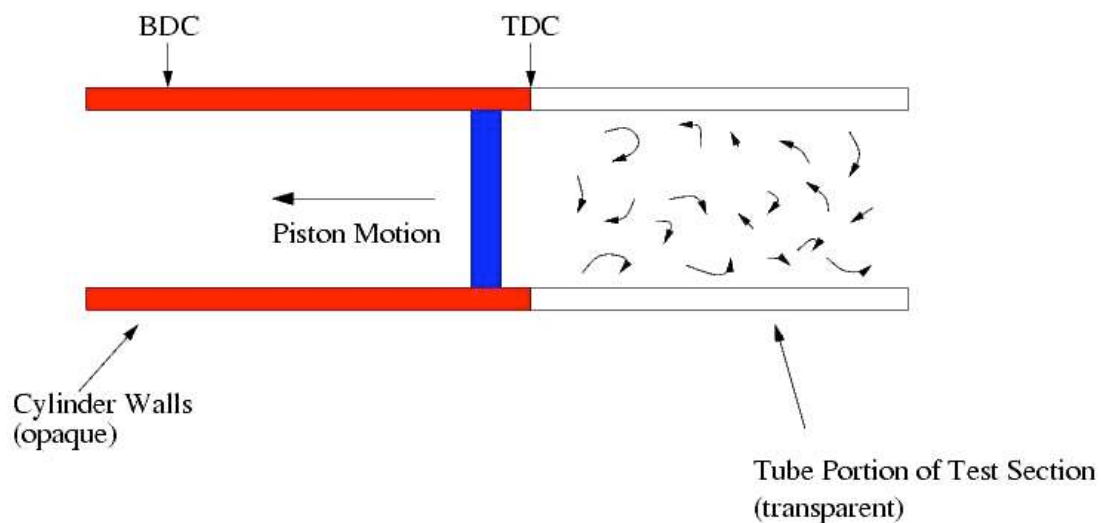
Figure 2.10.—Flow visualization summary for the degree range 0° < θ <15° for Case Ia (tube space flow, Va = 2300, *S*/*D* = 0.251).
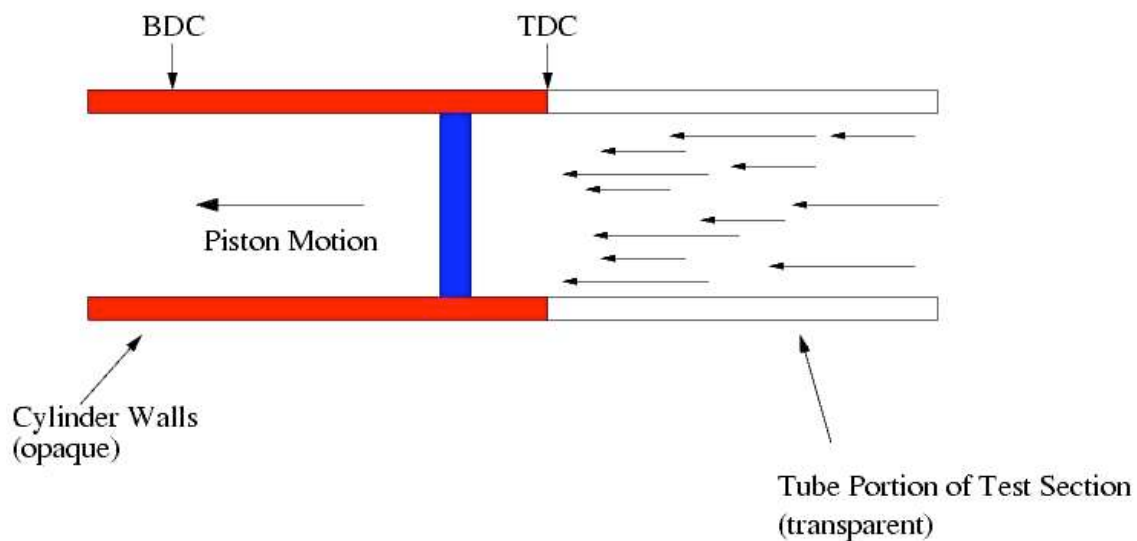
Figure 2.11.—Flow visualization summary for 15 to 45 CAD for Case Ia (tube space flow, Va = 2300, *S*/*D* = 0.251).
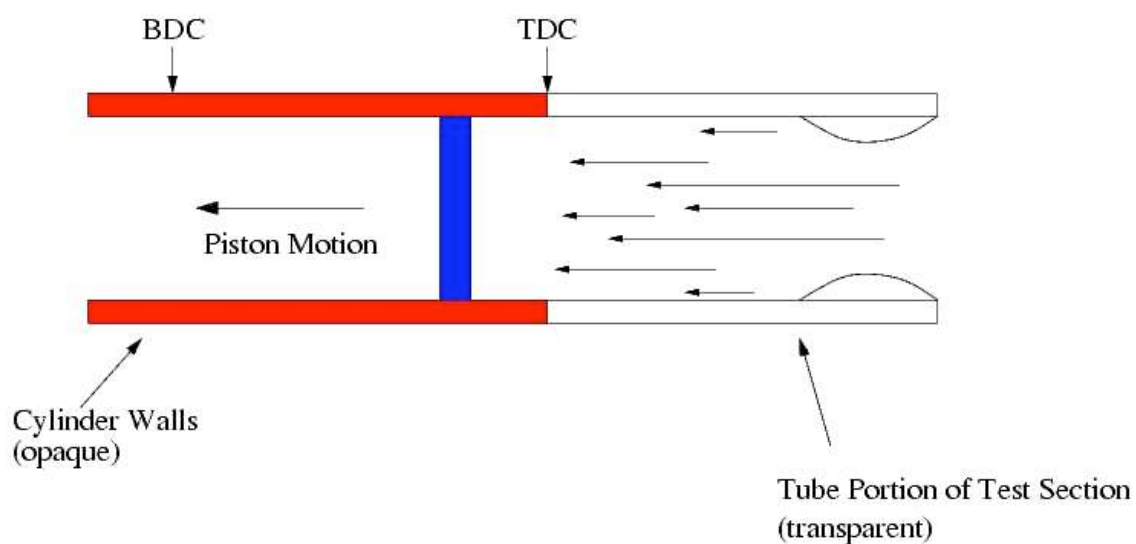
Figure 2.12.—Flow visualization summary for 45 to 75 CAD for Case Ia (tube space flow, Va = 2300, *S/D* = 0.251).
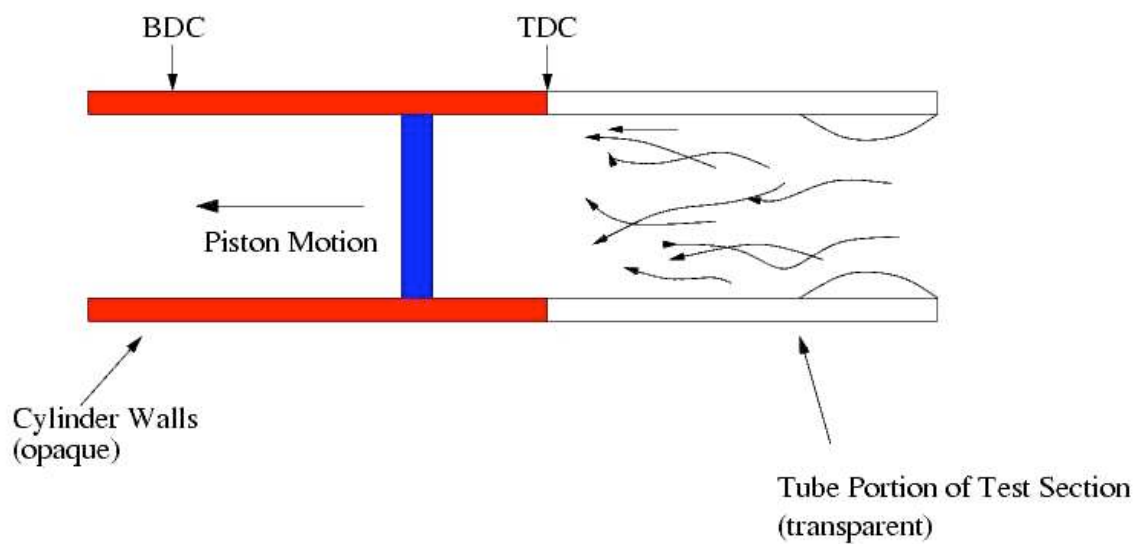
Figure 2.13.—Flow visualization summary for 75 to 105 CAD for Case Ia (tube space flow, Va = 2300, *S/D* = 0.251).
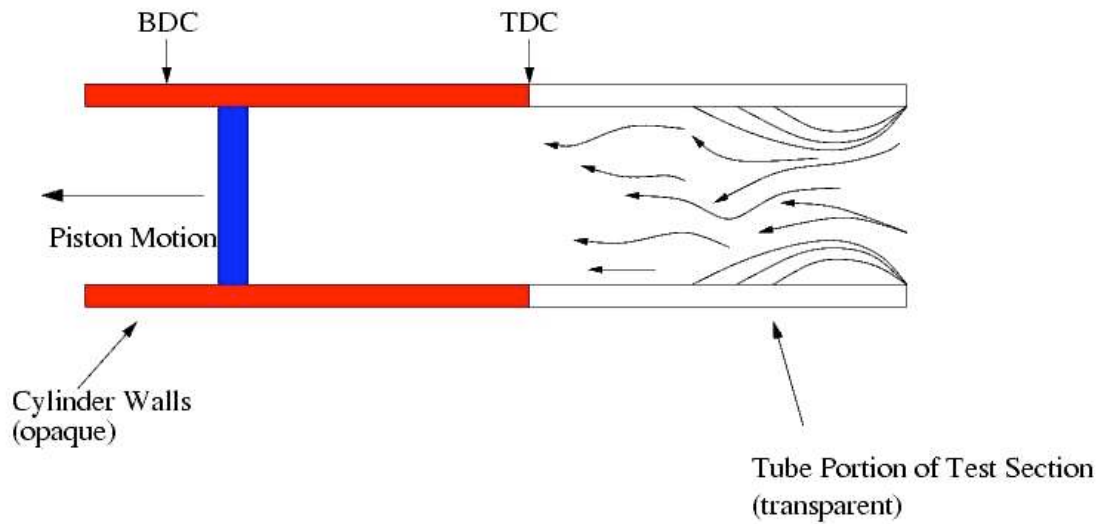
Figure 2.14.—Flow visualization summary for 105 to 180 CAD for Case Ia (tube space flow, Va = 2300, *S*/*D* = 0.251).
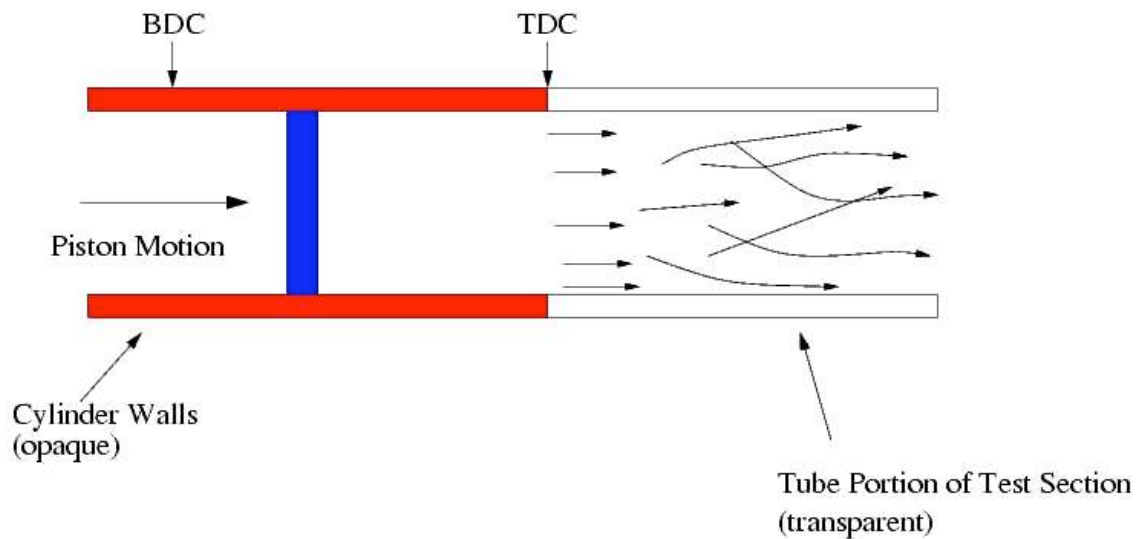
Figure 2.15.—Flow visualization summary for 210 to 240 CAD for Case Ia (tube space flow, Va = 2300, *S*/*D* = 0.251).

Figure 2.16. Flow visualization summary for 240 to 330 CAD for Case Ia (tube space flow, Va = 2300, *S/D* = 0.251).

Figure 2.17.—A summary of flow visualization results for the degree range 30° < θ < 165° for Case Ib (disc space flow, Va = 2300, *S/D* = 0.251).
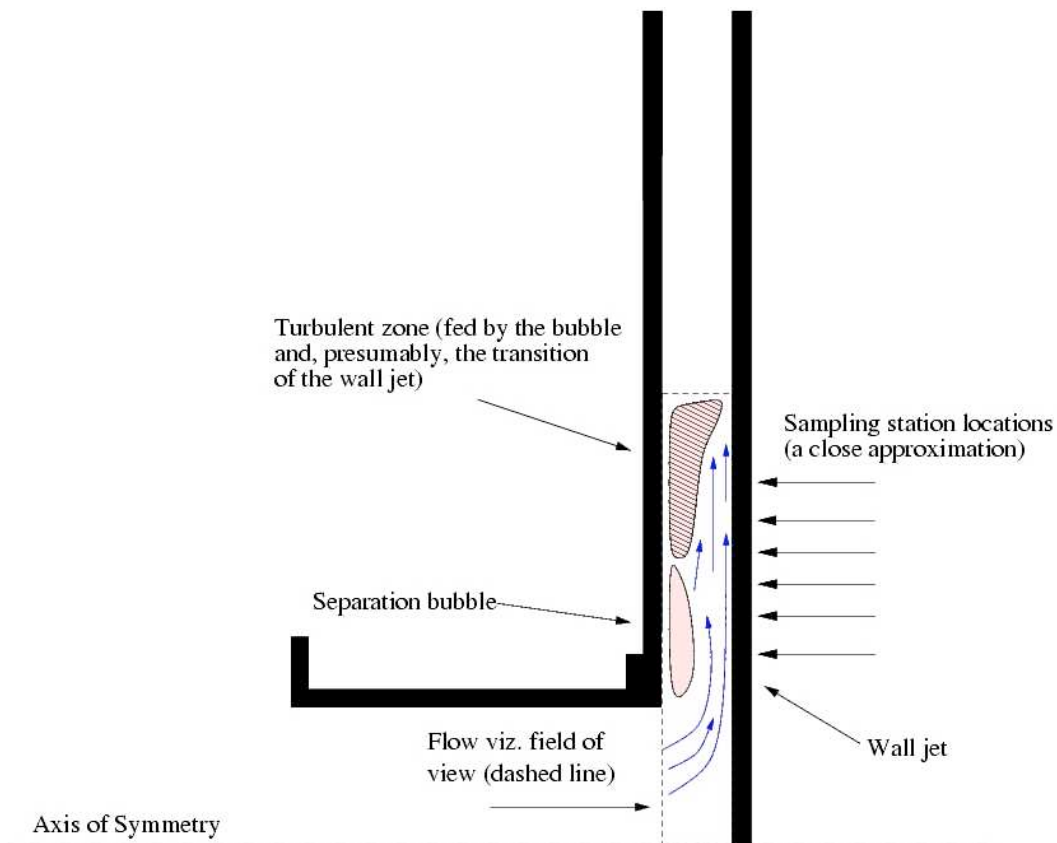
Figure 2.18.—A summary of flow visualization results for the blowing stroke for Case Ib (disc space flow, Va = 2300, *S/D* = 0.251).
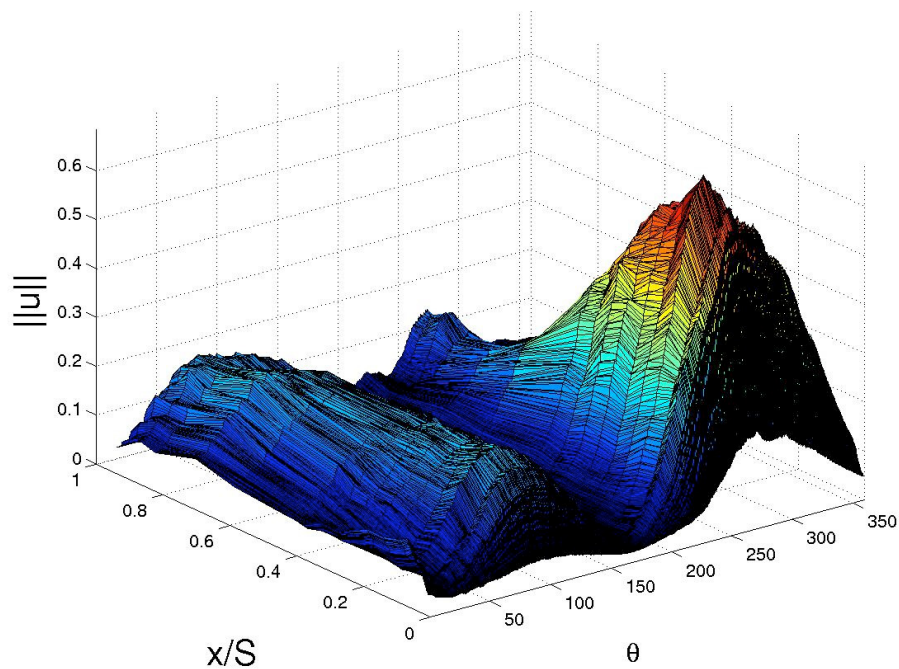
Figure 2.19.—Ensemble averaged velocity profile at *r/D* = 0.68 for Case Ib (disc space flow, Va = 2300, *S/D* = 0.251).
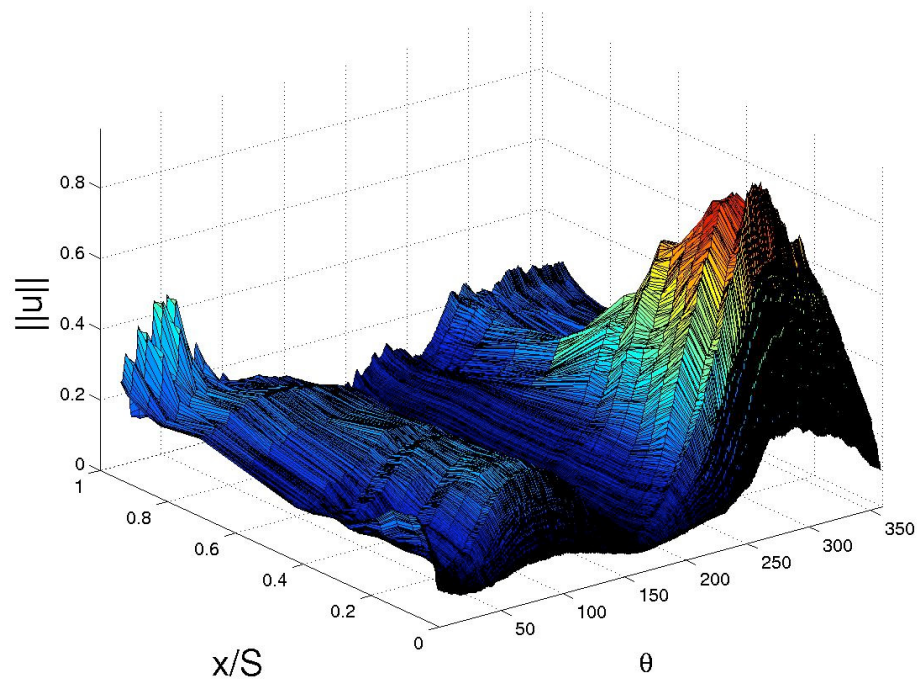
Figure 2.20.—Ensemble averaged velocity profile at $r/D = 0.81$ for Case Ib (disc space flow, Va = 2300, $S/D = 0.251$).
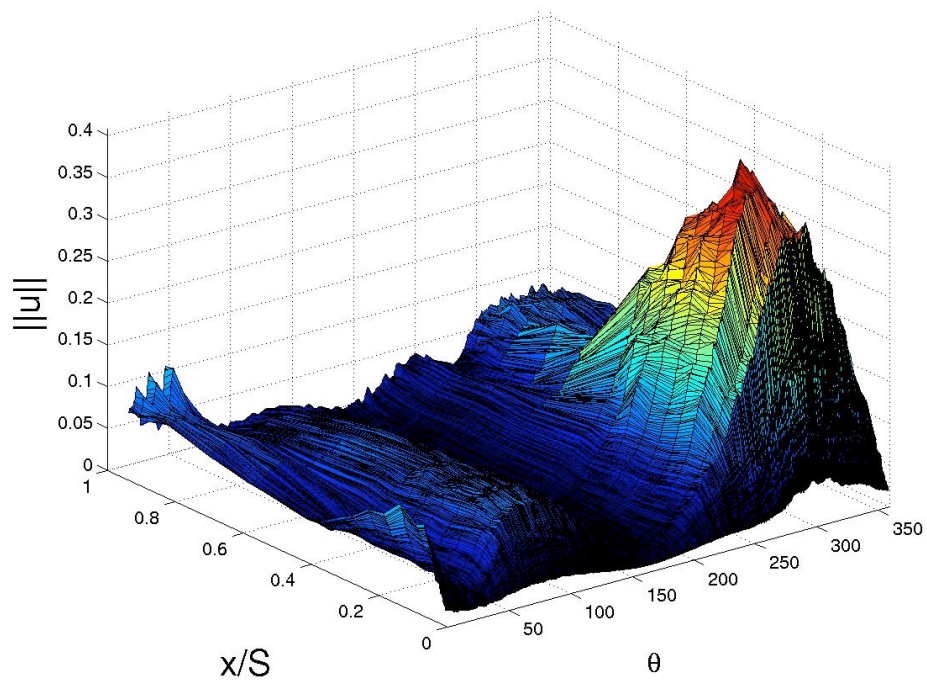
Figure 2.21.—Ensemble averaged velocity profile at $r/D = 0.93$ for Case Ib (disc space flow, Va = 2300, $S/D = 0.251$).
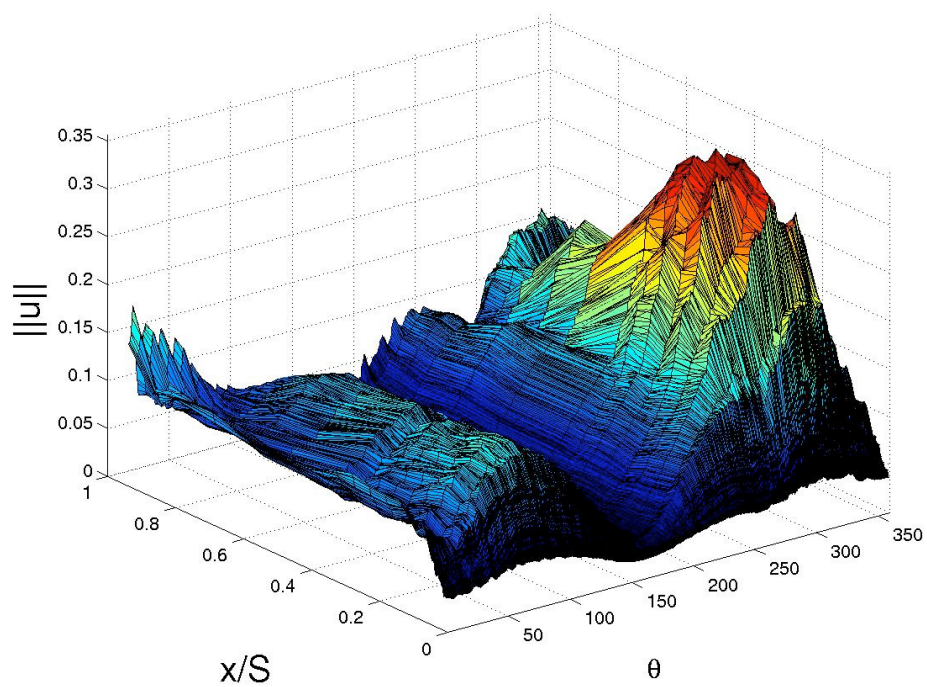
Figure 2.22.—Ensemble averaged velocity profile at *r*/*D* = 1.05 for Case
Ib (disc space flow, Va = 2300, *S*/*D* = 0.251).
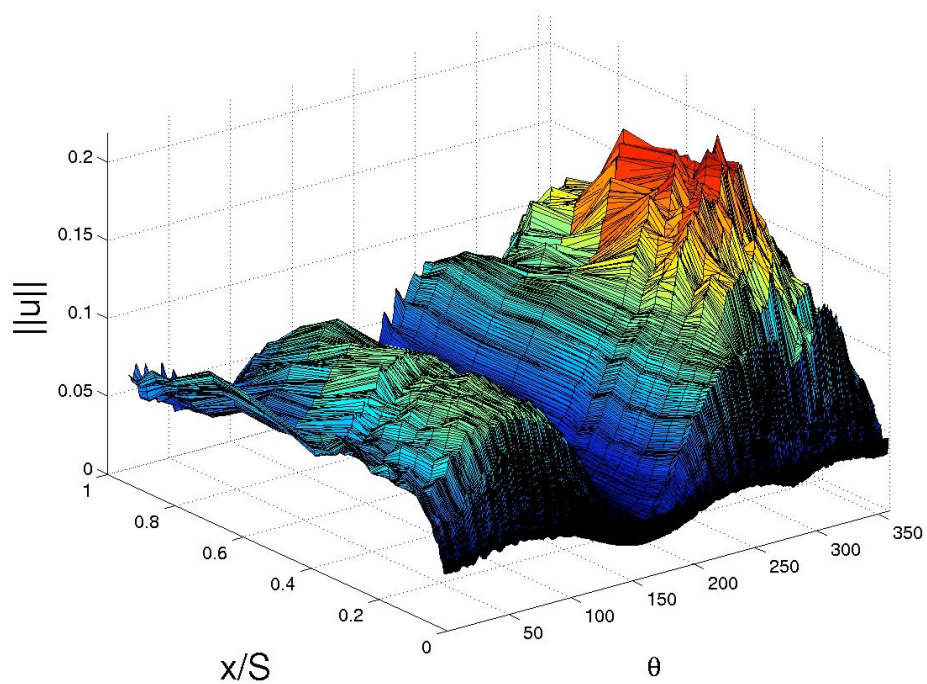
Figure 2.23.—Ensemble averaged velocity profile at *r*/*D* = 1.17 for Case
Ib (disc space flow, Va = 2300, *S*/*D* = 0.251).
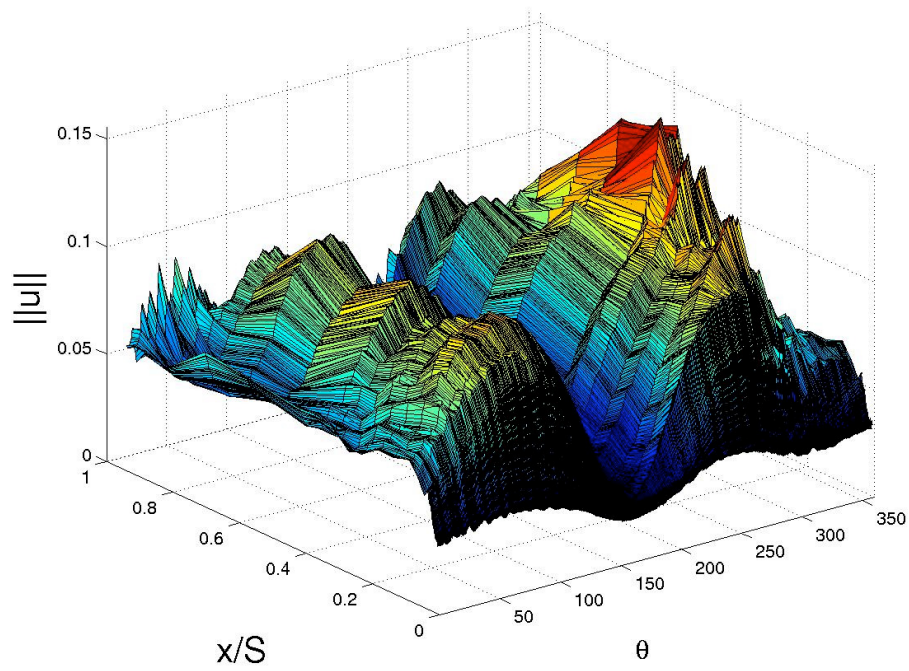
Figure 2.24.—Ensemble averaged velocity profile at r/D = 1.30 for Case
Ib (disc space flow, Va = 2300, S/D = 0.251).
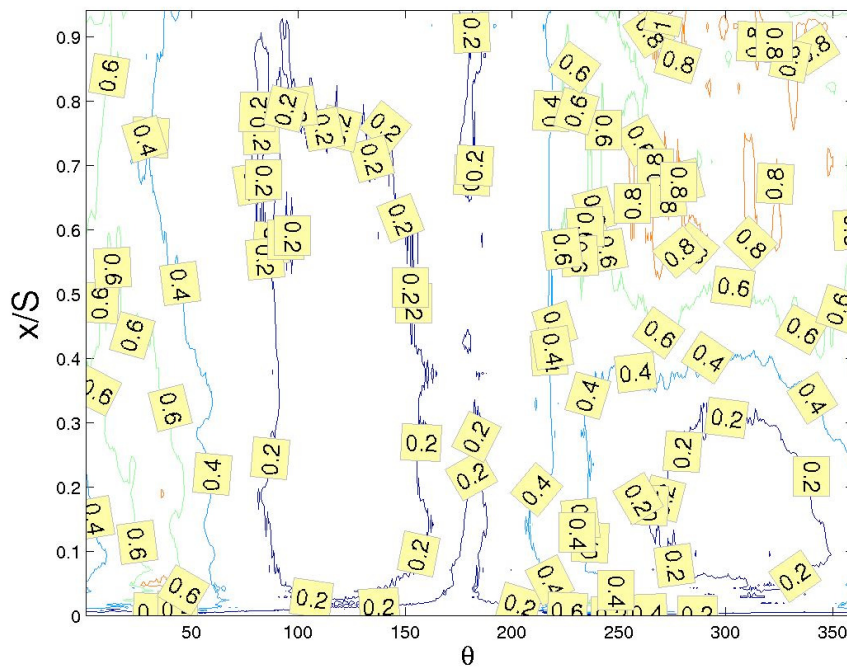
Figure 2.25.—Turbulence intensity contour map at r/D = 0.68 for Case
Ib (disc space flow, Va = 2300, S/D = 0.251).
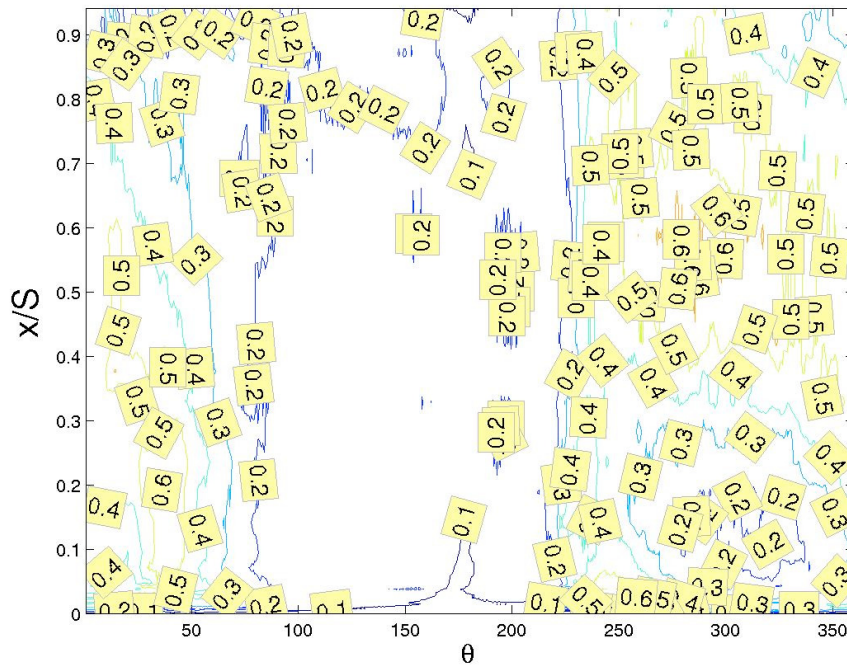
Figure 2.26.—Turbulence intensity contour map at $r/D = 0.81$ for Case Ib (disc space flow, Va = 2300, $S/D = 0.251$).
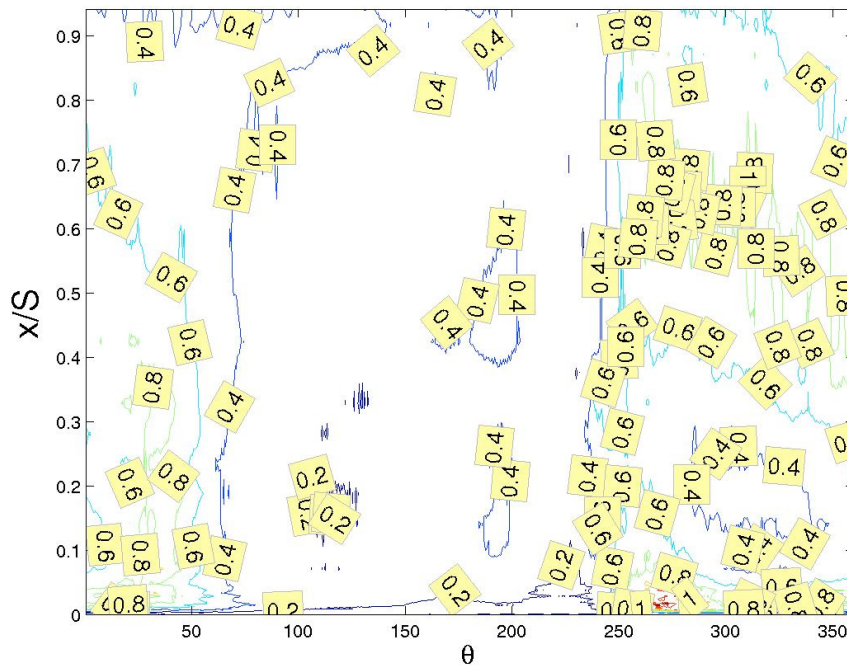
Figure 2.27.—Turbulence intensity contour map at $r/D = 0.93$ for Case Ib (disc space flow, Va = 2300, $S/D = 0.251$).
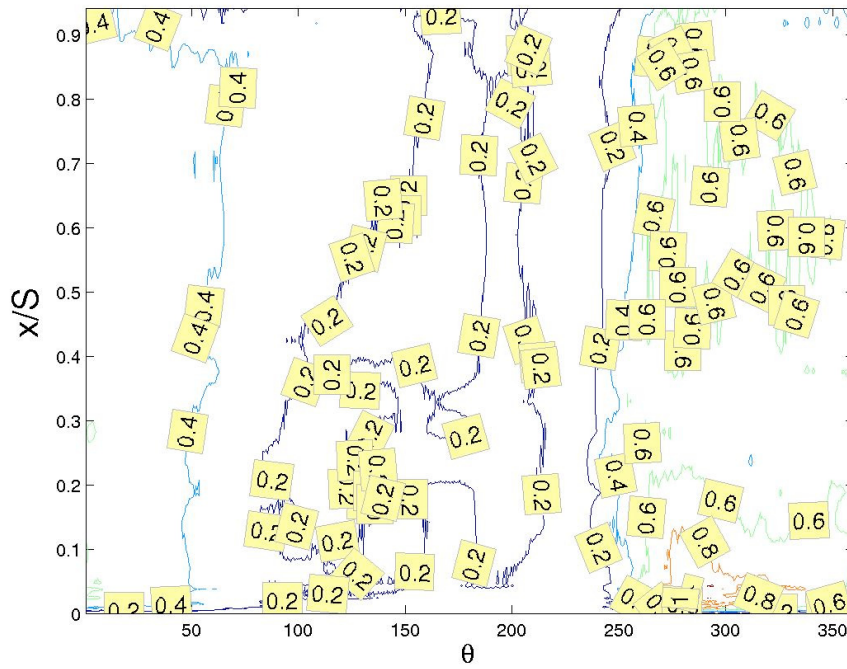
Figure 2.28.—Turbulence intensity contour map at $r/D = 1.05$ for Case Ib (disc space flow, Va = 2300, $S/D = 0.251$).
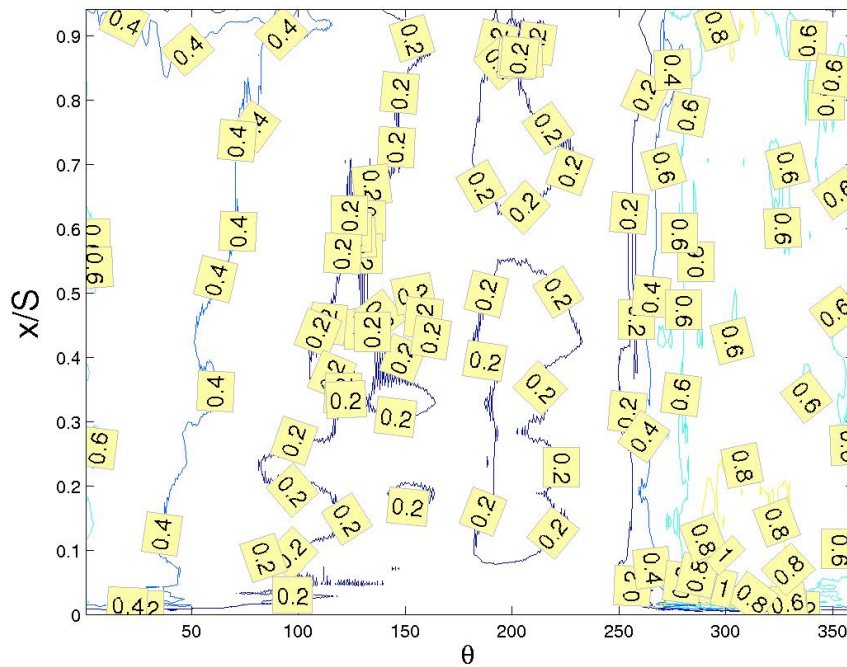
Figure 2.29.—Turbulence intensity contour map at $r/D = 1.17$ for Case Ib (disc space flow, Va = 2300, $S/D = 0.251$).
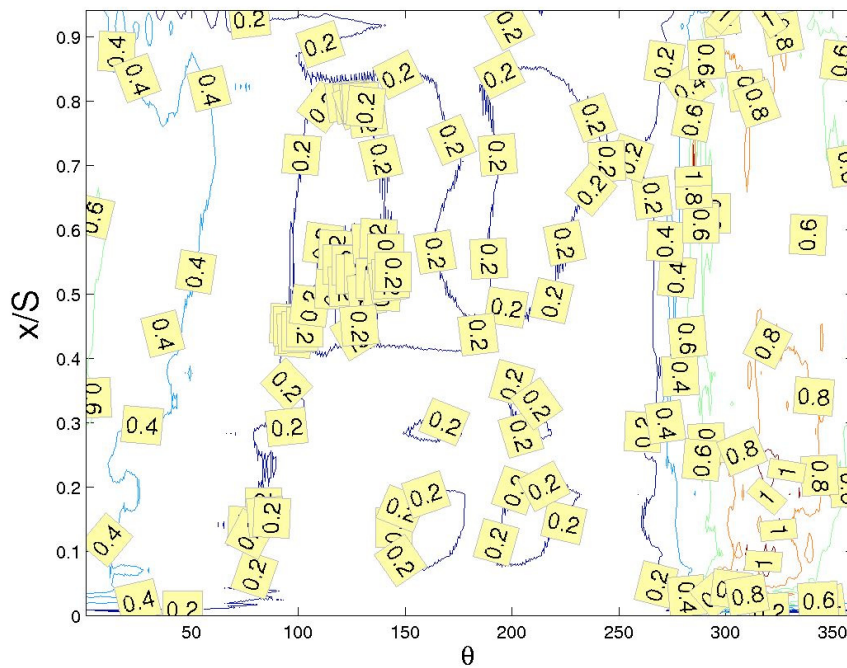
Figure 2.30.—Turbulence intensity contour map at *r*/*D* = 1.30 for Case
Ib (disc space flow, Va = 2300, *S*/*D* = 0.251).
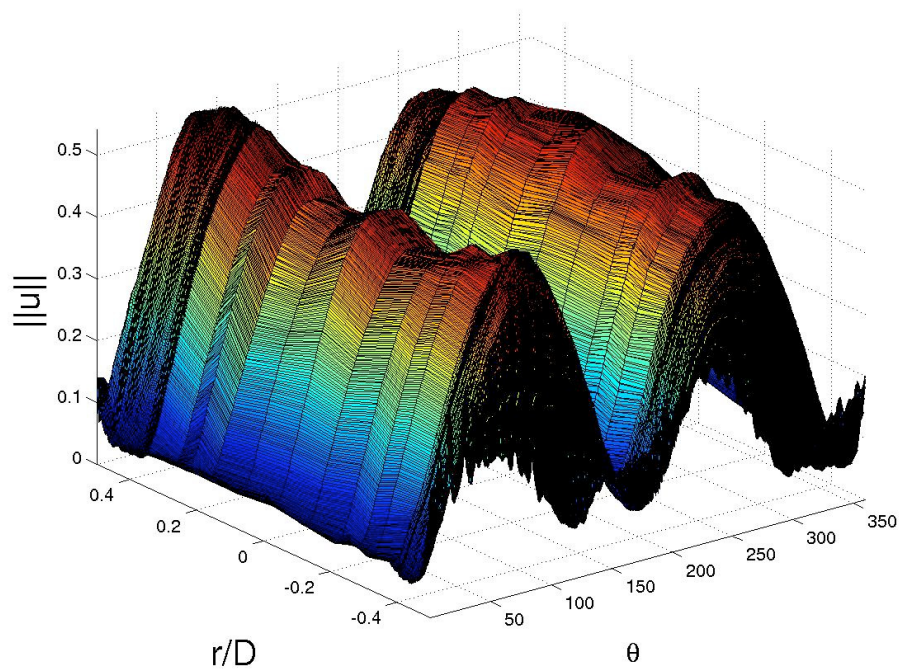
Figure 2.31.—Ensemble averaged velocity profile for case IIa (tube flow,
Va = 2300, *S*/*D* = 0.591).
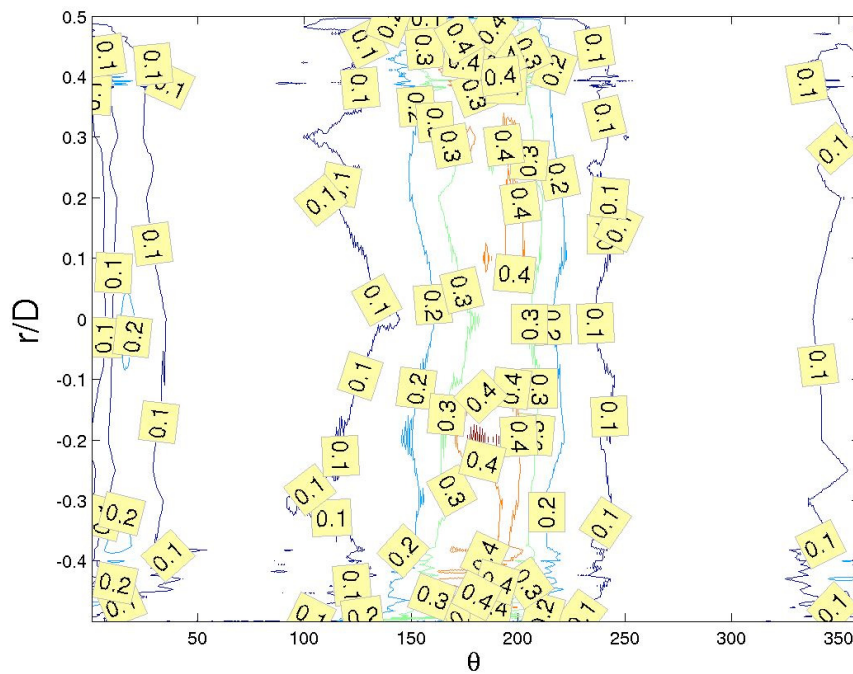
Figure 2.32.—*TI* contour map for case IIa (tube flow, Va = 2300, *S/D* = 0.591).
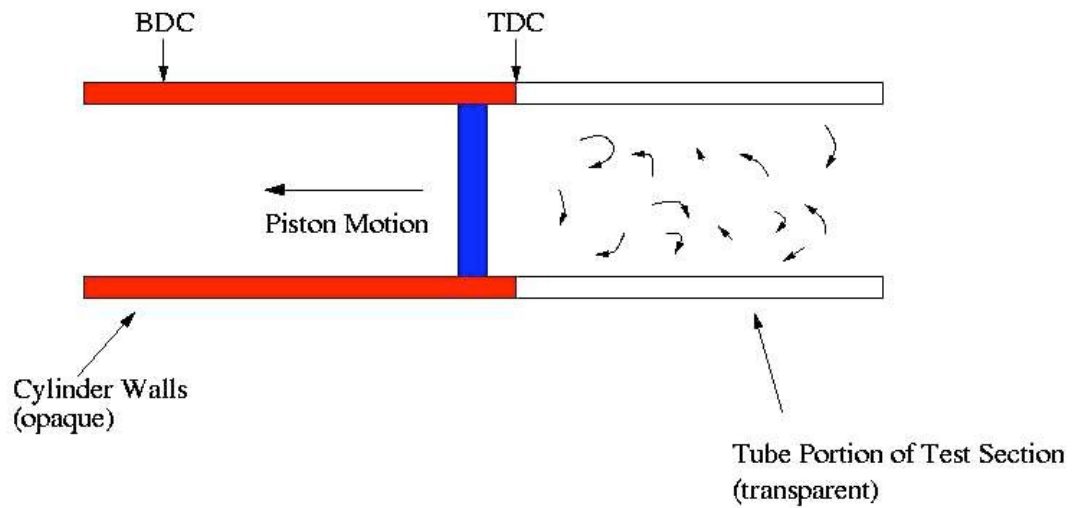
Figure 2.33.—Flow visualization results in the degree range 0° < θ < 15° for case IIa (tube flow, Va = 2300, *S/D* = 0.591).
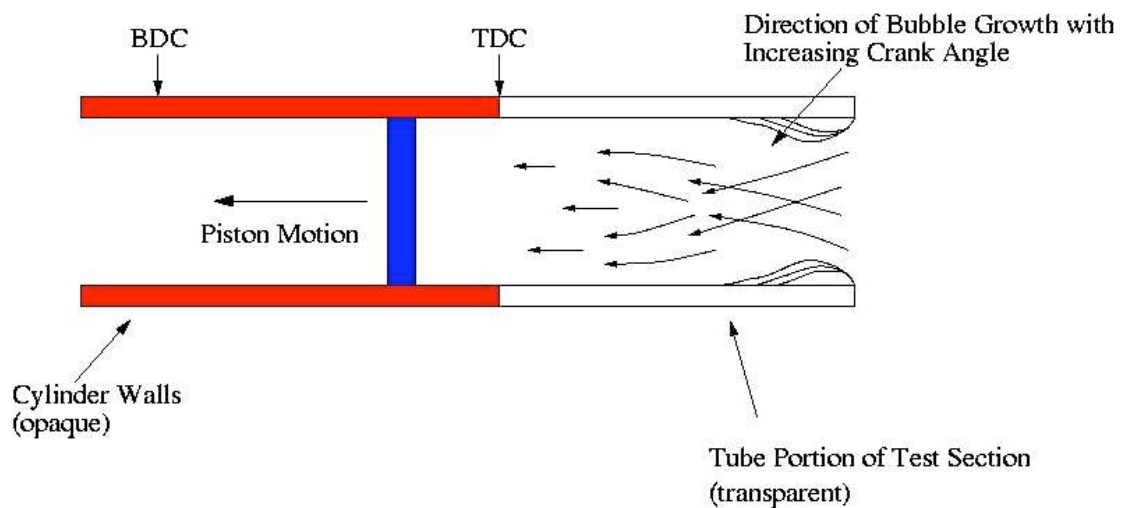
Figure 2.34.—Flow visualization results in the degree range 15° < θ < 60° for case IIa (tube flow, Va = 2300, *S*/*D* = 0.591).
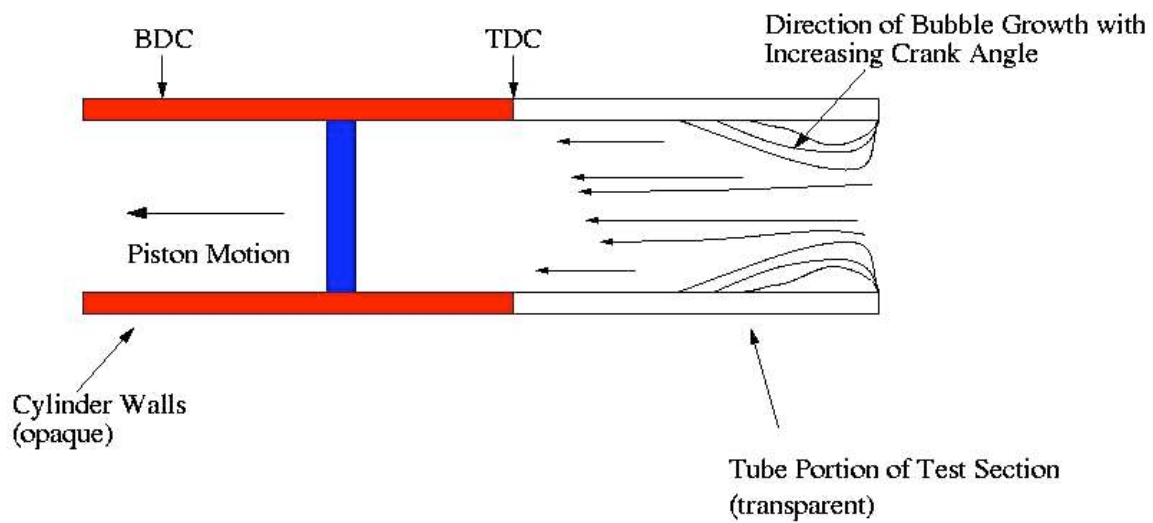
Figure 2.35.—Flow visualization results in the degree range 60° < θ < 90° for case IIa (tube flow, Va = 2300, *S*/*D* = 0.591).
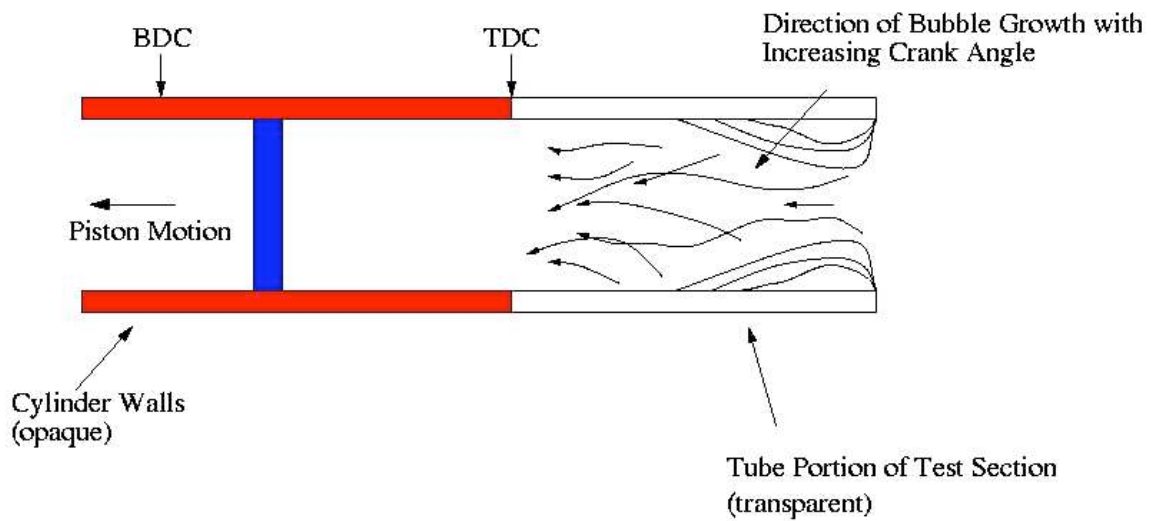
Figure 2.36.—Flow visualization results in the degree range 90° < θ < 150° for case IIa (tube flow, Va = 2300, *S*/*D* = 0.591).
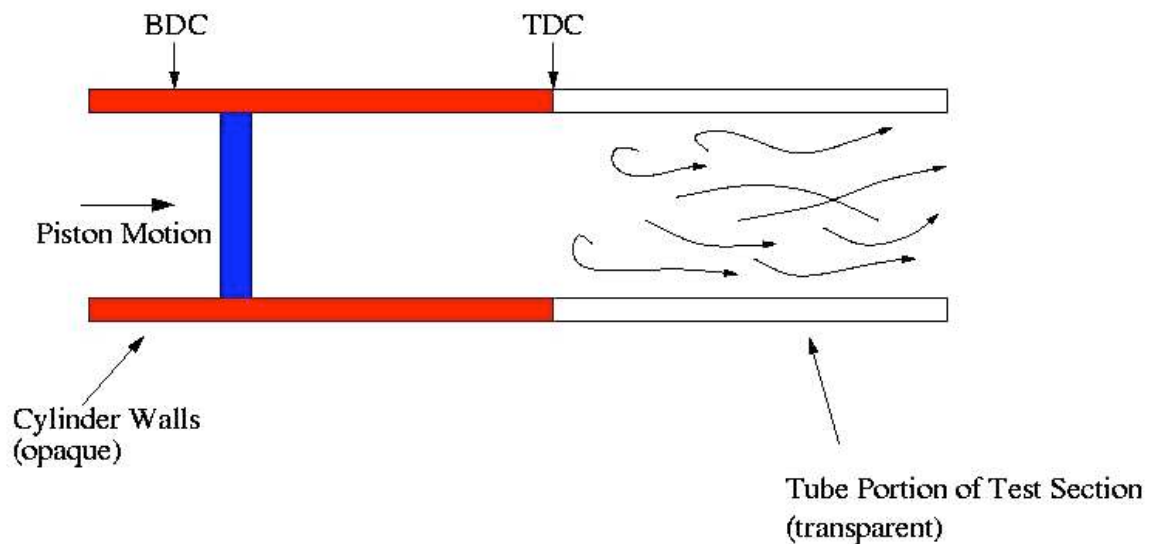
Figure 2.37.—Flow visualization results in the degree range 180° < θ < 240° for case IIa (tube flow, Va = 2300, *S*/*D* = 0.591).
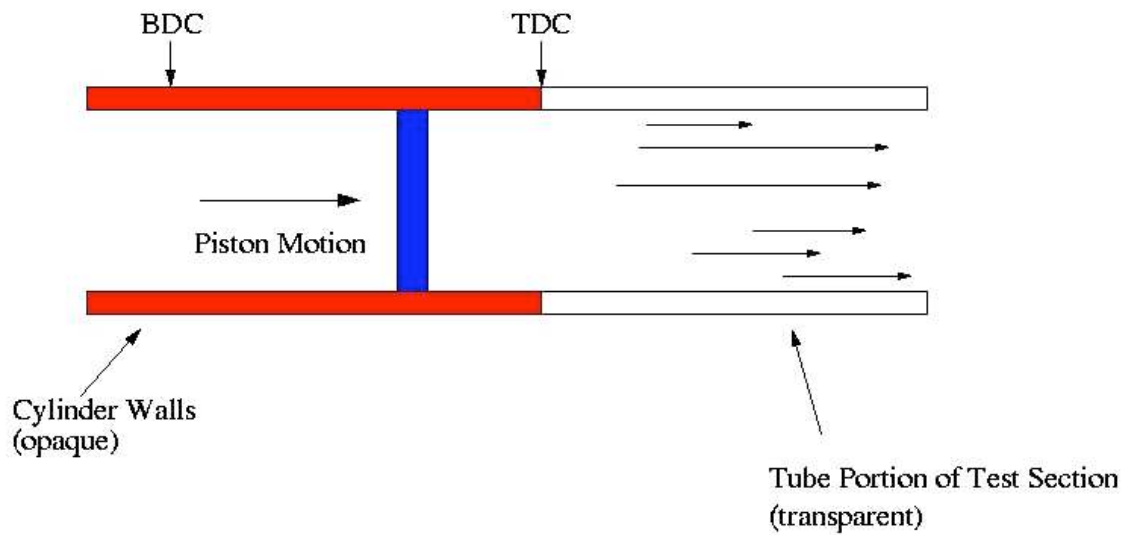
Figure 2.38.—Flow visualization results in the degree range 240° < θ < 330° for case IIa (tube flow, Va = 2300, *S/D* = 0.591).
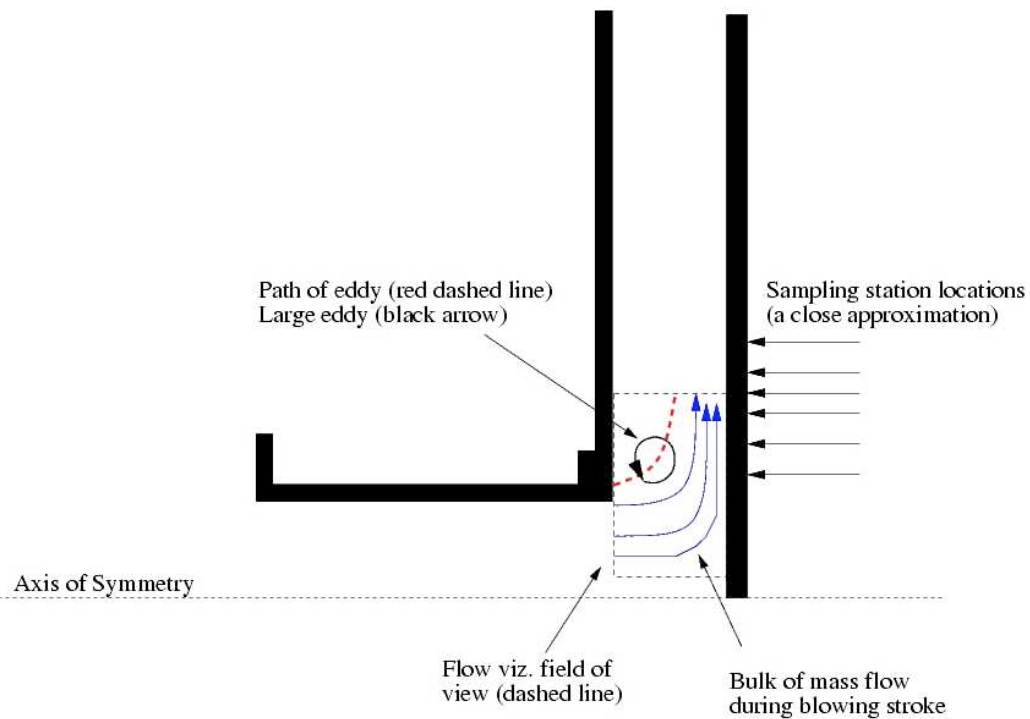
Figure 2.39.—The main features of the blowing stroke as revealed by flow visualization techniques for case IIb (disc space flow, Va = 2300, *S/D* = 0.591).
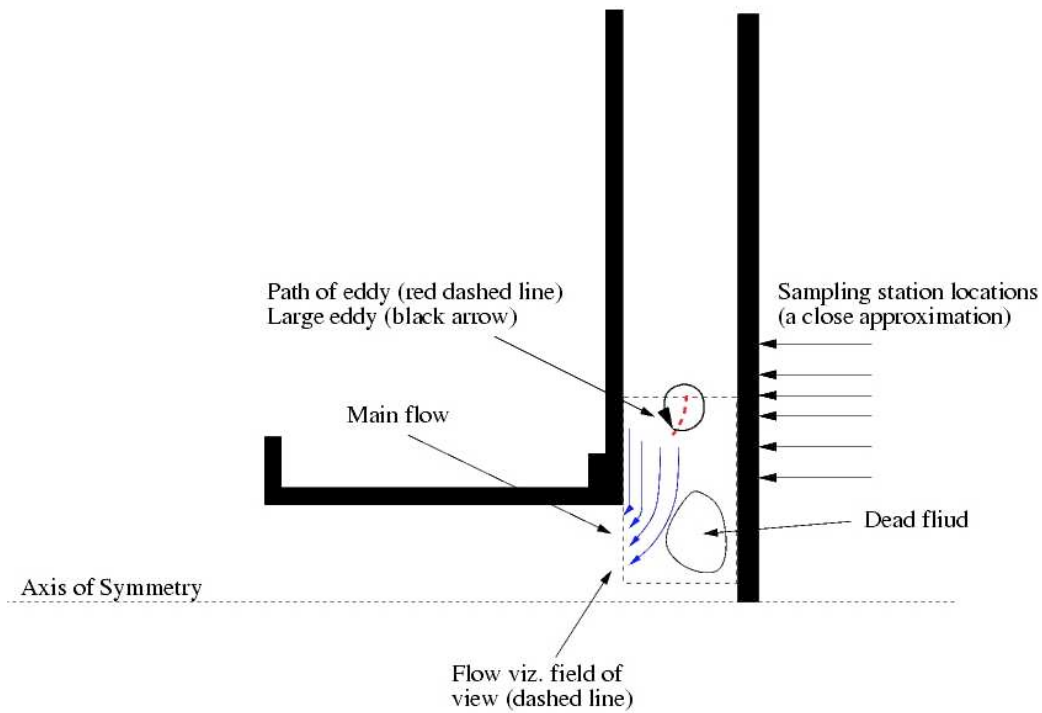
Figure 2.40.—The main features of the suction stroke as revealed by flow visualization techniques for case IIb (disc space flow, Va = 2300, *S/D* = 0.591).
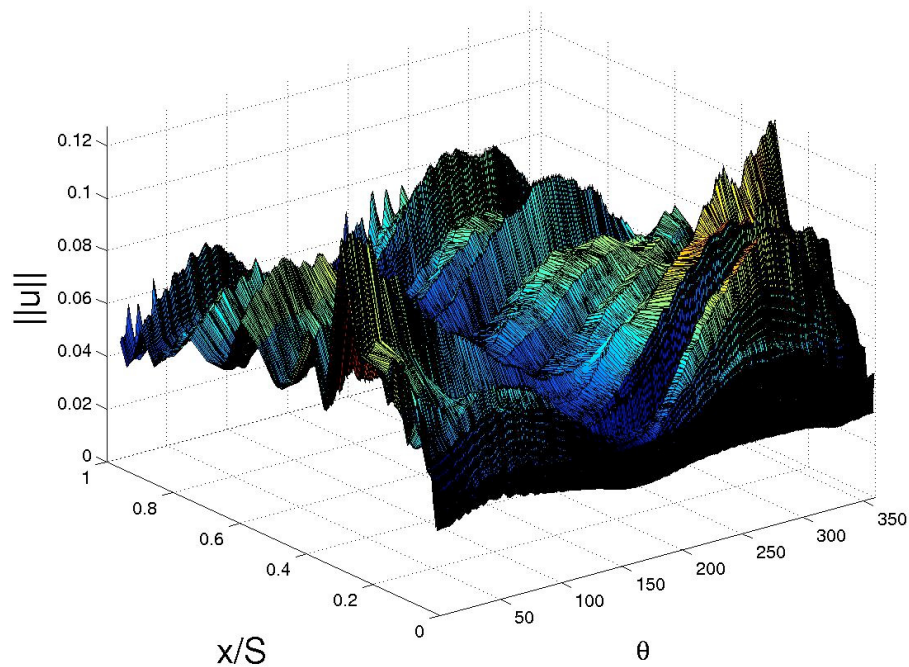
Figure 2.41.—Velocity profile at *r/D* = 1.30 for case IIb (disc space flow, Va = 2300, *S/D* = 0.591).
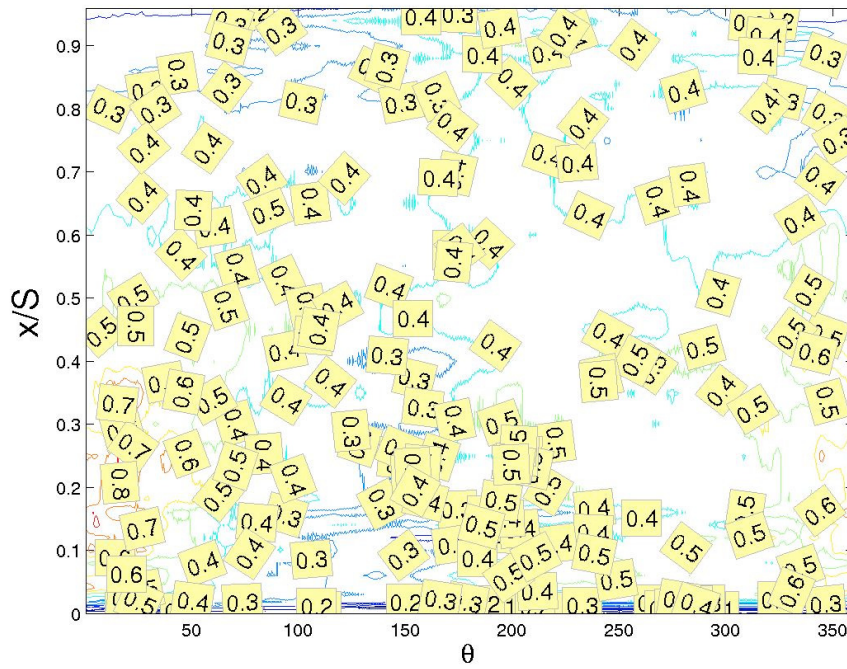
Figure 2.42.—Turbulence intensity contour map at r/D = 1.30 for case IIb (disc space flow, Va = 2300, S/D = 0.591).
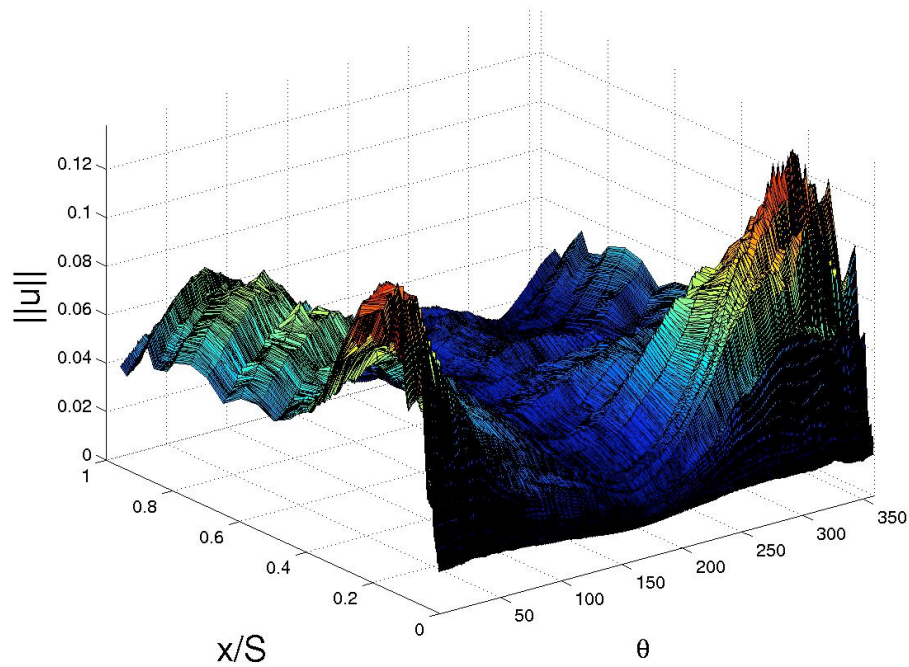
Figure 2.43.—Velocity profile at r/D = 1.17 for case IIb (disc space flow, Va = 2300, S/D = 0.591).
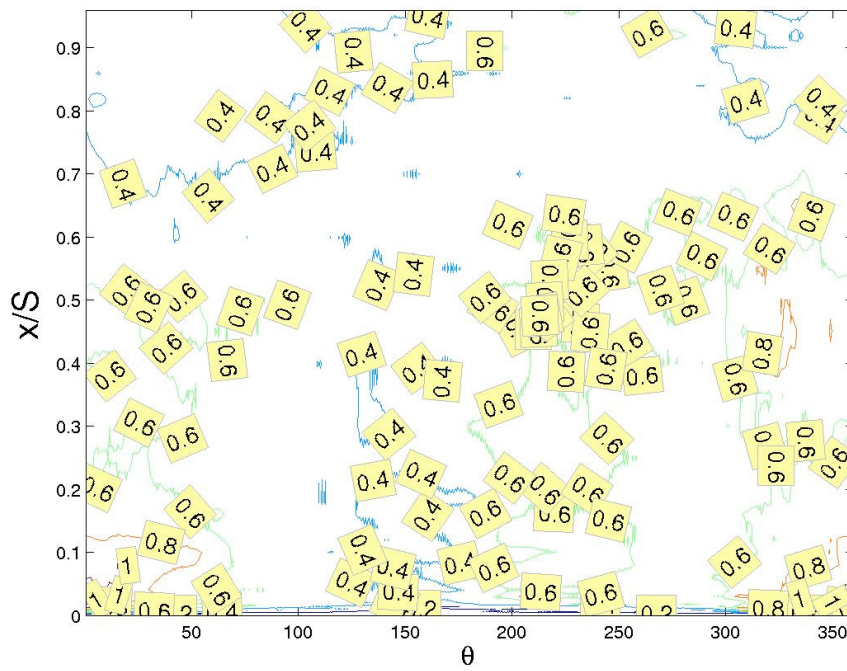
Figure 2.44.—Turbulence intensity contour map at $r/D = 1.17$ for case IIb (disc space flow, Va = 2300, $S/D = 0.591$).
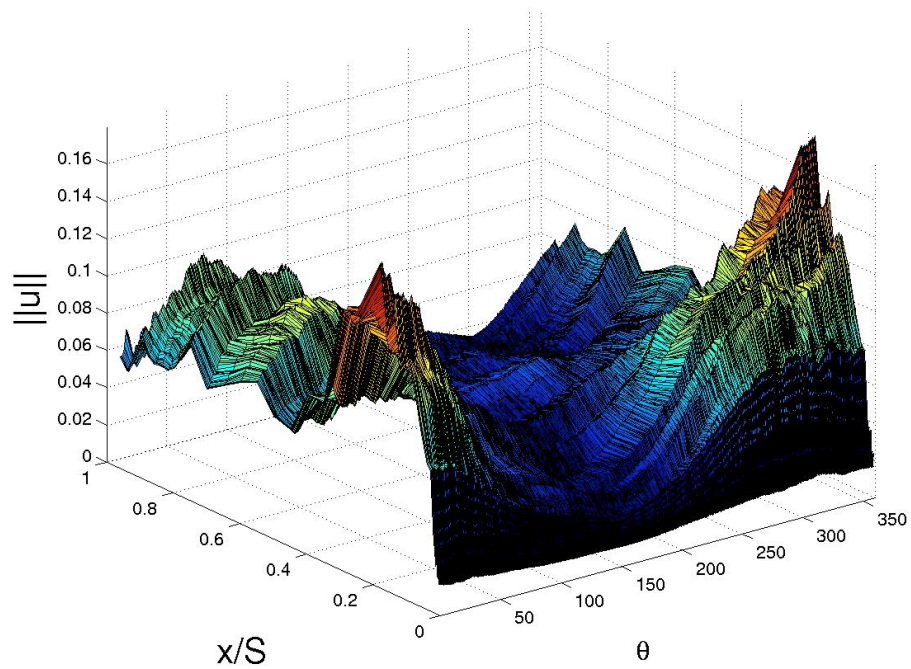
Figure 2.45.—Velocity profile at $r/D = 1.05$ for case IIb (disc space flow, Va = 2300, $S/D = 0.591$).
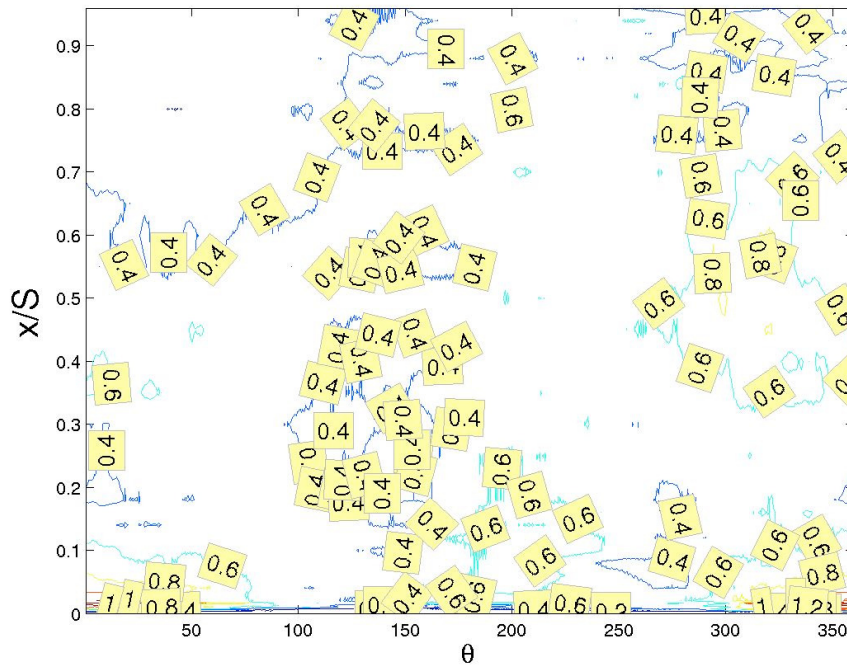
Figure 2.46.—Turbulence intensity contour map at r/D = 1.05 for case IIb (disc space flow, Va = 2300, S/D = 0.591).
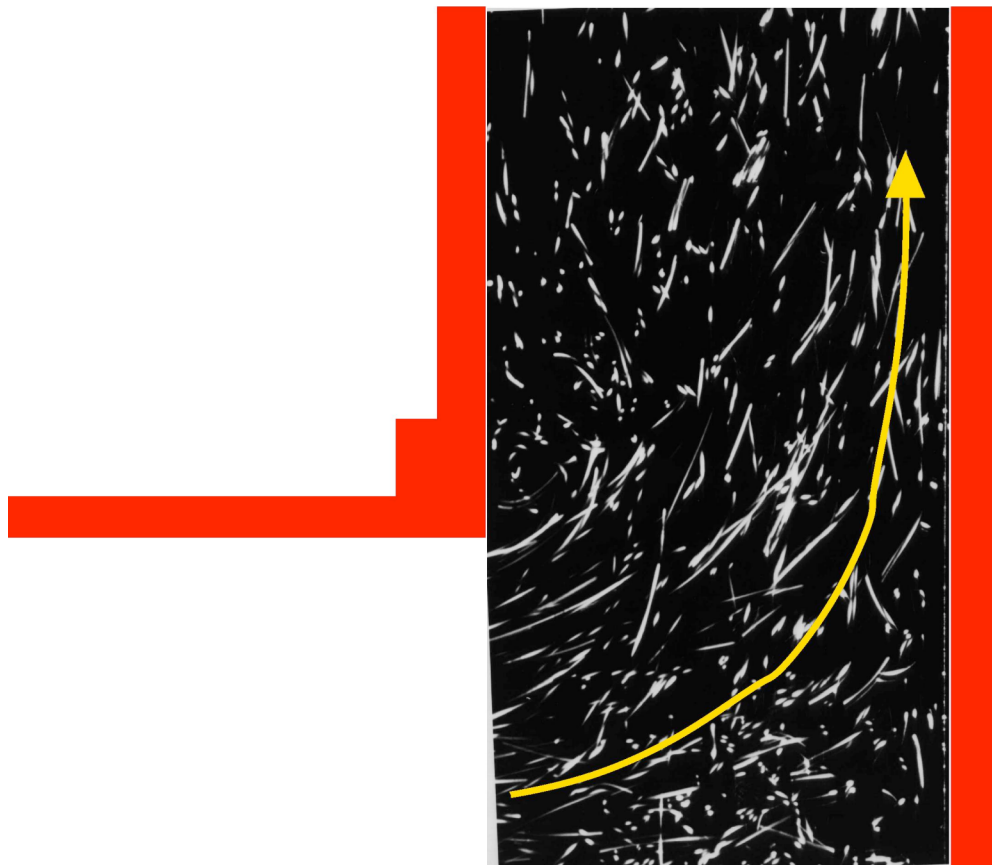
Figure 2.47.—A sample of flow visualization data for case IIb (disc space flow, Va = 2300, S/D = 0.591).
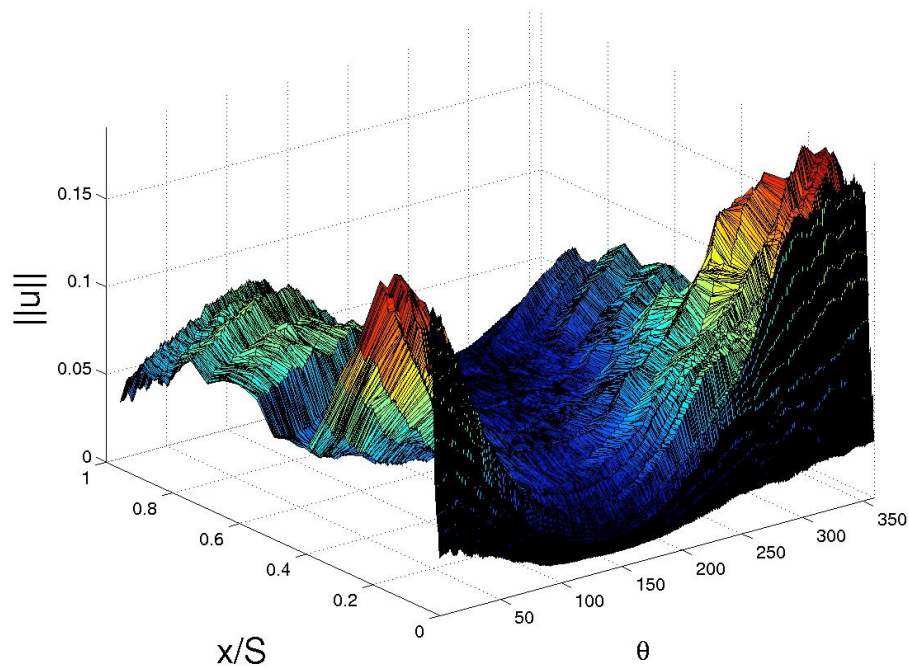
Figure 2.48.—Velocity profile at r/D = 0.93 for case IIb (disc space flow, Va = 2300, S/D = 0.591).
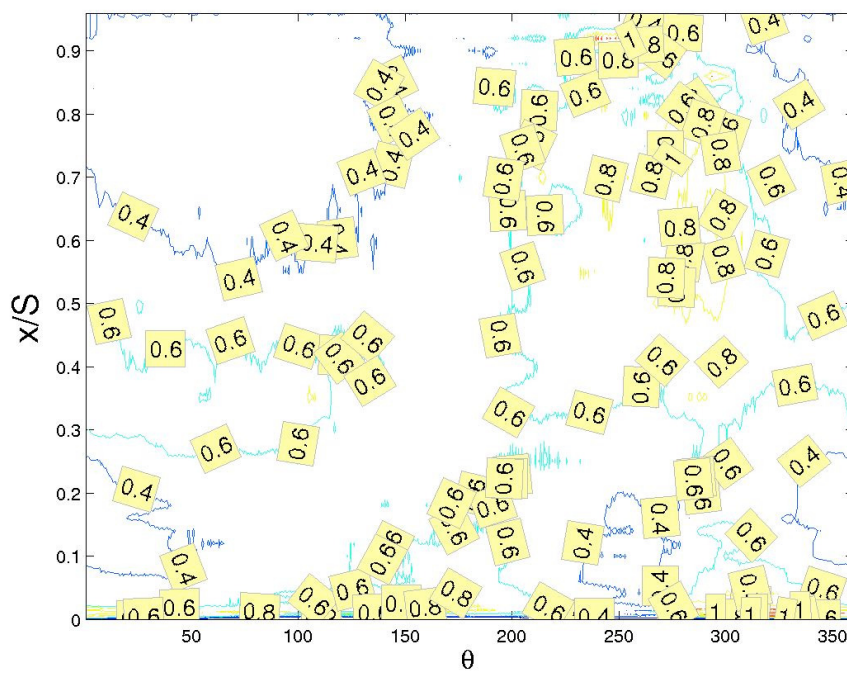
Figure 2.49.—Turbulence intensity contour map at r/D = 0.93 for case IIb (disc space flow, Va = 2300, S/D = 0.591).
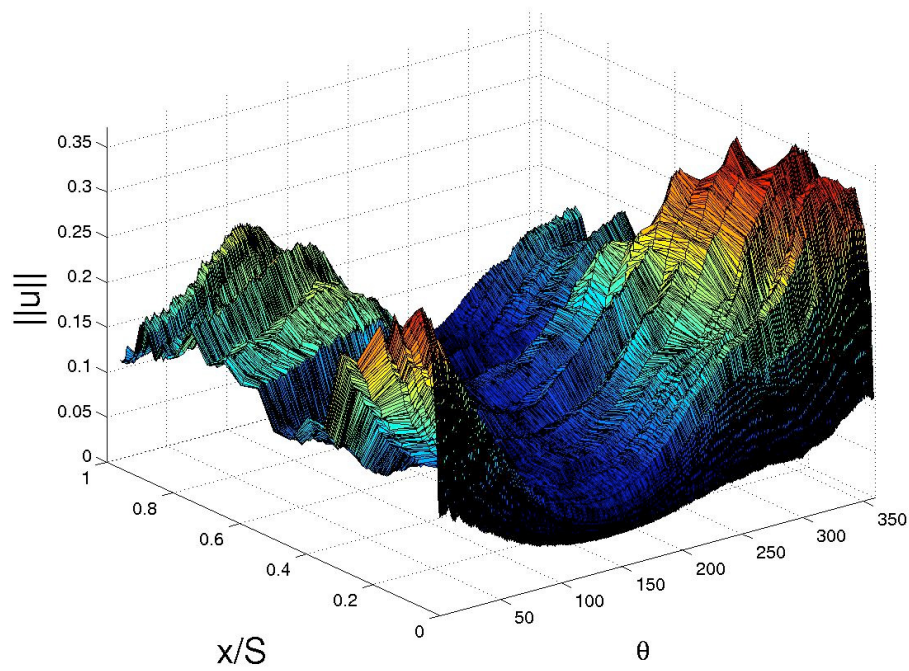
Figure 2.50.—Velocity profile at $r/D = 0.81$ for case IIb (disc space flow, Va = 2300, $S/D = 0.591$).
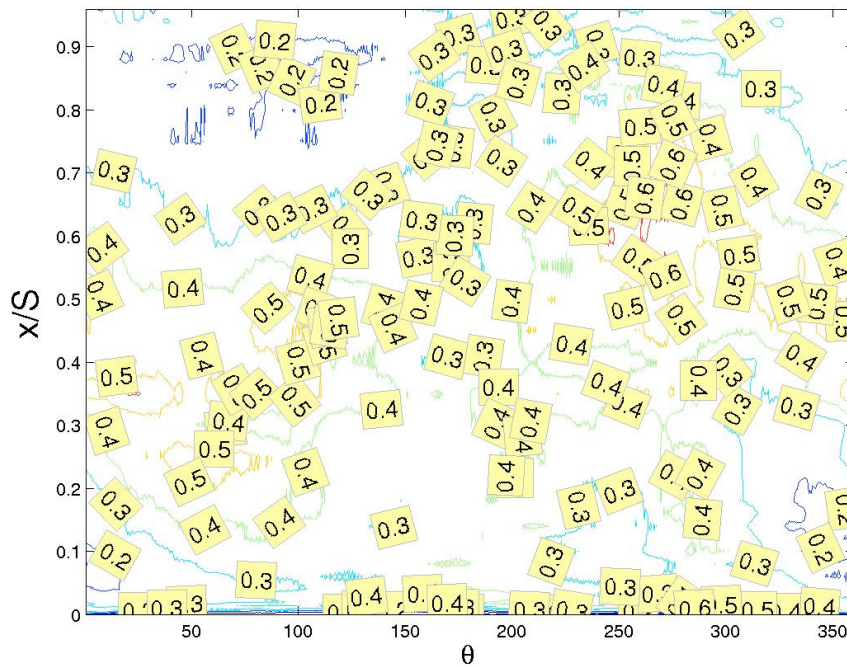
Figure 2.51.—Turbulence intensity contour map at $r/D = 0.81$ for case IIb (disc space flow, Va = 2300, $S/D = 0.591$).
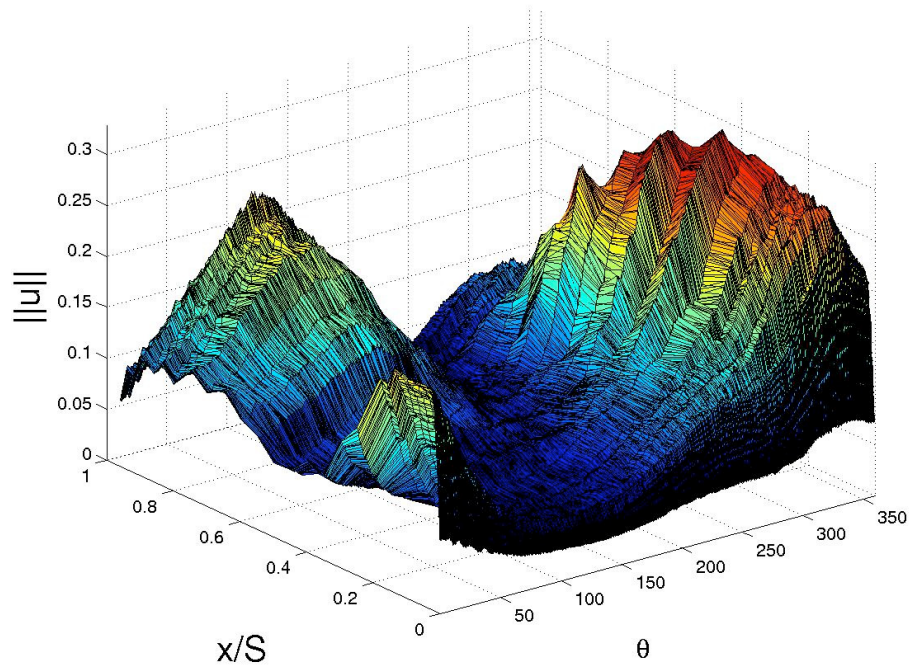
Figure 2.52.—Velocity profile at $r/D = 0.68$ for case IIb (disc space flow, Va = 2300, $S/D = 0.591$).
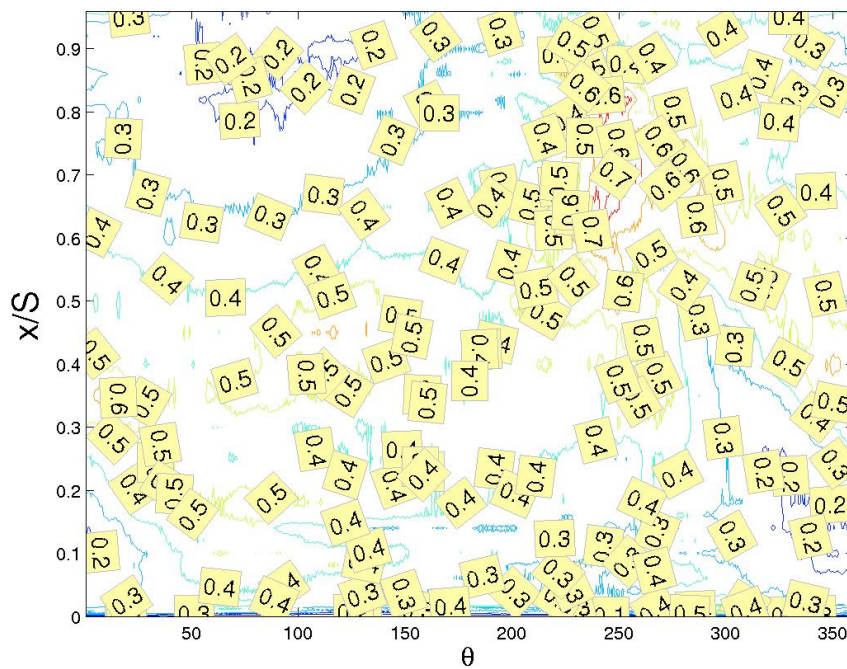
Figure 2.53.—Turbulence intensity contour map at $r/D = 0.68$ for case IIb (disc space flow, Va = 2300, $S/D = 0.591$).
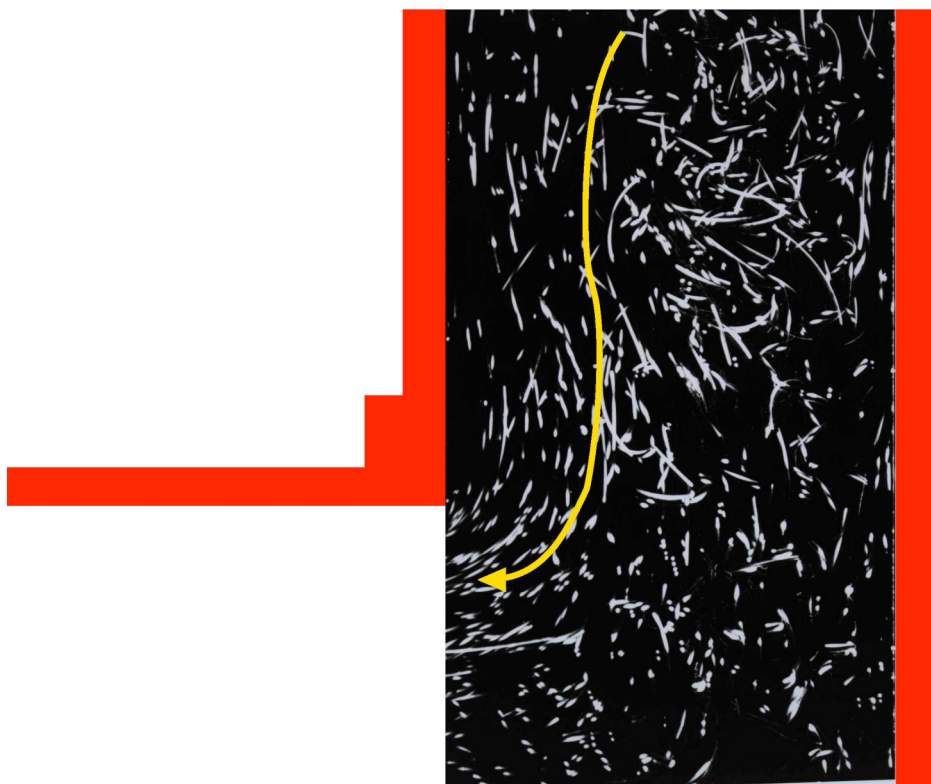
Figure 2.54.—A flow visualization result for 45 < θ < 60 for case IIb (disc space flow, Va = 2300, *S/D* = 0.591).
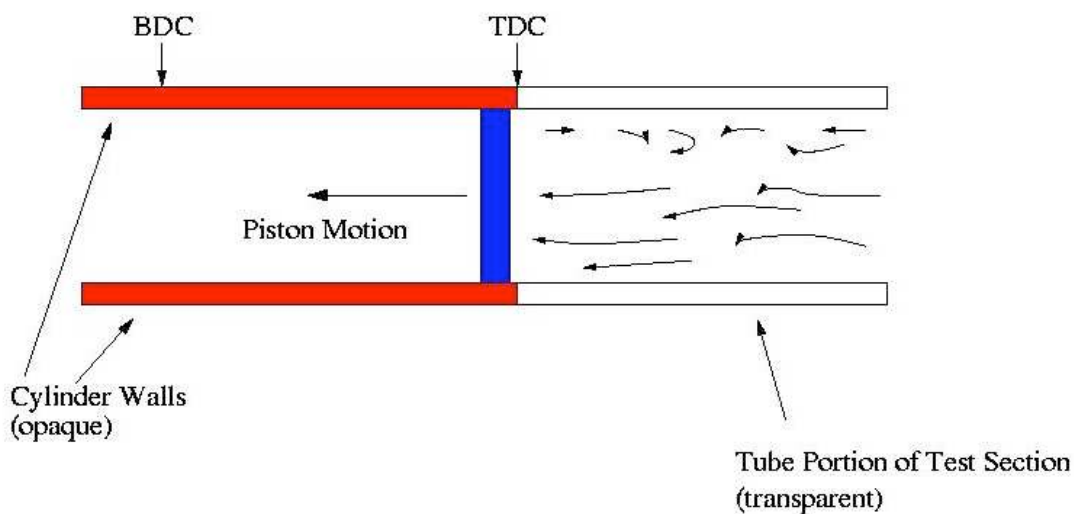
Figure 2.55.—Shortly after TDC for Case IIIa (tube flow, Va = 5400, *S/D* = 0.251). The leftward facing (long) arrows represent particles that are rapidly accelerated, the (shorter) curved arrows represent particles that maintained momentum in the opposite direction of the previous half-cycle and are still reversing.
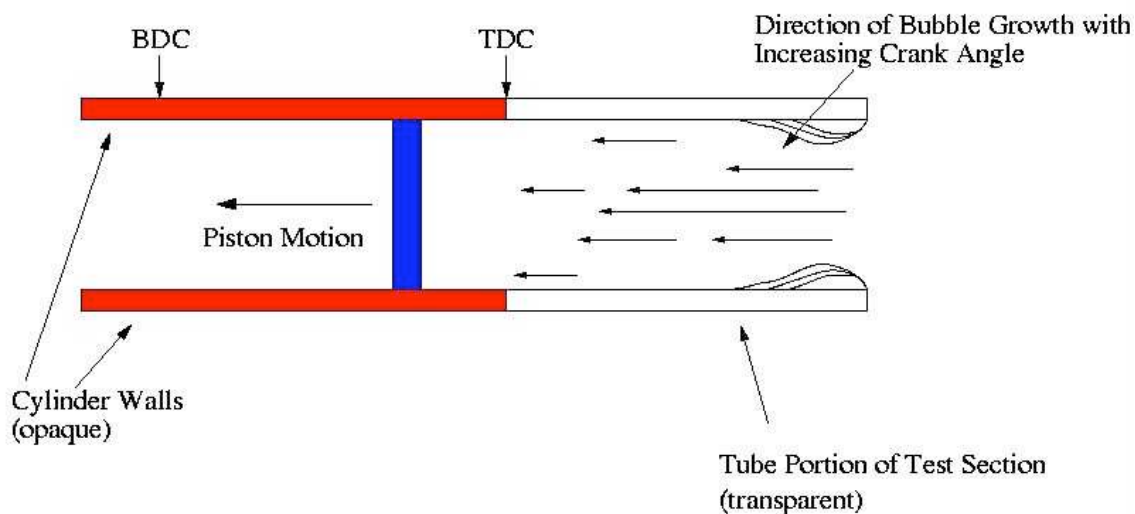
Figure 2.56.—$18° < θ < 72°$ after TDC for Case IIIa (tube flow, Va = 5400, S/D = 0.251). Growing separation bubbles with a low turbulence core.
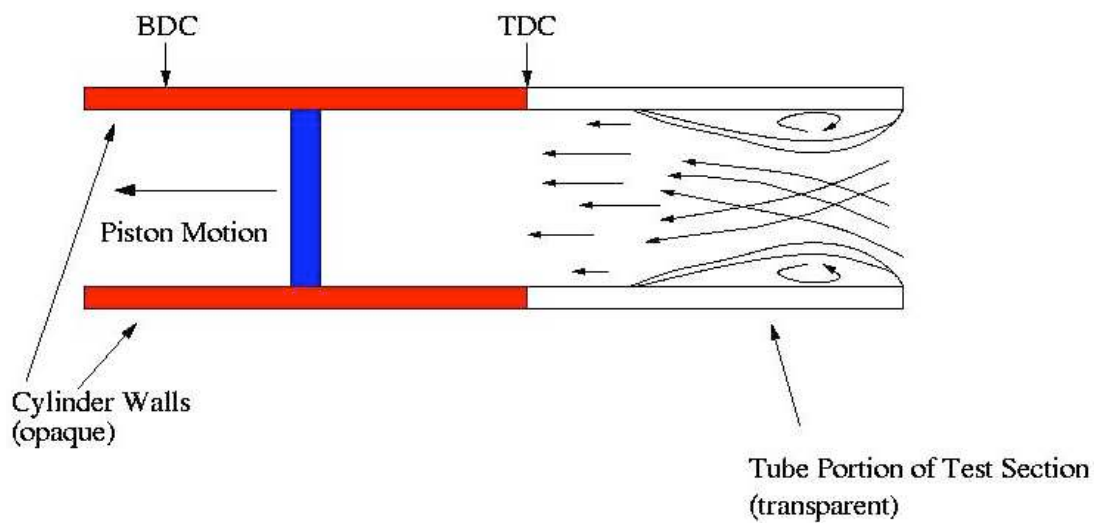
Figure 2.57.—$72° < θ < 126°$ after TDC for Case IIIa (tube flow, Va = 5400, S/D = 0.251) . Continued bubble growth with oscillating inlet conditions.
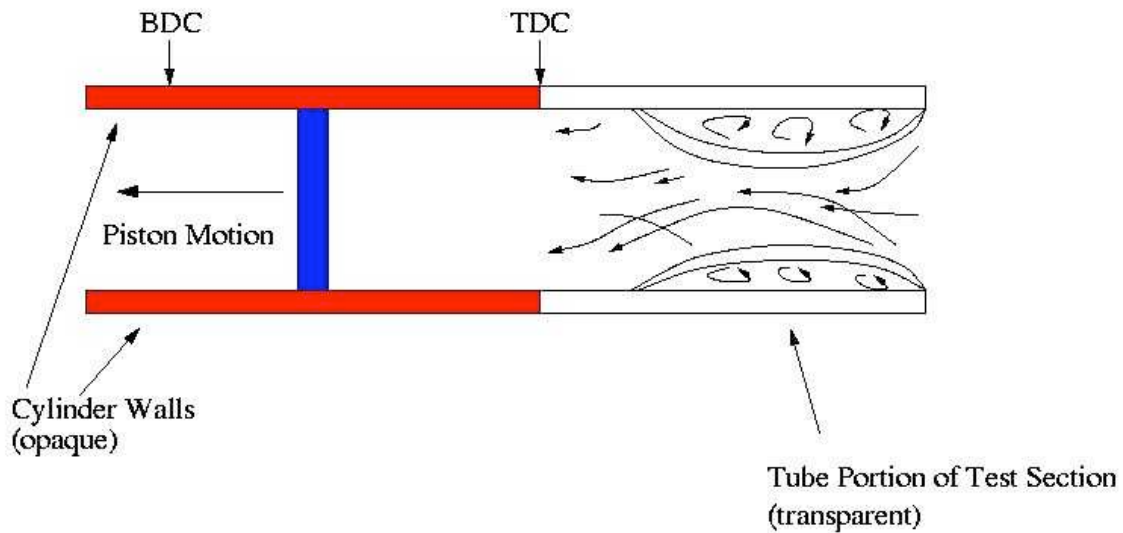
Figure 2.58.— 26° < θ < BDC for Case IIIa (tube flow, Va = 5400, *S*/*D* = 0.251). Fully turbulent core flow, higher growth rate of 'top' separation bubble in cross-stream direction. Within the separation bubbles, random turbulent behavior is observed.
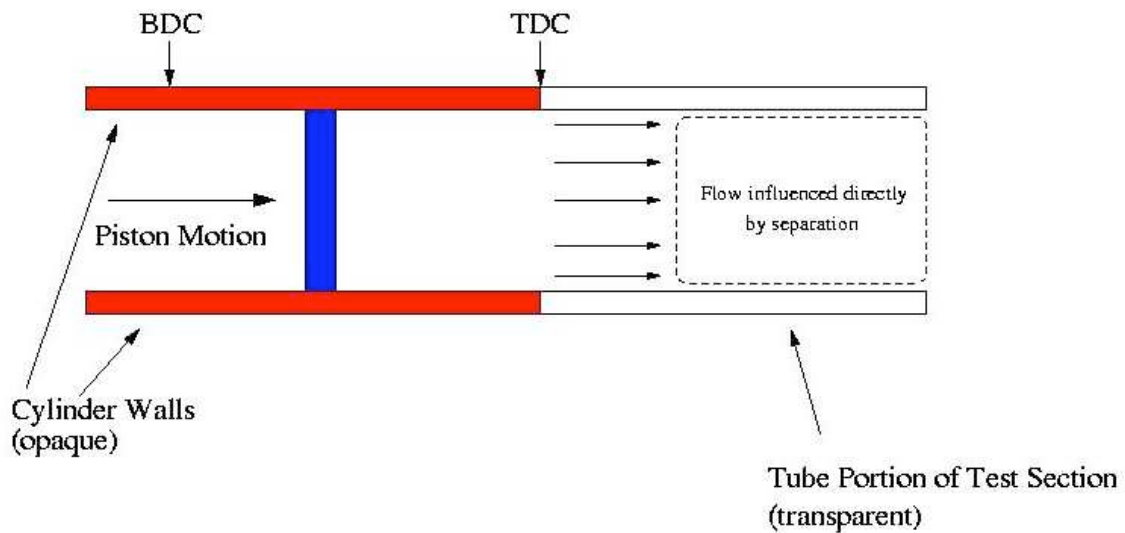
Figure 2.59.—Low-turbulence slug (left) pushing highly-turbulent slug out of the cylinder (right). This regime applies to all crank angles from BDC to TDC for Case IIIa (tube flow, Va = 5400, *S*/*D* = 0.251).
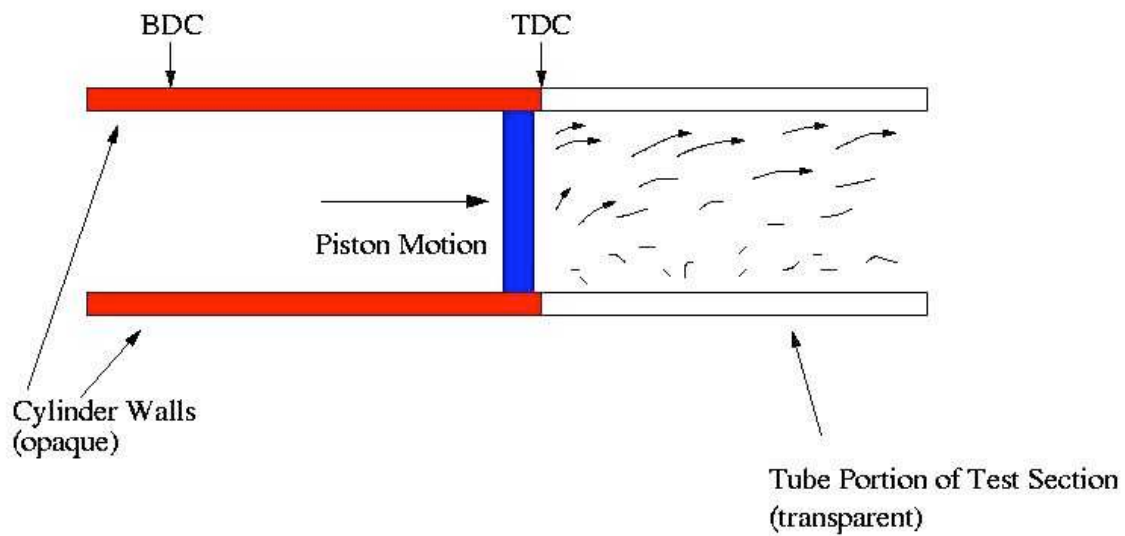
Figure 2.60.—End of cycle for Case IIIa (tube flow, Va = 5400, *S/D* = 0.251). Note that there is a non-uniform velocity distribution in the approximately stagnant fluid. The fluid in the upper portion of the cylinder maintains some residual momentum. It slowly displaces the fluid below.
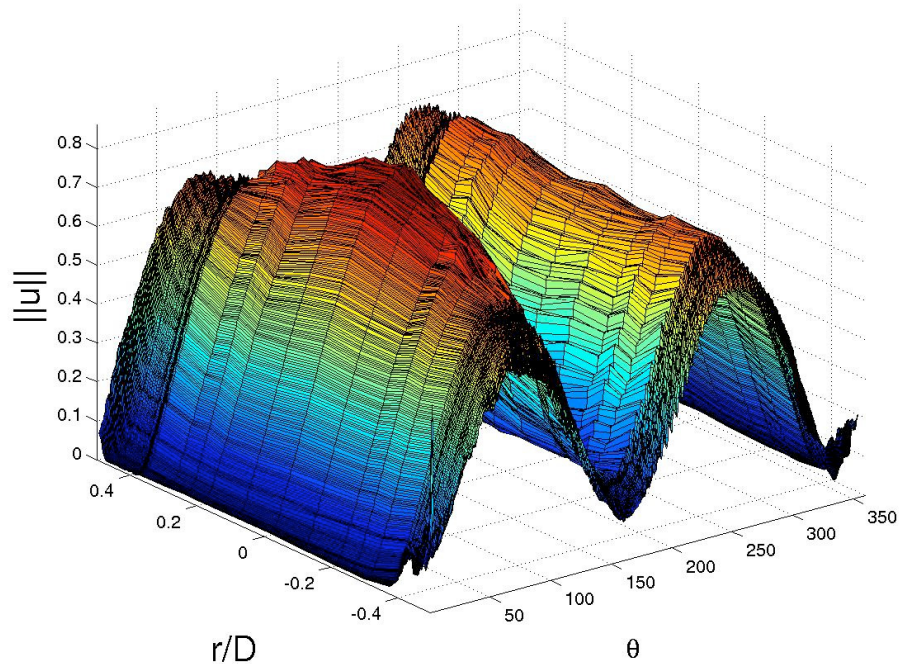
Figure 2.61.—Velocity profile for Case IIIa (tube flow, Va = 5400, *S/D* = 0.251).
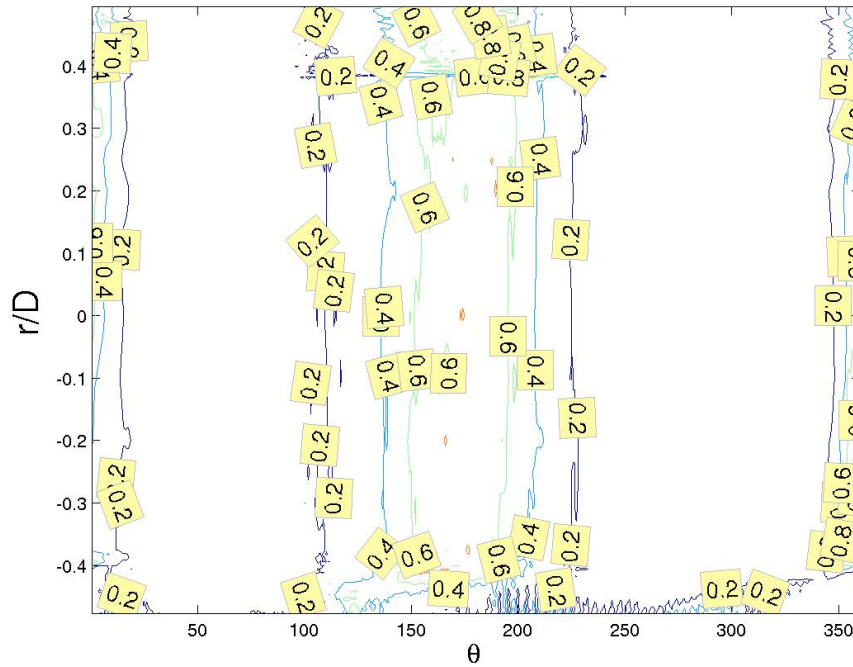
Figure 2.62.—Turbulence intensity contour map for Case IIIa (tube flow, Va = 5400, *S/D* = 0.251).
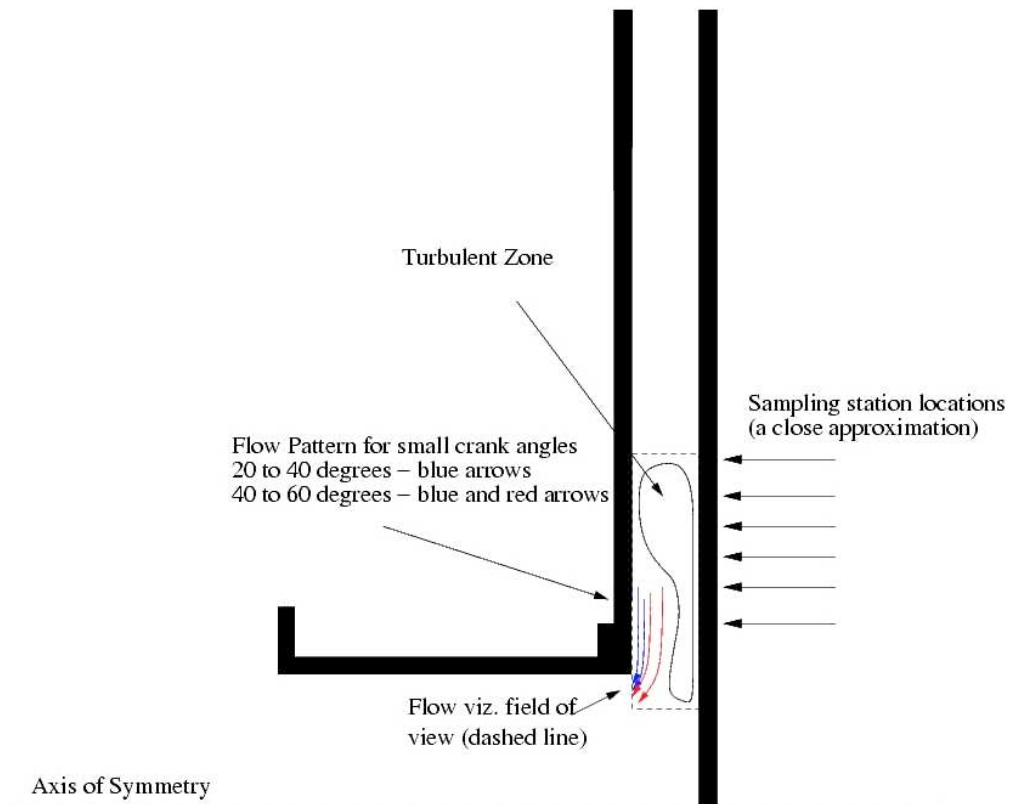
Figure 2.63.—Flow pattern for small crank angles of the suction stroke for case IIIb (disc space flow, Va = 5400, *S/D* = 0.251).
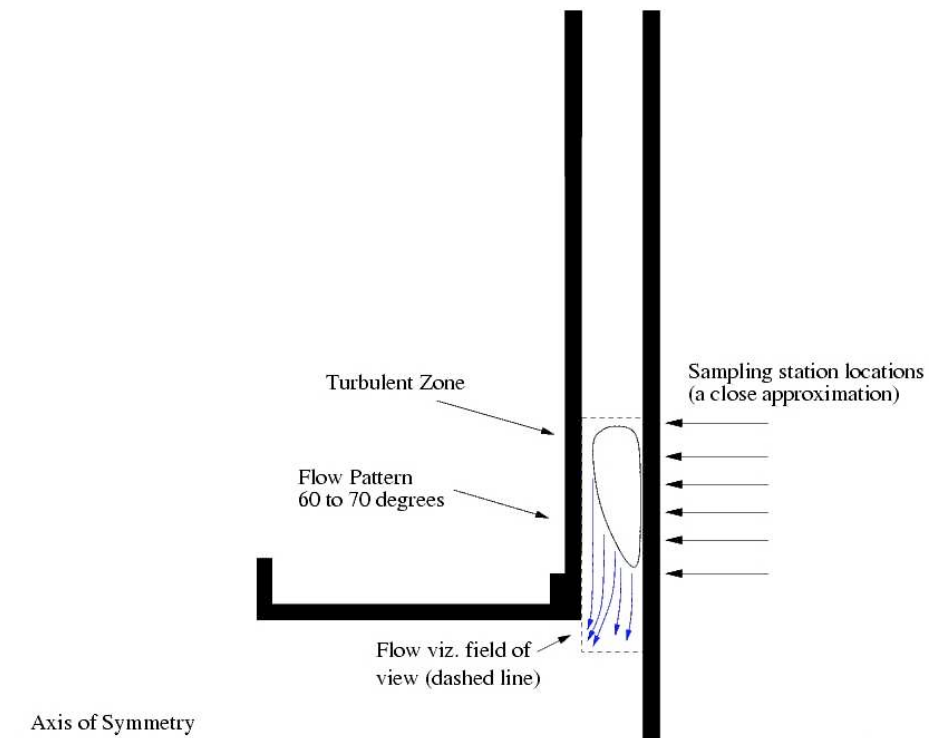
Figure 2.64.—Flow pattern for intermediate crank angles for Case IIIb (disc space flow, Va = 5400, S/D = 0.251).
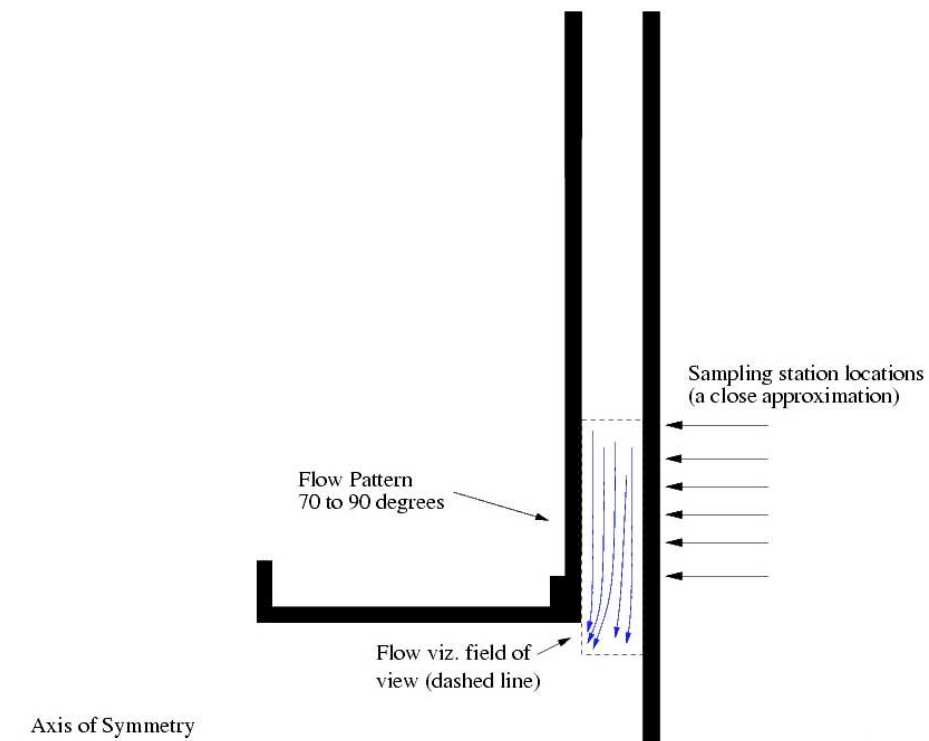
Figure 2.65.—Flow pattern for crank angles near maximum piston speed for Case IIIb (disc space flow, Va = 5400, S/D = 0.251).

The fluid in the wall jet and downstream of the separation bubble has a very high momentum and appears laminar–like

Separation bubble growth (the smallest bubble corresponds to about 195 CAD, the largest bubble corresponds to about 305 CAD)

Sampling station locations (a close approximation)

Flow viz. field of view (dashed line)

Axis of Symmetry
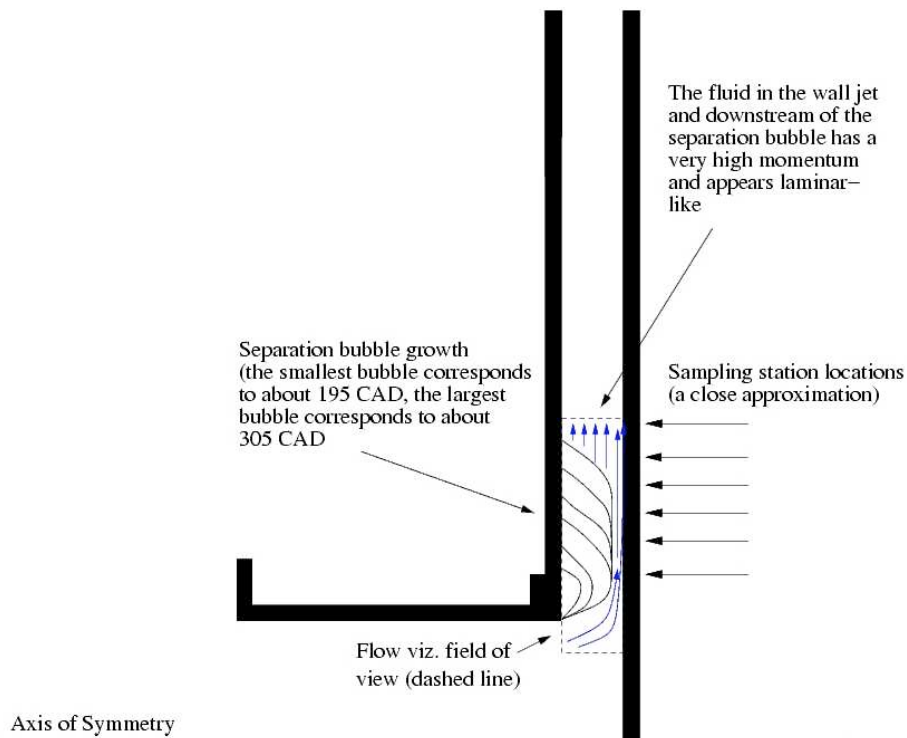
Figure 2.66.—Flow pattern during the blowing stroke period of strong acceleration (190° < θ < 310°) for Case IIIb (disc space flow, Va = 5400, *S*/*D* = 0.251).

Highly turbulent zone

Sampling station locations (a close approximation)

Flow viz. field of view (dashed line)

Remnants of a wall jet

Axis of Symmetry
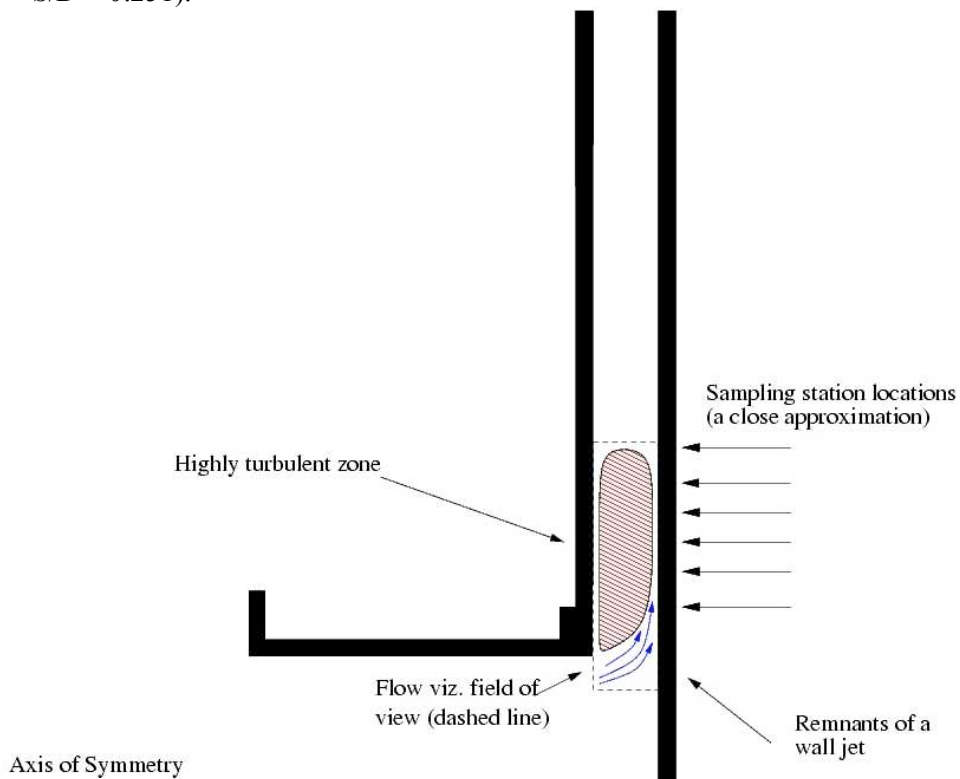
Figure 2.67.—The blowing stroke for crank angles greater than 310° for Case IIIb (disc space flow, Va = 5400, *S*/*D* = 0.251).
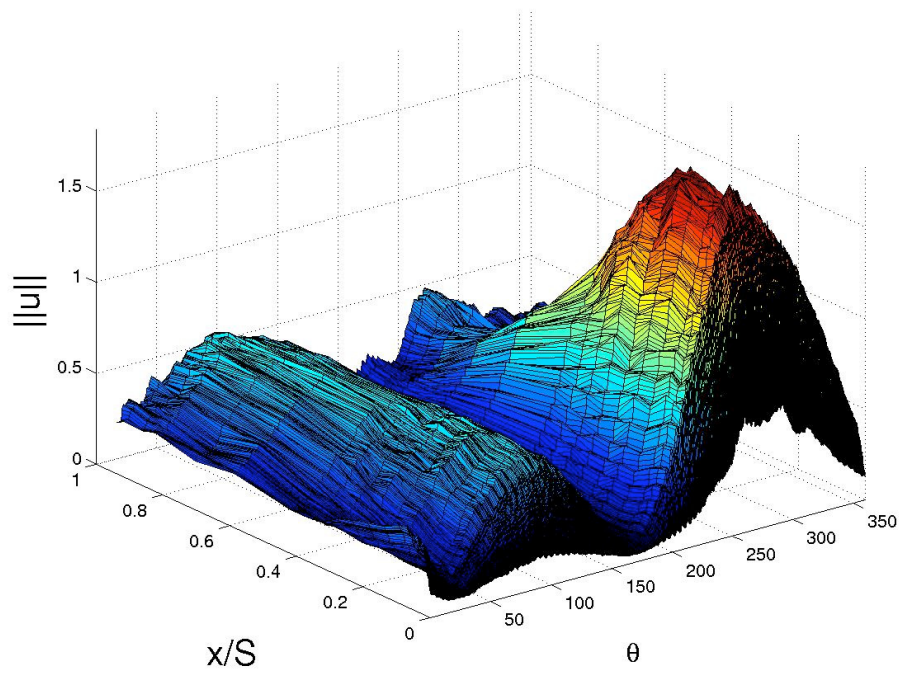
Figure 2.68.—Velocity profile at r/D = 0.68 for Case IIIb (disc space
flow, Va = 5400, S/D = 0.251).
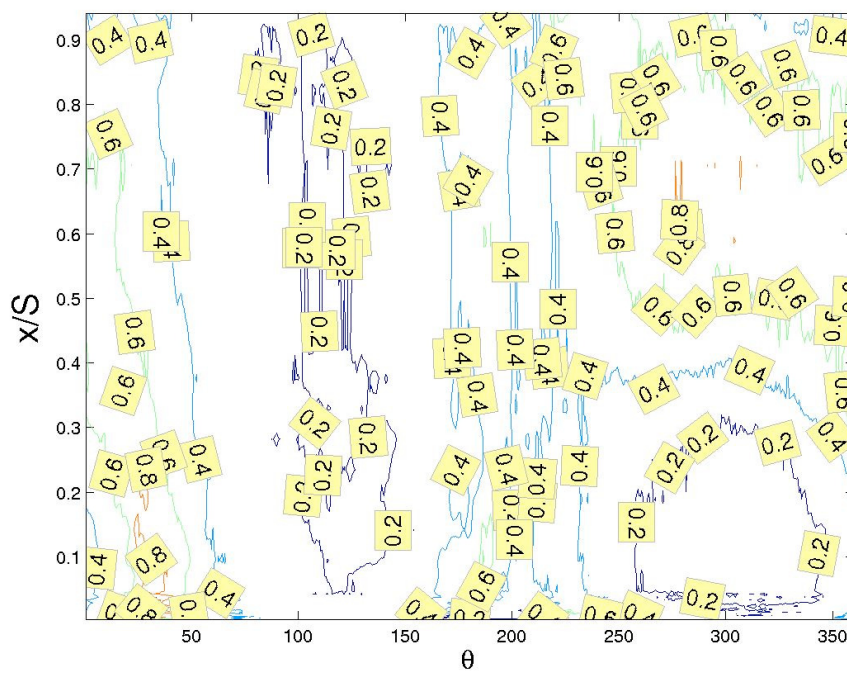
Figure 2.69.—*TI* contour plot at r/D = 0.68 for Case IIIb (disc space
flow, Va = 5400, S/D = 0.251).
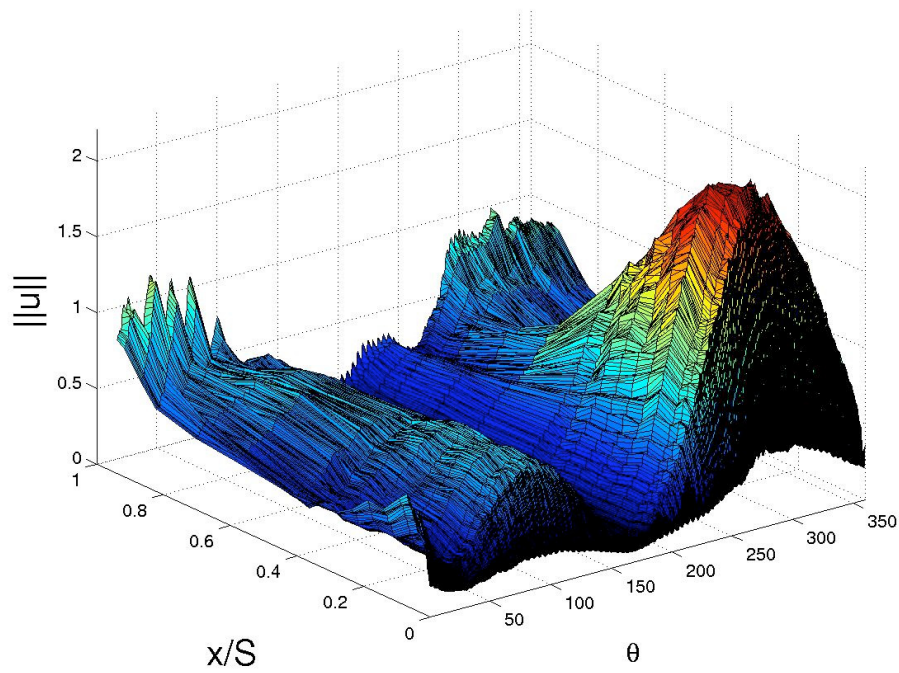
Figure 2.70.—Velocity profile at $r/D = 0.81$ for Case IIIb (disc space flow, Va = 5400, $S/D = 0.251$).
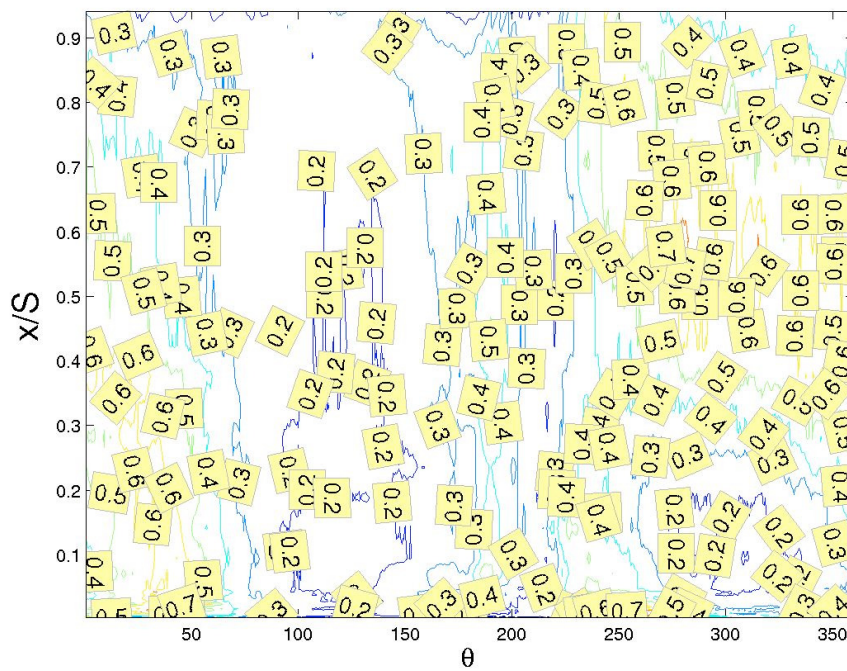
Figure 2.71.—*TI* contour plot at $r/D = 0.81$ for Case IIIb (disc space flow, Va = 5400, $S/D = 0.251$).
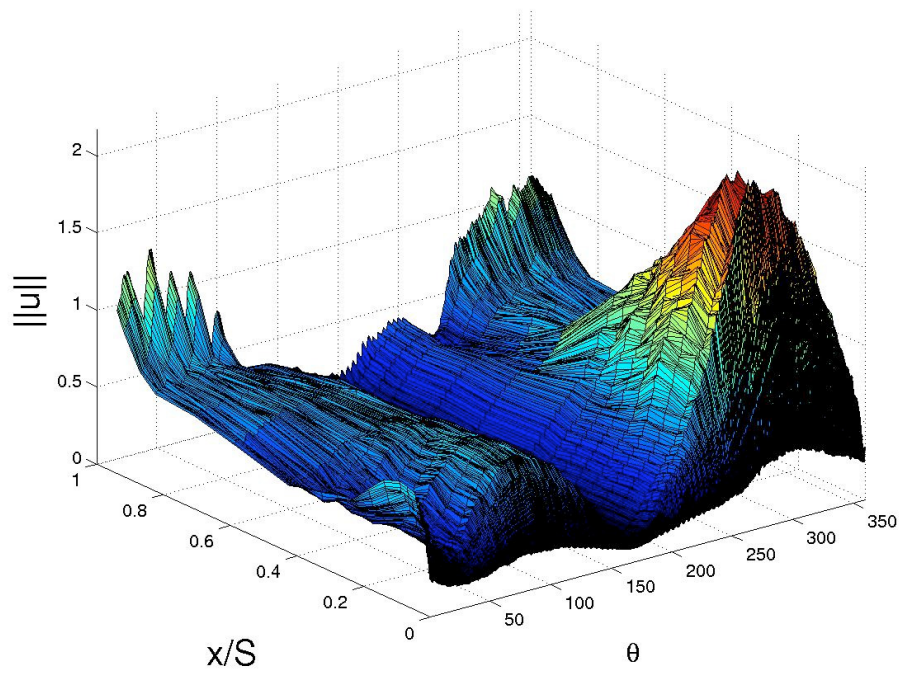
Figure 2.72.—Velocity profile at *r*/*D* = 0.93 for Case IIIb (disc space flow, Va = 5400, *S*/*D* = 0.251).
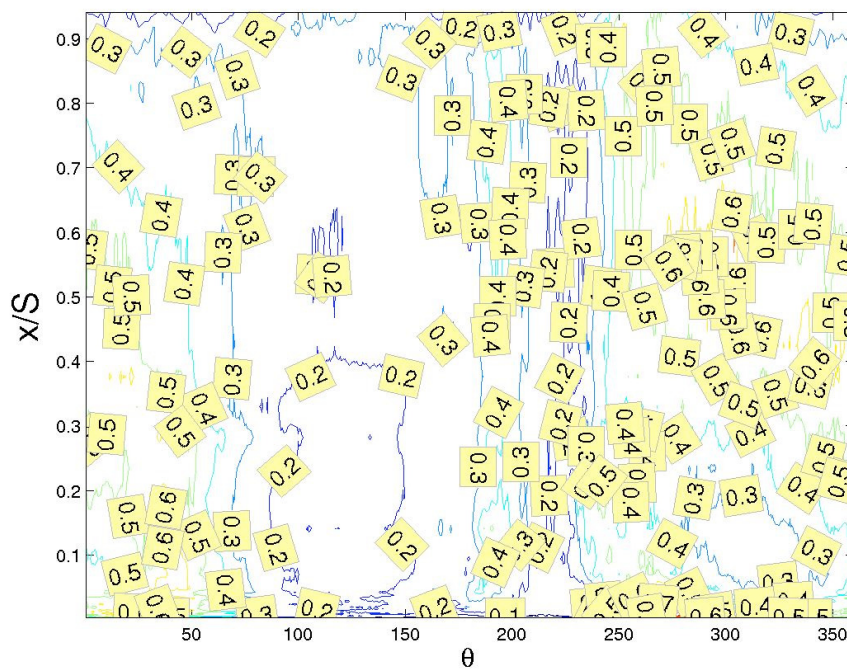
Figure 2.73.—*TI* contour plot at *r*/*D* = 0.93 for Case IIIb (disc space flow, Va = 5400, *S*/*D* = 0.251).
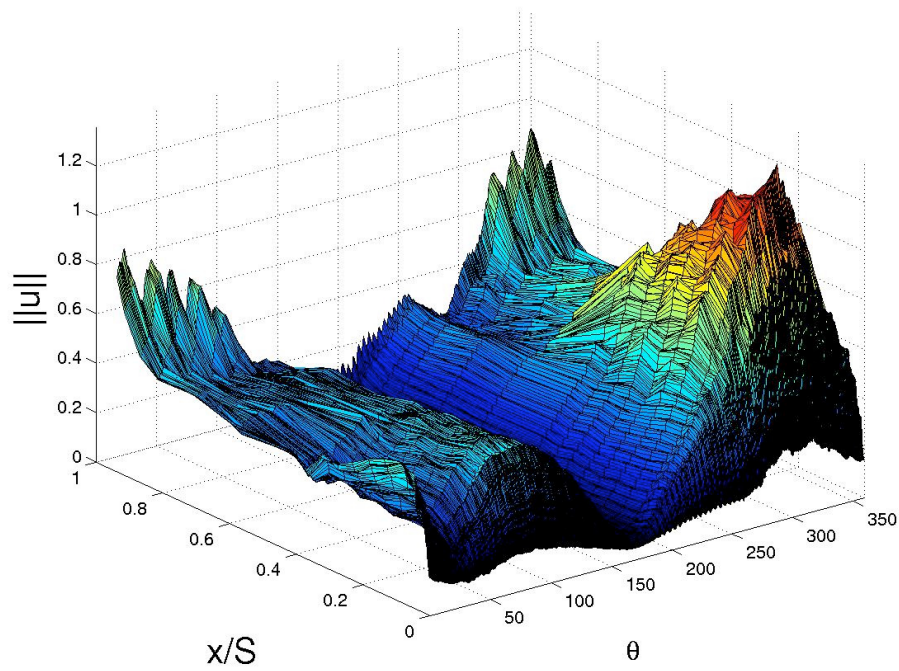
Figure 2.74.—Velocity profile at r/D = 1.05 for Case IIIb (disc space flow, Va = 5400, S/D = 0.251).
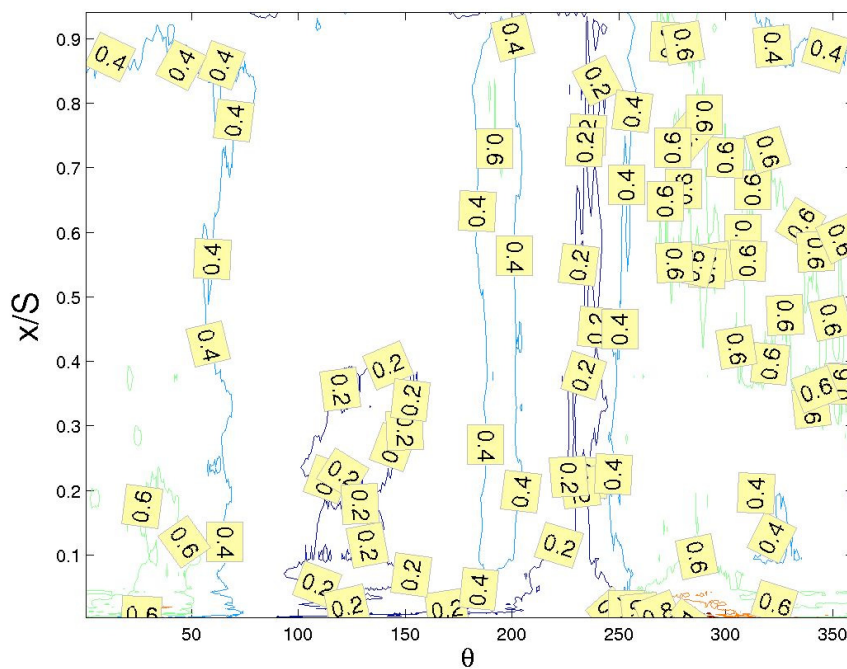
Figure 2.75.—*TI* contour plot at r/D = 1.05 for Case IIIb (disc space flow, Va = 5400, S/D = 0.251).
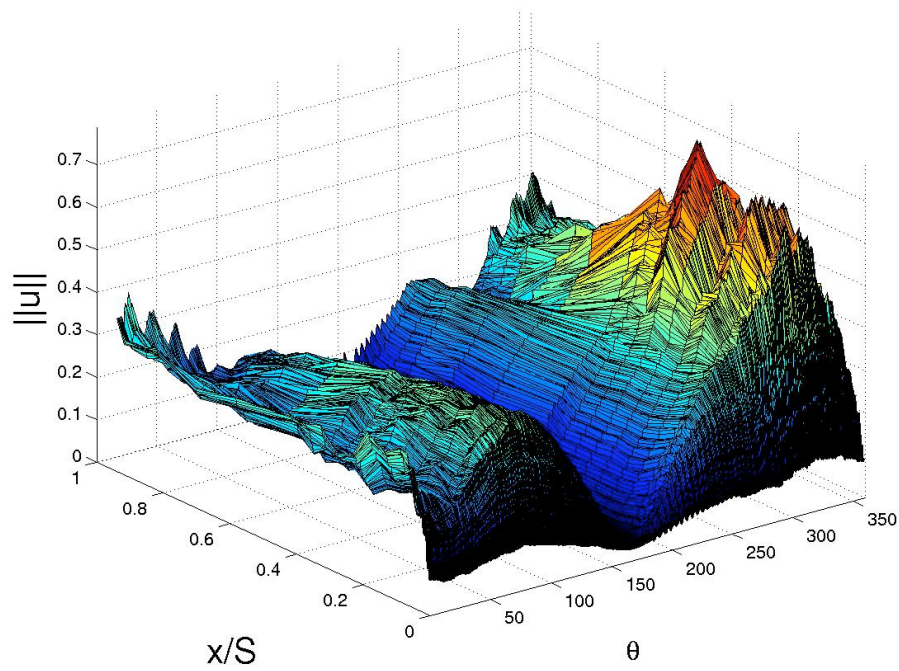
Figure 2.76.—Velocity profile at $r/D = 1.17$ for Case IIIb (disc space flow, Va = 5400, $S/D = 0.251$).
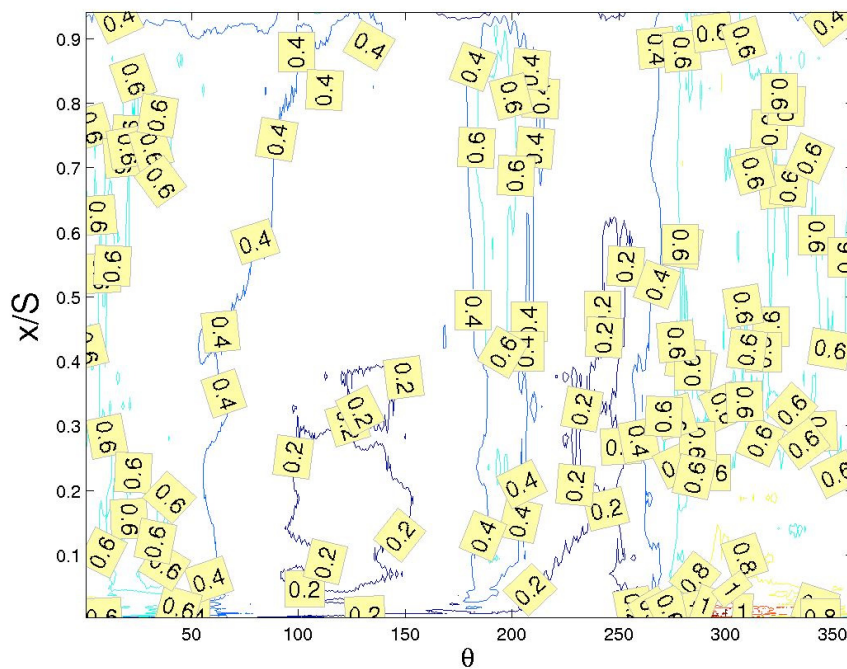
Figure 2.77.—*TI* contour plot at $r/D = 1.17$ for Case IIIb (disc space flow, Va = 5400, $S/D = 0.251$).
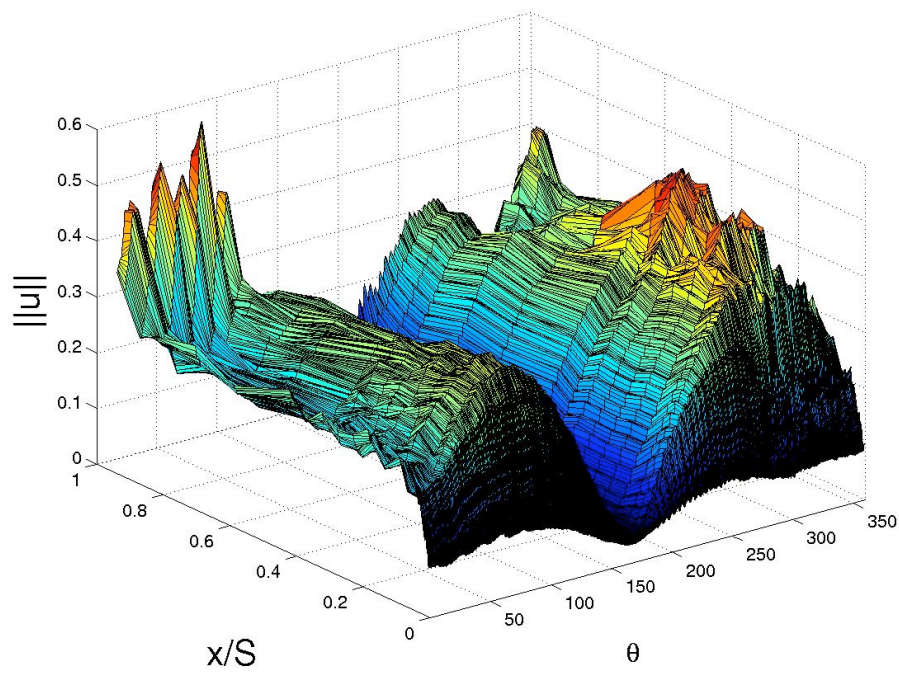
Figure 2.78.—Velocity profile at r/D = 1.30 for Case IIIb (disc space flow, Va = 5400, S/D = 0.251).
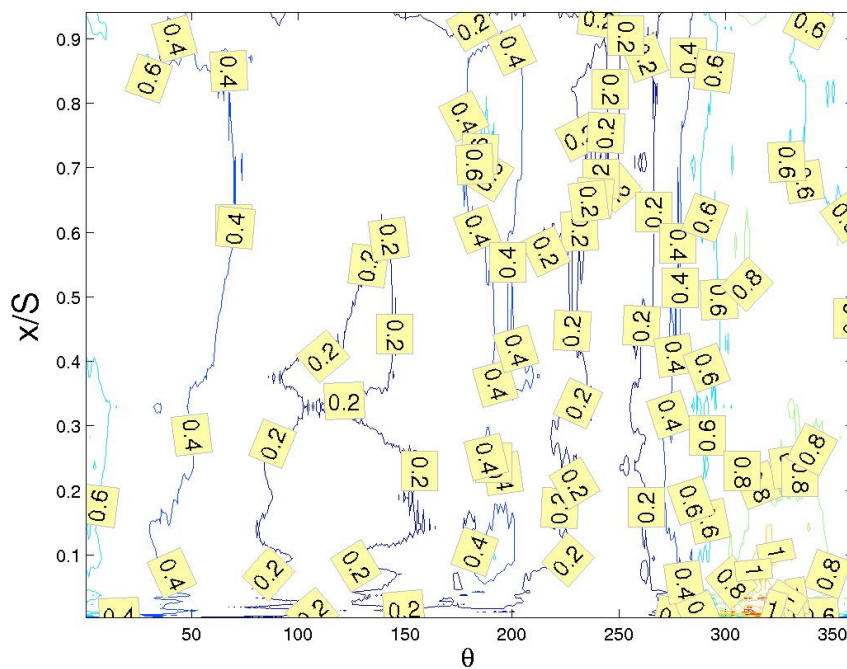
Figure 2.79.—*TI* contour plot at r/D = 1.30 for Case IIIb (disc space flow, Va = 5400, S/D = 0.251).
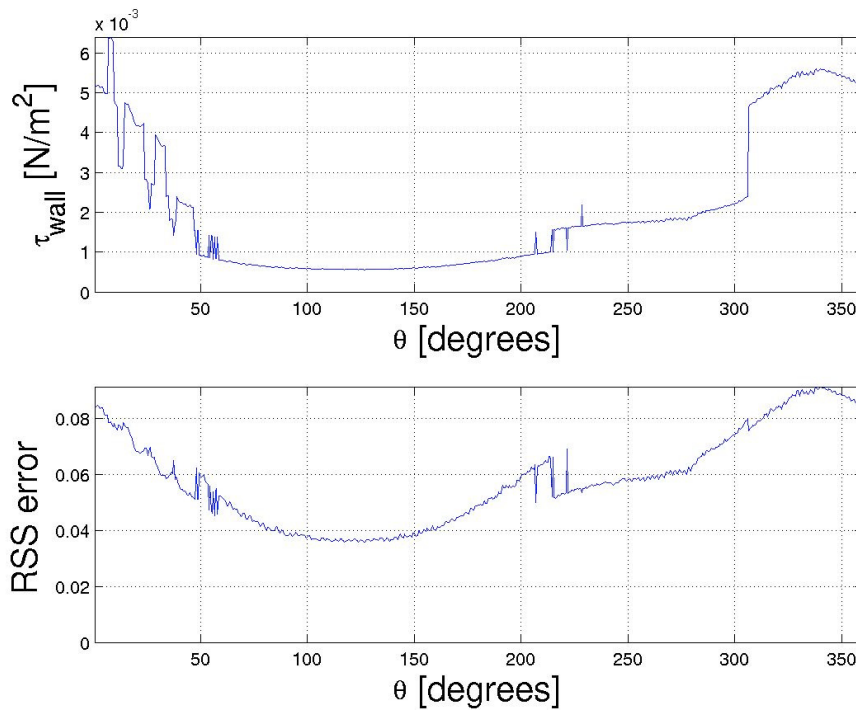
Figure 2.80.—Wall Shear Stress and the associated error at $r/D = 0.68$ for Case IIb ($Re_{max} = 7600$, Va = 2300, $S = 127$ mm, $S/D = 0.591$).
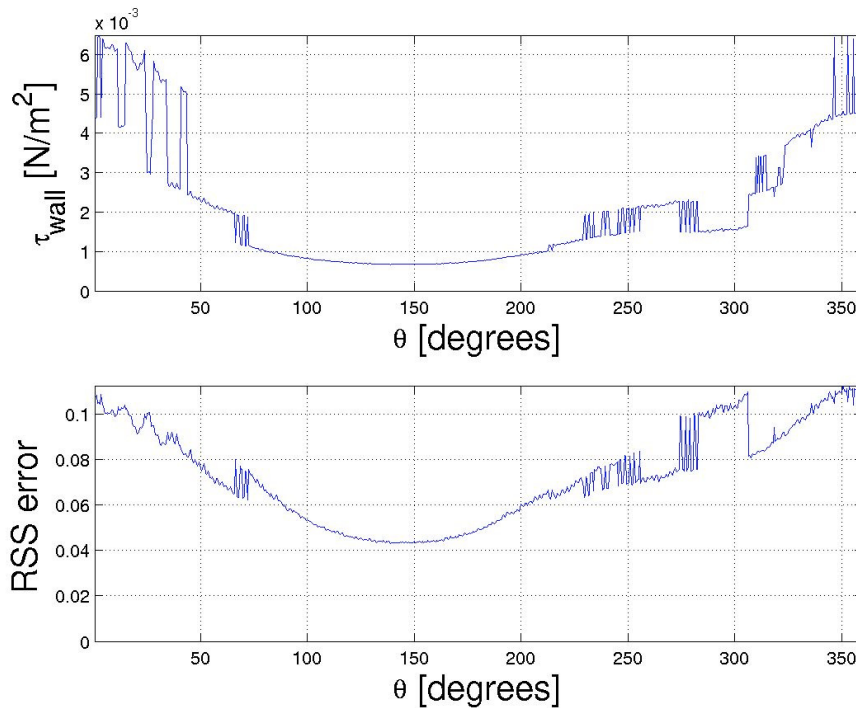
Figure 2.81.—Wall Shear Stress and the associated error at $r/D = 0.81$ for Case IIb ($Re_{max} = 7600$, Va = 2300, $S = 127$ mm, $S/D = 0.591$).
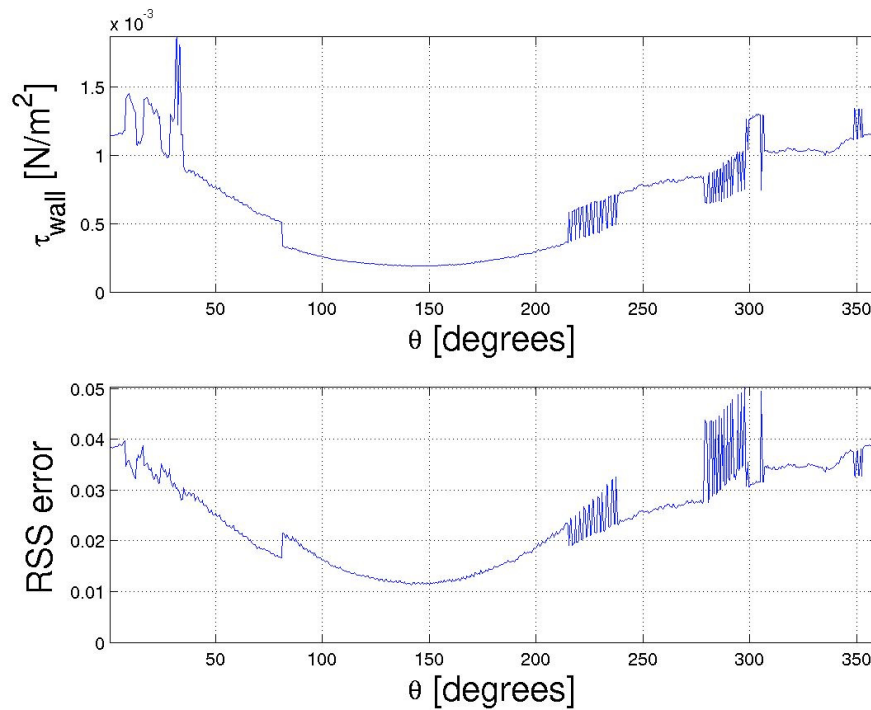
Figure 2.82.—Wall Shear Stress and the associated error at $r/D = 0.93$ for Case IIb ($Re_{max} = 7600$, Va = 2300, $S = 127$ mm, $S/D = 0.591$).
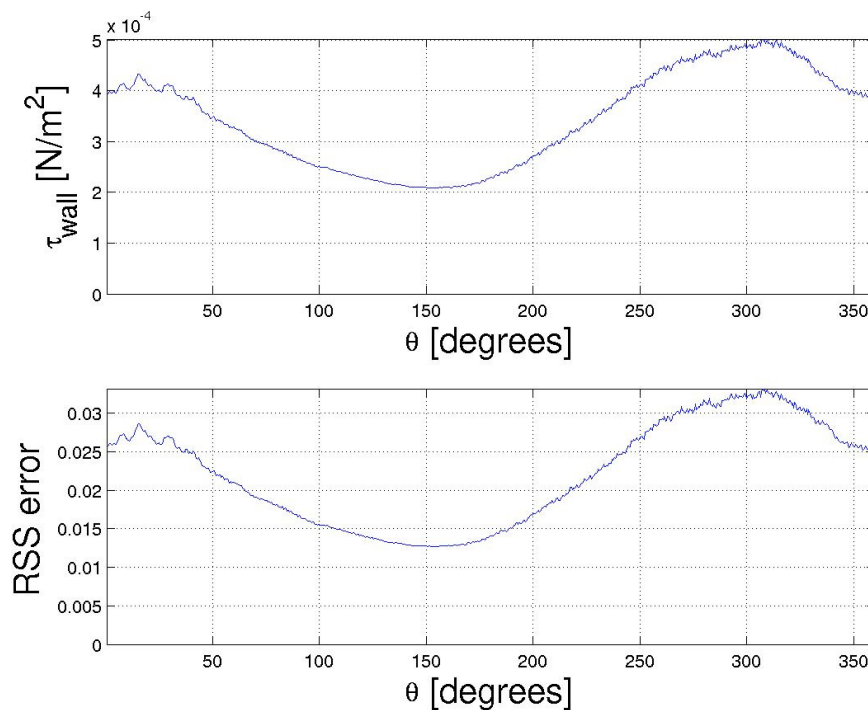
Figure 2.83.—Wall Shear Stress and the associated error at $r/D = 1.05$ for Case IIb ($Re_{max} = 7600$, Va = 2300, $S = 127$ mm, $S/D = 0.591$).
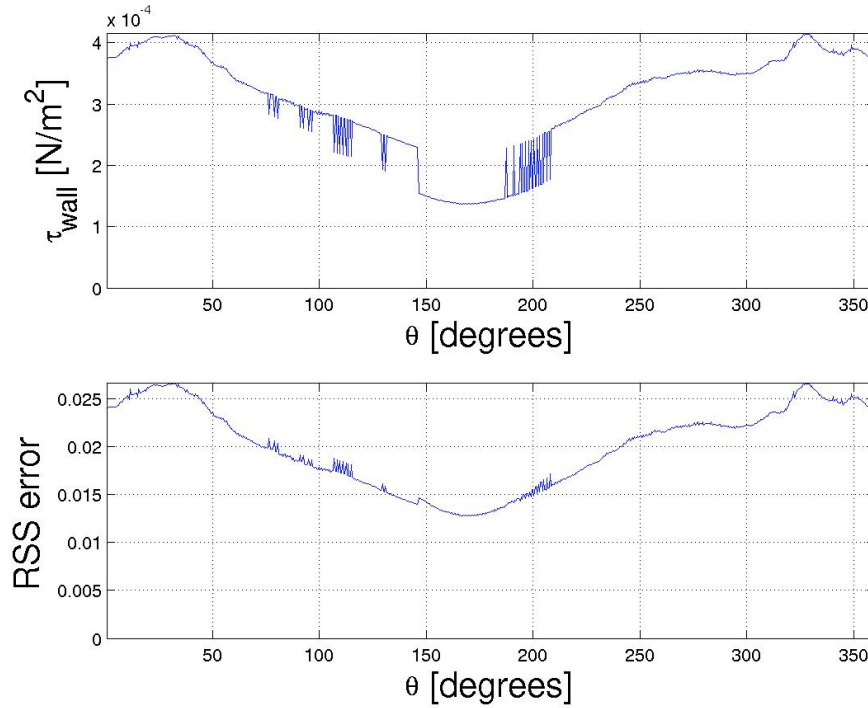
Figure 2.84.—Wall Shear Stress and the associated error at $r/D = 1.17$ for Case IIb ($Re_{max} = 7600$, Va = 2300, $S = 127$ mm, $S/D = 0.591$).
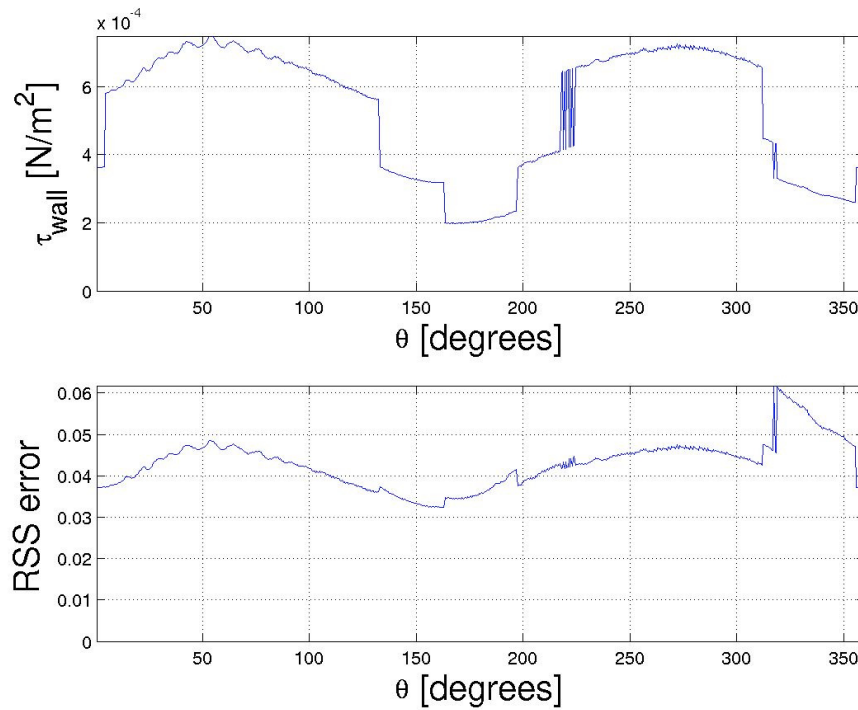
Figure 2.85.—Wall Shear Stress and the associated error at $r/D = 1.30$ for Case IIb ($Re_{max} = 7600$, Va = 2300, $S = 127$ mm, $S/D = 0.591$).
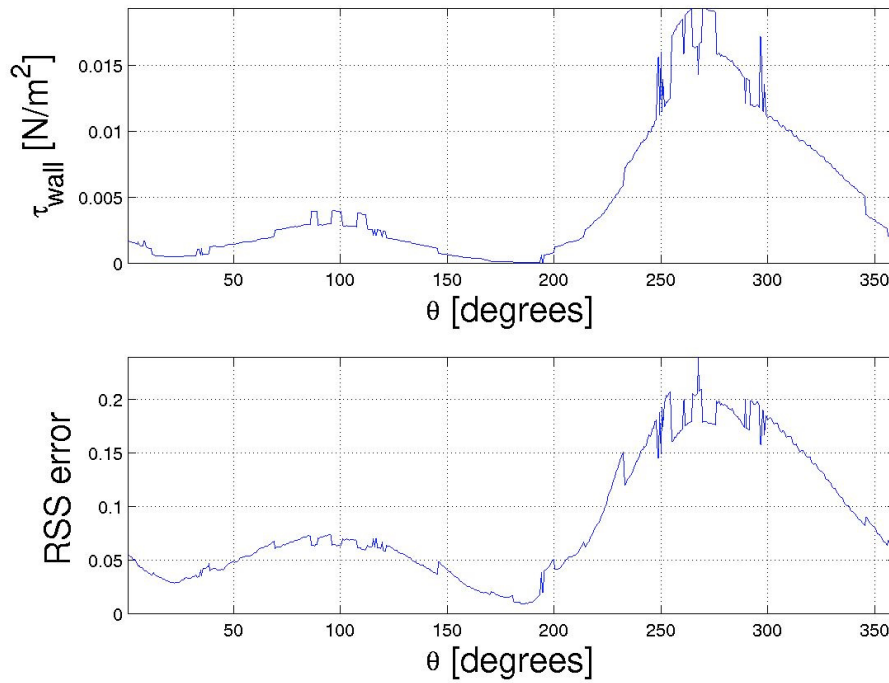
Figure 2.86.—Wall Shear Stress and the associated error at r/D = 0.68 for Case Ib (Re_{max} = 7600, Va = 2300, S = 54 mm, S/D = 0.251).
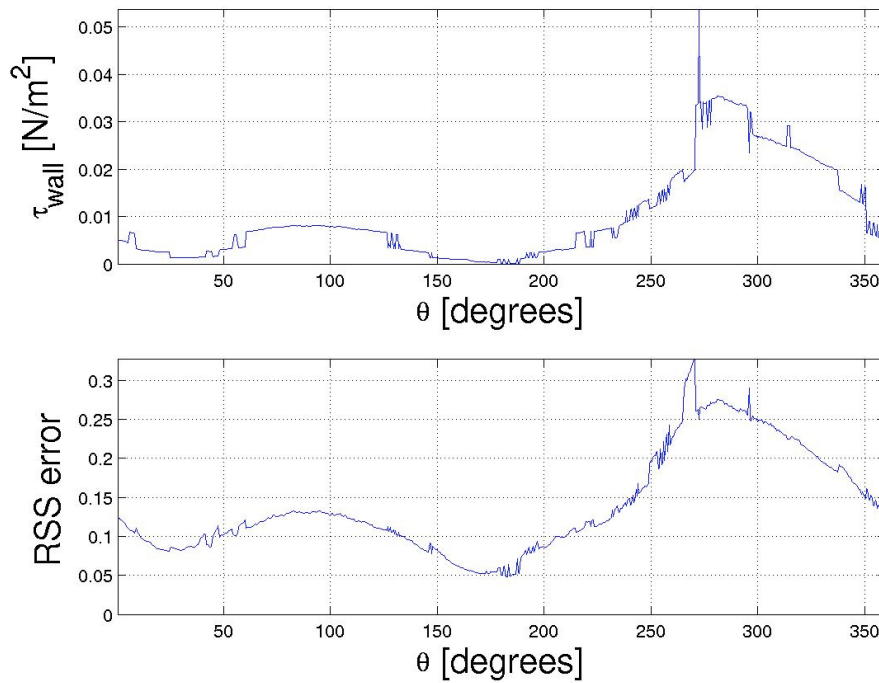
Figure 2.87.—Wall Shear Stress and the associated error at r/D = 0.81 for Case Ib (Re_{max} = 7600, Va = 2300, S = 54 mm, S/D = 0.251).
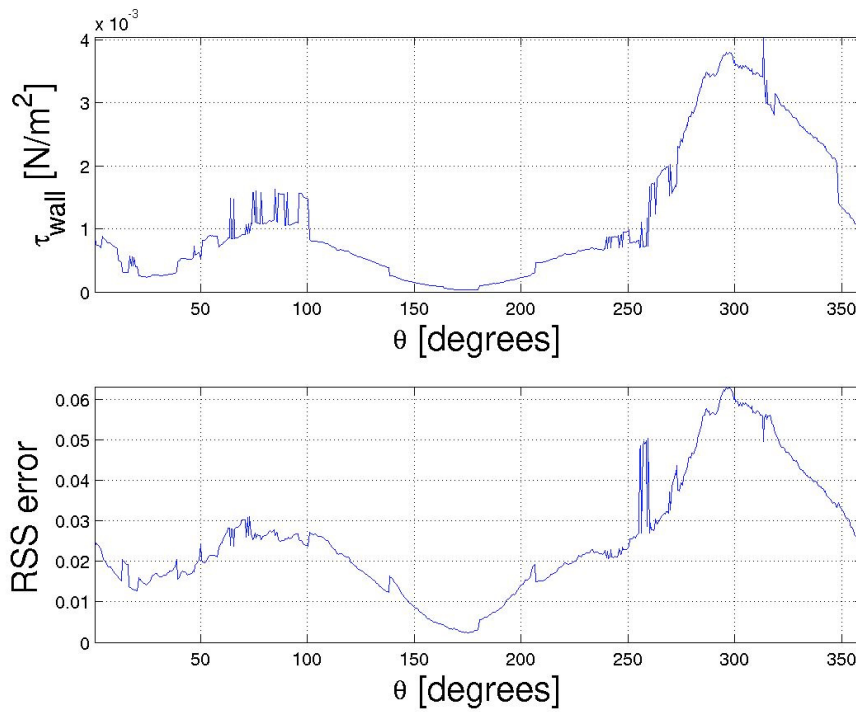
Figure 2.88.—Wall Shear Stress and the associated error at r/D = 0.93 for Case Ib (Re$_{max}$ = 7600, Va = 2300, S = 54 mm, S/D = 0.251).
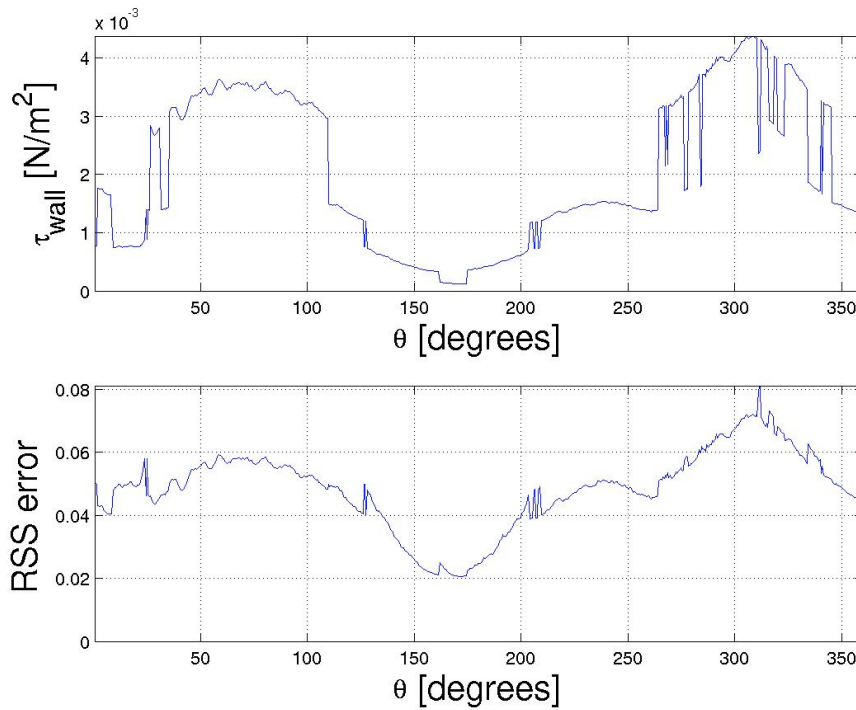
Figure 2.89.—Wall Shear Stress and the associated error at r/D = 1.05 for Case Ib (Re$_{max}$ = 7600, Va = 2300, S = 54 mm, S/D = 0.251).
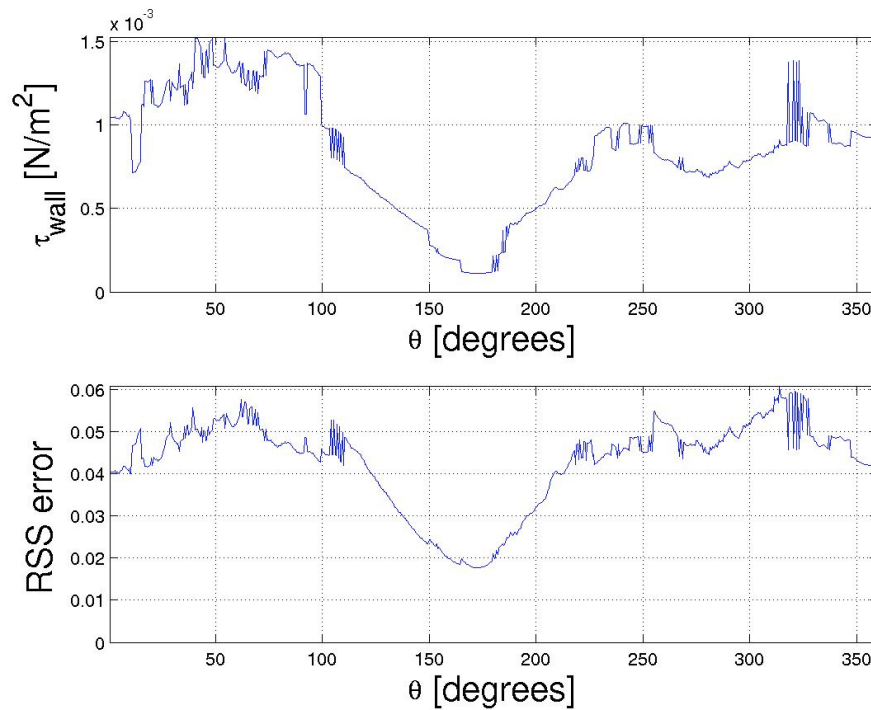
Figure 2.90.—Wall Shear Stress and the associated error at r/D = 1.17 for Case Ib (Re$_{max}$ = 7600, Va = 2300, S = 54 mm, S/D = 0.251).
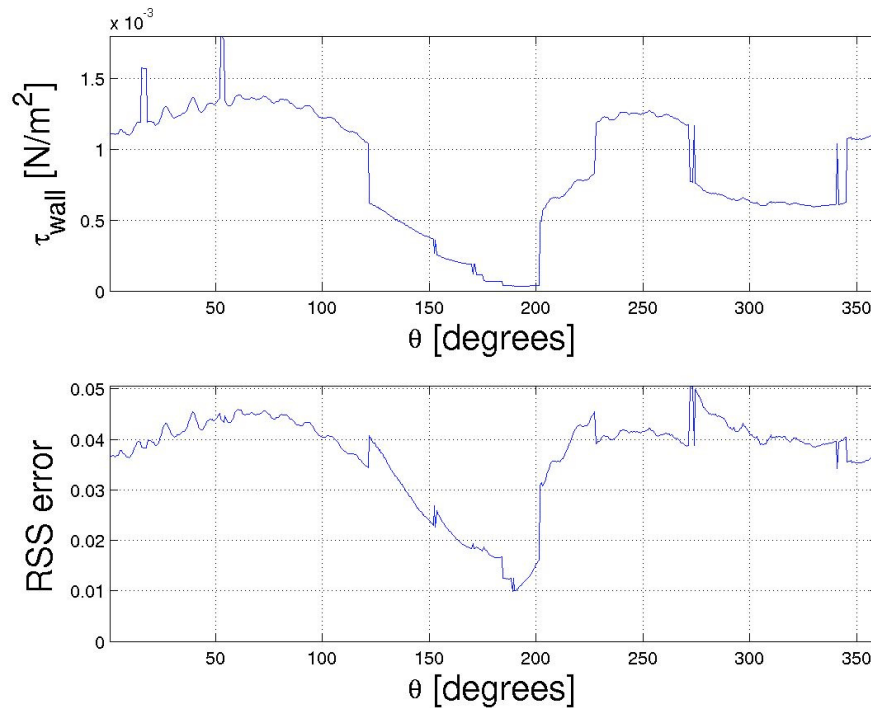
Figure 2.91.—Wall Shear Stress and the associated error at r/D = 1.30 for Case Ib (Re$_{max}$ = 7600, Va = 2300, S = 54 mm, S/D = 0.251).
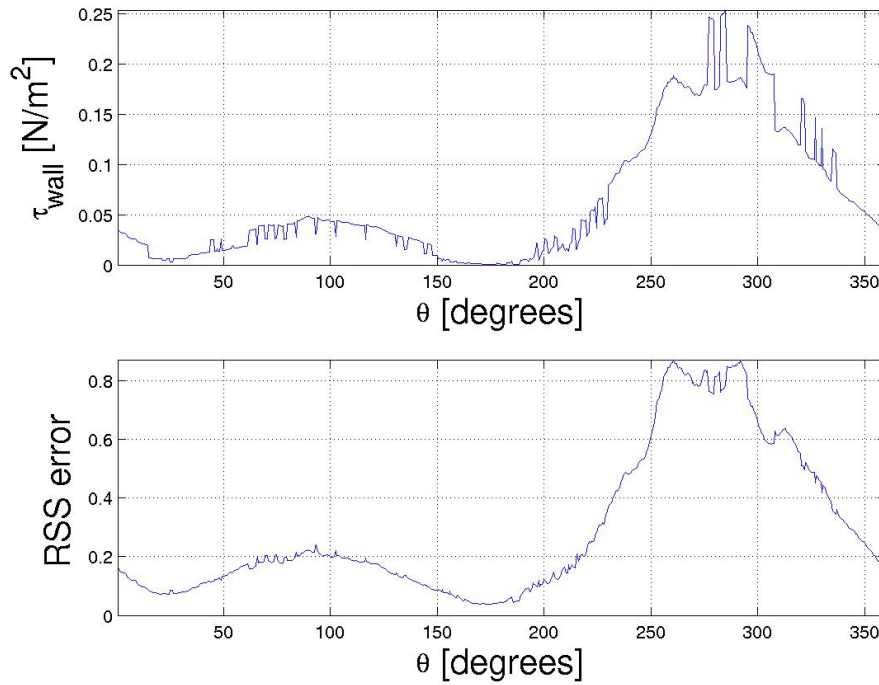
Figure 2.92.—Wall Shear Stress and the associated error at $r/D = 0.68$ for Case IIIb (Re$_{max}$ = 7600, Va = 2300, S = 54 mm, S/D = 0.251).
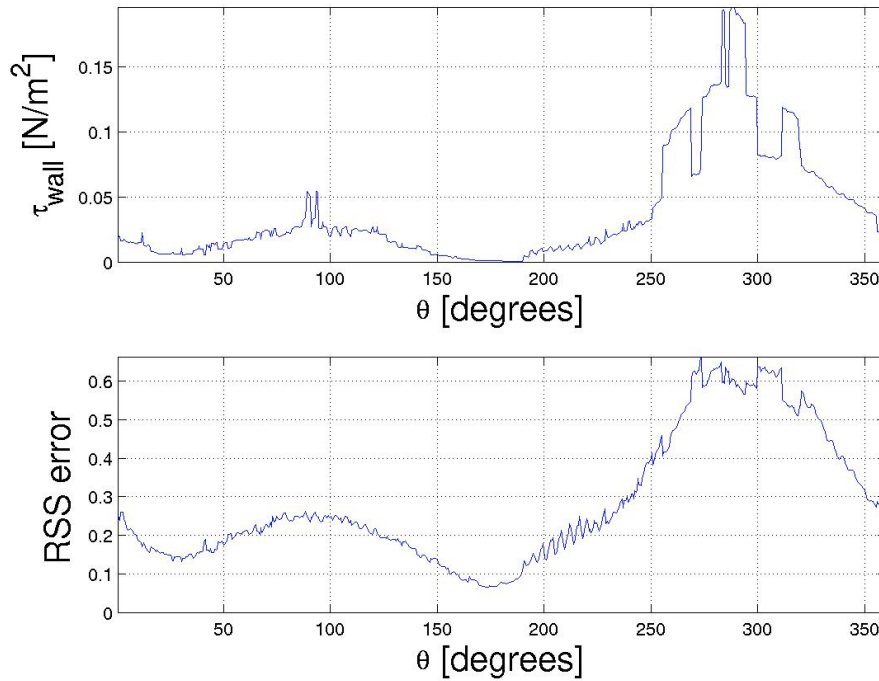
Figure 2.93.—Wall Shear Stress and the associated error at $r/D = 0.81$ for Case IIIb (Re$_{max}$ = 7600, Va = 2300, S = 54 mm, S/D = 0.251).
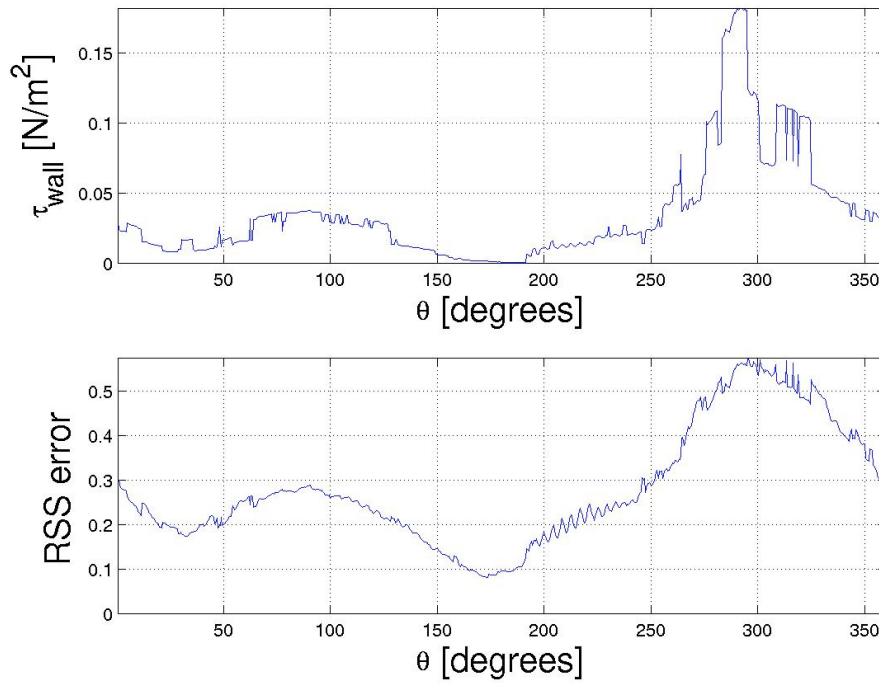
Figure 2.94.—Wall Shear Stress and the associated error at $r/D = 0.93$ for Case IIIb ($Re_{max} = 7600$, $Va = 2300$, $S = 54$ mm, $S/D = 0.251$).
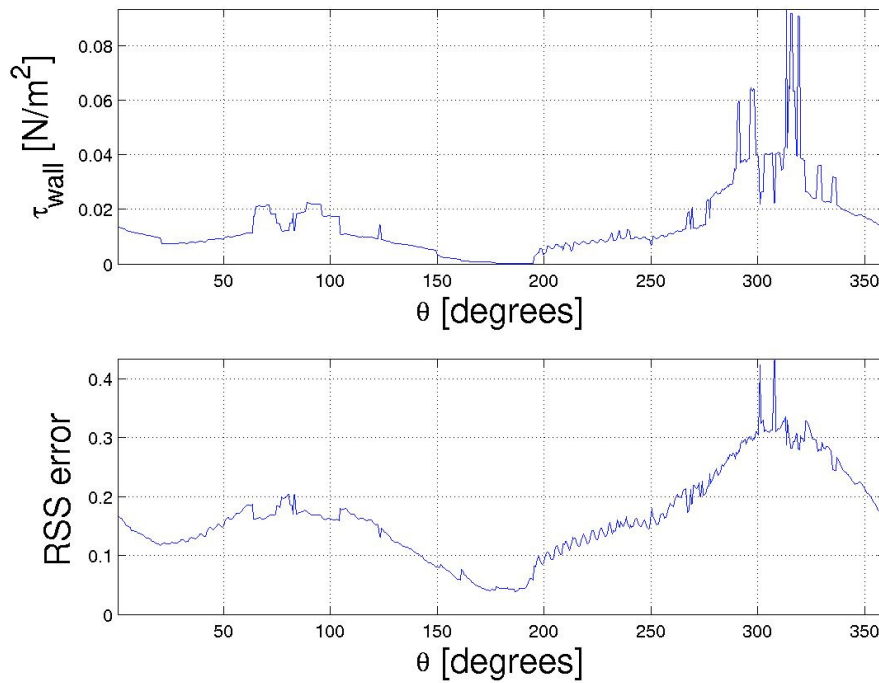
Figure 2.95.—Wall Shear Stress and the associated error at $r/D = 1.05$ for Case IIIb ($Re_{max} = 7600$, $Va = 2300$, $S = 54$ mm, $S/D = 0.251$).
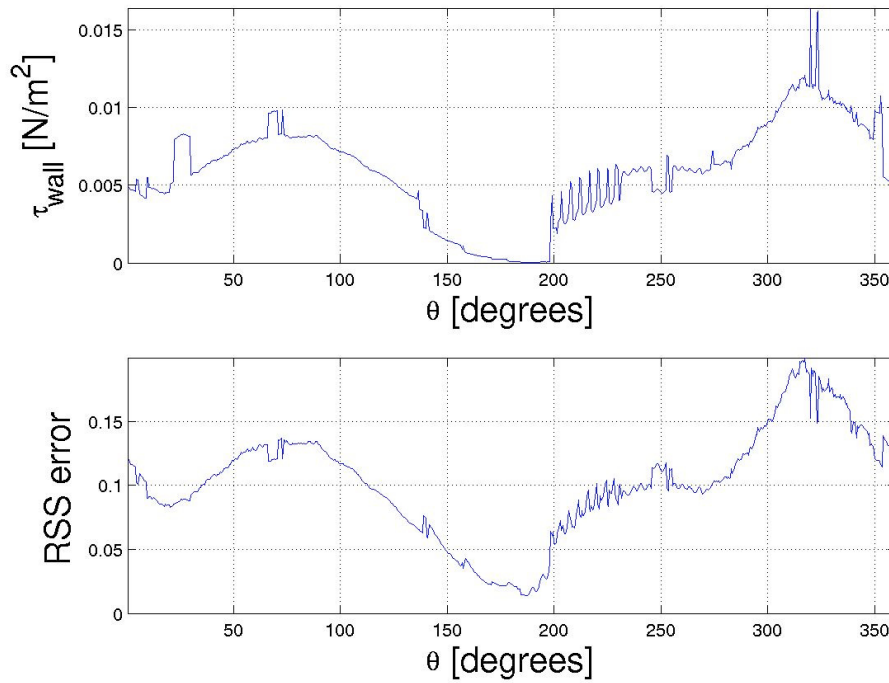
Figure 2.96.—Wall Shear Stress and the associated error at $r/D = 1.17$ for Case IIIb ($Re_{max} = 7600$, Va = 2300, S = 54 mm, S/D = 0.251).
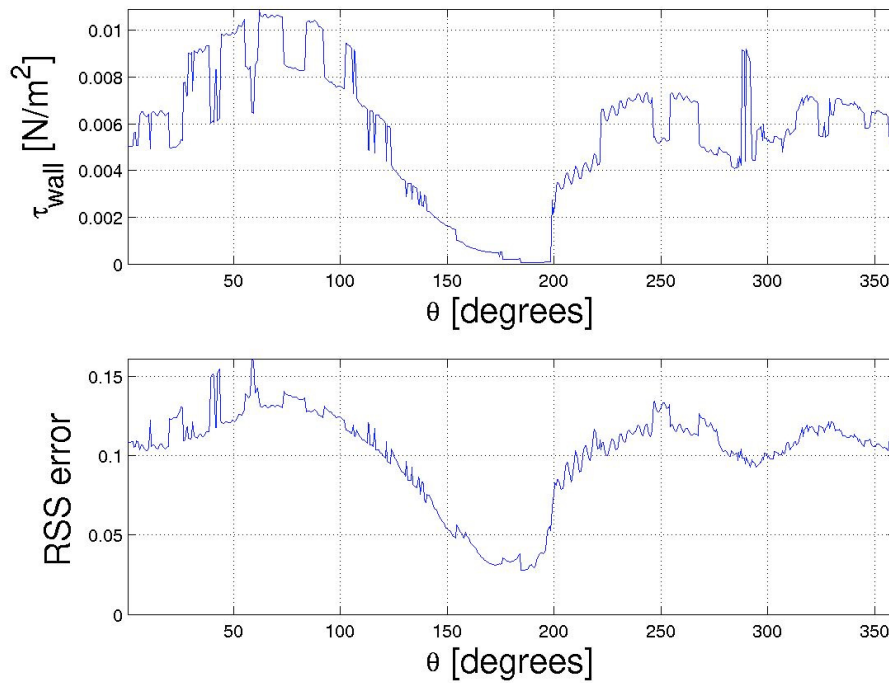
Figure 2.97.—Wall Shear Stress and the associated error at $r/D = 1.30$ for Case IIIb ($Re_{max} = 7600$, Va = 2300, S = 54 mm, S/D = 0.251).

Side View (Flow is into or out of the plane of the paper)

Probe Support

Probe

Support Prongs

Wire

Side View (color conventions are preserved)

Probe Wake

Main Flow
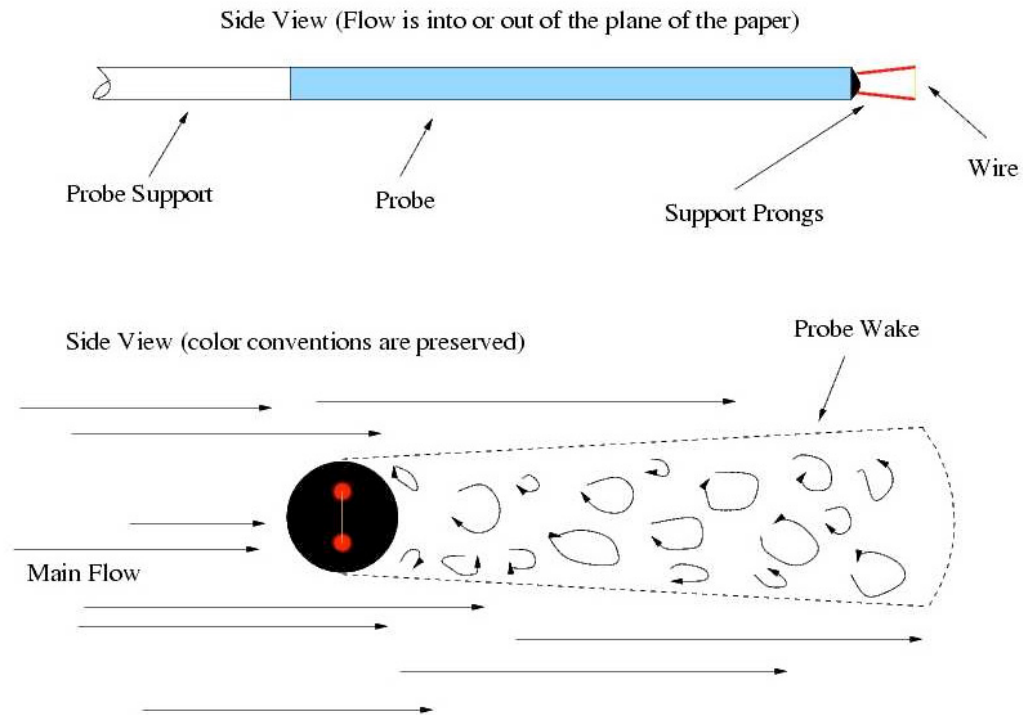
Figure 2.98.—An approximate picture of the flow around the probe and probe support.

Flow is into or out of the plane of the paper

Test Section Wall

Wire

A
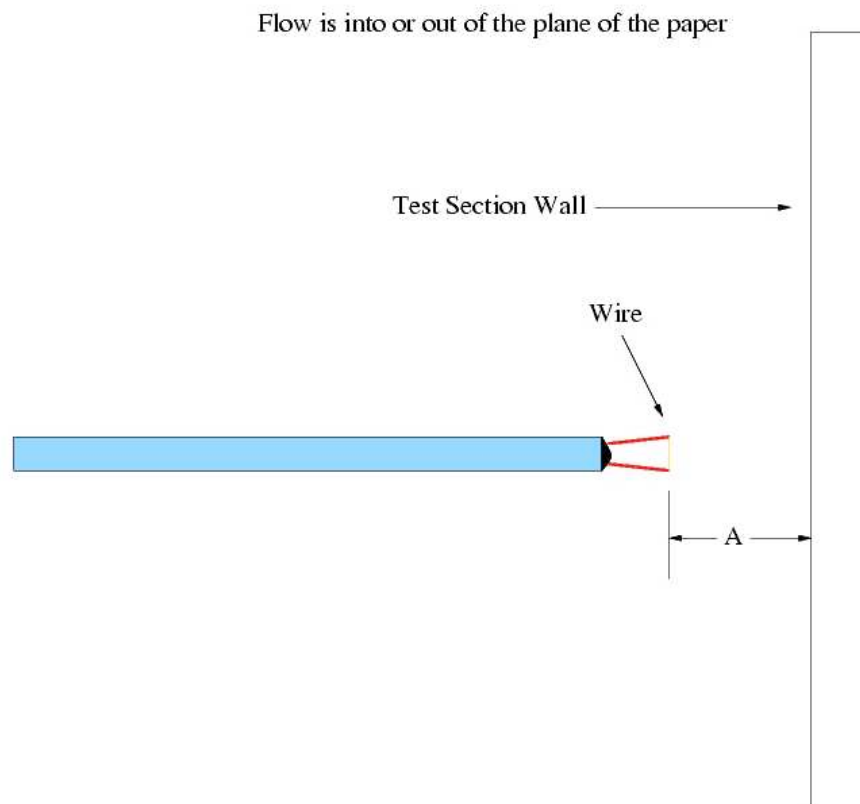
Figure 2.99.—Near wall measurements and wall conduction effects.
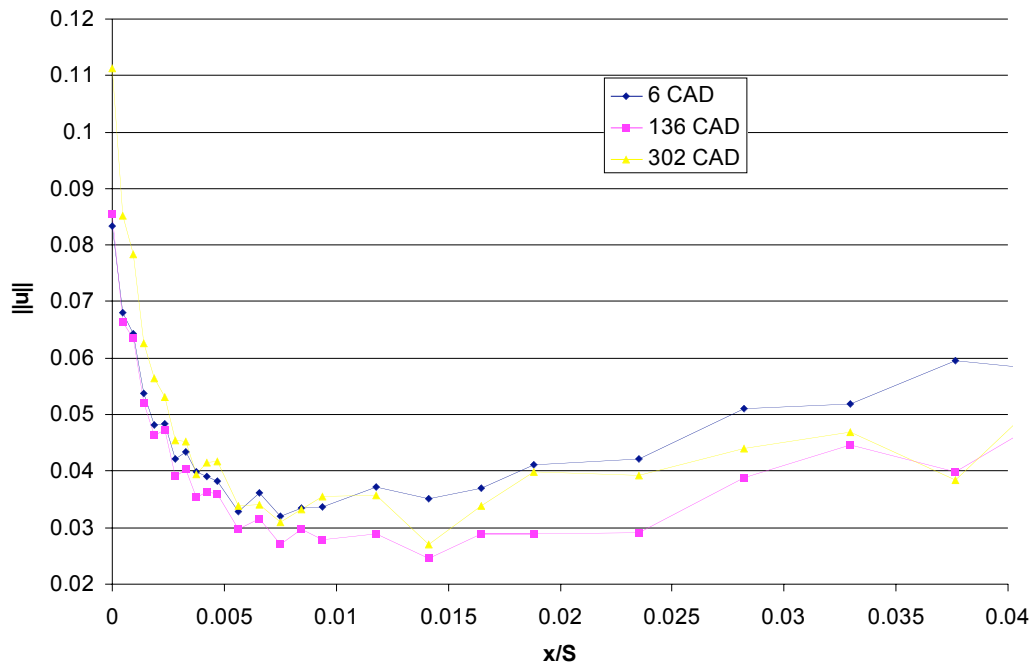
Figure 2.100.—An example of wall conduction effects.

Flow is into or out of the plane of the paper

Test Section Wall

Alternating Low and High Pressure Air (depending on the phase of the oscillation cycle)

Atmospheric Air

Leakage

Hole in Wall

000
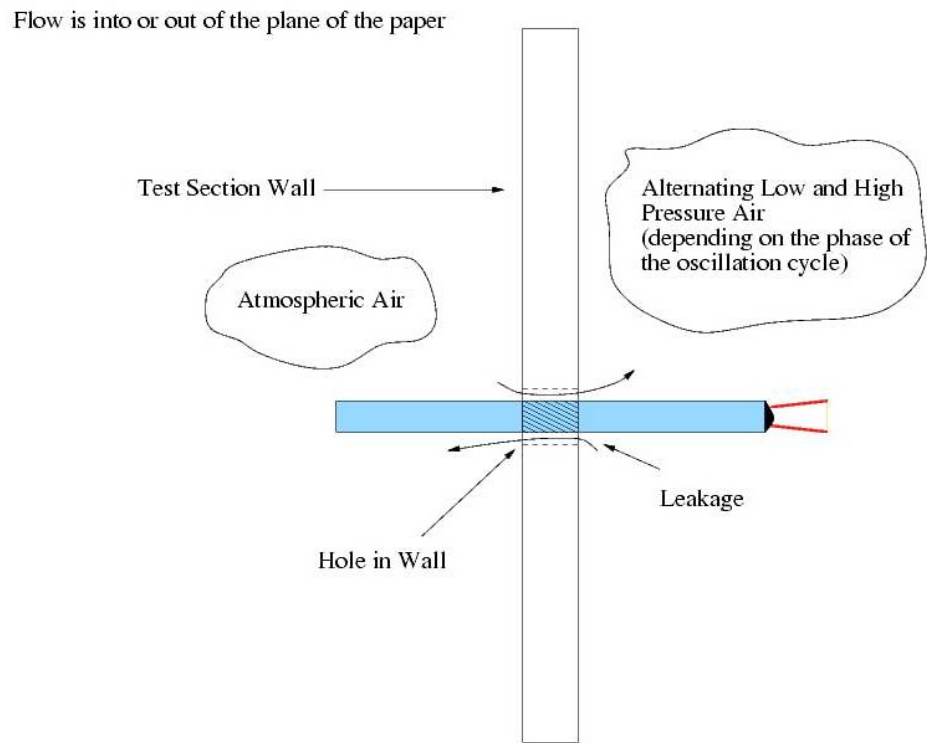
Figure 2.101.—Flow leakage through access hole.
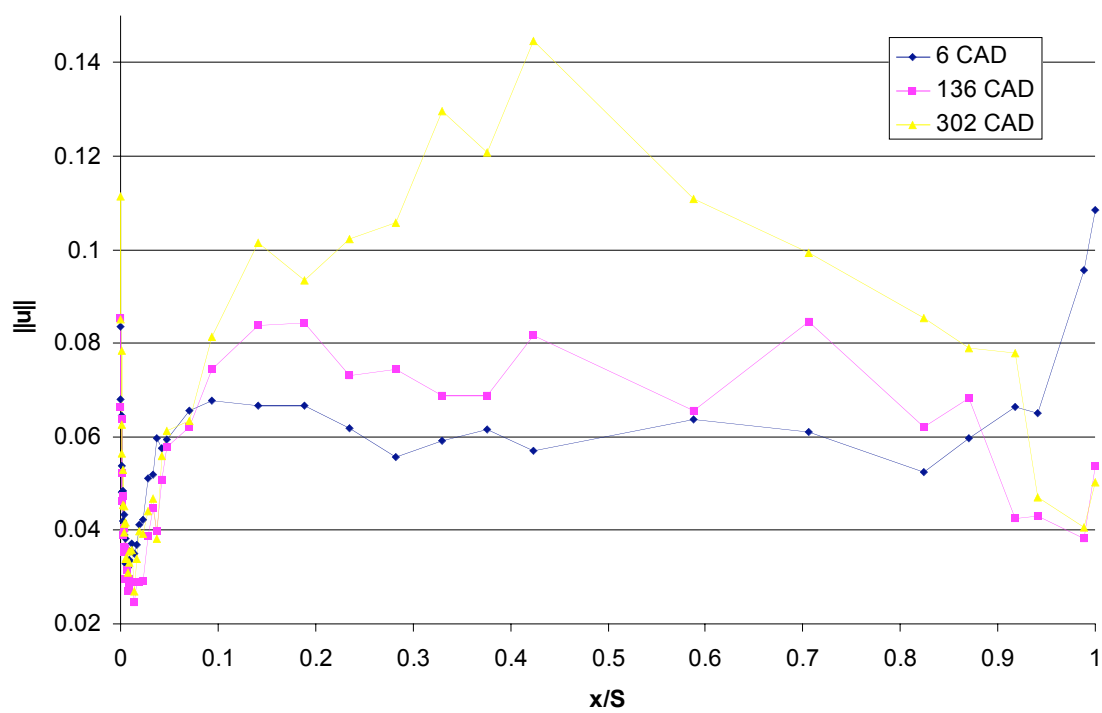
Figure 2.102.—Velocity disturbance near $x/S = 1$.

2.10 References

1. Burmeister, Louis, C., "Convective Heat Transfer," 2nd Edition, John Wiley and Sons, Inc.
2. Friedman, G.T., and Simon, T.W., 1990, "The University of Minnesota Oscillating Flow Experiments," 25th IECEC Conf., Aug. 1990, Reno Nevada, Vol. 5, pp. 393–397, Ed., P.A. Nelson, W.W. Schertz and R.H. Till, Am. Inst. of Chem. Engr., NY.
3. Hinze, "Turbulence," 2nd edition, McGraw-Hill Series in Mechanical Engineering, McGraw-Hill Book Company, 1975.
4. Kornhauser, A. 1989, "Gas-Wall Heat Transfer During Compression and Expansion," Ph.D. Thesis, Mechanical Engineering Department, Massachusetts Institute of Technology.
5. Niu, Y., Simon, T.W., Ibrahim, M. and Gedeon, D., 2002, "Thermal Dispersion of Discrete Jets upon Entrance to a Stirling Engine Regenerator under Oscillatory Flow Conditions," 2002 IECEC Conf., Proc. paper No. 20141.
6. Niu, Y., Simon, T.W., Ibrahim, M. and Gedeon, D., 2003, "Measurements of Unsteady convective h.t. rates subjected to Oscillatory flow," 2003 IECEC Conf., Proc. paper No. 2003–12176
7. Qiu, S., and Simon, T.W., 1994, "Measurements of Heat Transfer and Fluid Mechanics within an Oscillatory Flow in a Pipe," in Fundamentals of Heat Transfer in Forced Convection 1994, ASME HDT-Vol. 285, pp. 1–8, ed. F.W. Schmidt and R.J. Moffat, Winter Annual Meeting.
8. Qiu, S., and Simon T.W., 1992, "Visualization of Entry Flow Separation for Oscillating Flow in Tubes," Proc. of the 27th IECEC Conf., Vol. 5, pp. 517–522, paper No. 929465.
9. Seume, J. and Simon, T., 1986, "Oscillating Flow in Stirling Engine Heat Exchangers," 1986 IECEC Conf., Proc. paper No. 869118, pp. 533–538.
10. Seume, J., Simon, T. and Goldberg, L., 1987, "Description of the Oscillating Flow Test Program," 1987 IECEC Conference, Proc. 22nd IECEC, paper, No. 879029, pp. 1753–1758.
11. Seume, J., and Simon, T.W., 1987, "Flow Oscillation Effects in Tubes and Porous Material: Unresolved Issues," HTD-Vol. 93/FED - Vol. 62, pp. 55–62.
12. Seume, J., and Simon, T.W., 1988, "Effect of Transition on Oscillation Flow Losses in Stirling Engine Coolers and Heaters," 1988 IECEC Conf. Proc. paper No. 889283, pp. 127–132.
13. Seume, J., Friedman, G. and Simon, T.W., 1992, "Fluid Mechanics Experiments in Oscillatory Flow," NASA–CR 189127.
14. Simon, T.W., Niu, Y., and Sun, L., "Some Comments on Dynamic Similitude," November 2003, University of Minnesota Department of mechanical Engineering Heat Transfer Lab internal memorandum.
15. Smits, A.J., "Hot-Wire Anemometry – A Short Introductory Course," Gas Dynamics Laboratory Internal Memorandum No. 51. (NOTE: quoting the author "These Notes were originally prepared for use in the graduate Experimental Methods course taught in the Mechanical and Aerospace Engineering Department at Princeton University.")

3. A Comparison Between Oscillatory Flow and Unidirectional Flow

3.1 Introduction

One may ask, given the data presented in sections 1 and 2, "How similar is oscillatory flow to steady unidirectional flow?" The impetus is that there is a large body of literature dedicated to impinging jet investigations, whereas, there is limited data available for oscillating flows in Stirling engines. Thus, to answer this question, we draw a comparison between steady and oscillatory flow. Presented below are comparisons between three different operating points.

In theory, one way to predict whether unidirectional results can be applied to oscillatory flow is by looking at the Valensi number,

$$Va = \frac{\omega D_h^2}{4\nu}$$

The Valensi number is a ratio of a recovery time (the effect of viscosity, i.e., if a fluid is quite viscous then it 'recovers' quickly – velocity gradients in the fluid will be quickly damped and the fluid will 'recover') to that of the rotational period (oscillation period). For example, if the viscosity of an oscillating fluid is very small compared to the oscillation period, then the Valensi number is large. Physically speaking, velocity gradients within the fluid are not equalizing throughout the cycle – in other words, the fluid is not behaving like it is under steady state conditions. The quantity D_h (the hydraulic diameter) appears in the Valensi number. This length scale tries to capture the length of a velocity gradient – that is, how far a disturbance must diffuse.

The Valensi numbers presented in table 2.1 of section 2 are based on crankshaft rotational frequency, the viscosity of air and the tube diameter. This leads to a question: Is it valid to use tube-based Valensi numbers in the disc space? The answer is no. Another question arises in light of the very turbulent nature of the flow in portions of the test section during certain portions of the oscillation cycle: Is it appropriate to use the molecular viscosity of air to compute a Valensi Number? The answer to that is more complicated. Niu et al.[1] have shown that, in a regenerator matrix, turbulent eddy viscosity can be as much a 500 times as large as molecular viscosity. The implications of the work by Niu et al.[1] on the investigations under consideration are unclear – it is however something to contemplate.

We present below a table (table 3.1) with Valensi numbers based on the length scale appropriate to the area of the test section under consideration.

TABLE 3.1.—ADJUSTED VALENSI NUMBERS

Case	Location	rpm	*S/D*	S (mm)	Lengthscale	Va Laminar	Va Turbulent
I.a	Tube	30	0.251	54	D	2300	23
I.b	Channel	30	0.251	54	S	580	6
II.a	Tube	30	0.591	127	D	2300	23
II.b	Channel	30	0.591	127	S	3213	32
III.a	Tube	70	0.251	54	D	5400	54
III.b	Channel	70	0.251	54	S	1361	14

Turbulent Valensi numbers were calculated by assuming that turbulent eddy viscosity is 100 times as large as molecular viscosity. This factor of 100 is strictly a guess at the effect of turbulent transport – further research is necessary to arrive at a more concrete value.

We see that all of the Valensi numbers in the disc space are much greater than unity regardless of the choice of viscosity[*]. Thus, we expect that for the cases presented below, there will be little to no correlation between oscillatory and unidirectional results.

3.2 Nomenclature

Symbol	Description	Units
D	Delivery tube diameter	[m]
Re	Reynolds Number	[dimensionless]
r	Radial Variable	[m]
r/D	Non-Dimensional radial variable	[dimensionless]
rpm	revolutions per minute	[1/min]
S	Disc Spacing	[m]
Va	Valensi number	[dimensionless]
x	Axial variable	[m]
x/S	Non-Dimensional axial variable	[dimensionless]
θ	Crank Angle	[degrees]
ω	Rotational speed	[1/min]

3.3 Re = 5989, S = 127 mm, ω = 30 rpm, Va – Laminar = 3213, Va – Turbulent = 32

In this case we look at the disc space flow and draw a comparison between the unidirectional case Re = 7600, S = 127 mm (Case 1 in section 1), and the oscillatory flow case, ω = 30 rpm, S = 127 mm (Case IIb in section 2). We begin with a note; in the unidirectional investigation, Case 1 is affiliated with a Reynolds number of 7600. This is not exactly correct (as explained in section 1 subheading 1.7.1). In section 1, heading 1.7.1, Reynolds numbers were based on tube centerline velocities. At present, this is not the correct course of action; we must observe a mass balance. To this end, we base Reynolds number on the bulk average velocity across the delivery tube under steady flow conditions. If the Reynolds number is based on bulk average velocity, then under unidirectional conditions, Re = 5989.

Now, under oscillatory flow, recall that in Case IIb of section 2, the cited maximum Reynolds Re_{max} number is 7600 (see table 2.1, section 2). Recall also that Reynolds number in the oscillatory studies is based on piston velocity, and, hence, is driven by a sinusoidal pressure gradient. Thus, to match a unidirectional Reynolds number of 5989, two crank angles are possible, one while the flow is accelerating on the blowing stroke, and one while the flow is decelerating on the blowing stroke. These two angles are denoted as $\theta_1 = 232°$ and $\theta_2 = 308°$. Note that the maximum piston velocity occurs at $\theta = 270$. The results of this comparison are presented in figures 3.1 and 3.2.

Figure 3.1 shows that there is little to no correlation between oscillatory and unidirectional flow results in terms of both profile shape and velocity magnitude. The lack of agreement clearly shows the influence of unsteady effects in such flows. As in the case of the accelerating flow (fig. 3.1), figure 3.2 shows no correlation with decelerating flow. Hence, figure 3.2 provides additional verification that unsteady flow effects govern the flow field. This is not surprising in light of the Valensi number associated with this case.

Figure 3.3 shows the effect of flow acceleration on the average velocity profiles. Both angles correspond to a Reynolds number Re = 5989. However, at θ_1, the piston acceleration is 62% of the peak value, whereas, at θ_2, the piston acceleration is –62% of it's peak value (i.e., the piston is decelerating). The effect that piston acceleration has on fluid velocity is remarkable.

---

[*] We see that one of the Valensi numbers based on turbulent viscosity is 6.0. We may hope that this case is *almost* quasi steady. We shall see.

The results of figures 3.1, 3.2, and 3.3 lead to a comment; it is now apparent that although the piston follows an exact sinusoid, there is no reason to expect the same from any given point in the flow field. This is clear to one who looks at the flow visualization results from section 2 (figs. 3.4 and 3.5). Figures 3.4 and 3.5 show the drastic change in the flow field across the maximum piston velocity ($\theta = 270$). The flow velocity definitely does not follow the piston velocity.

3.4 Re = 14937, S = 54 mm, ω = 70 rpm, Va – Laminar = 1361, Va – Turbulent = 14

Here we compare unidirectional results from Case 4 of section 1 (RE = 17,700 S = 54 mm) to oscillatory results from Case IIIb of section 2 (ω = 70 rpm, S = 54 mm). Once again, with regard to unidirectional flow, we have a Reynolds number based on average velocity across the tube and tube diameter of Re = 14937, which corresponds to two crank angles under oscillatory flow. The crank angles of interest are $\theta_1 = 237.5°$ and $\theta_2 = 302.5°$. Presented in figure 3.6 is a comparison between unidirectional results and oscillatory results at $\theta_1 = 237.5°$. We see that the profiles have similar shape but the velocity magnitudes are quite different. The wall jet in the unidirectional case is thinner and stronger. Turning to the second matching crank angle, we see (fig. 3.7) that there is general profile shape agreement and the velocity magnitudes seem to compare quite favorably in the wall jet region. For the sake of comparison, the two crank angles are plotted against each other in figure 3.8. We see that for $\theta_2 = 302.5°$, the wall jet is stronger and the flow may be starting to reverse near the back wall. It seems that the fluid gains momentum as the blowing stroke proceeds, hence, stronger jets are seen at larger crank angles. The importance of the Valensi number is underscored in this case; figure 3.7 may suggest that in this case unidirectional results may be used to predict oscillatory behavior. However, the large Va value associated with this case, and the information presented in figure 3.8 suggest that this is not the truth.

3.5 Re = 5839, S = 54 mm, ω = 30 rpm, Va – Laminar = 580, Va – Turbulent = 6

This is a comparison between Case 2 of section 1 (RE = 7600, S = 54 mm) and case Ib of section 2 (ω = 30 rpm, S = 54 mm). With a unidirectional bulk average Reynolds number of 5839, the matching crank angles under oscillatory flow are $\theta_1 = 230°$ and $\theta_2 = 310°$. Presented in figure 3.9 is a comparison between unidirectional results and $\theta_1 = 230°$. Once again, the overall correlation between the two flow regimes is poor. The profile for the oscillatory case at r/D of 0.930 is remarkable; in this case the wall jet dies very rapidly in the radial direction. Looking at the other crank angle of interest (fig. 3.10) we see that for the smaller of the two radial locations, under oscillatory flow, the profile in the jet region surpasses that of the unidirectional flow profiles. In contrast, for the larger radial oscillatory flow profile, the velocity magnitude is considerably less than that of steady flow. Presented in figure 3.11 is a comparison between the two oscillatory cases. The effect of the addition of momentum and the utility of the Valensi number is reiterated.

3.6 Conclusions

The main and important result of this section is that Stirling engine designers should not try to apply steady-unidirectional impinging jet data to oscillatory flows for regions of the engine where the Valensi number is greater than unity. If an appropriate Va value were chosen (based on laminar diffusion or turbulent transport) then one would suspect that steady flow results would be applicable when the Valensi numbers are sub-unity. The problem lies in the determination of the Valensi number. In the test section under consideration, under oscillatory flow, highly turbulent regions were generated and stimulated by the oscillatory nature of the flow (For example, the separation zone that forms on the back wall and its re-ingestion into the tube space on the next half cycle). Thus, to apply unidirectional results, information would be required about the turbulent transport within the test section or engine for the purpose of determining turbulent viscosity. Further investigation into this topic is beyond the scope of this work.
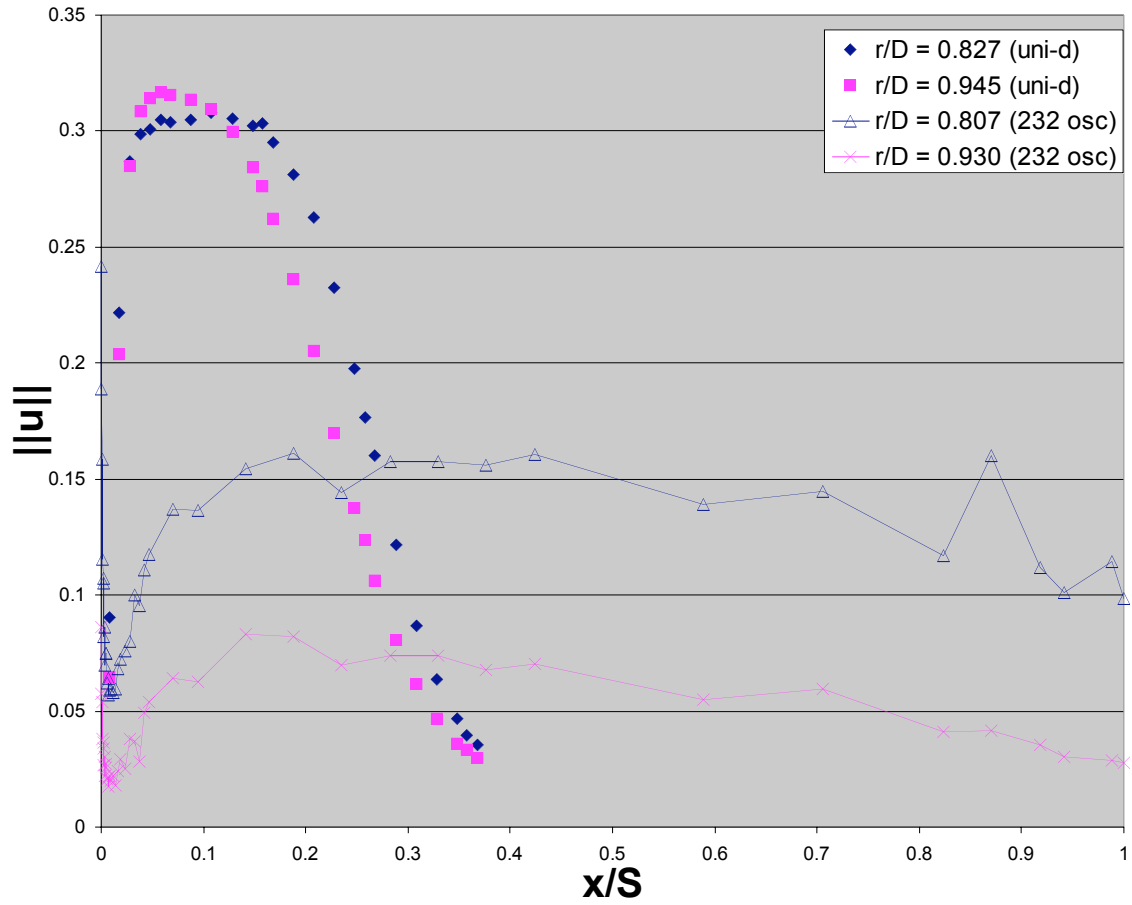
Figure 3.1.—A comparison of unidirectional results (Re = 5989) with oscillatory work at $\theta_1 = 232° \Rightarrow \text{Re} = 5989$.
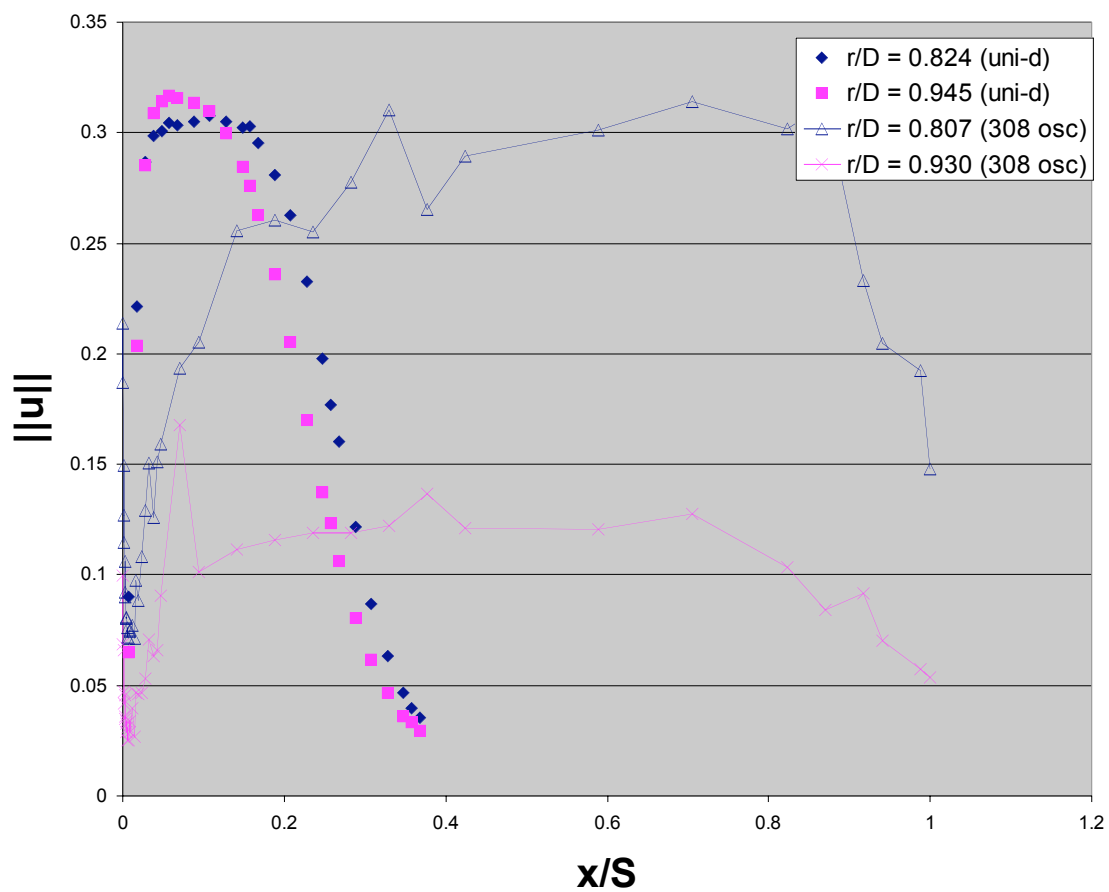
Figure 3.2.—A Comparison of unidirectional results (Re = 5989) with oscillatory work at $\theta_2 = 308° \Rightarrow \mathrm{Re} = 5989$.
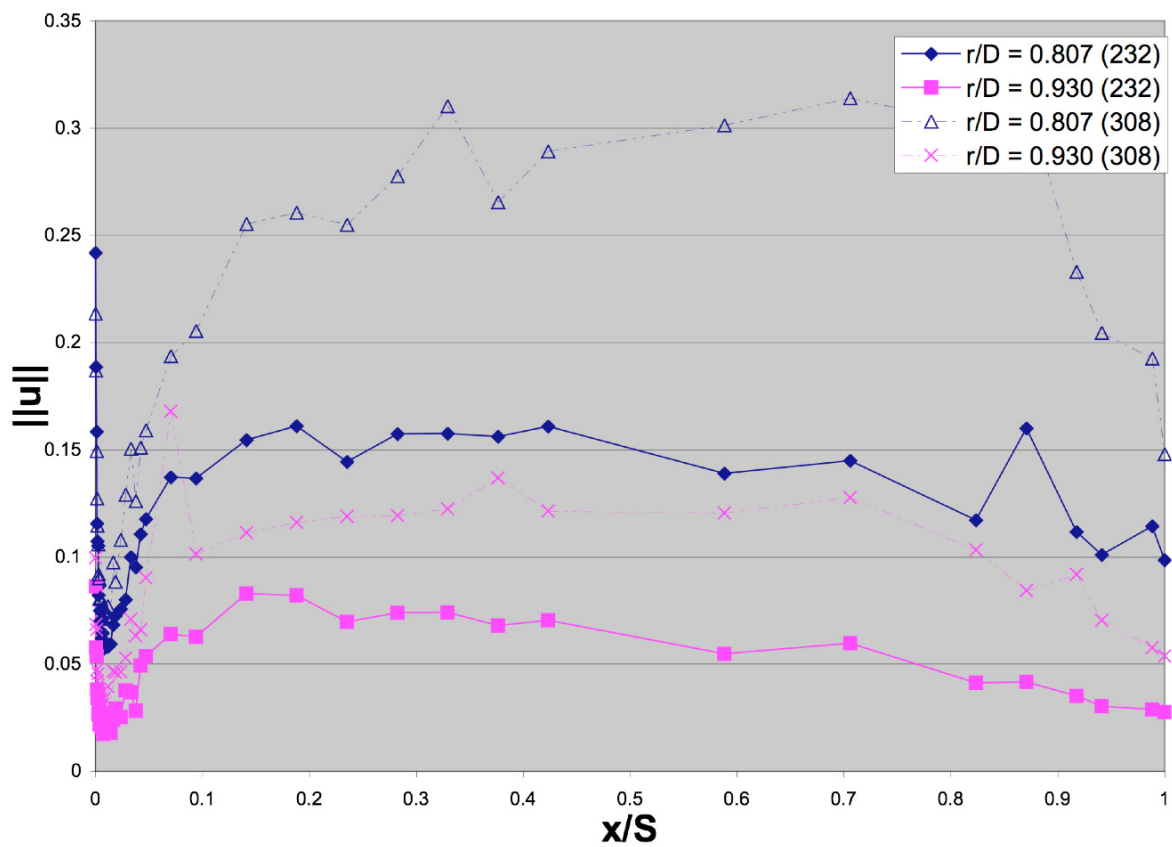
Figure 3.3.—A comparison between $\theta_1 = 232°, \theta_2 = 308°$.
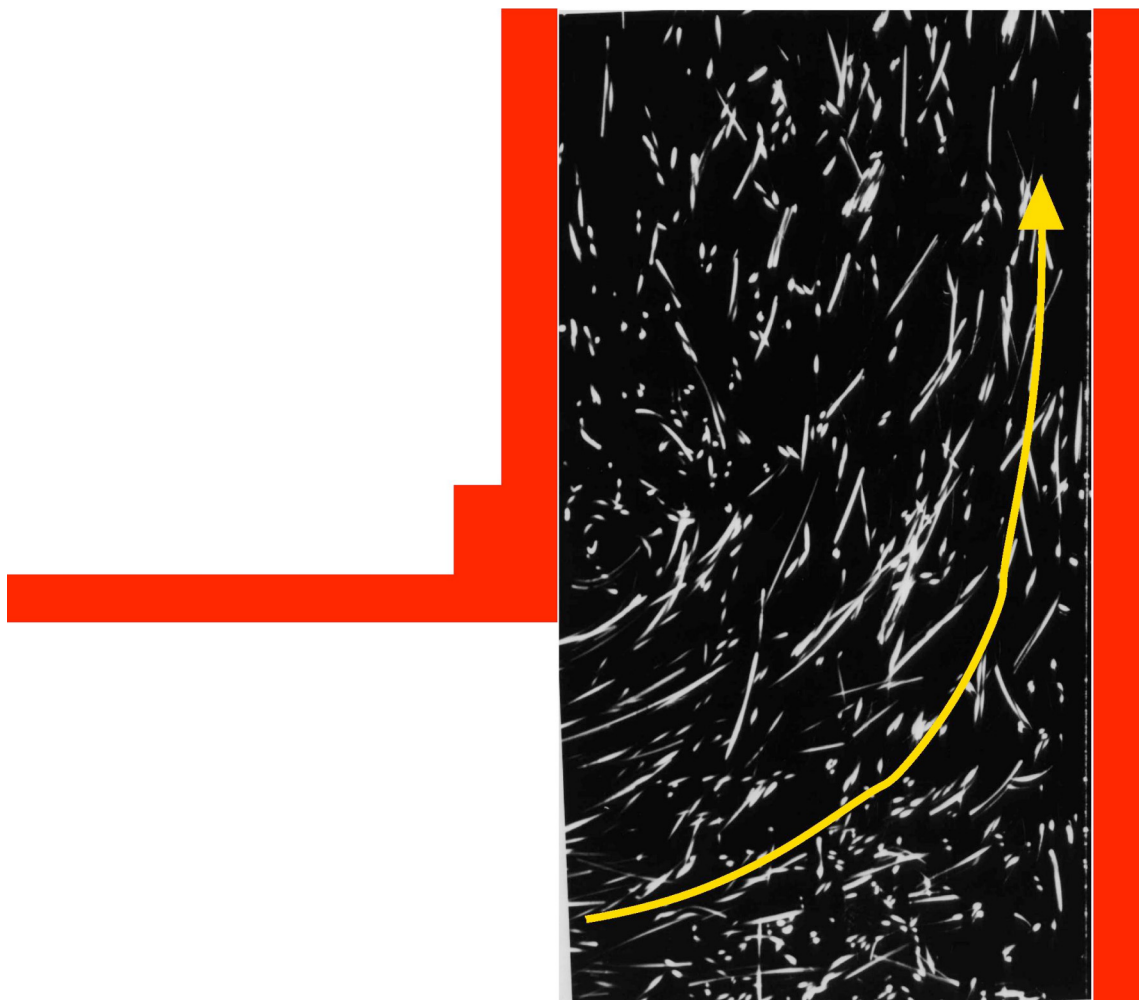
Figure 3.4.—Flow Visualization for $240 < \theta < 255$ (same piston velocity as that of fig. 3.5).
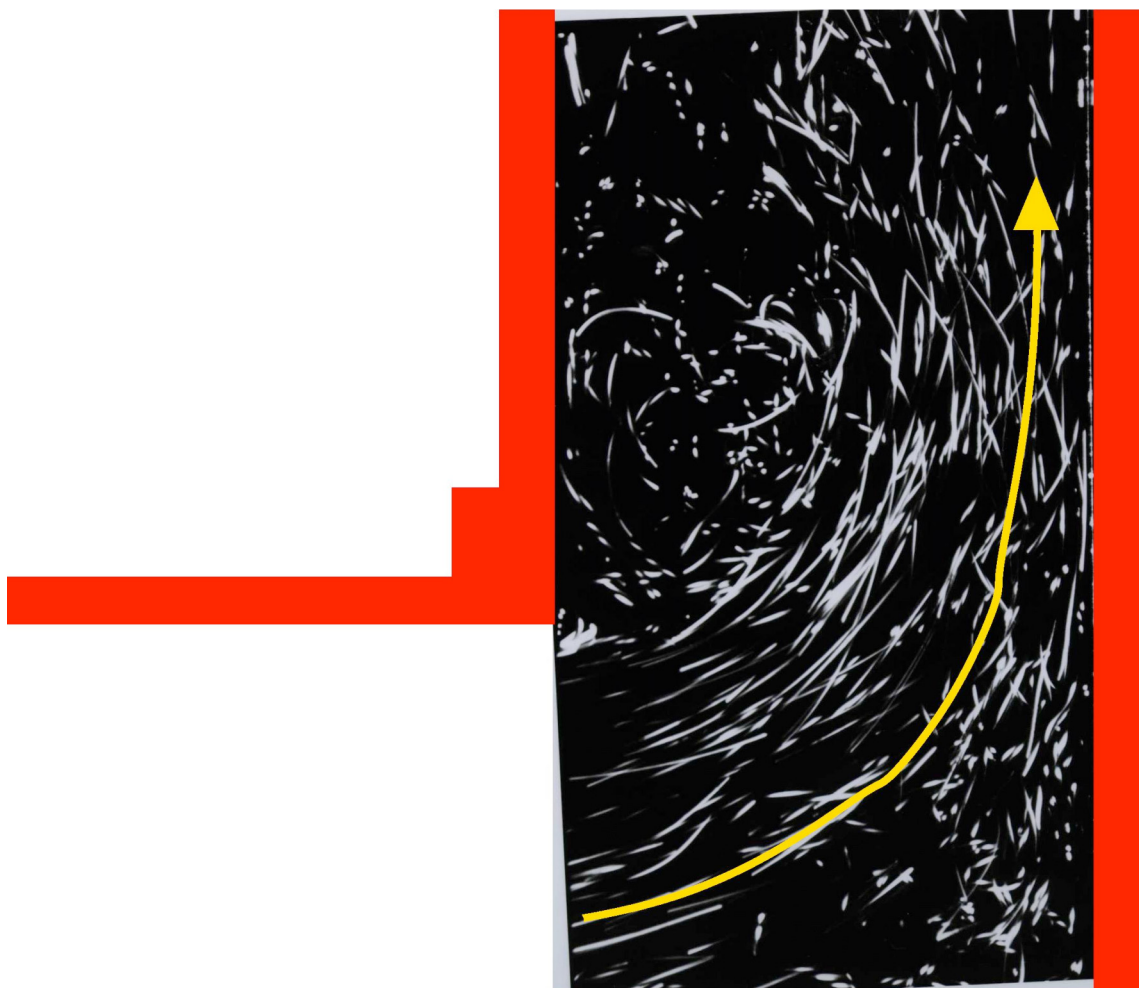
Figure 3.5.—Flow visualization for $285 < \theta < 300$ (same piston velocity as that of fig. 3.4).
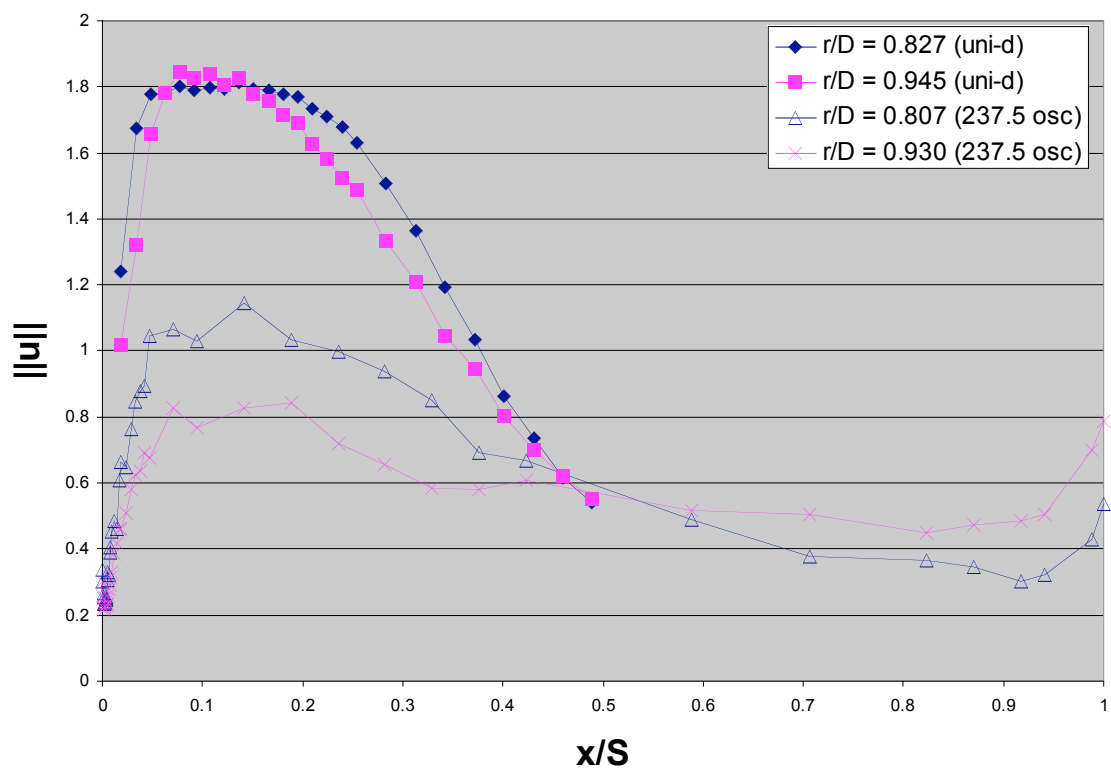
Figure 3.6.—A comparison between steady unidirectional flow and oscillatory flow at $\theta_1 = 237.5°$ with matching Reynolds numbers.
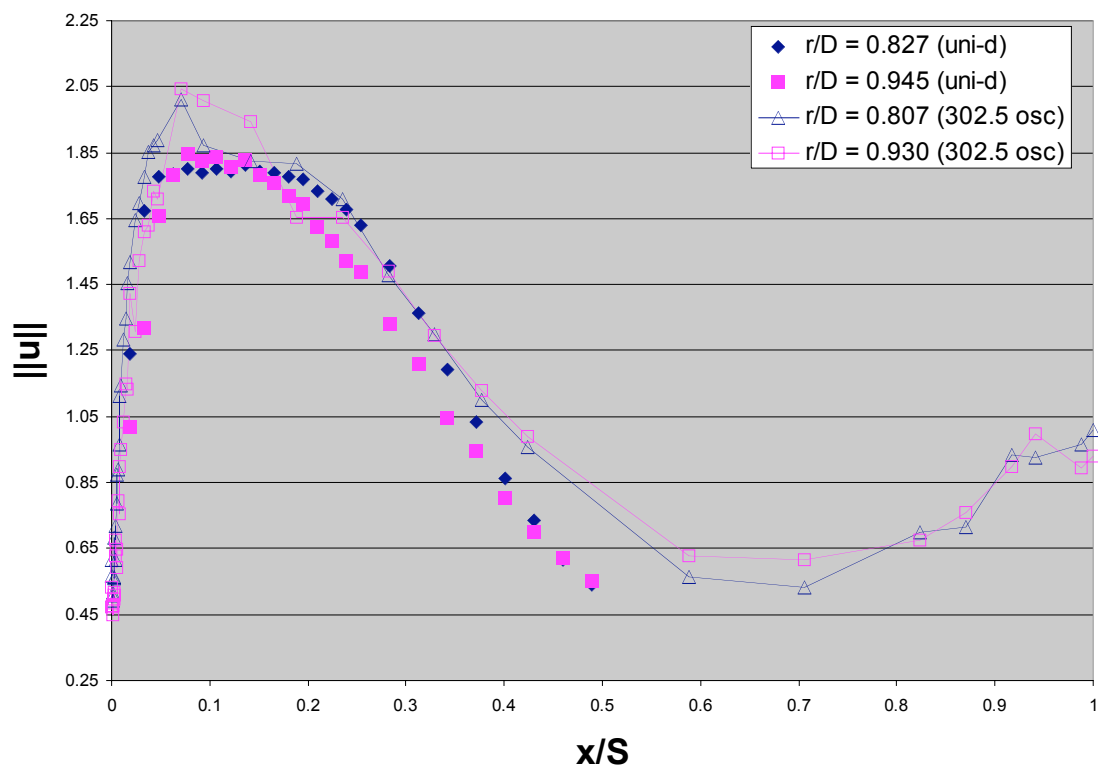
Figure 3.7.—A comparison between steady unidirectional flow and oscillatory flow at $\theta_2 = 302.5°$ with matching Reynolds numbers.
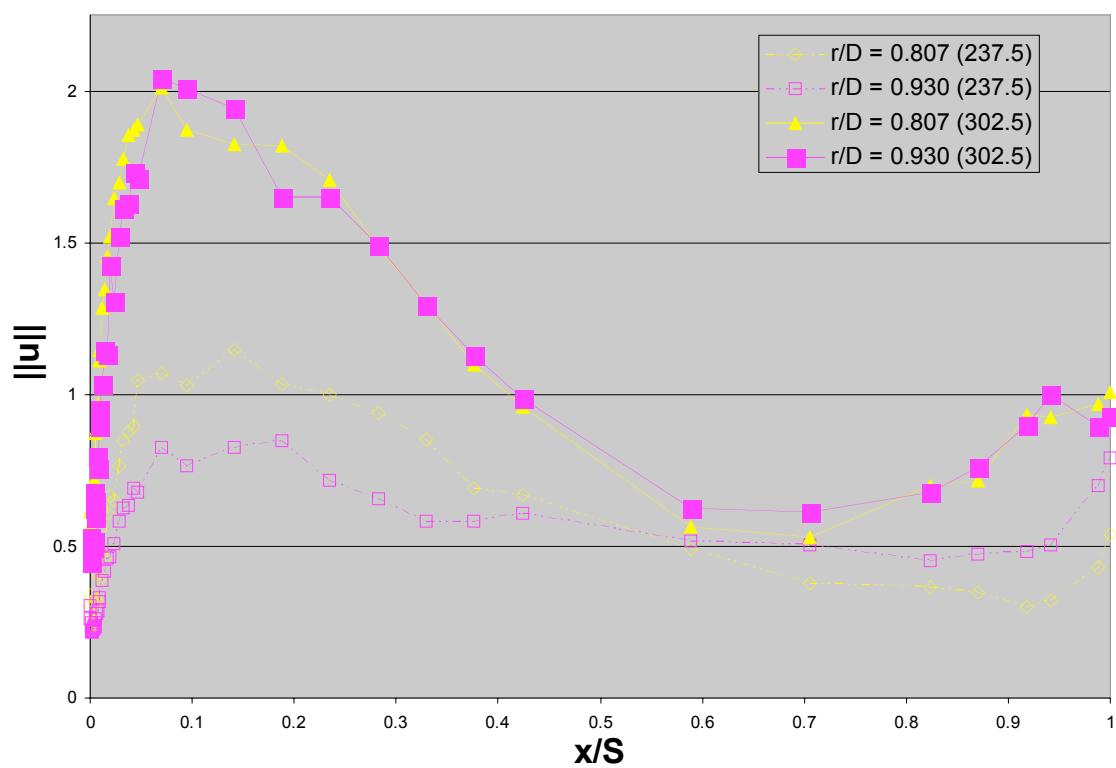
Figure 3.8.—A comparison between two crank angles ($\theta_1 = 237.5°$ and $\theta_2 = 302.5°$) with matching Reynolds numbers on the blowing stroke.
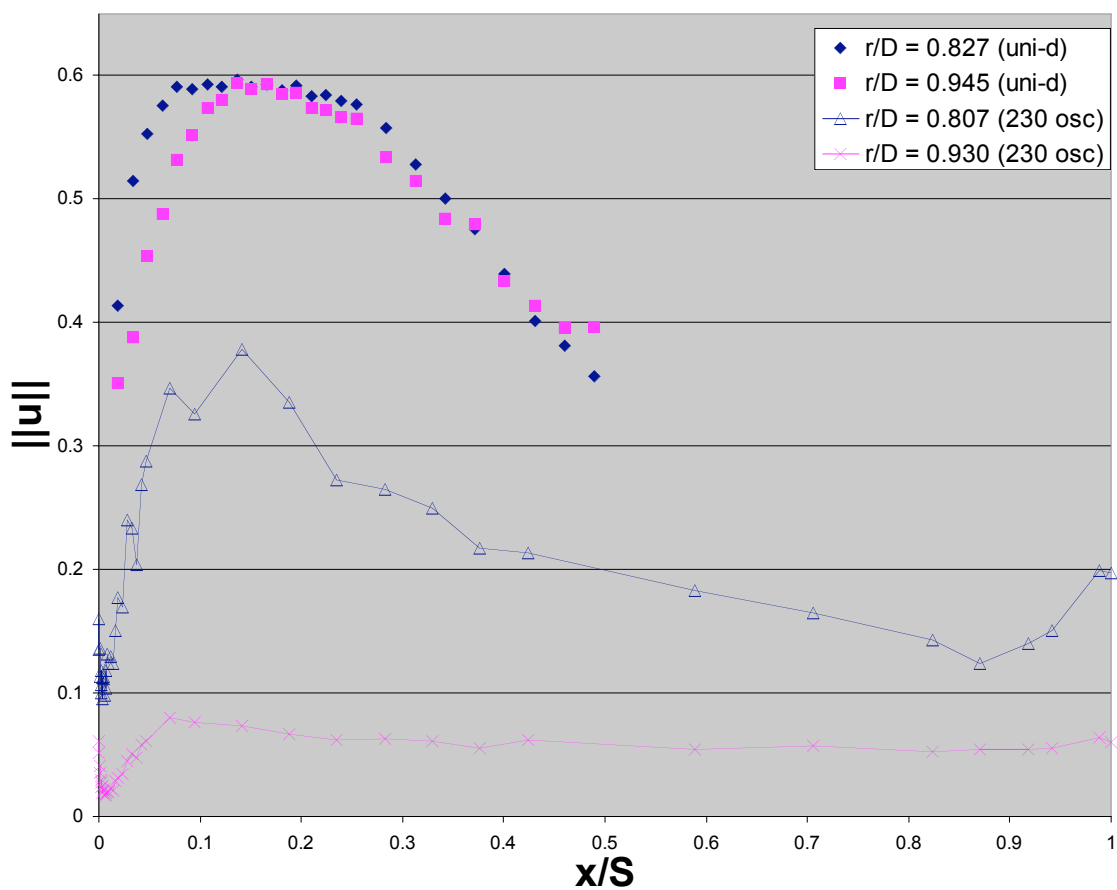
Figure 3.9.—A comparison between steady unidirectional flow and oscillatory flow at $\theta_1 = 230°$ with matching Reynolds numbers.
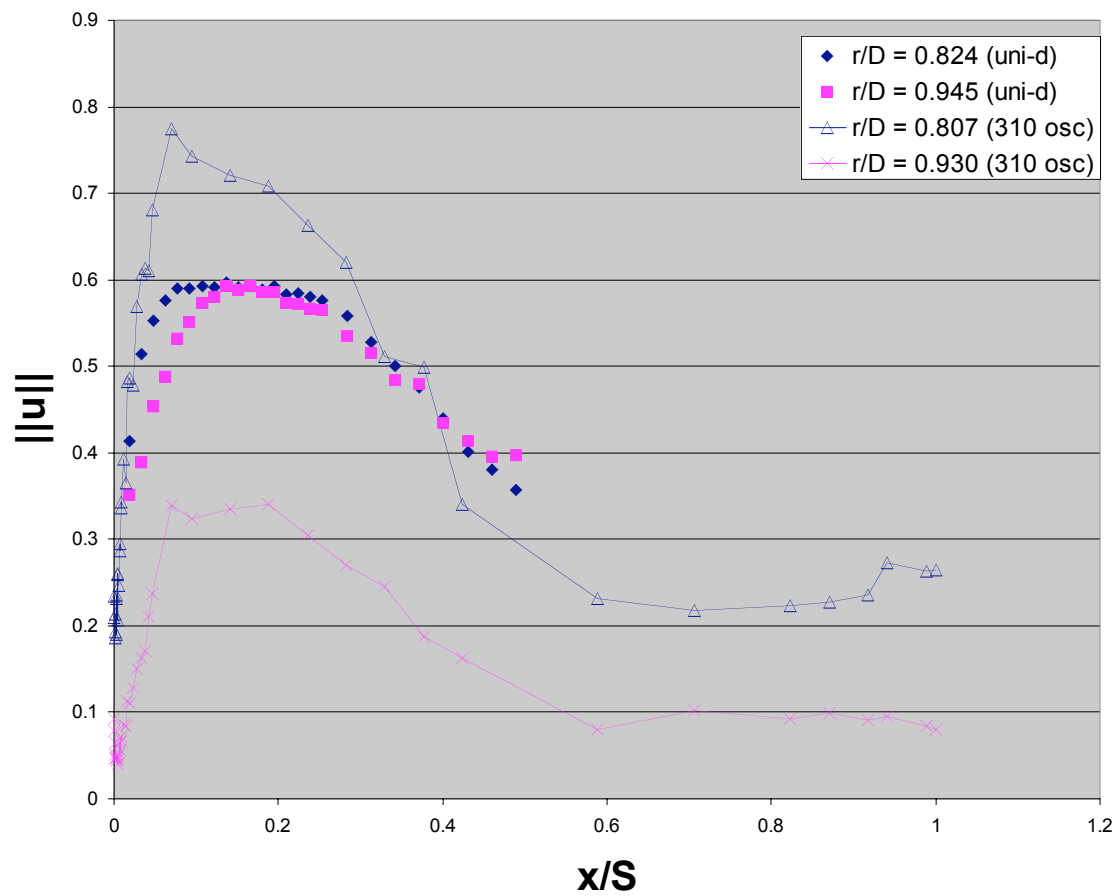
Figure 3.10.—A comparison between steady unidirectional flow and oscillatory flow at $\theta_2 = 310°$ with matching Reynolds numbers.
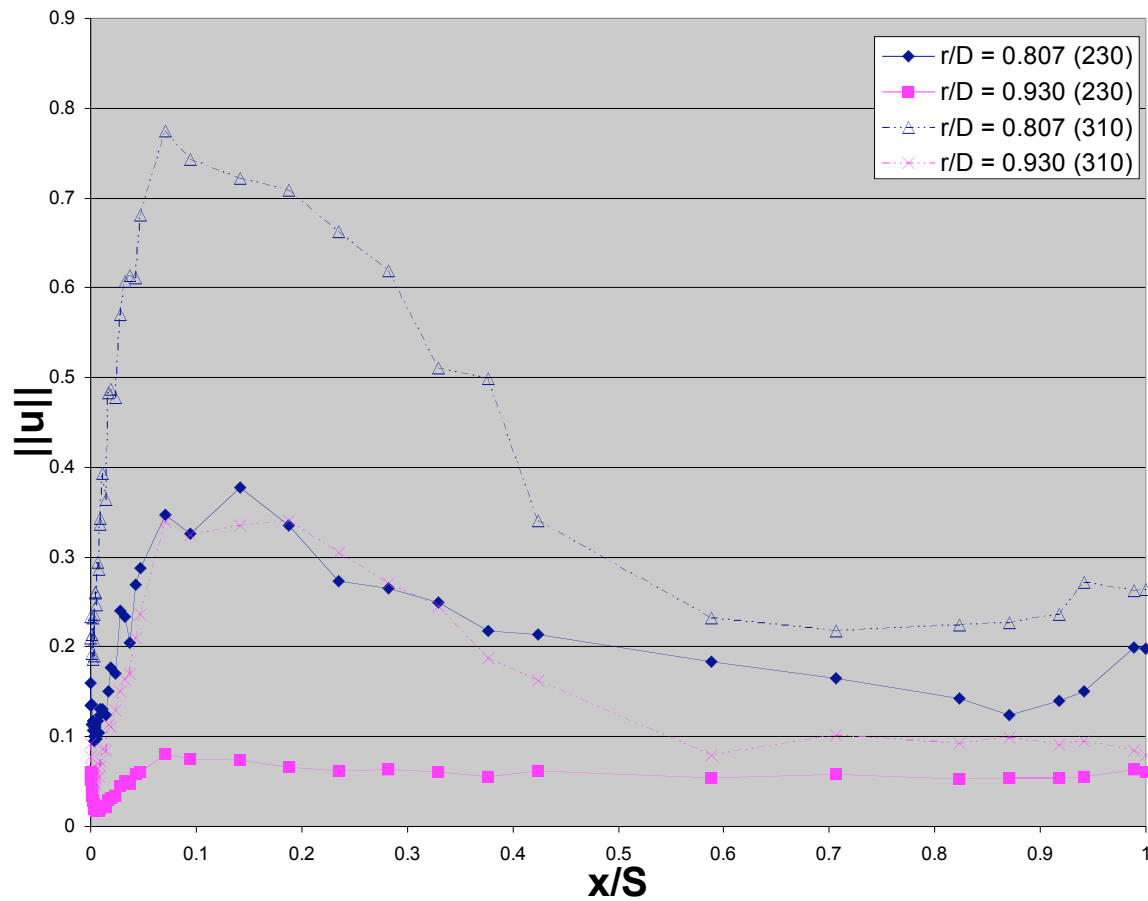
Figure 3.11.—A comparison between two crank angles ($\theta_1 = 248°$ and $\theta_2 = 292°$) with matching Reynolds numbers on the blowing stroke.

3.8 References

1. Niu, Y., Simon, T.W., Ibrahim, M.B., and Gedeon, D., 2003, "Thermal Dispersion of Discrete Jets upon Entrance to a Stirling Engine Regenerator under Oscillatory Flow Conditions," 6th ASME-JSME Thermal Engineering Joint Conference.

4. Comparisons Between Experimentally Gathered Results and CFD Generated Data

4.1 Introduction

As has been alluded to several times prior to this point, one of the main reasons that this project was undertaken was code validation support. In this section, we make comparisons between the data presented in sections 1 and 2 and numerically simulated CFD results. We state now that the CFD results that will be presented below *were not* generated at the University of Minnesota. The computational results were generated at Cleveland State University. Before we proceed we wish to give credit to the following people at Cleveland State: Mounir B. Ibrahim, Principal Investigator, Zhiguo Zhang, Graduate Research Assistant and Sundeep Kembhavi, Graduate Research Assistant.

4.2 Nomenclature

Symbol	Description	Units
Re	Reynolds Number	[dimensionless]
S	Disc Spacing	[m]
u	x-direction velocity component	[m/s]
$\| u \|$	Velocity magnitude ($\| u \| = \sqrt{u^2 + v^2}$)	[m/s]
Va	Valensi Number	[dimensionless]
θ	Crank Angle	[degrees]
ω	Rotational Frequency	[1/min]

4.3 Oscillatory Investigations

4.3.1 A Comparison of Experimental Flow Visualization Results to CFD Generated Data for the Case Re$_{max}$ = 7600, S = 127 mm, Va = 2300, ω = 30 rpm

A comparison of the flow field in the disc space was made for an entire cycle. Velocity vectors and streamlines are plotted in the computational results (see fig. 4.1). Figure 4.1 also shows the area where the comparison with flow visualization is made. The flow visualization technique was explained in section 2, section 2.5.1. We will not repeat that discussion but will comment that the flow visualization pictures are *ensemble-averaged* results. The comparison is presented in figures 4.2 through 4.25. Note that the comparisons are made every 15° of crank angle. In general, the code seems to very accurately capture both the sink flow from the back wall on the suction stroke ($0° < \theta < 180°$) and the wall jet on the blowing stroke $180° < \theta < 360°$. However, the recirculation zones are not described perfectly. For example, the code identifies eddies present in the flow. However, the locations of the eddies are not in accordance with the flow visualization results. In other words the computation is not accurately capturing the recirculation features of the flow. This is not surprising in the least when one considers that the computational pictures shown in this section were developed using no turbulence model. In other words, the computations were run without turbulence effects.

4.3.2 A Comparison of Experimentally Derived Velocity Data to CFD Generated Values for the Case $Re_{max} = 7600$, $S = 127$ mm, Va = 2300, $\omega = 30$ rpm

Presented in figures 4.26 through 4.33 are a comparison of CFD generated results vs. experimental data for oscillatory flow. Figures 4.26 through 4.29, focus on the crank angle $\theta = 246.5°$ and each figure steps out (in order of appearance) in radial dimension, $r/D = 0.473$, 0.591, 0.827, and 0.945. The reader may notice that these radial locations are not the same as those discussed in section 2. The explanation is that the data for this comparison were generated specifically for two papers by Adolfson et al.,[1] and Ibrahim et al.[2] However, outside of the differences in radial locations, the methods for data collection and processing were for all practical purposes identical to those discussed in section 2. Figure 4.26 presents a comparison between experimental data and CFD generated results using two turbulence closure models; a laminar model and a K-ω model. It seems that for this radial location ($r/D = 0.473$) the K-ω model does a better job of capturing the flow features near the target wall (small x/S). One can see that for $x/S > 0.3$, the models start to diverge from the experimental data. This is not entirely surprising in the sense that for larger x/S, the probe was (and hence the experimental data were) in a highly turbulent zone and the hot-wire measurements were not accurate. Thus, one should not expect a match in this area (for TI plots for this case, see Adolfson et al.[1]). Moving radially outward to $r/D = 0.591$, we see (fig. 4.27) that the laminar model does a better job of approximating the flow for $0 < x/S < 0.3$. Again, for $x/S > 0.3$, turbulence quantities are too high to expect good hot wire measurements. Figures 4.28 and 4.29 present comparisons at $r/D = 0.827$ and 0.945, respectively. There is little correlation between either of the models and the experimental data at these radial locations.

Figures 4.30 through 4.34 present results at a different crank angle, namely, $\theta = 293.5°$. The figures present results at the radial locations $r/D = 0.473$, 0.591, 0.827, and 0.945. Figures 4.30 and 4.31 show that the K-ω model accurately captures the velocity profile shapes but not the velocity magnitudes at the radial locations $r/D = 0.473$ and $r/D = 0.591$. Moving radially outward, figures 4.32 and 4.33 present comparisons between experiment and computation at the radial locations $r/D = 0.827$ and $r/D = 0.945$, respectively. At these radial locations, both models seems to capture profile shape reasonably well, but neither captures velocity magnitude.

One further thing to notice about the CFD results is that they were presented at the crank angles $\theta = 293.5°$ and $\theta = 246.5°$. This corresponds to the cases discussed in section 3 where the accelerating and decelerating flow cases for the same Reynolds number are discussed. The computational model captures the effects discussed in section 3 (fig. 4.26 vs. 4.30, fig. 4.27 vs. 4.31, fig. 4.28 vs. 4.32, and fig. 4.29 vs. 4.33).

4.4 Unidirectional Investigations

4.4.1 A Comparison of Experimental Flow Visualization Results to CFD Generated Data for the Case $Re = 7600$, $S = 127$ mm

In section 1, subheading 1.6.1 we presented steady unidirectional flow visualization results. We now compare these experimental flow visualization results to CFD generated streamlines. For the readers' information, this was originally presented by Ibrahim et al.[2] In figure 4.34 two models are presented; the leftmost figure plots streamlines as generated by a laminar flow model and the middle figure presents streamlines as generated with the same flow equation solver but using a K-ω turbulence closure model. Quoting Ibrahim et al.[2] "As the flow turns into the channel [disc space], a large-scale vortex is created between the two discs. The flow accelerates from the stagnation zone, with additional acceleration due to the vortex generated between the two discs. Near r/R = 1 [$r/D = 0.5$] (r is the radial location from the axis of symmetry and R is the tube radius) the flow starts to decelerate due to the increase in flow area. The CFD results using the K-ω model seem to predict these flow features very well. On the other hand, the laminar flow model shows only a thin flow layer near the right [target] disc and not enough mixing to spread the flow across the channel."

4.4.2 A Comparison of Experimentally Derived Velocity Data to CFD Generated Values for the Case Re = 7600, S = 127 mm

Here, we present a comparison between unidirectional, steady flow anemometry measurements and CFD generated predictions using laminar and turbulent K-ω closure models. In figure 4.35 results are presented at the radial location $r/D = 0.473$. One thing to note is that a CFD program will produce velocity components $\vec{u} = <u,v>$, whereas the hotwire only measures velocity normal to the wire, $\| u \| = <u,v> \circ <u,v> = (u^2 + v^2)^{1/2}$, in this case. Consequently, the magnitudes of the CFD generated velocity components had been computed and plotted in figure 4.35. Looking at figure 4.35, one sees that in the near-wall region (small x/S), the K-ω model compares well with experimental data. It is also apparent that for larger x/S, the laminar model is a closer approximation. Moving on to figure 4.36, a comparison is made at the radial location $r/D = 0.591$. It is apparent that for $x/S < 0.5$, neither model accurately captures velocity magnitude $\|u\|$. However, the laminar model quite accurately captures the profile *shape*. Regarding figures 4.37 and 4.38, the plots are somewhat different. In these two plots, the radial velocity component u, as computed by the CFD routine, is plotted and compared to the hot wire measured speed, $\|u\|$. The rational for this is that for the larger radial locations ($r/D = 0.827$ and $r/D = 0.945$, presented in figs. 4.37 and 4.38, respectively) the flow is mainly in the radial direction. This idea is supported by figure 1.9 of section 1. For larger radial locations, the flow is in one of two regimes; either it is in a wall jet that is moving radially outward, or it is in a separation bubble where hot wire derived measurements are not reliable. Regarding figure 4.37, it can be seen that the K-ω model does a good job of approximating the flow near $x/S = 0$. Once again, the laminar model does a decent job of simulating the profile shape, but misses in magnitude. Moving radially out to $r/D = 0.941$ (fig. 4.38), the same type of behavior is observed.

With regards to figures 4.35 through 4.38 we quote Ibrahim et al.[2] "Figure 3a [fig. 4.35] is for a radial location of $r = 0.1016$ m [$r/D = 0.473$]…Here, near the wall region, the K-ω model is in closer agreement with the experiment. The laminar flow is in a better agreement with the data a distance away from the wall. Figure 3b [fig. 4.36] shows a similar plot to the one shown in 3a but at $r = 0.127$m [$r/D = 0.591$]. The laminar flow seems to be in overall better agreement with the data than the K-ω model results. Figures 3c and d [figs. 4.37 and 4.38] show the CFD data for the radial velocity component v [u]. Here we see the predictions using the K-ω model are in closer agreement with the experiment. This is consistent with the discussion shown earlier for figure 2 [see the quote by Ibrahim et al. in section 4.5.1, i.e. the CFD generated streamlines vs. experimental flow viz.], where the vortex was predicted well using the K-ω model and more spread of the velocity fields is noticed at higher radial locations."

4.5 Conclusions

By and large, the CFD models do a very good job in approximating the bulk flow behavior within the test section under oscillatory and unidirectional flow conditions. The testament to this statement is the comparison with the flow visualization. However, in terms of accurately predicting velocities within the test section, the CFD routines fall short. It has been observed that under certain conditions, the laminar closure does a better job of capturing velocities, whereas, under different conditions, the K-ω model yields superior results. The moral is that a CFD routine needs to be developed that has an adaptive closure model with regard to laminar or turbulent flow. Another point to note is that neither model captures transition to turbulence. This is problematic in the sense that transition influences the entire flowfield (by influencing the location of the separation bubble on the back disc). Thus, until transition is either accurately captured via the CFD routine (or accurately modeled for), one cannot expect accurate comparisons between CFD results and experimental data.

4.6 Figures

In the figures that follow, you will see enlargements of CFD pictures generated by CSU. The enlargements were created from pictures like the one below.

The enlargements to follow are focused on this area.
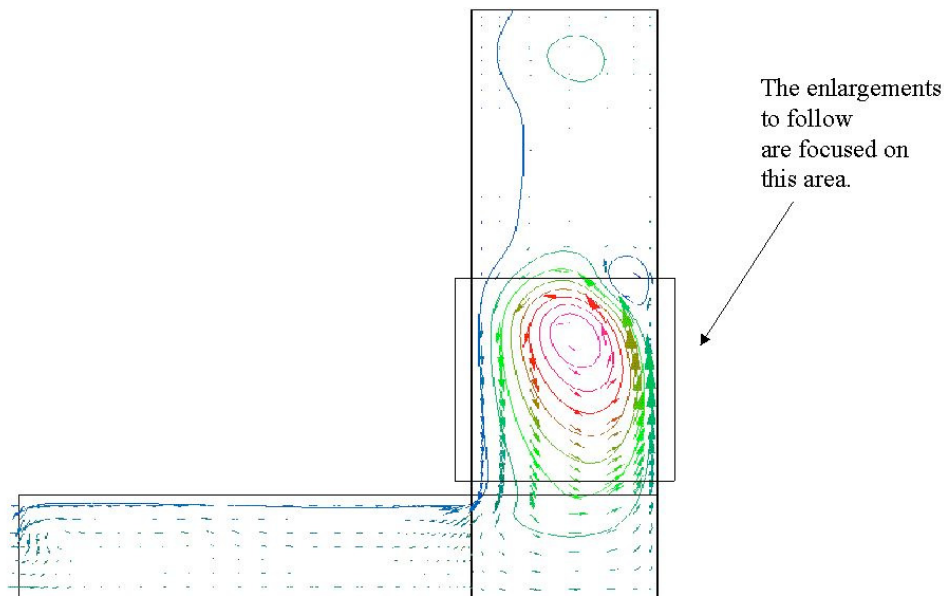
Figure 4.1.—A sample of the type of data that can be generated with the CFD-ACE program used at Cleveland State University. Notice that streamlines and velocity vectors are plotted.

$0° \leq \theta \leq 15°$

(intake)

Bulk Flow Direction

Centerline of Cylinder
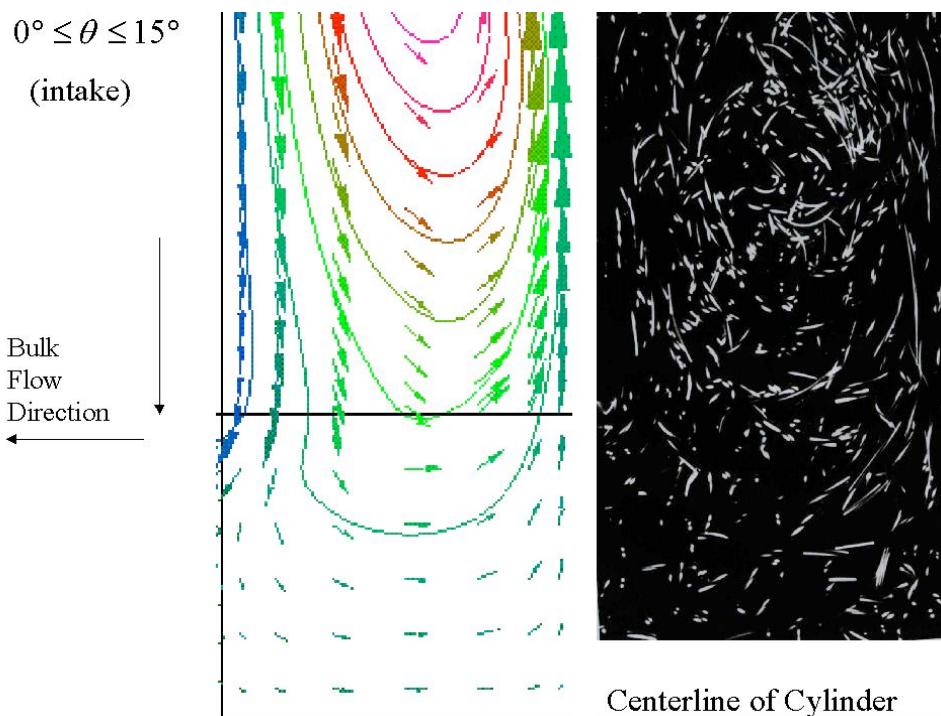
Figure 4.2.—CFD generated results vs. flow visualization data for the oscillatory case $Re_{max} = 7600$, $Va = 2300$, $S = 127$ mm during the crank angle range $0° < \theta < 15°$.
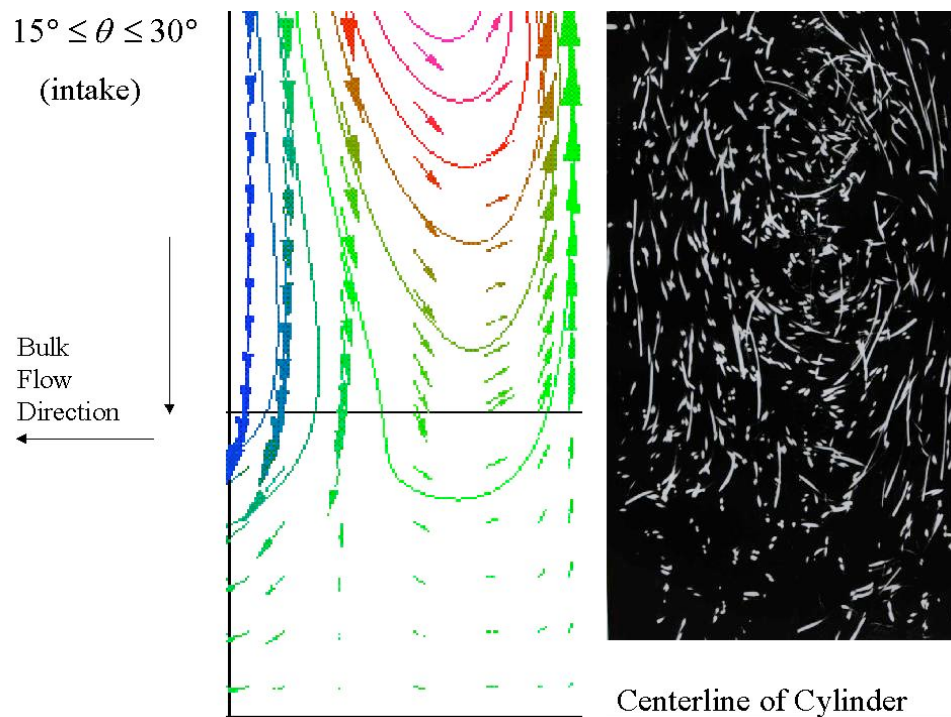
Figure 4.3.—CFD generated results vs. flow visualization data for the oscillatory case $Re_{max} = 7600$, $Va = 2300$, $S = 127$ mm during the crank angle range $15° < θ < 30°$.
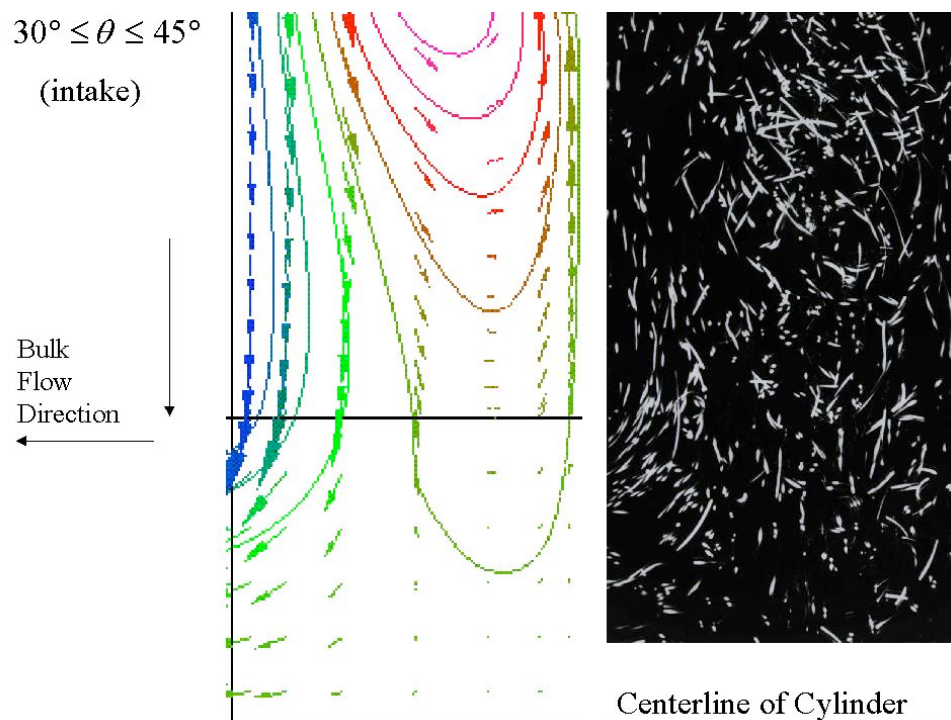
Figure 4.4.—CFD generated results vs. flow visualization data for the oscillatory case $Re_{max} = 7600$, $Va = 2300$, $S = 127$ mm during the crank angle range $30° < θ < 45°$.

$45° \leq \theta \leq 60°$

(intake)

Bulk
Flow
Direction

Centerline of Cylinder
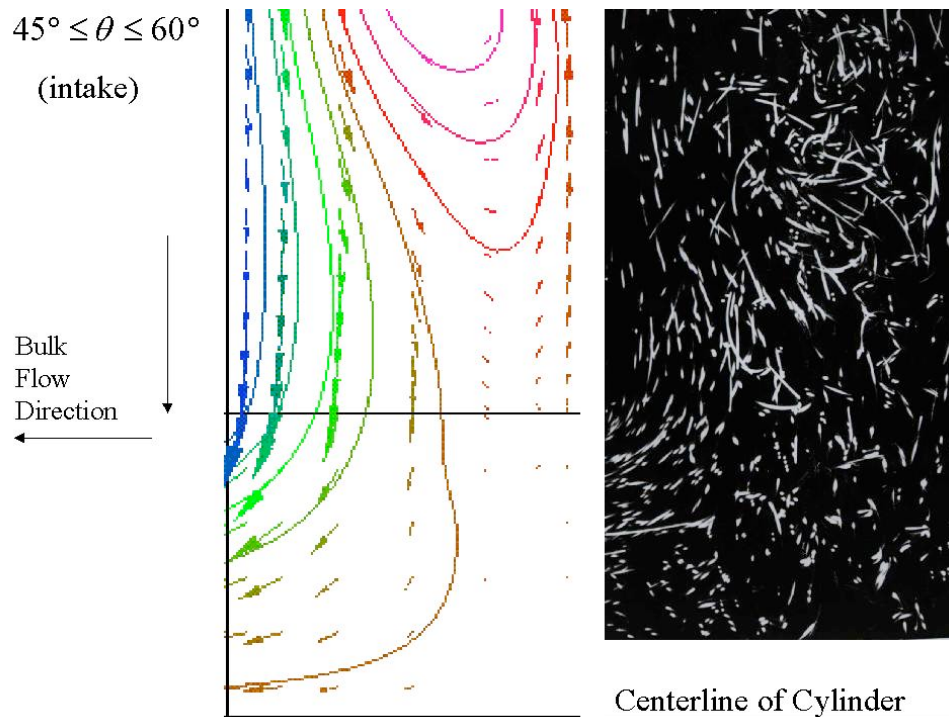
Figure 4.5.—CFD generated results vs. flow visualization data for the oscillatory case $Re_{max} = 7600$, $Va = 2300$, $S = 127$ mm during the crank angle range $45° < \theta < 60°$.

$60° \leq \theta \leq 75°$

(intake)

Bulk
Flow
Direction

Centerline of Cylinder
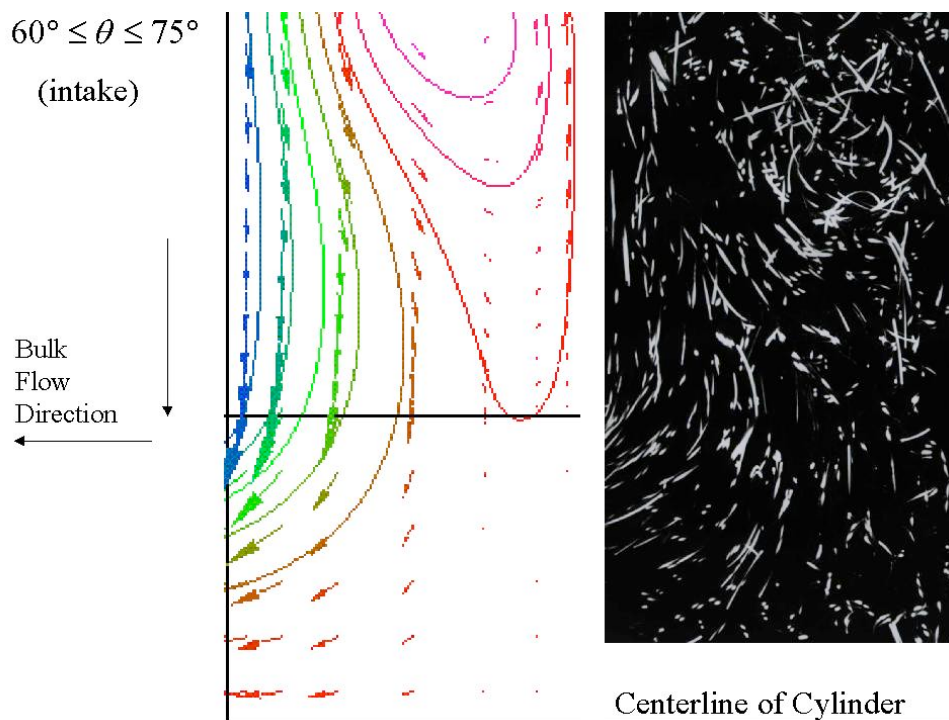
Figure 4.6.—CFD generated results vs. flow visualization data for the oscillatory case $Re_{max} = 7600$, $Va = 2300$, $S = 127$ mm during the crank angle range $60° < \theta < 75°$.
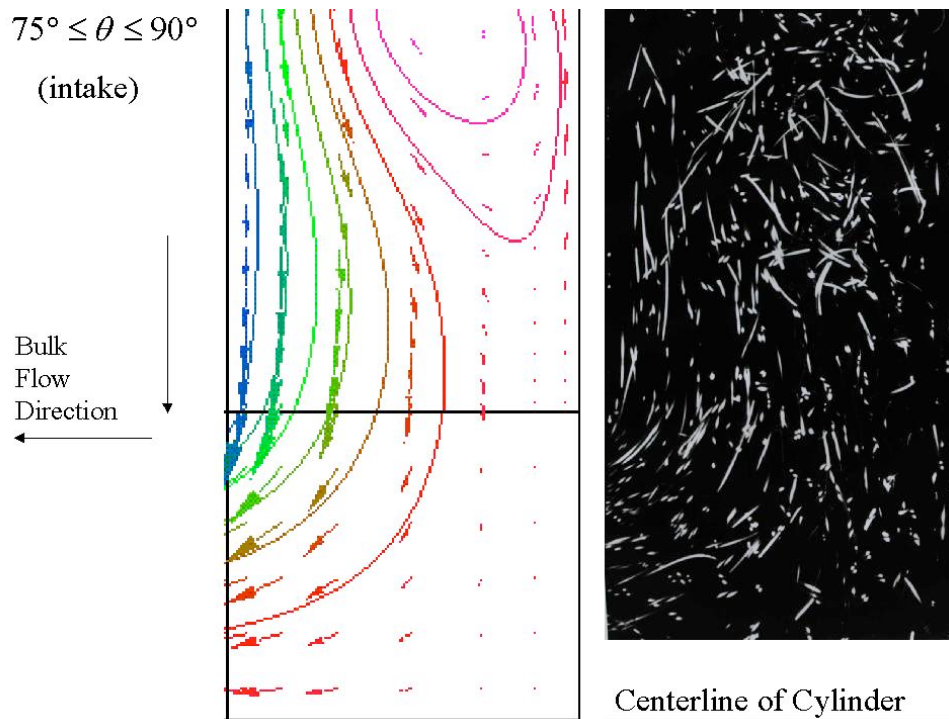
Figure 4.7.—CFD generated results vs. flow visualization data for the
oscillatory case $Re_{max} = 7600$, Va = 2300, $S = 127$ mm during the crank angle
range $75° < \theta < 90°$.
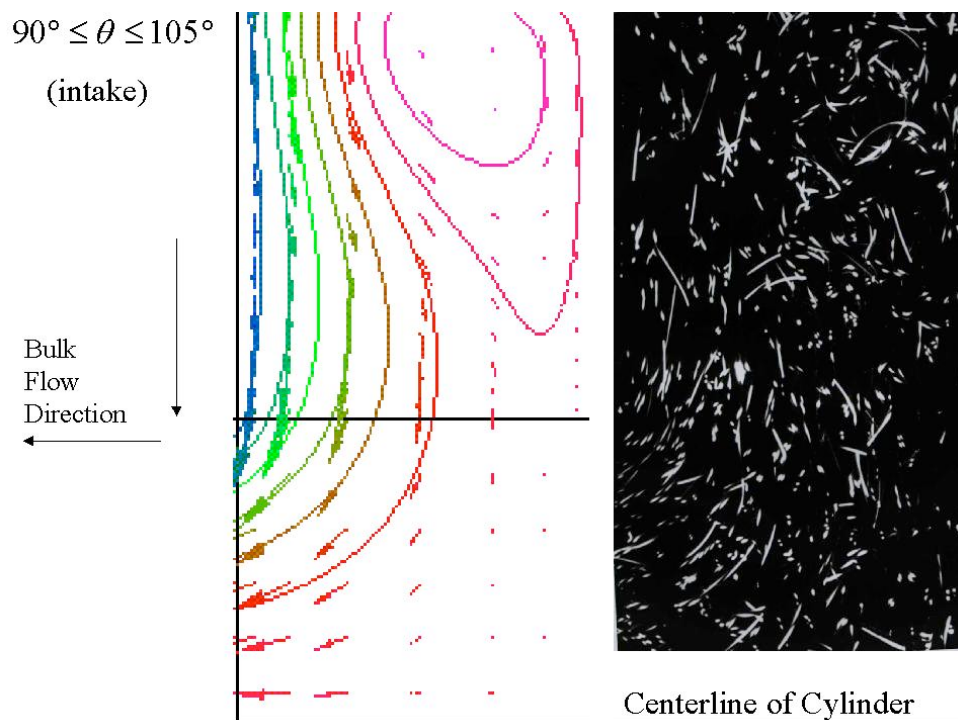
Figure 4.8.—CFD generated results vs. flow visualization data for the
oscillatory case $Re_{max} = 7600$, Va = 2300, $S = 127$ mm during the crank angle
range $90° < \theta < 105°$.

$105° \leq \theta \leq 120°$

(intake)

Bulk
Flow
Direction

Centerline of Cylinder
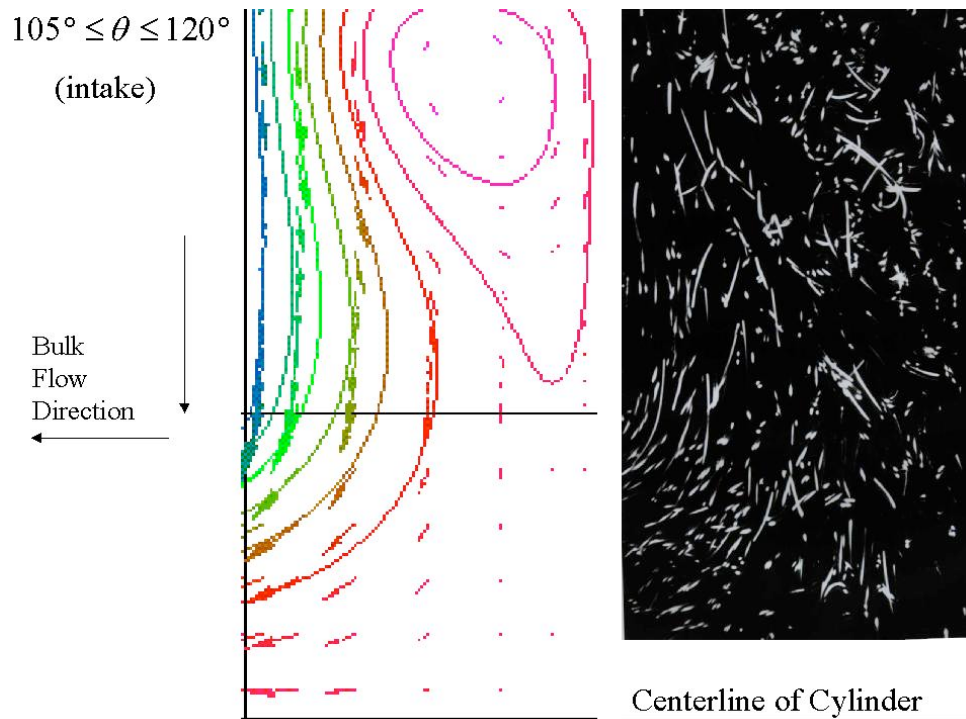
Figure 4.9.—CFD generated results vs. flow visualization data for the oscillatory case $Re_{max} = 7600$, $Va = 2300$, $S = 127$ mm during the crank angle range $105° < \theta < 120°$.

$120° \leq \theta \leq 135°$

(intake)

Bulk
Flow
Direction

Centerline of Cylinder
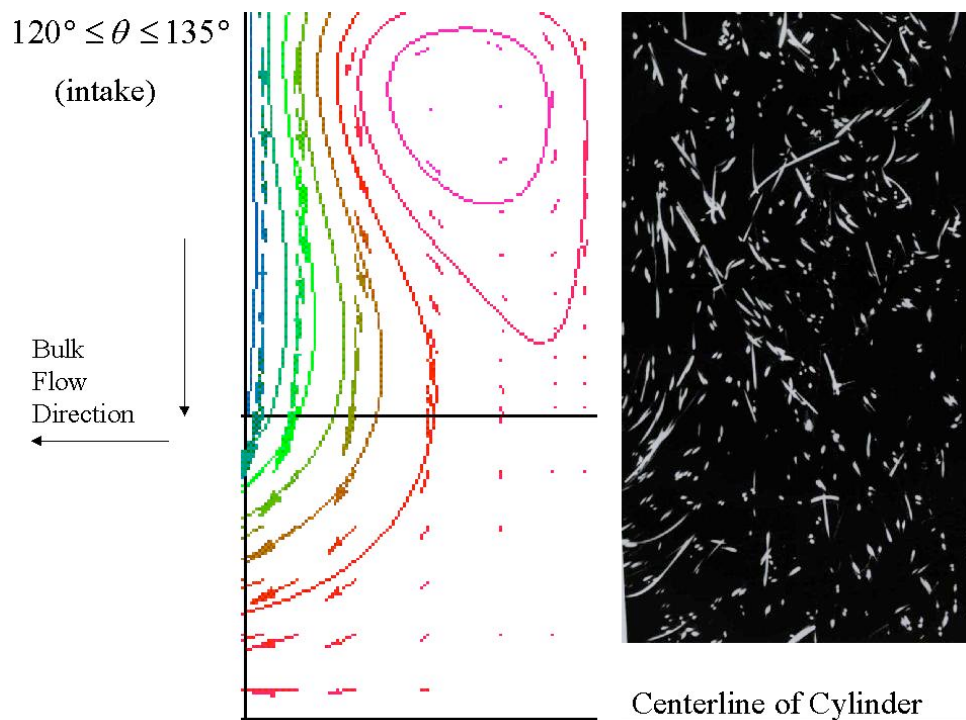
Figure 4.10.—CFD generated results vs. flow visualization data for the oscillatory case $Re_{max} = 7600$, $Va = 2300$, $S = 127$ mm during the crank angle range $120° < \theta < 135°$.

135° ≤ θ ≤ 150°

(intake)

Bulk
Flow
Direction

Centerline of Cylinder
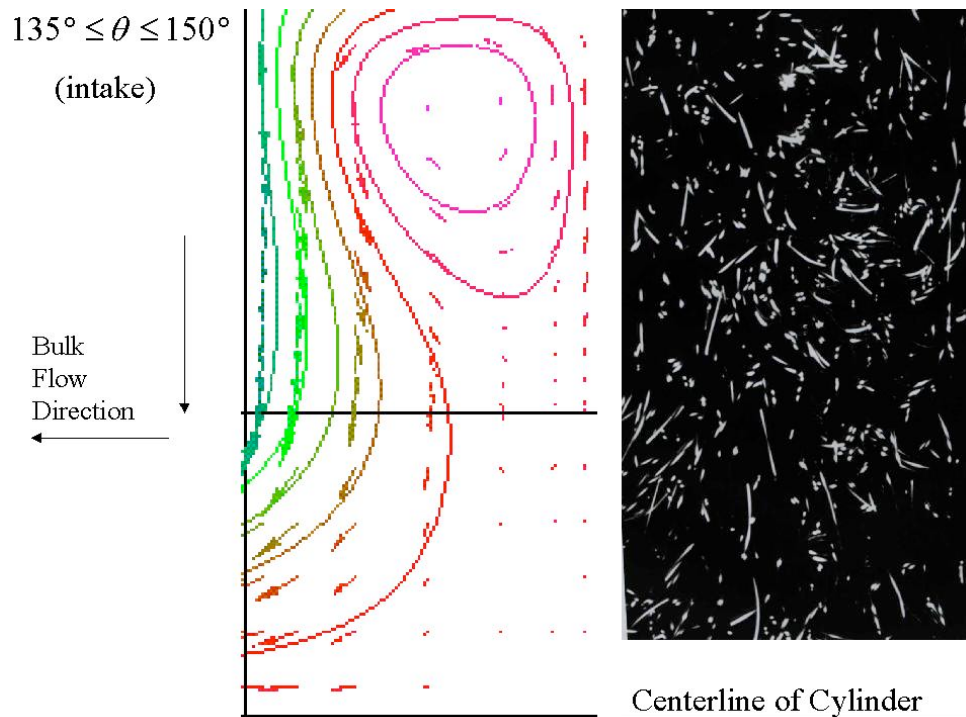
Figure 4.11.—CFD generated results vs. flow visualization data for the
oscillatory case $Re_{max} = 7600$, $Va = 2300$, $S = 127$ mm during the crank angle
range $135° < θ < 150°$.

150° ≤ θ ≤ 165°

(intake)

Bulk
Flow
Direction

Centerline of Cylinder
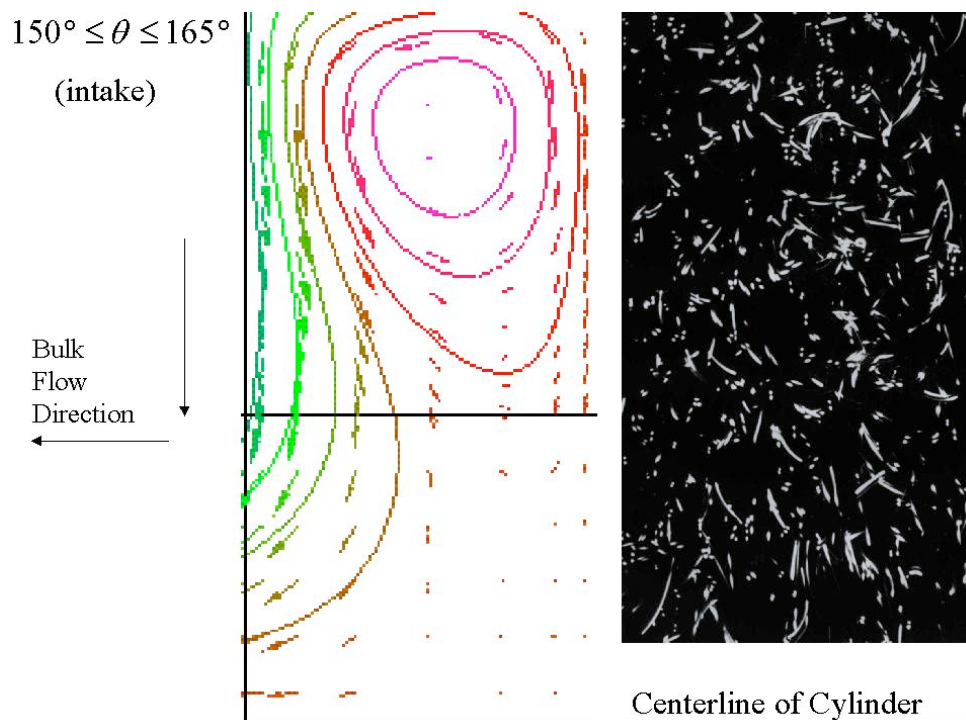
Figure 4.12.—CFD generated results vs. flow visualization data for the
oscillatory case $Re_{max} = 7600$, $Va = 2300$, $S = 127$ mm during the crank angle
range $150° < θ < 165°$.

$165° \leq \theta \leq 180°$

(intake)

Bulk
Flow
Direction

Centerline of Cylinder
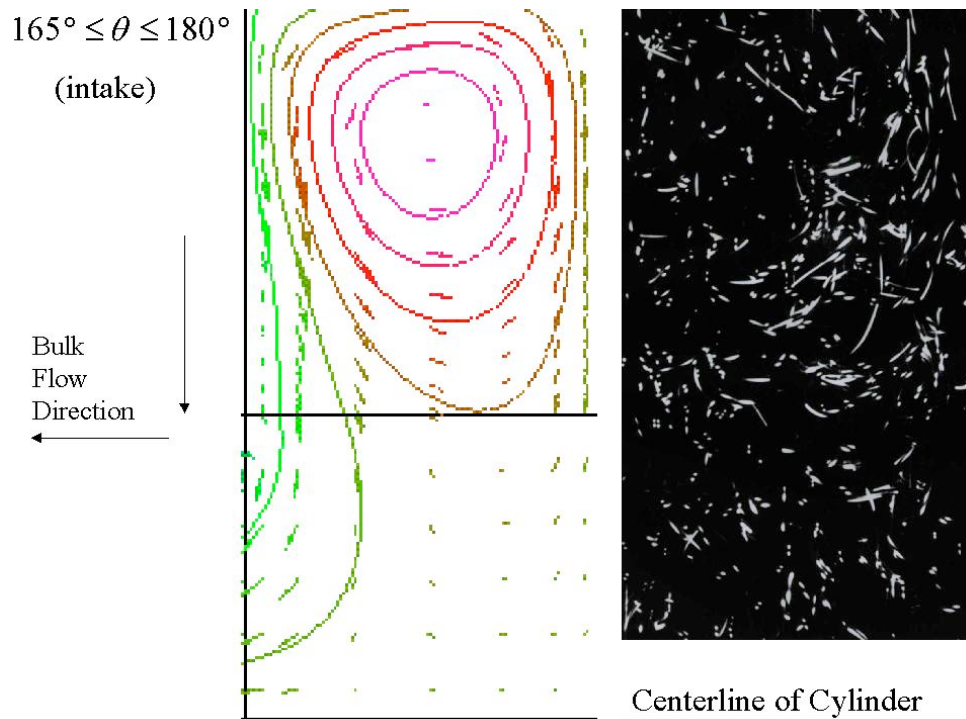
Figure 4.13.—CFD generated results vs. flow visualization data for the
oscillatory case $Re_{max} = 7600$, $Va = 2300$, $S = 127$ mm during the crank angle
range $165° < \theta < 180°$.

$180° \leq \theta \leq 195°$

(exhaust)

Bulk
Flow
Direction

Centerline of Cylinder
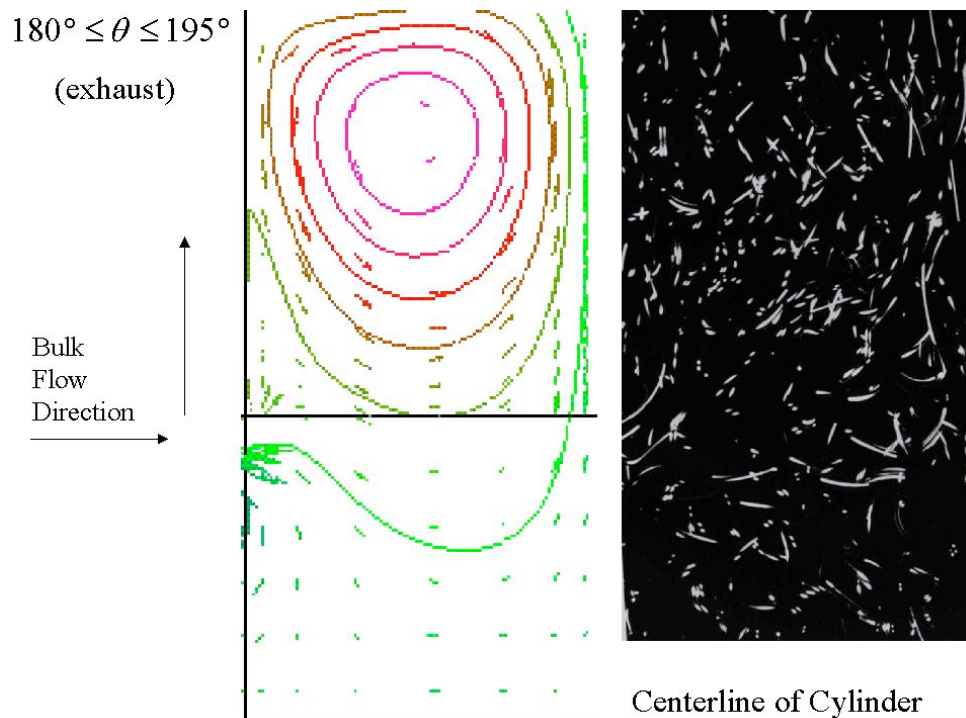
Figure 4.14.—CFD generated results vs. flow visualization data for the
oscillatory case $Re_{max} = 7600$, $Va = 2300$, $S = 127$ mm during the crank angle
range $180° < \theta < 195°$.

$195° \leq \theta \leq 210°$

(exhaust)

Bulk
Flow
Direction

Centerline of Cylinder
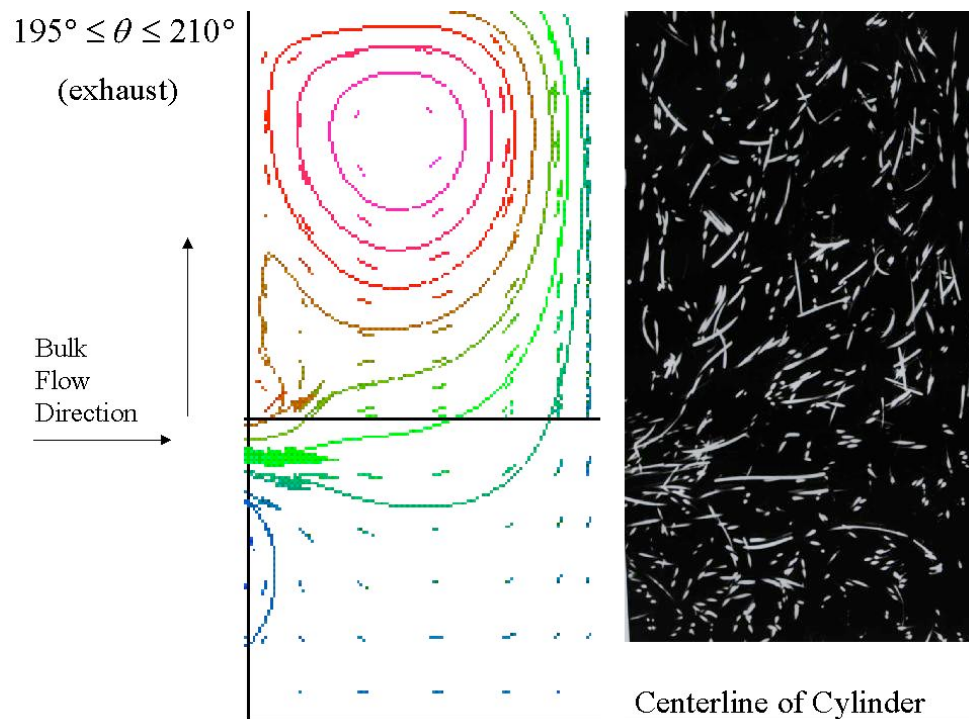
Figure 4.15.—CFD generated results vs. flow visualization data for the oscillatory case Re_{max} = 7600, Va = 2300, S = 127 mm during the crank angle range $195° < \theta < 210°$.

$210° \leq \theta \leq 225°$

(exhaust)

Bulk
Flow
Direction

Centerline of Cylinder
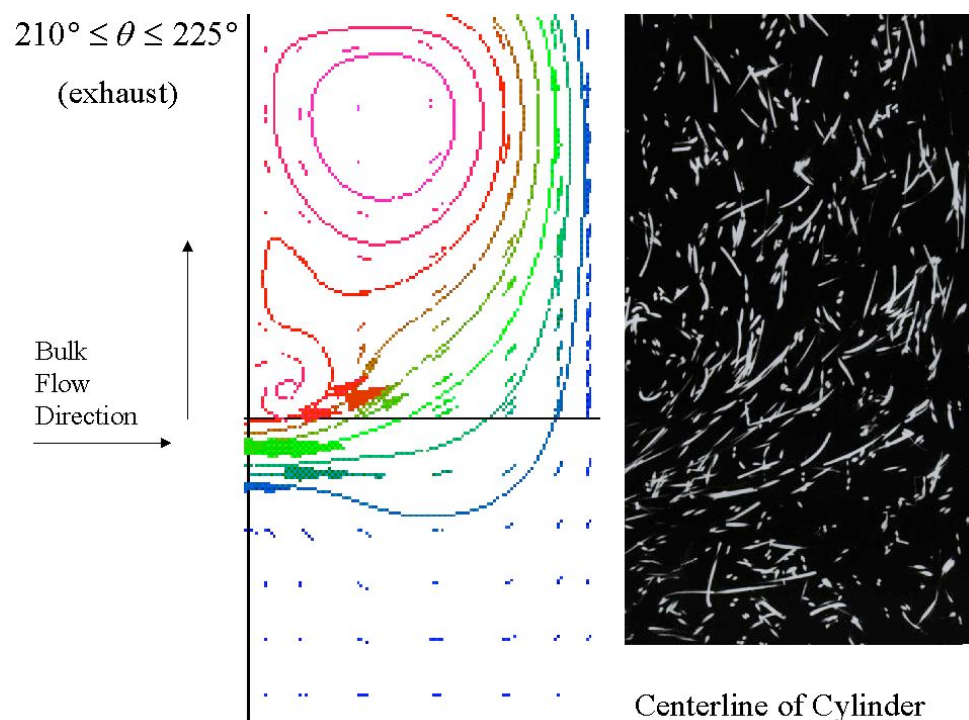
Figure 4.16.—CFD generated results vs. flow visualization data for the oscillatory case Re_{max} = 7600, Va = 2300, S = 127 mm during the crank angle range $210° < \theta < 225°$.
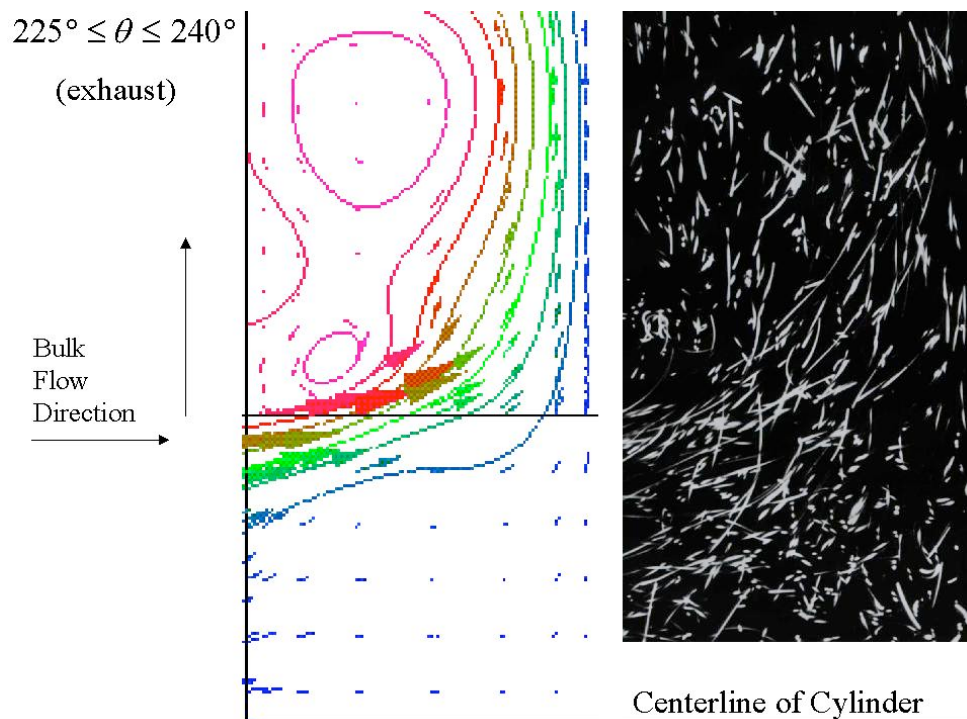
Figure 4.17.—CFD generated results vs. flow visualization data for the oscillatory case $Re_{max} = 7600$, $Va = 2300$, $S = 127$ mm during the crank angle range $225° < \theta < 240°$.
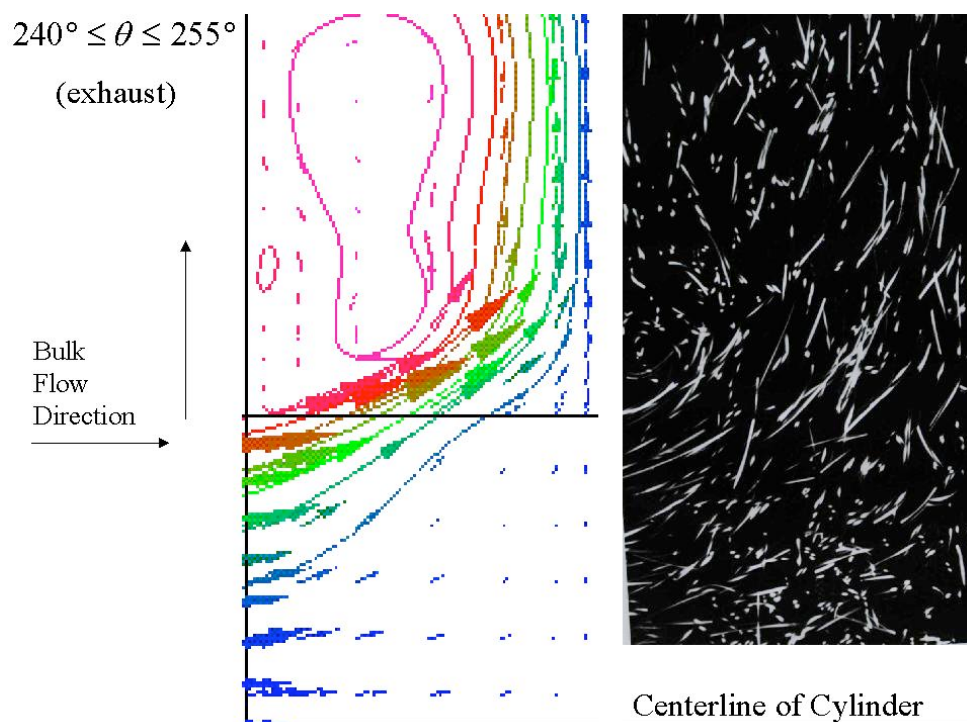
Figure 4.18.—CFD generated results vs. flow visualization data for the oscillatory case $Re_{max} = 7600$, $Va = 2300$, $S = 127$ mm during the crank angle range $240° < \theta < 255°$.

$255° \leq \theta \leq 270°$

(exhaust)

Bulk
Flow
Direction

Centerline of Cylinder
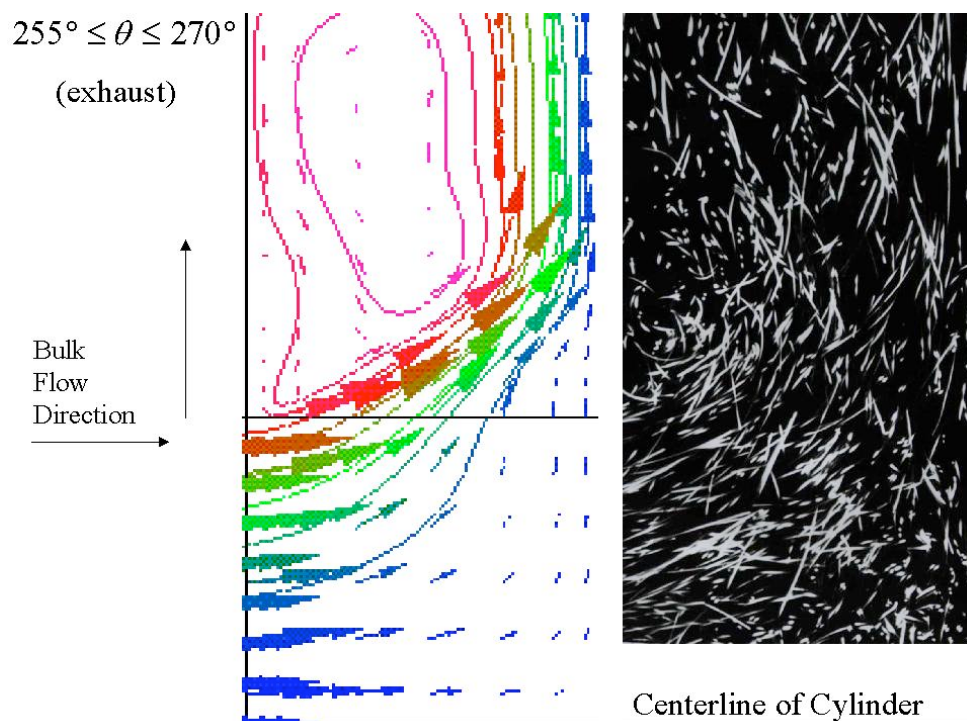
Figure 4.19.—CFD generated results vs. flow visualization data for the
oscillatory case $Re_{max} = 7600$, Va = 2300, $S = 127$ mm during the crank angle
range $255° < \theta < 270°$.

$270° \leq \theta \leq 285°$

(exhaust)

Bulk
Flow
Direction

Centerline of Cylinder
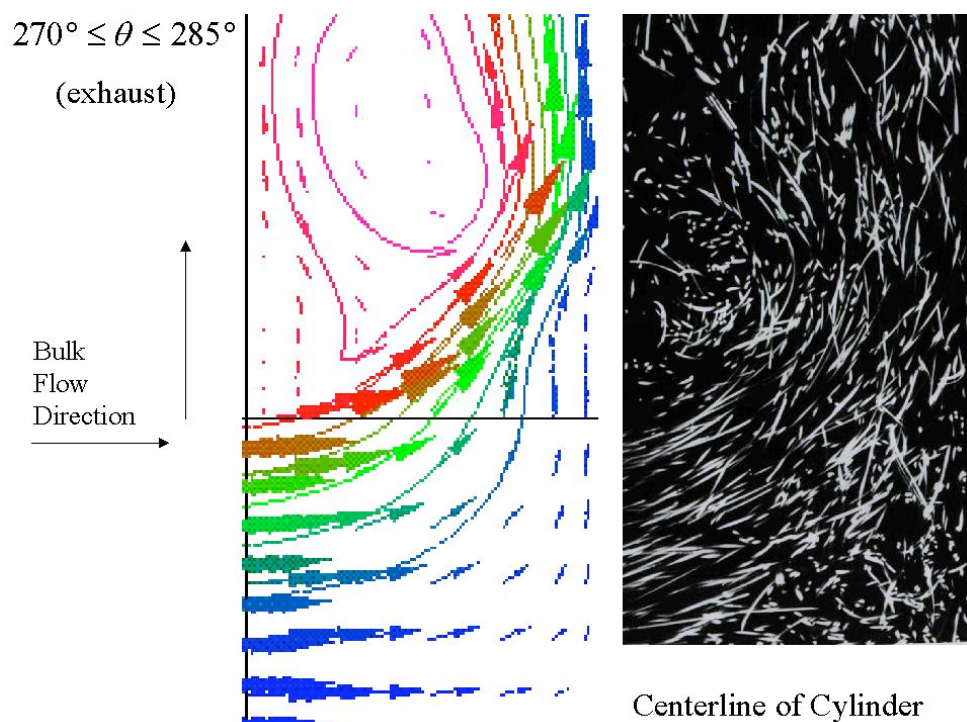
Figure 4.20.—CFD generated results vs. flow visualization data for the
oscillatory case $Re_{max} = 7600$, Va = 2300, $S = 127$ mm during the crank angle
range $270° < \theta < 285°$.

$285° \leq \theta \leq 300°$

(exhaust)

Bulk
Flow
Direction

Centerline of Cylinder
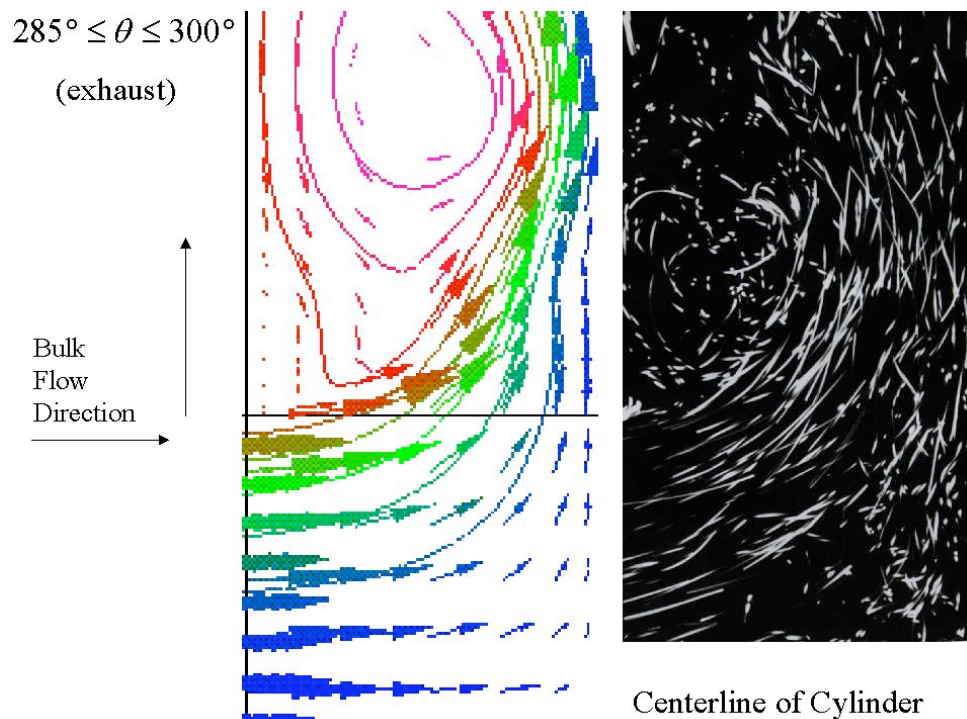
Figure 4.21.—CFD generated results vs. flow visualization data for the oscillatory case $Re_{max} = 7600$, $Va = 2300$, $S = 127$ mm during the crank angle range $285° < \theta < 300°$.

$300° \leq \theta \leq 315°$

(exhaust)

Bulk
Flow
Direction

Centerline of Cylinder
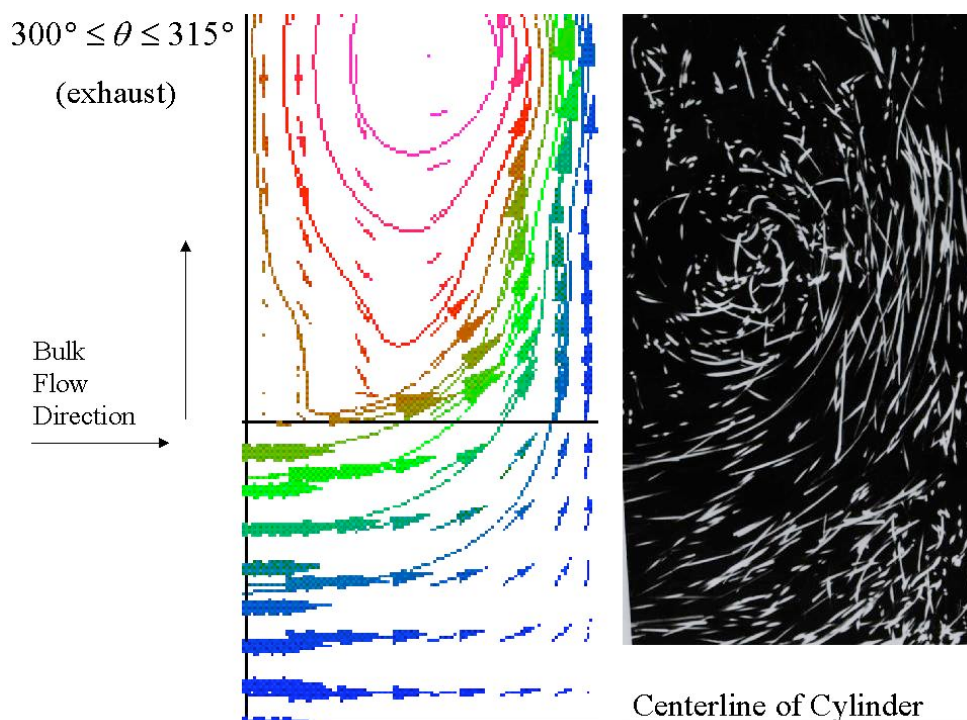
Figure 4.22.—CFD generated results vs. flow visualization data for the oscillatory case $Re_{max} = 7600$, $Va = 2300$, $S = 127$ mm during the crank angle range $300° < \theta < 315°$.

$315° \leq \theta \leq 330°$

(exhaust)

Bulk
Flow
Direction

Centerline of Cylinder
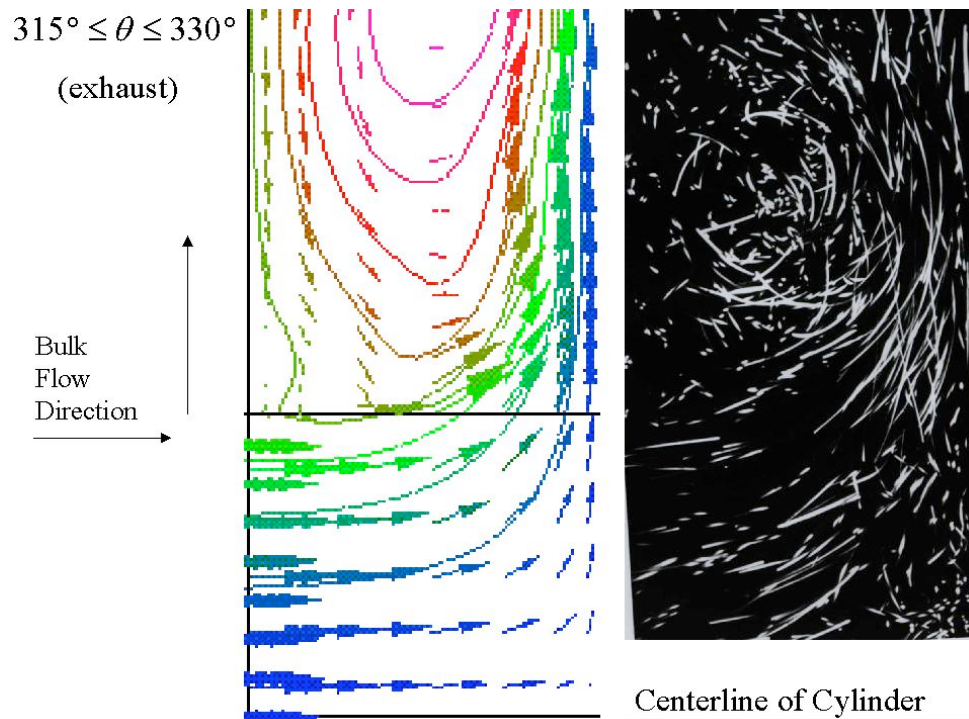
Figure 4.23.—CFD generated results vs. flow visualization data for the oscillatory case $Re_{max} = 7600$, $Va = 2300$, $S = 127$ mm during the crank angle range $315° < \theta < 330°$.

$330° \leq \theta \leq 345°$

(exhaust)

Bulk
Flow
Direction

Centerline of Cylinder
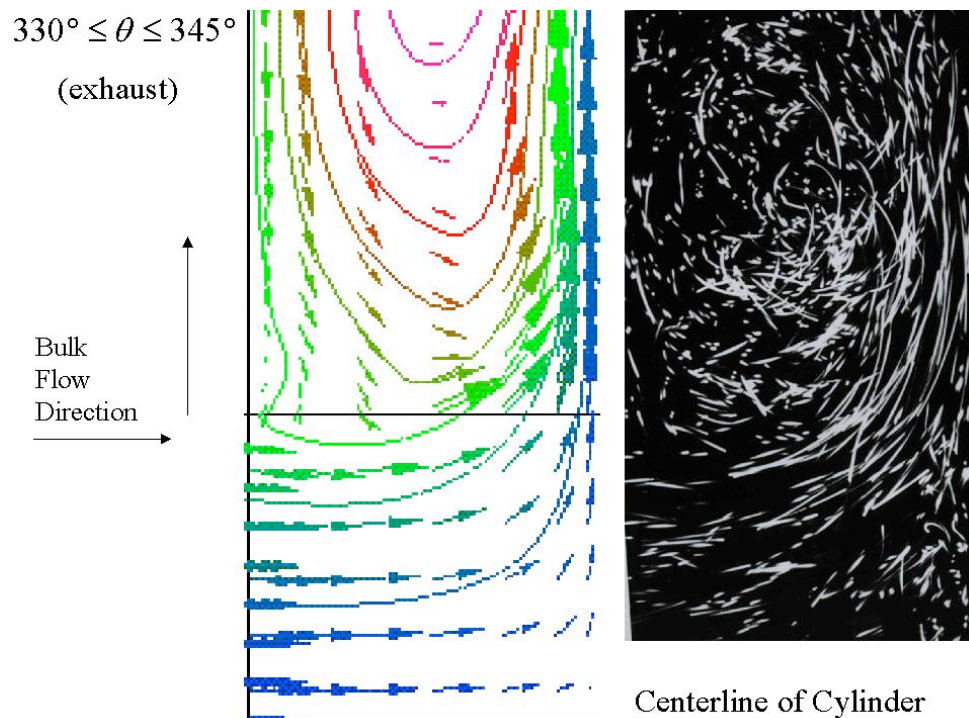
Figure 4.24.—CFD generated results vs. flow visualization data for the oscillatory case $Re_{max} = 7600$, $Va = 2300$, $S = 127$ mm during the crank angle range $330° < \theta < 345°$.

$345° \leq \theta \leq 360°$

(exhaust)

Bulk
Flow
Direction

Centerline of Cylinder
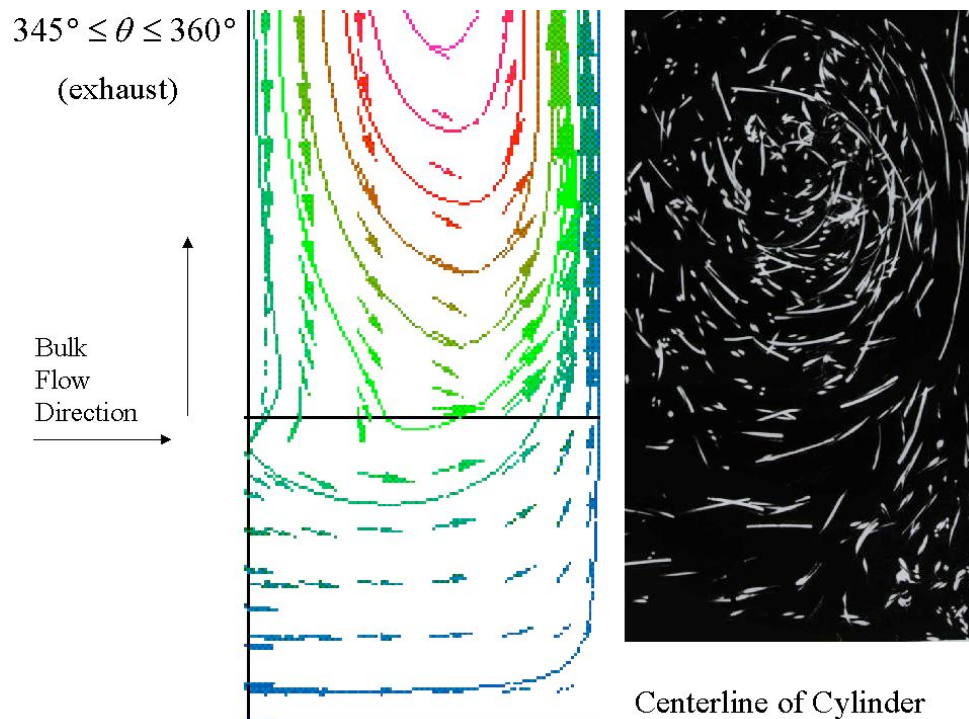
Figure 4.25.—CFD generated results vs. flow visualization data for the oscillatory case $Re_{max} = 7600$, $Va = 2300$, $S = 127$ mm during the crank angle range $345° < \theta < 360°$.
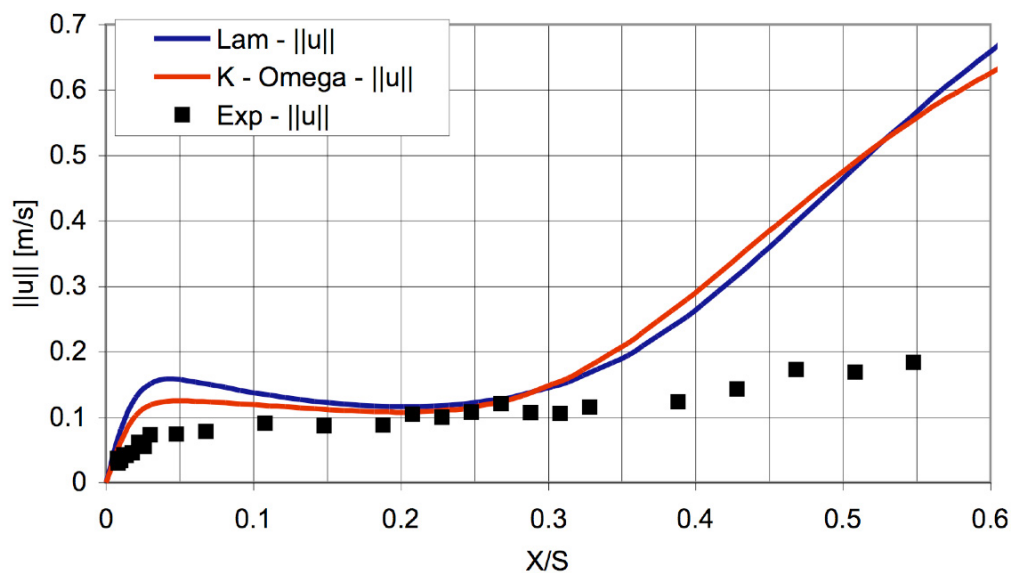
Figure 4.26.—CFD vs. experimental data under oscillatory flow when $\theta = 246.5°$ at the radial location $r/D = 0.473$.
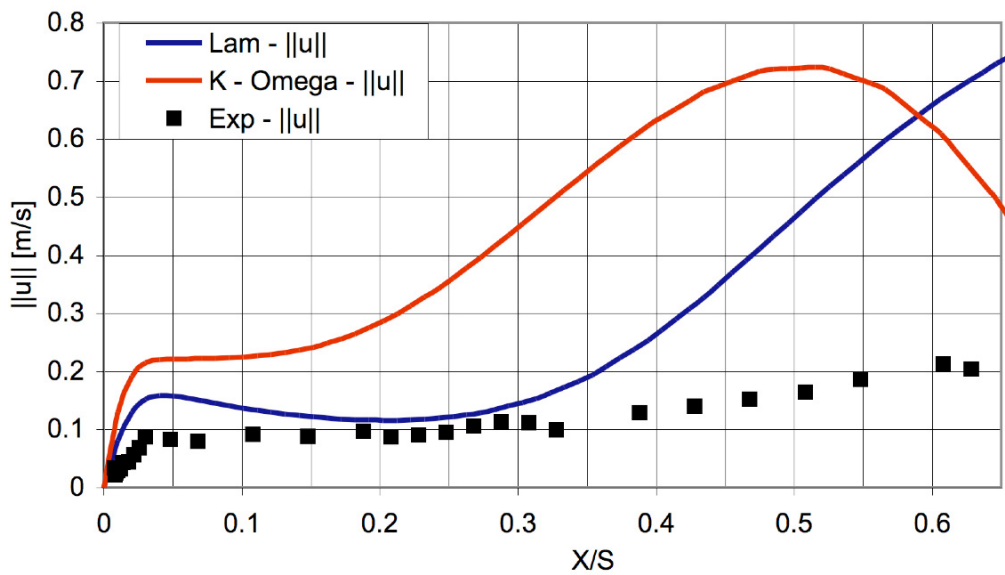
Figure 4.27.—CFD vs. experimental data under oscillatory flow when $\theta = 246.5°$ at the radial location $r/D = 0.591$.
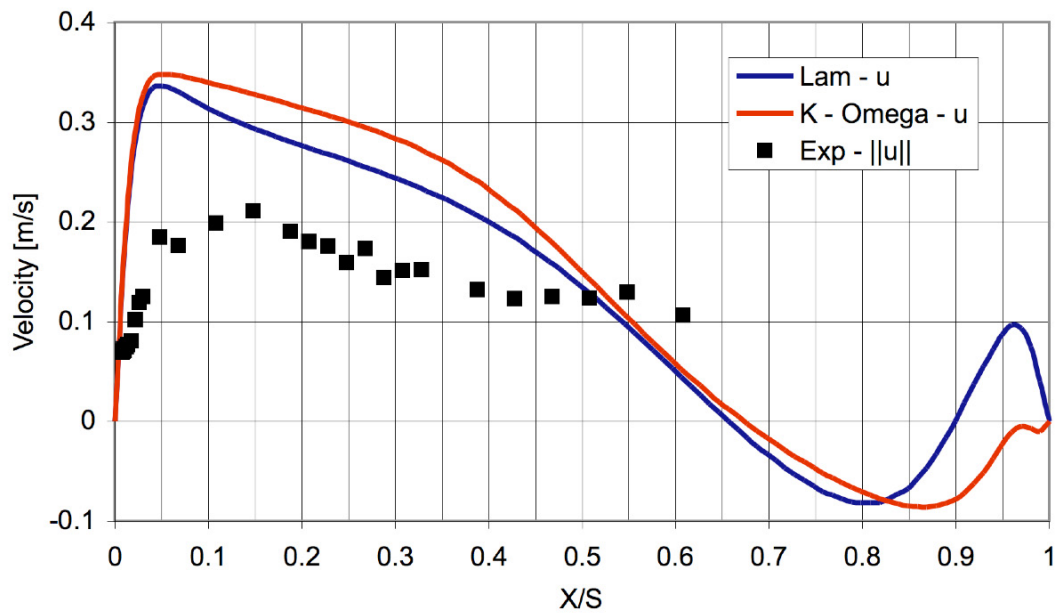
Figure 4.28.—CFD vs. experimental data under oscillatory flow when $\theta = 246.5°$ at the radial location $r/D = 0.827$.
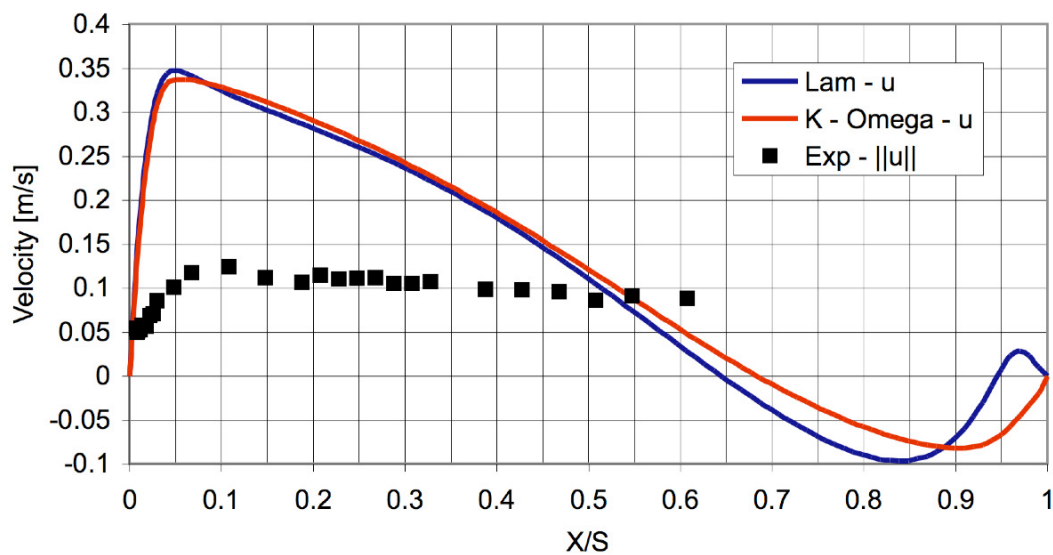
Figure 4.29.—CFD vs. experimental data under oscillatory flow when θ = 246.5° at the radial location r/D = 0.945.
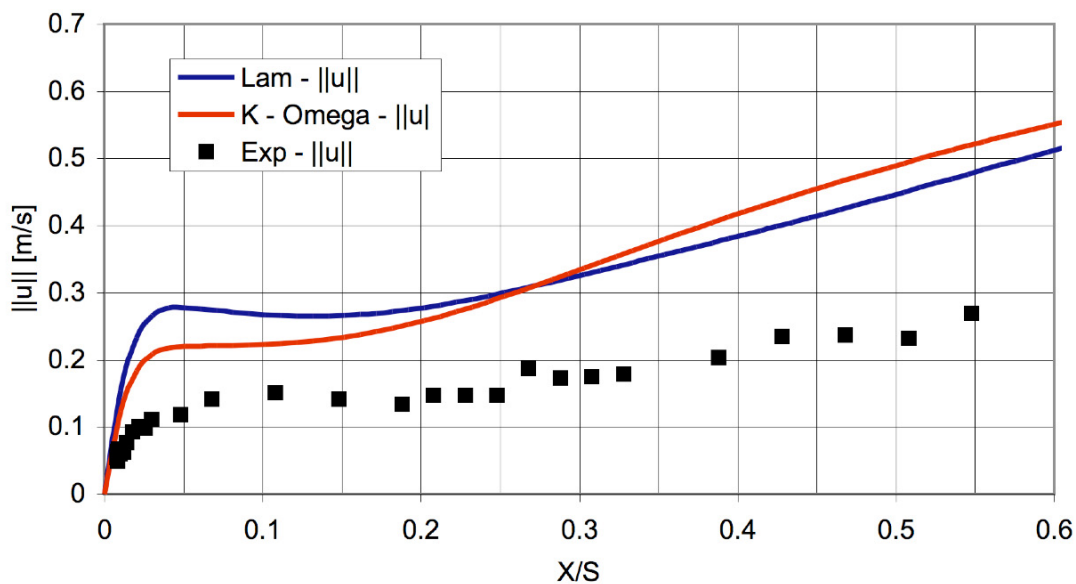
Figure 4.30.—CFD vs. experimental data under oscillatory flow when θ = 293.5° at the radial location r/D = 0.473.
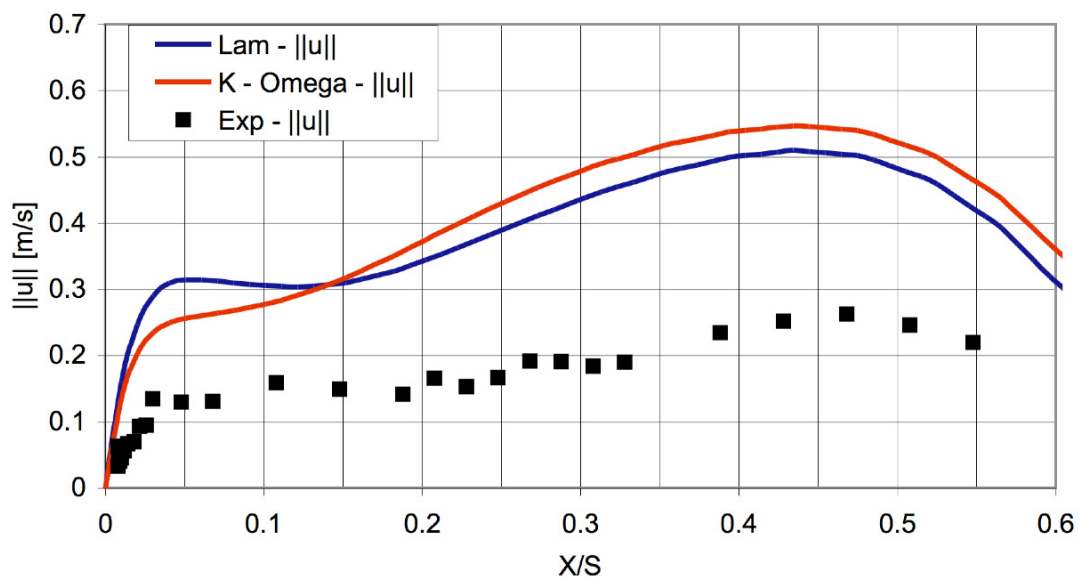
Figure 4.31.—CFD vs. experimental data under oscillatory flow when θ = 293.5° at the radial location r/D = 0.591.
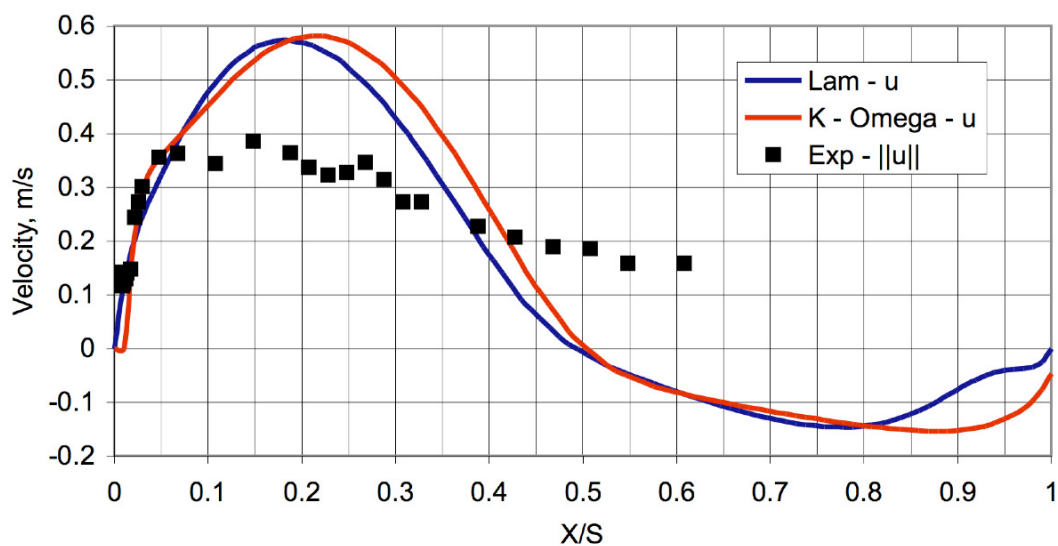
Figure 4.32.—CFD vs. experimental data under oscillatory flow when θ = 293.5° at the radial location r/D = 0.827.
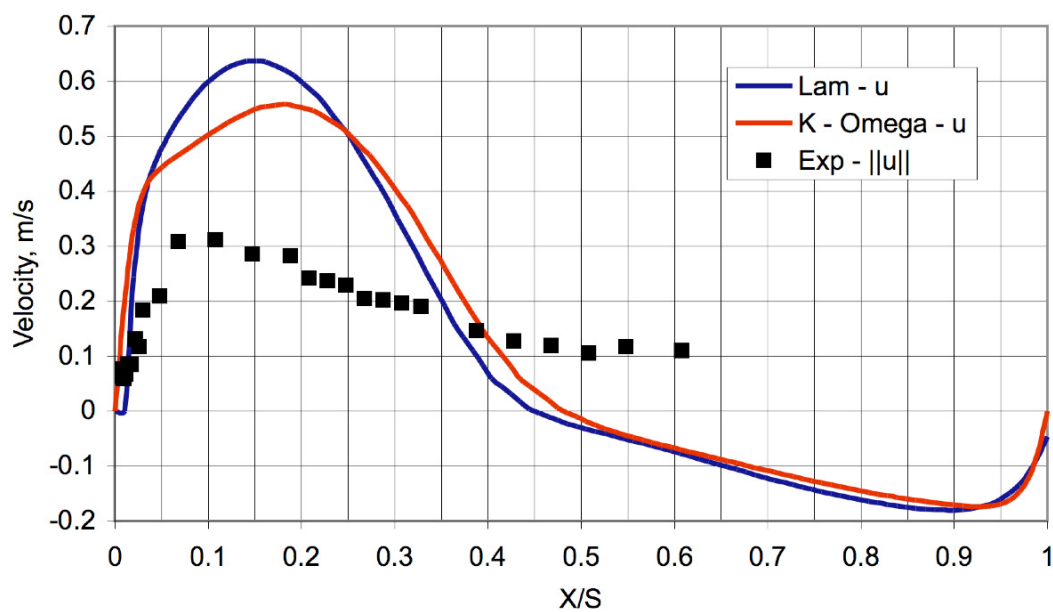
Figure 4.33.—CFD vs. experimental data under oscillatory flow when θ = 293.5° at the radial location $r/D = 0.945$.
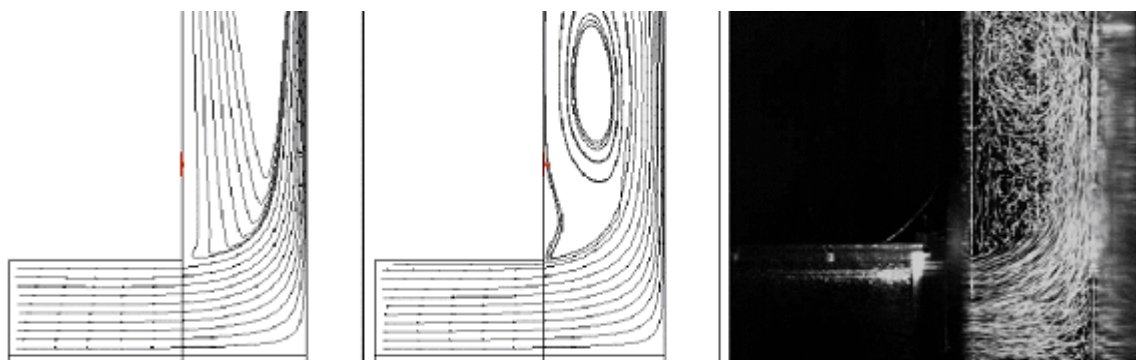
Figure 4.34.—A comparison between CFD generated streamlines and experimental flow visualization under unidirectional flow when Re = 7600, $S = 127$ mm.
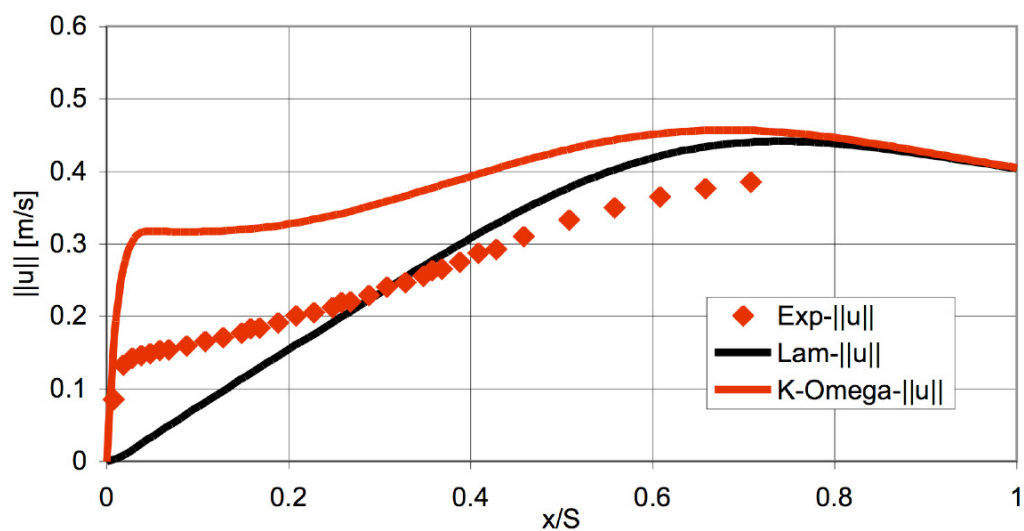
Figure 4.35.—CFD vs. experimental data for the case Re = 7600, S = 127 mm at the radial location r/D = 0.473.
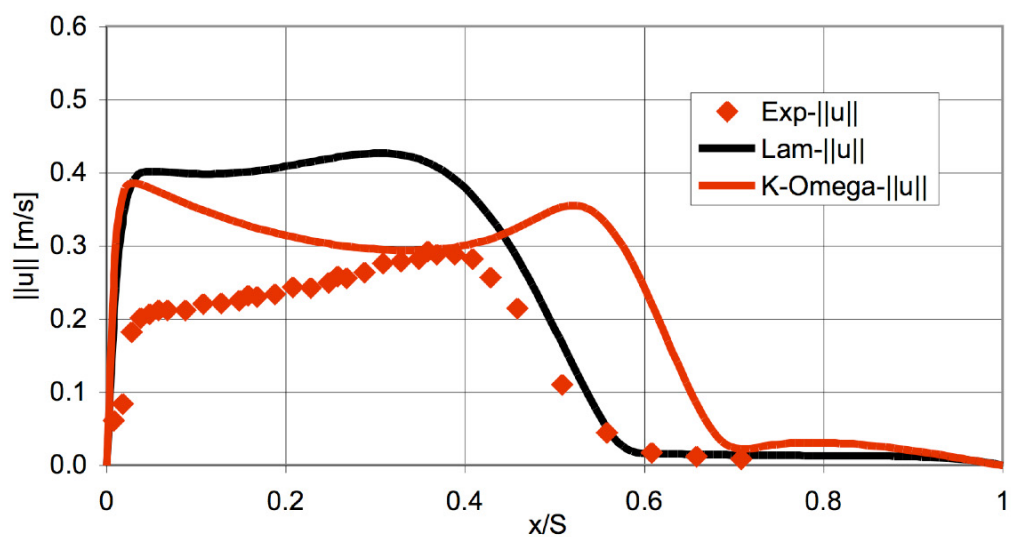
Figure 4.36.—CFD vs. experimental data for the case Re = 7600, S = 127 mm at the radial location r/D = 0.591.
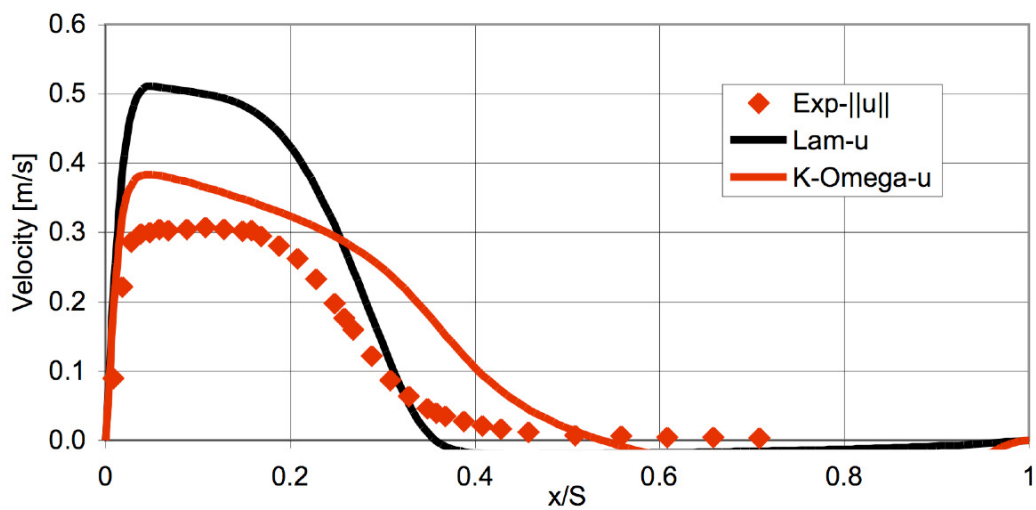
Figure 4.37.—CFD vs. experimental data for the case Re = 7600, S = 127 mm at the radial location r/D = 0.827.
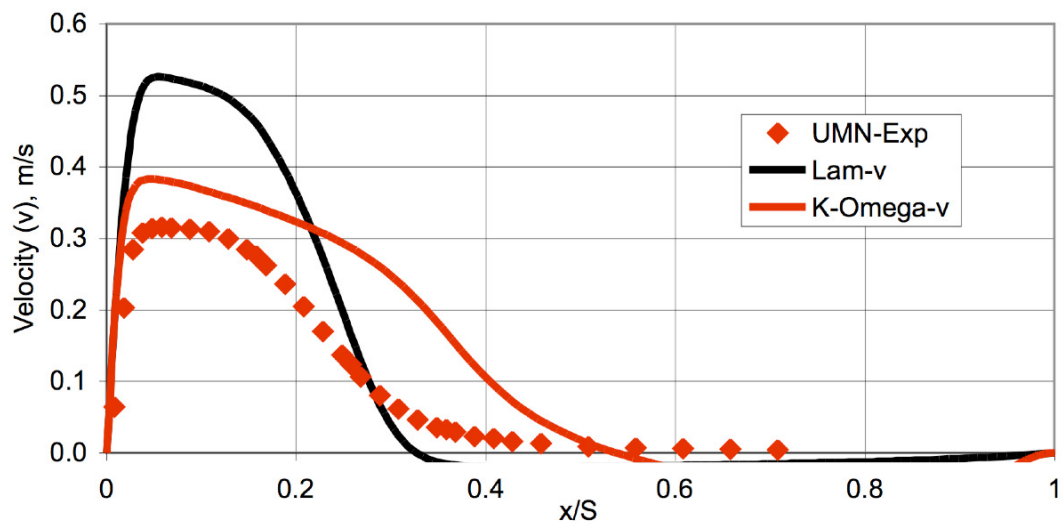
Figure 4.38.—CFD vs. experimental data for the case Re = 7600, S = 127 mm at the radial location r/D = 0.945.

4.7 References

1. Adolfson, D.A., Simon, T.W., Ibrahim, M.B., Gedeon, D., "Unsteady Fluid Dynamics Simulation of A Stirling Engine Heater Head," 2003 AIAA Conf. Proc.
2. Ibrahim, M.B., Zhang, Z., Kembhavi, S., Simon, T.W., Tew, R. Gedeon, D., "A Model of 90 Degree Turn Oscillatory Flow," 2003 AIAA Conf. Proc. Paper AIAA–2003–5935.

Appendix A—Hot Wire Anemometry Basics

A.1 Introduction

In this appendix, we attempt to familiarize the reader with a hot wire anemometer. To this end, we provide a picture of an anemometry system, list the quantities it measures, and explain how it works. Starting out simply, the hot wire anemometer is a device that can be used to measure the product of density and velocity (ρu). From this quantity, under certain assumptions (i.e., constant, or deterministically variable density and velocity) the velocity, temperature, or density of a flowing fluid can be measured.

Before we proceed, we present a picture of a hot wire anemometer system in figure A.1. Shown in the figure is an anemometer, a probe cable, a probe support and a probe. The general idea is that the user exposes the probe to a flow. The probe then measures the velocity of the fluid around it. The actual mechanics of the measurement will be discussed shortly, but before that, we introduce one more figure, figure A.2. This figure shows a typical hot-wire probe. The main features of the probe are a wire, support prongs, a probe body, and leads. The main object of concern is the wire. It is generally made of platinum, tungsten or a platinum-tungsten alloy. The diameter of the wire is generally on the order of 5 μm.

A.2 Nomenclature

Symbol	Description	Units
D_w	Wire diameter	$[m]$
e	Voltage differential across a Wheatstone bridge	$[V]$
h	Average convective heat transfer coefficient	$\left[W/m^2 \circ K\right]$
i	Electrical current	$[A]$
k	Fluid thermal conductivity	$[W/m \circ K]$
L	Wire length	$[m]$
Nu	Average Nusselt number	$[\ ]$
Pr	Prandtl number	$[\ ]$
q'	Heat transfer per unit length	$[W/m]$
R	Electrical resistance	$[\Omega]$
Re_w	Wire diameter Reynolds number	$[\ ]$
T_{amb}	Ambient temperature	$[K]$
T_w	Wire temperature	$[K]$
V	Measured voltage	$[V]$
$\dot{x}$	Velocity magnitude (speed)	$[m/s]$
η	Variable resistance	$[\Omega]$
ω	Total probe resistance	$[\Omega]$

A.3 Basic Anemometer Circuitry

For the present discussion, the main thing to keep in mind is that the wire is a *temperature sensitive resistive element*. In other words, given a wire temperature, there is an associated resistance and vice versa. This concept will be of use shortly in the discussion of operating resistance; namely, in specifying an operating resistance, an operating temperature is implied.

Shown in figure A.3 is a Wheatstone bridge. The Wheatstone bridge is the fundamental circuit in an anemometer. This circuit is said to be in balance if there is a net flow of current and:

$$e = 0 \ V.$$

For the above equation to be satisfied, it must be the case that (referring to fig. A1.3):

$$\frac{R}{\omega} = \frac{R}{\eta}.$$

In the case of a hot wire anemometer, we let η be a variable resistor and let ω be the "operating resistance" of the probe. "The probe [operating] resistance is a composite of the resistance of the sensor [at the operating temperature] plus the resistance of the support needles, probe body, leads and probe cable" (Lomas,[3] p. 85).

If the probe resistance and the operating resistance are equal, then the bridge is in balance. Exposing a probe to a flow will cause a change in heat transfer via convection (to be explained shortly). As a result, its temperature and, hence, its resistance will change. The net result is that:

$$e \neq 0 \ V.$$

This voltage information is supplied to a control system (a series of amplifiers that are not shown in the figure) which varies the current through the probe. The change in current induces a change in resistive dissipation. This raises or lowers the heating rate of the probe and returns it to the specified operating resistance; i.e., the bridge is in balance again.

A.4 Physical Principles of an Anemometer Probe

A thermal anemometer measures the cooling rate of a small cylinder in cross flow. From the measured cooling rate, a speed associated with the flowing fluid can be deduced. We set forth to explain the physics behind an anemometer probe in a somewhat heuristic manner.[1]

As a simple model, imagine an infinitely long cylinder. Imagine further that there is a one dimensional, constant property, flowing fluid with its velocity vector normal to the cylinder. We allow the fluid velocity to vary. Now, suppose that we can somehow heat the cylinder such that its temperature is uniform in space and time. Given these assumptions, we begin a "simple" hot-wire analysis. For clarity, the situation is presented pictorially in figure A.4.

We begin by focusing on how thermal energy is lost from the cylinder. The most fundamental starting point is Newton's law of cooling:

$$q' = \pi D_w h (T_w - T_{amb}).$$

We introduce the fluid thermal conductivity and rearrange the above equation to yield:

$$\frac{q'}{k\pi(T_w - T_{amb})} = \frac{hD_w}{k} = Nu.$$

---

[1] When we say heuristic, we are seeking to give the reader a quick and dirty derivation of King's law that is easy to grasp. We have not followed "conventional" derivations to the letter of the law; instead we have made a tractable physical argument. For a more conventional derivation (which is beyond the scope of this work) the reader is referred to Lomas[3] (pp. 55–72).

Nusselt numbers are tabulated in a wide variety of basic texts on heat transfer. To find a correlating function, we cite Incropera and De Witt.[1] (p. 344):

$$\frac{q'}{k\pi(T_w - T_{amb})} = Nu = C\,\mathrm{Re}_w^m\,\mathrm{Pr}^{1/3}.$$

where C and m are given for various Re_w ranges.

Solving for the heat transfer from the cylinder per unit length, we have:

$$q' = Ck\pi(T_w - T_{amb})\,\mathrm{Re}_w^m\,\mathrm{Pr}^{1/3}.$$

We now turn our attention to the heating of the cylinder. In the case of a hot-wire anemometer, the cylinder (wire) is heated electrically. Recall that the resistance of the wire is a function of temperature; thus, if temperature is constant (which we demanded initially) then the resistance of the cylinder is constant. We now state Ohm's law:

$$V = iR,$$

from which we write the heat generation per unit length as:

$$q' = \frac{V^2}{RL}.$$

We have the necessary components to relate heat transfer by convection to heat generated by resistive dissipation, viz.

$$\frac{V^2}{RL} = Ck\pi(T_w - T_{amb})\,\mathrm{Re}_w^m\,\mathrm{Pr}^{1/3}.$$

Grouping all constants and rewriting we have:

$$V^2 = \overline{C}\dot{x}^m.$$

Where C and m are functions of the Reynolds and Prandtl numbers.

The above relation suggests that at zero velocity, the voltage output from the hot wire should be identically zero. This is invariantly not the case. At zero fluid velocity, there is *always* a non-zero anemometer voltage output. To explain this phenomenon, we turn to physical arguments.

The basic concept is simple, if we were to have zero voltage at zero flow, then there would be no loss of thermal energy from the wire. Since the wire is less than perfectly isolated from its surroundings, there is a loss of energy. First of all, the hot wire is not of infinite extent; at each end there is a support prong. At these prongs, there will be a conduction loss (i.e., heat will flow from the wire to the prongs). Also, it is the case that most fluids become less dense as their temperature increases (water near the freezing point, being and exception). In any case, the wire is hot and the fluid around it is cool. The wire heats the fluid around it (via convection) and the fluid rises away from the wire. The effect is that the wire is continuously losing thermal energy via 'natural convection.' A third form of energy loss is due to radiant effects. A typical hot wire operating temperature is 250 °C. The effects of radiation at these low temperatures may be small, but not zero.

The point is that at zero flow there is still heat transfer, and, hence, a current or voltage is needed to balance the Wheatstone bridge. This suggests that we may improve our above-derived result by adding a correction to it, namely:

$$V^2 = A + C\dot{x}^m$$

where *A*, *C*, and *m* are now *unknown* and considered to be constant. Thus, forms of heat transport other than forced convection are allowed and assumed to have an effect that is independent of velocity. Observe that at very low velocities, the main contribution to the voltage signal will come from these alternative modes.

Replacing *m* with 0.5 yields a well-known result called King's law (King[2]). If *m* is taken as a given constant (not necessarily 0.5), the above form is very useful. It allows one to (theoretically) take two voltage signals, calibrate the anemometer to two corresponding velocity points and with no further data required, plot a slope-intercept line that describes a wide range of voltage-velocity points. When we say theoretically, we suggest that one must know the value of *m* to carry out a 2-point calibration.

So, given a data set, how do we determine the value of *m*? Generally speaking, given a velocity-voltage data set, the procedure is to guess a value of *m*, plot V^2 vs. $\dot{x}^m$, fit a line to the result and check how well the linear fit approximates the data points. This process is carried out iteratively until a best fit is found. It turns out that the optimum value of *m* is 0.435 for the probes of the present study. As a benefit, when the best linear fit is found, both *A* and *C* are determined as well – this whole process is called calibration, which is the subject of appendix B.

A.5 Figures
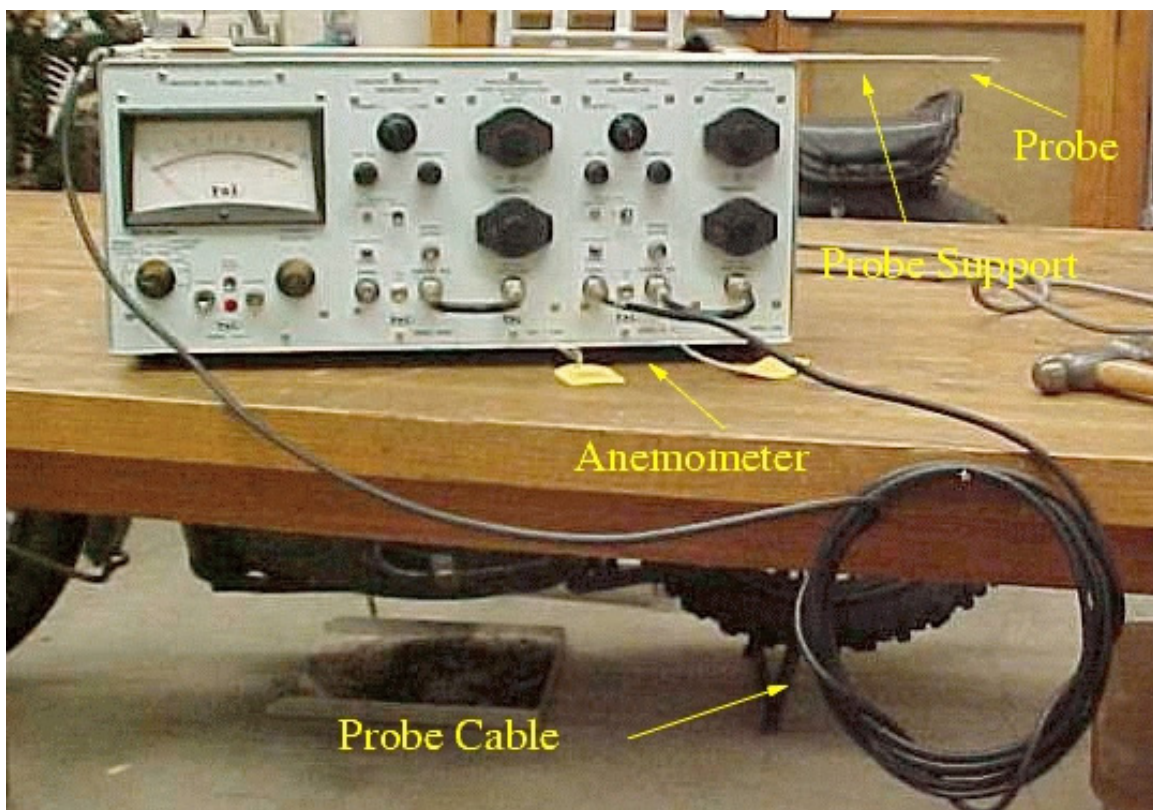
Figure A.1.—An example of a hot-wire anemometry system.
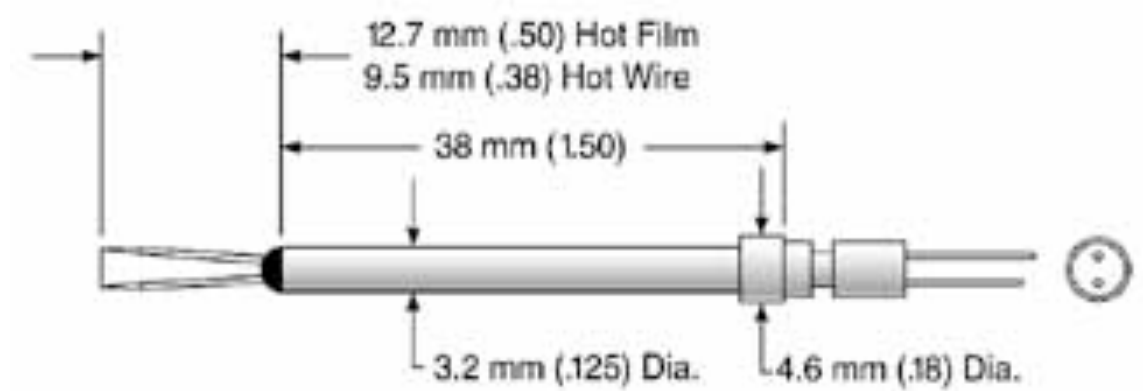
Figure A.2.—A TSI model 1210 hot-wire probe.
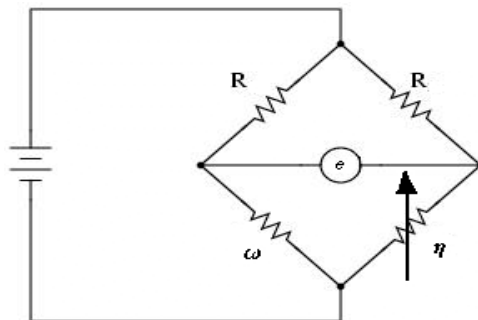
Figure A.3.—A schematic of a Wheatstone bridge.

To infinity

$\oslash = D_w$
$T = T_w$

$U_{amb} \quad T_{amb}$

To infinity
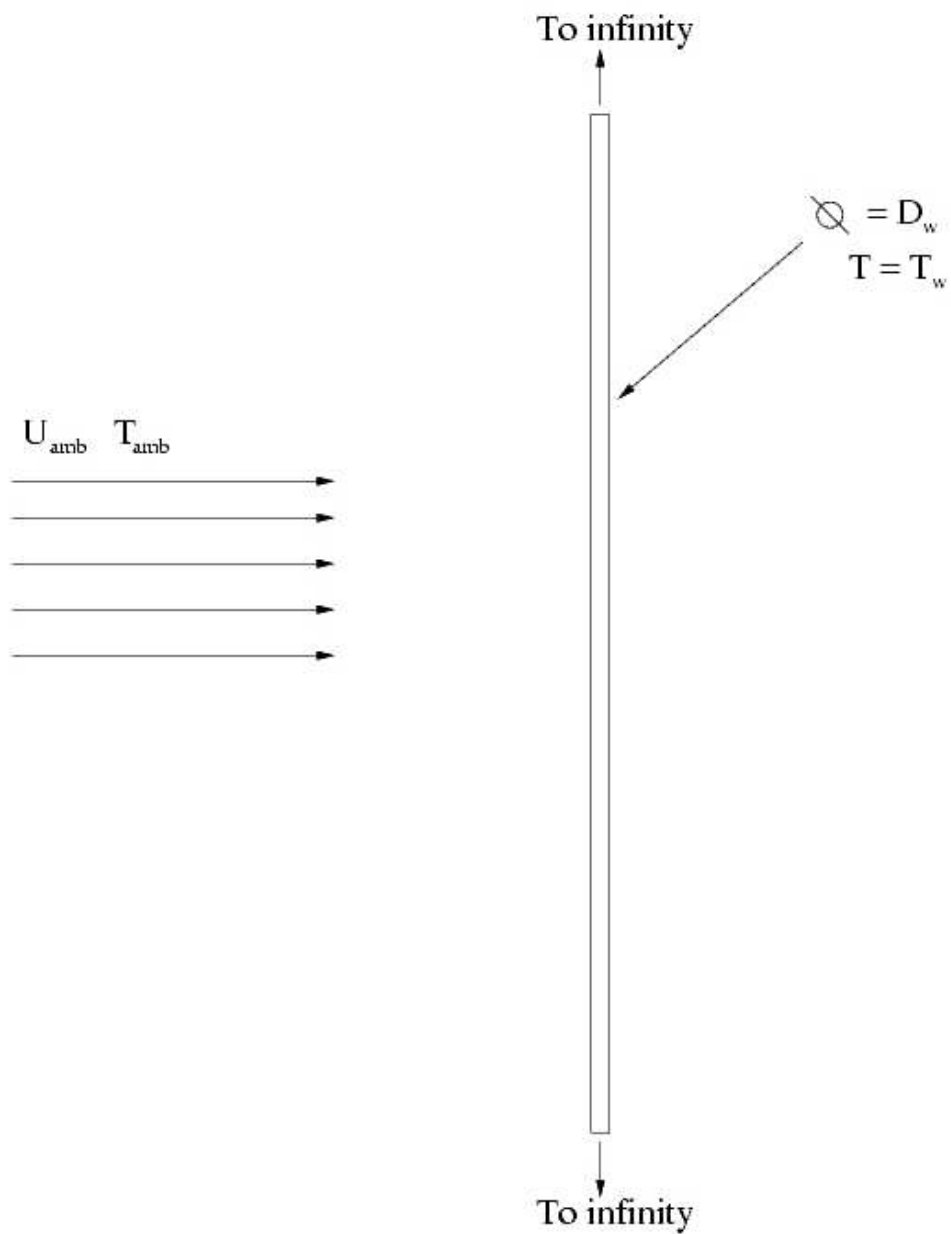
Figure A.4.—A schematic of the assumptions necessary for a simple hot wire analysis.

A.6 References

1. Incropera F.P. and DeWitt, D.P., "Introduction to Heat Transfer," third edition, 1996, John Wiley & Sons Inc.
2. King, L.V., "On the convection of heat from small cylinders in a stream of fluid: Determination of the convection constants of small platinum wires with applications to hot-wire anemometry," 1914, Phil. Trans. Roy. Soc. A, 214, 373–432.
3. Lomas C.G., "Fundamentals of Hot Wire Anemometry," 1986, Cambridge University Press.

Appendix B—Qualification, Error and
Calibration of a Hot-Wire in a Low Speed Flow

B.1 Introduction

Of particular interest in the investigations above is the behavior of a hot wire under low velocity flow conditions. In an oscillating flow, there are portions of the cycle where the flow has zero velocity. Furthermore, all of the velocities measured above, both under oscillatory and unidirectional flow conditions, were lower than 2 m/s (sometimes by an order of magnitude or more). The question of interest is when does the anemometer output drift from linear behavior (see appendix A if clarification of this statement is required).

B.2 Nomenclature

Symbol	Description	Units
C_{ch}	Chamber calibration coefficient	[ ]
d	Nozzle diameter	$[m]$
D_w	Wire diameter	$[m]$
D_{ch}	Chamber diameter	$[m]$
$DelP$	Measured pressure differential	$[in_{H_2 0}]$
e	Voltage differential across a Wheatstone bridge	$[V]$
g	Gravitational constant	$[m/s^2]$
Gr_w	Wire diameter Grashof number	[ ]
h	Average convective heat transfer coefficient	$[W/m^2 \circ K]$
i	Electrical current	$[A]$
k	Fluid thermal conductivity	$[W/m \circ K]$
L	Wire length	$[m]$
Nu	Average Nusselt number	[ ]
P_{atm}	Atmospheric pressure	$[N/m^2]$
P_{ch}	Static chamber pressure	$[N/m^2]$
Pr	Prandtl number	[ ]
q'	Heat transfer per unit length	$[W/m]$
R	Electrical resistance	$[\Omega]$
Ra_w	Wire diameter Rayleigh number	[ ]
Re_{ch}	Chamber diameter Reynolds number	[ ]
Re_w	Wire diameter Reynolds number	[ ]
$RTDR$	4-Wire RTD reading	$[\Omega]$
T_{amb}	Ambient temperature	$[K]$
T_{ch}	Chamber temperature	$[K]$
T_f	Film temperature	$[K]$
T_w	Wire temperature	$[K]$

V	Measured voltage	$[V]$
$\dot{x}$	Velocity magnitude (speed)	$[m/s]$
Y	Compressibility factor	$[\;]$
β	Volumetric thermal expansion coefficient	$[K^{-1}]$
δ	Perturbation marker	$[\;]$
γ	Specific heat ratio	$[\;]$
η	Variable resistance	$[\Omega]$
ρ_{amb}	Ambient density	$[kg/m^3]$
ρ_{ch}	Chamber density	$[kg/m^3]$
ρ_f	Film temperature density	$[kg/m^3]$
ρ_w	Wire temperature density	$[kg/m^3]$
ω	Total probe resistance	$[\Omega]$

B.3 Qualification of "Low-Speed" Anemometry

"Typical hot wire probe calibration curves show a marked decrease in sensitivity at low velocities. This leads us to ask what the lower limit is for practical hot wire and hot film measurements" (Lomas,[5] p. 66). We focus on answering this question in a concrete fashion. We know that if a probe is exposed to a quiescent fluid, natural convection currents develop and, as such, the probe loses thermal energy via convection in "still" air (from here out, we ignore conductive and radiant effects). When the probe is exposed to a low velocity flow, this natural convection cooling effect "masks" the forced convection cooling. We attempt to determine through analysis, and verify by calibration, when this masking becomes small enough that velocity can be properly determined.

As a first cut at quantifying where a King's law type relationship will break down, we cite a "rule of thumb" for measurements in air. In general, the minimum practical measurable velocity is in the neighborhood of 15 - 20 cm/s (Jorgenson[3]).

We next look at a relationship given by Collis and Williams[1] for large aspect ratio sensors ($L \gg D$).

$$\mathrm{Re}_{min} = 1.85 Gr_w^{0.39} \left(\frac{T_f}{T_{amb}} \right)^{0.76}$$

The above relation describes a minimum Reynolds number for which a hot wire may be used. We define the Grashof number based on wire diameter as:

$$Gr_w = g\beta(T_w - T_{amb})D_w^3 / \nu^2 \,.$$

The Grashof number is a "ratio of buoyancy to viscous forces" (Incropera and De Witt[2] p. 320). The familiar Reynolds number based on wire diameter is introduced as:

$$\mathrm{Re}_w = xD_w / \nu \,.$$

Finally, we introduce (Incropera and DeWitt[2] p. 449):

$$\beta \approx -\frac{1}{\rho_w} \frac{\rho_{amb} - \rho_w}{T_{amb} - T_w} \,.$$

The above approximation is known as the volumetric thermal expansion coefficient. It is a thermodynamic property of the fluid that relates changes in density to changes in temperature at constant pressure.

Suppose we are given the following representative data:

$$T_w = 525K$$
$$T_{amb} = 300K$$
$$T_f = 412.5K$$
$$g = 9.81 \, m/s$$
$$D = 5\,\mu m$$
$$L = 1mm$$
$$\nu = 15.89 \times 10^{-6} \, m^2/s$$
$$\nu_f = 27.91 \times 10^{-6} \, m^2/s$$
$$\rho_w = 0.6647 \, kg/m^3$$
$$\rho_{amb} = 1.1614 \, kg/m^3$$
$$\rho_f = 0.8466 \, kg/m^3$$

The property values above are for air at STP (Incropera and DeWitt[2] p. 839). The probe dimensions are characteristic of the ones used in the lab. Combining the above definitions and solving for the minimum measurable fluid velocity, we find:

$$\dot{x}_{min} = 1.85 \frac{\nu}{D_w} \left(g \left(-\frac{1}{\rho_w} \frac{\rho_{amb} - \rho_w}{T_{amb} - T_w} \right) (T_w - T_{amb}) \frac{D_w^3}{\nu^2} \right)^{0.39} \left(\frac{T_f}{T_{amb}} \right)^{0.76}.$$

Numerically speaking,

$$\dot{x}_{min} \approx 6 \, cm/s.$$

We have arrived at a contradiction to our "rule of thumb." We now depart from accepting published suggestions and look at the problem from a more analytic point of view. Recall that the Reynolds number describes the relative importance of momentum effects to viscous effects. As mentioned earlier, the Grashof number is a ratio of buoyancy to viscous forces. This suggests that one may take the ratio:

$$Gr_w / \mathrm{Re}_w^2$$

and attach some kind of significance to it. A moment of reflection suggests that the above ratio is a measure of the relative effect of natural convection (buoyancy) to forced convection. Thus, if the ratio is large, then natural convection effects are significant. Suppose we demand that:

$$Gr_D / \mathrm{Re}_D^2 \ll 1.$$

Given fluid properties and wire geometry, one can get a rough feel for a minimum measurable velocity. Turning back to the example at hand:

$$Gr_w = 3.629 \times 10^{-6}$$
$$\mathrm{Re}_w^2 = \dot{x}^2 (0.0990 \ s^2/m^2)^{\cdot}$$

If we boldly assume that natural convection is negligible provided that:

$$Gr_w / \mathrm{Re}_w^2 \leq 1/10$$

we immediately solve for a lower limit of:

$$\dot{x} \geq 2 \ cm/s.$$

Our analysis suggests that we may set another lower limit.

For the sake of completeness, we include one more idea. We balance Nusselt numbers for forced and natural convection. Suppose the flow under consideration varies from 0 to 1 m/s. Evaluating the Reynolds number at the film temperature we find

$$0 \leq \mathrm{Re}_w \leq 0.18$$

This range of Reynolds numbers is lower than what is commonly tabulated for a cylinder in cross flow. Nevertheless, using Reynolds analogy, one can extrapolate the behavior of Nusselt numbers from tabulated drag coefficient data. Looking at Incropera and DeWitt[2] (p. 343) one observes smooth, non-accelerating drag coefficient behavior for flow over a circular cylinder. With this in mind, we extrapolate on available Nusselt number data (Incropera and DeWitt[2] p. 344), and state:

$$Nu_{w,forced} = 0.989 \, \mathrm{Re}_w^{0.33} \, \mathrm{Pr}^{1/3}.$$

For purely free convection we have: (Incropera and DeWitt[2] p.465):

$$Nu_{w,free} \approx C Ra_w{}^n$$

Where the Rayleigh number is defined as:

$$Ra_w = Gr_w \, \mathrm{Pr}.$$

Evaluating the Rayleigh number in air at the *film* temperature we find:

$$Ra_w = 4.09 \times 10^{-7}.$$

We have (Incropera and DeWitt[2] p. 465):

$$Nu_{w,free} \approx 0.675 Ra_w{}^{0.058} \approx 0.280.$$

At this point we make a similar argument to what was done earlier. Suppose that we demand that:

$$\frac{Nu_{w,free}}{Nu_{w,forced}} << 1.$$

In other words we are demanding that the dominating mode of heat transfer is forced convection. Again we boldly suppose that forced convection dominates if:

$$\frac{Nu_{w,free}}{Nu_{w,forced}} = \frac{0.675 Ra_w{}^{0.058}}{0.989 \, Re_w^{0.33} \, Pr^{1/3}} \leq 0.1.$$

This assumption allows us to back out a minimum measurable velocity. Carrying out the algebra, we find:

$$\dot{x} \geq 11 \; cm/s.$$

Given four different points of departure, we find four different lowest measurable velocities. However, all four are in the neighborhood of 0.1 *m/s*. This gives one an idea of where to begin looking for non-linearities in a King's law type calibration curve. In a different light, the last statement suggests that, given a data set, one can *expect* that all fluid velocities outside (and larger) than the neighborhood 0.1 *m/s* can be made to lie on a straight line for the correct choice of the exponent in a King's law curve.

B.4 Low Speed Hot Wire Calibration

Our in-house laboratory calibration facility consists of a micro-manometer, a RTD temperature sensing device, several voltmeters and a test chamber, as shown in figure B.1. The facility will accept any type of compressed gas. In the present case, we speak of bottled compressed air. Regarding figure B.2, the air enters on the left-hand side of the picture and passes over a baffle, which is immediately followed by an RTD (not shown). It then flows through a series of "quieting" screens. The air then passes through a large nozzle into a straight section (the "chamber"). It then passes through a second nozzle and exits into the room.

The probe is inserted into the chamber and is aligned such that the wire is normal to the flow. Directly across from the probe is a static pressure tap, where the manometer is connected. A data point is collected by turning on the flow, measuring the resistance across the RTD, the voltage across the probe and the fluid level inside the manometer. Iterating this procedure for different flow rates produces a collection of data similar to those presented in table B.1.

The next step is to convert the measured pressure to a velocity. According to Wilson,[9] the equations (which are specific to our calibration rig, but similar to commercial rigs) to make this conversion are:

$$\dot{x}_{ch} = C_{ch} \left(\frac{d}{D_{ch}} \right) \left(\frac{P_{atm}}{P_{ch}} \right)^{1/\gamma} Y \sqrt{\frac{2g(P_{ch} - P_{atm})}{\rho_{ch}}}.$$

where:

$$
\begin{aligned}
d &= 0.8128 \text{ cm} \\
D_{ch} &= 2.5654 \text{ cm} \\
\gamma &= 1.4
\end{aligned}
$$

$$Y = \left[\frac{1}{1 - \left(\frac{P_{atm}}{P_{ch}} \right)^{2/\gamma} \left(\frac{d}{D_{ch}} \right)^4} \left(\frac{\frac{\gamma}{\gamma-1} \left(1 - \left(\frac{P_{atm}}{P_{ch}} \right)^{\frac{\gamma-1}{\gamma}} \right)}{1 - \frac{P_{atm}}{P_{ch}}} \right) \right]^{1/2}$$

$$C_{ch} = 1.1518 - 4.4131 \times 10^{-6} \left(\frac{\dot{x}_{ch} D_{ch}}{\nu_{ch}} \right) + 1.7252 \times 10^{-11} \left(\frac{\dot{x}_{ch} D_{ch}}{\nu_{ch}} \right)^2 + 3.7937 \times 10^{-15} \left(\frac{\dot{x}_{ch} D_{ch}}{\nu_{ch}} \right)^3$$

The actual computation of velocity is tedious and will be omitted for the sake of brevity. However, the velocity-voltage relationship that results from transforming table B.1 is interesting and is presented in figure B.3. We see a square root like behavior. If we choose the exponent, m, in King's law to be $m = 0.435$, then we arrive at a result like figure B.4. Figure B.4 presents the result of several calibration runs. In this figure, one may observe that, upon casting the voltage and velocity data upon these coordinates, the results lie on a straight line. The linear approximation of the data can be expressed as:

$$\dot{x}^{0.435} = -1.5931 + .5033 V^2$$

Recall in our earlier analysis, we predicted that our minimum measurable velocity would be in the neighborhood of 0.1 m/s. In other words, we would expect linear behavior into the neighborhood of 0.1 m/s. The information presented in figure B.4 agrees with this prediction (for example, the left-hand end of the curve fit corresponds to a velocity of 4.8 cm/s).

Regarding figure B.4, we note that for all abscissal values less than 4, the pressure differential is on the order of 0.0001 in. of water. This is problematic in the sense that the pressure measurement device is graduated by 0.001 in. of water.

B.5 Calibration Error Analysis

We have generated a calibration curve and, through it, we can relate voltage and velocity. We now ask; how good is our calibration relationship? This boils down to answering three questions; what is the error associated with the abscissa, the error associated with the ordinate and the error associated with the curve fit in figure B.4?

We begin by determining the error associated with pressure-derived velocity measurements (the ordinate of fig. B.4). Following the methodology of Yavuzkurt,[10] we write (substituting our calibration device relationship for his):

$$\dot{x}_{ch} =$$

$$\left[1.1518 - 4.4131 \times 10^{-6} \left(\frac{\dot{x}_{ch} D_{ch}}{\nu_{ch}} \right) + 1.7252 \times 10^{-11} \left(\frac{\dot{x}_{ch} D_{ch}}{\nu_{ch}} \right)^2 + 3.7937 \times 10^{-15} \left(\frac{\dot{x}_{ch} D_{ch}}{\nu_{ch}} \right)^3 \right] \times$$

$$\left(\frac{d_i}{D_{ch}} \right) \left(\frac{P_{atm}}{P_{ch}} \right)^{1/\gamma} \left[\frac{1}{1 - \left(\frac{P_{atm}}{P_{ch}} \right)^{2/\gamma} \left(\frac{d}{D_{ch}} \right)^4} \left(\frac{\frac{\gamma}{\gamma-1} \left(1 - \left(\frac{P_{atm}}{P_{ch}} \right)^{\frac{\gamma-1}{\gamma}} \right)}{1 - \frac{P_{atm}}{P_{ch}}} \right) \right]^{1/2} \sqrt{\frac{2g(P_{ch} - P_{atm})}{\rho_{ch}}}$$

We have incorporated the above equation into a Matlab code.[1] The user supplies the code with RTD and pressure measurements. The code solves the above polynomial equation (in $\dot{x}$), strips off the

---

[1] See appendix C.

unreasonable velocity values (the above equation is 3rd order, and, as such, has 3 zeros) and returns the chamber velocity.

Several reduction equations are buried in the code. We state them now.

$$T_{ch}°C = \frac{RTDR - 200.43}{0.771429}$$

Where *RTDR* indicates the RTD reading observed on a digital voltmeter (where the DVM is assumed to be free of error). We state that a measured and converted resistance is within 0.05% of the actual temperature. We do not propagate any uncertainty in this calibration; instead, we make our range of potential room temperature fluctuations large enough to capture any RTD calibration errors.

We also have:

$$P_{ch} = \frac{2DelP}{4.019 \times 10^{-3}} + P_{atm}$$

This is a conversion from the measured pressure to absolute chamber pressure. We assume that the conversion factor is free of error.

Owing to the complexity of the above equation, we choose the following method for determining uncertainty associated with it (Strykowski[7]):

Step 1

We calculate "average values" by feeding the above calibration equation the list of values shown in table B.2. We call the output of table B.2 the average velocity, $\dot{x}$.

Step 2

We rewrite our calibration equation in the following form:

$$\dot{x}_{perturbed} =$$

$$\left[1.1518 - 4.4131 \times 10^{-6} \left(\frac{\dot{x} D_{ch}}{\nu_{ch}} \right) + 1.7252 \times 10^{-11} \left(\frac{\dot{x} D_{ch}}{\nu_{ch}} \right)^2 + 3.7937 \times 10^{-15} \left(\frac{\dot{x} D_{ch}}{\nu_{ch}} \right)^3 \right] \times$$

$$\left(\frac{d}{D_{ch}} \right) \left(\frac{P_{atm}}{P_{ch}} \right)^{1/\gamma} \left[\frac{1}{1 - \left(\frac{P_{atm}}{P_{ch}} \right)^{2/\gamma} \left(\frac{d}{D_{ch}} \right)^4} \left(\frac{\frac{\gamma}{\gamma-1} \left(1 - \left(\frac{P_{atm}}{P_{ch}} \right)^{\frac{\gamma-1}{\gamma}} \right)}{1 - \frac{P_{atm}}{P_{ch}}} \right) \right]^{1/2} \sqrt{\frac{2g(P_{ch} - P_{atm})}{\rho_{ch}}}$$

Observe that if we do not perturb any of the quantities (e.g., viscosity) in the above equation then we find $\dot{x} \equiv \dot{x}_{perturbed}$.

Step 3

We define the variable quantities:

$$D_{ch} = 0.025654m \pm 0.000001m \text{ @ 95\% confidence}$$

$$d = 0.008128m \pm 0.000001m \text{ @ 95\% confidence}$$
$$P_{atm} = 98902N/m^2 \pm 3000N/m^2 \text{ @ 95\% confidence}$$
$$T_{ch} = \frac{RTDR - 200.43}{.771429} \pm 5°C \text{ @ 95\% confidence}$$
$$P_{ch} = \frac{2(DelP \pm .0002)}{4.019 \times 10^{-3}} + P_{atm} \text{ @ 95\% confidence}$$

Implicitly linked to the chamber temperature is viscosity, which we state as:

$$\mu_{ch}(T_{ch}) = 182.1 \times 10^{-7} N \circ s/m^2 \pm 2.5 \times 10^{-7} N \circ s/m^2 \text{ @ 95\% confidence}$$

The chamber density can vary with both temperature and pressure through the relationship:

$$\rho_{ch}(T_{ch}, P_{ch}) = \frac{P_{ch}(P_{atm})}{R_{air}T_{ch}}$$

The only quantity that does not fall into the above framework is the chamber calibration coefficient:

$$C_{ch} = 1.1518 - 4.4131 \times 10^{-6}\left(\frac{\dot{x}D_{ch}}{\nu_{ch}}\right) + 1.7252 \times 10^{-11}\left(\frac{\dot{x}D_{ch}}{\nu_{ch}}\right)^2 + 3.7937 \times 10^{-15}\left(\frac{\dot{x}D_{ch}}{\nu_{ch}}\right)^3.$$

The data provided by Wilson[9] suggest that a safe uncertainty value for the chamber coefficient is:

$$\delta C_{ch} = \pm 3\% \text{ @ 95\% confidence}.$$

We assume that the gas and gravitational constants are free of error. Lastly, a quick glance at a thermodynamics book will reveal that for all practical purposes, the specific heat ratio can be assumed to be constant over our range of temperature perturbation.

Step 4

We use the equation of step three with all things evaluated at their average value with the exception of the perturbed quantity. We calculate the deviation that results by perturbing each quantity independently (unless perturbing a quantity implicitly perturbs another i.e., pressure and density) and record their effects.

Suppose, for the sake of clarity, we are perturbing temperature (but keep in mind that it could apply to any of the variable quantities). We make the following definitions:

$$T_{ch} + \delta T_{ch} \rightarrow \dot{x}_T^+$$
$$T_{ch} - \delta T_{ch} \rightarrow \dot{x}_T^-.$$

This is read as; perturbing temperature leads to a velocity perturbation based on temperature. The results that fall out of applying the equation of step 2 and the definitions of steps 3 and 4 are presented in table B.3.

Step 5

We define the total velocity perturbation due to temperature as:

$$\delta \dot{x}_T = \frac{\left|1 - \frac{\dot{x}_T^+}{\dot{x}}\right| + \left|1 - \frac{\dot{x}_T^-}{\dot{x}}\right|}{2}.$$

That is, we are taking the average of the magnitudes of the perturbations. Finally, we define the total effect of all perturbations as:

$$\delta \dot{x}_{pdv} = \sqrt{\sum_i \delta \dot{x}_i^2}$$

where i ranges over all of the variable quantities. The results are presented in table B.4.

We have described the error associated with a pressure derived velocity measurement. We turn to uncertainties associated with fitting a line to a set of data points. This will add a second error, δx_{fit}. Turning back to our calibration data, we have the curve fit:

$$\dot{x}_{fit}^{0.435} = -1.5931 + 0.5033 V^2.$$

According to Strykowski,[8] the error associated with a curve fit is described by the product of the standard estimate of error and a Student t tabular value at 95% confidence:

$$SEE \times \tau_{9,95\%} = \tau_{9,95\%} \times \sqrt{\frac{\sum_{i=1}^{11}(\dot{x}_i - \dot{x}_{fit,i})^2}{9}} \qquad @ \ 95\% \ \text{confidence}$$

We transform the above linear relation back to $\dot{x}_{fit}$ and compare this with our "average velocity," $\dot{x}$ as presented in table B.2. This process gives the standard estimate of error as:

$$SEE = 0.001437$$

Looking to a Student t table, we find:

$$\tau_{9,95\%} = 2.262$$

Thus, we expect the curve fit to differ from measured velocity be the amount:

$$\delta \dot{x}_{fit} = SEE * \tau_{9,95\%} = \pm 0.33\% \ @ \ 95\% \ \text{confidence}$$

Having quantified the error associated with a pressure-derived velocity and the error associated with a curve fit, we now collect these two quantities and call it the total velocity error:

$$\delta \dot{x}_{tot}(\dot{x}) = \sqrt{\delta \dot{x}_{fit}^2 + \delta \dot{x}_{pdv}^2} \ @ \ 95\% \ \text{confidence}$$

The above result is presented in table B.5 and figure B.5.

The last source of calibration error is due to voltage measurement uncertainty. Owing to the quality of our DVM, we take this error as negligible.

B.6 Further Errors

We now mention some noteworthy sources of error that are beyond the scope of this appendix.

Probe Misalignment

It was assumed that the flow was normal to the wire. There are situations, both in calibration and in actual measurement where this may not be the case. Instead of measuring "u" only, now "v" and perhaps "w" are involved. There is no sure-fire way to deal with this type of error outside of using multi-wire probes in flows where more than one component of velocity is expected.

Calibration Drift

As time passes, the wire may collect some kind of filth. An accumulation of dirt influences the wire's heat transfer coefficient and hence makes a calibration curve inaccurate. Moreover, owing to the fact that the wire is maintained at an elevated temperature, its thermophysical properties may change with time. In other words, its resistance-voltage-temperature relationship may change. How are these effects quantified? Who knows? The moral is that the wire should be calibrated often.

Relative Humidity Effects

The calibration analysis that was presented did not take this error into account. If significant variations are encountered, a correction should be made. For the conditions of the present experiment, this effect can be neglected.

Changes in Ambient Pressure

A change of ambient pressure between calibration time and measurement or a significant change over the course of an experiment can lead to errors. If these conditions are encountered, a correction should be made. For the period of this study, such corrections were considered to be unimportant.

A final note: figure B.5 might lead the reader to believe that hot-wire velocity measurements are within 3% of the true value (except at low velocities). In reality, due to errors outside of calibration (e.g., the ones cited above and others), the error band is on the order of 5% (this value of 5% is typical of many references where hot-wire error in carefully conducted experiments is given).

B.7 Figures and Tables
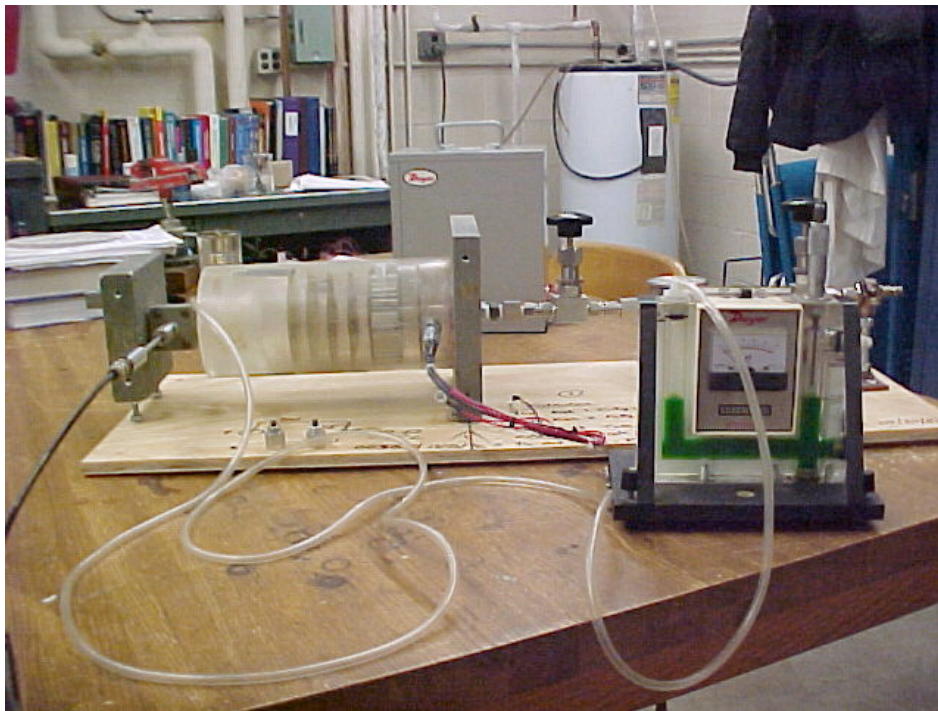
Figure B.1.—The hotwire calibration facility.
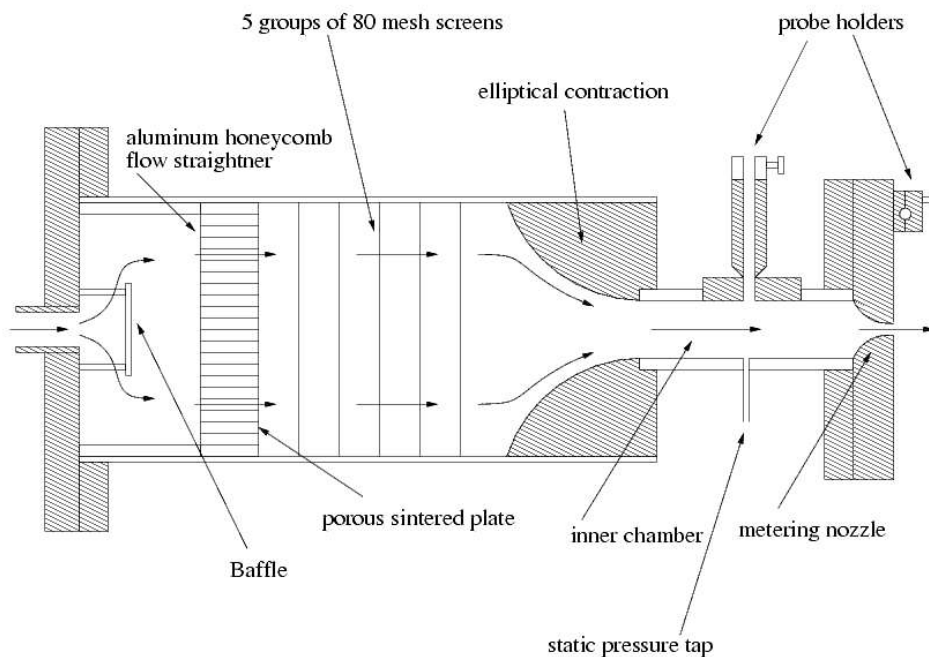
Figure B.2.—Schematic of the calibration facility.
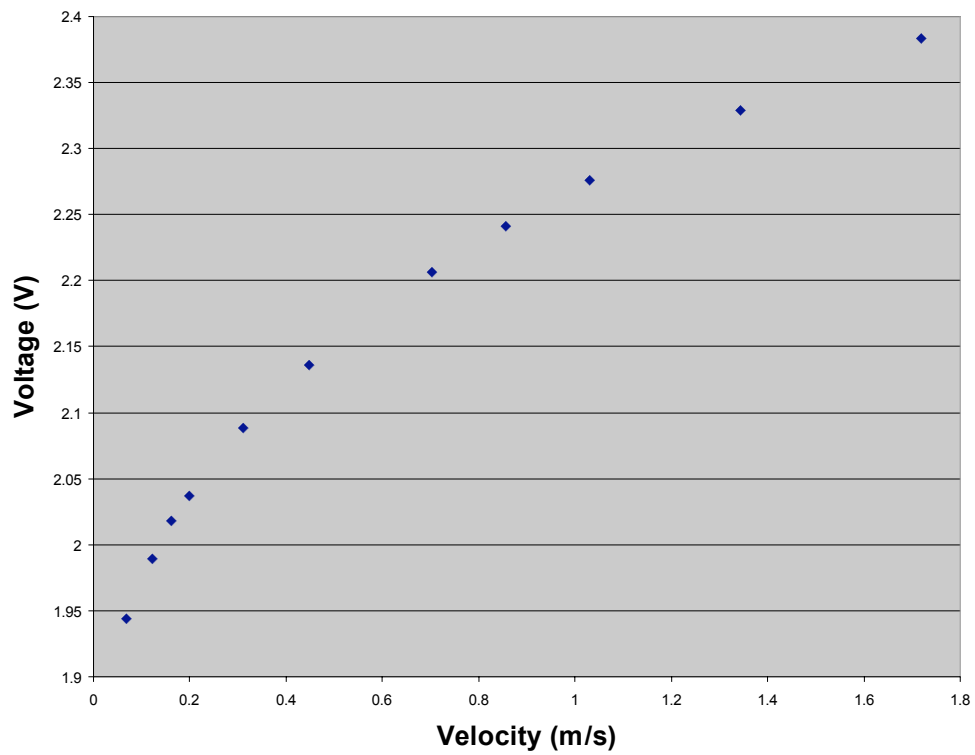
Figure B.3.—Velocity vs. voltage as obtained from tables B.1 and B.2.
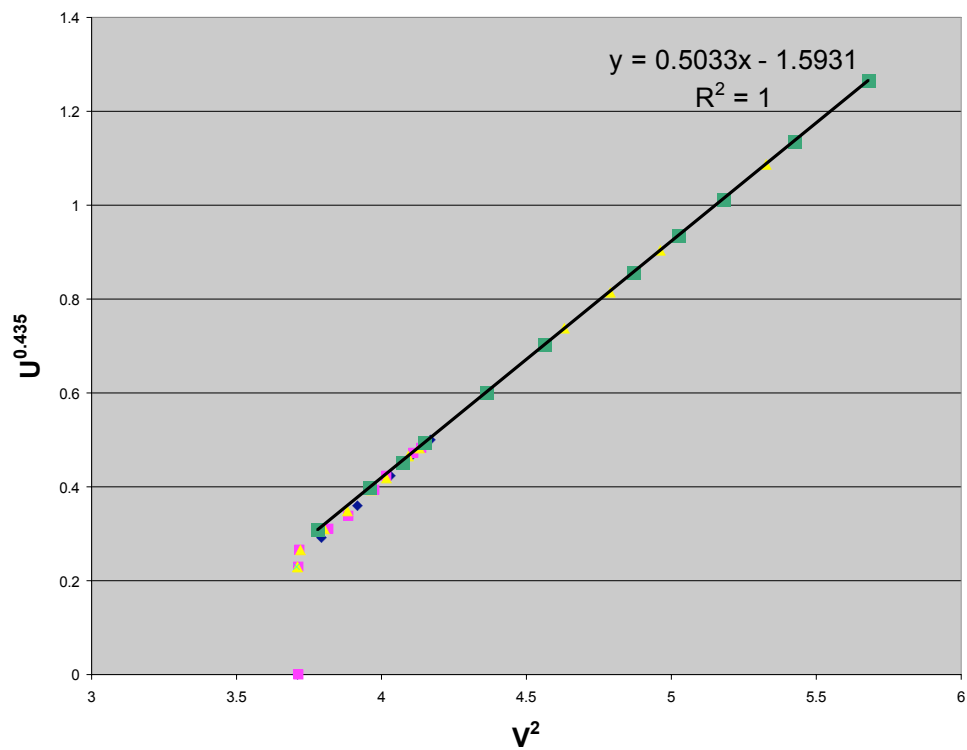
Figure B.4.—A typical calibration curve.
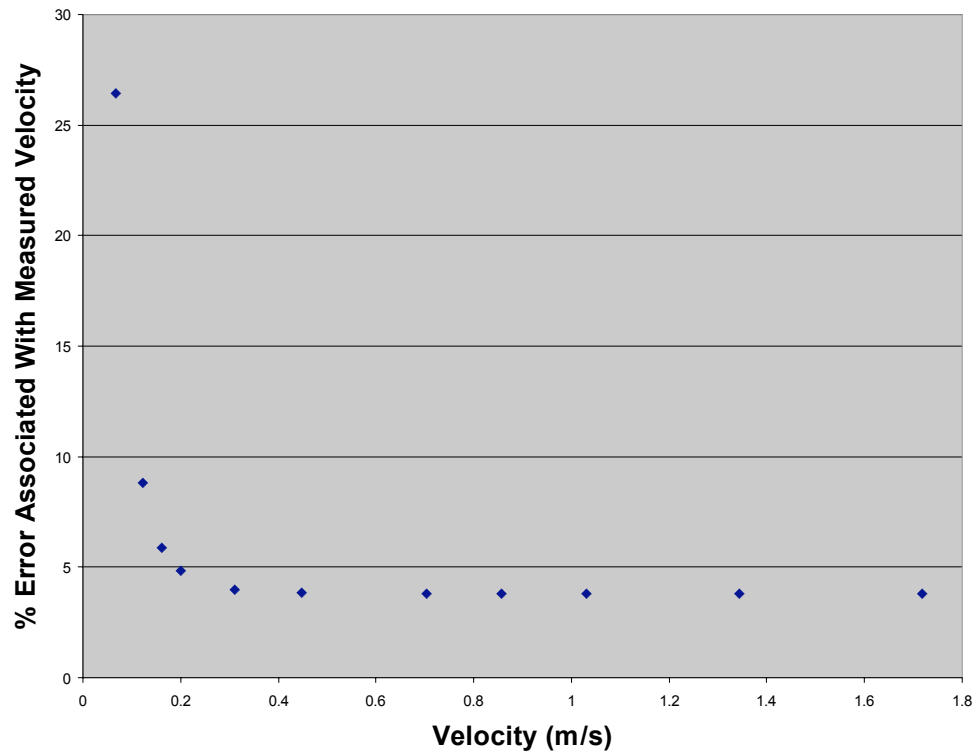
Figure B.5.—Percent error as a function of velocity at 95% confidence.

TABLE B.1.—DIFFERENTIAL PRESSURE MEASUREMENTS
(IN. OF WATER), VOLTAGE MEASUREMENTS (V)
AND RTD RESISTANCE READINGS (OHMS)

FPVO	RTDR	DelP
1.9439	217.36	0.0004
1.9892	217.35	0.0013
2.018	217.34	0.0023
2.0367	217.33	0.0035
2.0887	217.33	0.0085
2.1362	217.34	0.0176
2.2067	217.34	0.0437
2.2413	217.34	0.0651
2.2757	217.34	0.0943
2.3288	217.3	0.1609
2.3832	217.27	0.2651

TABLE B.2.—CODE INPUTS AND OUTPUTS

Code Input		Code Output
RTDR	DelP	x_dot
217.36	0.0004	0.067572
217.35	0.0013	0.12177
217.34	0.0023	0.16193
217.33	0.0035	0.1997
217.33	0.0085	0.31098
217.34	0.0176	0.4471
217.34	0.0437	0.70328
217.34	0.0651	0.85745
217.34	0.0943	1.0307
217.3	0.1609	1.3432
217.27	0.2651	1.719

TABLE B.3.—PERTURBATION RESULTS

D		Atmospheric pressure		Chamber pressure	
+	-	+	-	+	-
0.067567	0.067578	0.066569	0.068622	0.082759	0.047781
0.12176	0.12178	0.11996	0.12367	0.13081	0.11202
0.16192	0.16194	0.15952	0.16445	0.16882	0.15473
0.19968	0.19972	0.19673	0.20281	0.20533	0.19391
0.31096	0.31101	0.30635	0.31583	0.31462	0.3073
0.44706	0.44713	0.44043	0.45407	0.44963	0.44455
0.70322	0.70333	0.69276	0.71428	0.70488	0.70167
0.85738	0.85752	0.84461	0.87089	0.85877	0.85613
1.0306	1.0308	1.0152	1.0469	1.0318	1.0296
1.3431	1.3433	1.3229	1.3643	1.344	1.3423
1.7189	1.7192	1.6931	1.7462	1.7197	1.7184

d		Chamber constant		Temperature and viscosity	
+	-	+	-	+	-
0.067589	0.067556	0.0696	0.065545	0.068145	0.066995
0.1218	0.12174	0.12543	0.11812	0.12281	0.12073
0.16197	0.16189	0.16679	0.15707	0.1633	0.16054
0.19975	0.19965	0.20569	0.19371	0.2014	0.19799
0.31106	0.31091	0.32031	0.30165	0.31363	0.30831
0.44721	0.44698	0.46051	0.43368	0.45092	0.44324
0.70345	0.7031	0.72438	0.68218	0.70932	0.69718
0.85766	0.85724	0.88317	0.83173	0.86484	0.84999
1.031	1.0305	1.0616	0.99979	1.0396	1.0217
1.3435	1.3428	1.3835	1.3029	1.3549	1.3314
1.7195	1.7186	1.7706	1.6675	1.7341	1.7038

TABLE B.4.— $\delta \dot{x}_{pdv} = f(\dot{x})$

Velocity	RSS % error
0.067572	26.1134943
0.12177	8.460908194
0.16193	5.5659778
0.1997	4.49661477
0.31098	3.666309389
0.4471	3.520029483
0.70328	3.484234107
0.85745	3.481403994
1.0307	3.481605379
1.3432	3.485216863
1.719	3.486751534

TABLE B.5.—TOTAL ERROR ASSOCIATED WITH
VELOCITY MEASUREMENT AT 95% CONFIDENCE

Velocity	RSS % error
0.067572	26.4434943
0.12177	8.790908194
0.16193	5.8959778
0.1997	4.82661477
0.31098	3.996309389
0.4471	3.850029483
0.70328	3.814234107
0.85745	3.811403994
1.0307	3.811605379
1.3432	3.815216863
1.719	3.816751534

B.8 References

1. Collis, D.C., and Williams, M.J., "Two-Dimensional Convection From Heated Wires at Low Reynolds Numbers," 1959, Journal of Fluid Mechanics, 6, 357–384.
2. Incropera F.P. and DeWitt, D.P., "Introduction to Heat Transfer," third edition, 1996, John Wiley & Sons Inc.
3. Jorgenson, F.E., "An Omnidirectional Thin-Film Probe for Indoor Climate Research," 1979, DISA info., 24, 24–29.
4. King, L.V., "On the Convection of Heat from Small Cylinders in a Stream of Fluid: Determination of the Convection Constants of Small Platinum Wires with Applications to Hot-Wire Anemometry," 1914, Phil. Trans. Roy. Soc. A, 214, 373–432.
5. Lomas C.G., "Fundamentals of Hot Wire Anemometry," 1986, Cambridge University Press
6. Perry A.E., "Hot-Wire Anemometry," 1982, Oxford University Press.
7. Strykowski, P.J., "Conversations in Dr. Strykowski's Office," 2003, this material may also be available in the course notes for University of Minnesota course - ME 8337 "Experimental Methods in Heat Transfer" or University of Minnesota course ME 3031 "Basic Mechanical Measurements Laboratory."
8. Strykowski, P.J., "Regression Analysis," 2002, Course notes for University of Minnesota course - ME 8337 "Experimental Methods in Heat Transfer."

9. Wilson, D.J., "An Experimental Investigation of the Mean Velocity, Temperature and Turbulence Fields in Plane and Curved Two-Dimensional Wall Jets: Coanda Effect," University of Minnesota Ph. D. Thesis, 1970.

10. Yavuzkurt, S., "A Guide to Uncertainty Analysis of Hot-Wire Data," June 1984, Journal of Fluids Engineering, vol. 106, pp. 181–186.

Appendix C—Samples of C and Matlab Codes

C.1 Introduction

This appendix serves to acquaint the reader with the coding routines used for data reduction. It will provide the curious reader with the necessary information to fully understand the data presented in this report. It will also be of use to the future researcher as a point of departure for new or modified coding routines. For reference, comments (lines ignored by the program) in C programs appear in the following form: /*comment*/. In Matlab programs comments take on the following form: %comment.

C.2 A Simple Traverse Code in C

```
/*This code allows the user to specify a position file that consists
of absolute positions. In other words, you specify the locations that
you want to the probe to go to. One thing to know is that the way the
code is written, it takes the first point as a datum, i.e. the first
point should be some initial point that can be identified (e.g. a
wall, or a centerline or something). Thus, before the code runs, move
the probe to the initial point. As this code is written, one should be
able to cut and paste in into some kind of shell/scripting window and
expect it to run.*/

/*The command to make the thing run is "gcc -o {executable filename)
{codename} cib.o –lm. You must have the file "cib.o" in the same
directory as the source code. */

/* The next two lines are library inclusions relating to the GPIB
card. Depending on the machine that is being used, either may be
appropriate. */

#include "/usr/local/include/sys/ugpib.h"
/*#include<ugpib.h>*/

/* library inclusions*/
#include<math.h>
#include<stdio.h>
#include<unistd.h>
#include<stdlib.h>
#define BUFSIZE 65550
#define STEPSIZE 400
#define LOWSPEED 1000

/* this is the number of points in the traverse, it must be changed
as necessary*/
#define NUM_LOCATION 6

/* beginning of code*/
main()
{

/* variable definitions */
 int i;
```

```c
    int trav;
    int flag = 0;
    char command[20];
    double xini = 0;
    double xcur[NUM_LOCATION];
    double xstep;
    double xabs;
    long step, wait;

 /* file pointer definitions */
  FILE * fpposition;
  FILE * fpdatafilename;




 /* Initialize Traverse for movement. You will have to change the
traverse address as necessary. Also, you will have to change the
traverse settings to suit your needs. Refer to the operators manual
for this purpose. */
    trav=ibfind("dev3");
    ibwrt(trav,"E,B",1);
    sprintf(command,"S1MLOWSPEED,");
    ibwrt(trav,command,strlen(command));

 /* this tells the operator to move to the traverse to a datum. */
  printf("move the traverse to zero displacement\n");
  printf("when this is the case, press 1\n");

  scanf("%d",&flag);

  if(flag==1)
   {
     /* beginning of traverse movement code */

 /* This directs the program to look for a position file. The
position file should be in the same directory as the driving code
(i.e. what you are looking at right now. */

 /* The position file should have a name like "positionfile" and
should look like: /*

  /*
  0
  1
  2
  3
  3.1
  ...
  */
  /* you can specify any numbers you want. The first number need not
be zero (we established a datum above). You will need to count up the
```

number of positions in the file and insert this number in the
definition "#define NUM_LOCATION {fill in the number here}" above. two
notes: 1, all positioning is done in INCHES. 2. all positioning is
ABSOLUTE (i.e. not incremental) */

```
      fpposition=fopen("tester","r");

      for(i=0;i<NUM_LOCATION;i++)
      {
       fscanf(fpposition,"%lf",&xcur[i]);
   /*this reads in the absolute position file*/
      }

      for(i=0;i<NUM_LOCATION;i++)
      {0
       /* move to i'th point. */

       xabs = xcur[i];
       xstep = xabs-xini;

      printf("moving from %lf to the new absolute position of %lf\n",
xini, xabs);
      printf("step distance = %lf\n",xstep);


   /* this just tests if the step size is valid */
      if(fabs(xstep) >= 0.0001)
       {
        step = (long)(xstep*25.4*STEPSIZE);
   /* conversion to metric for the traverse */

         if(step < 0)
   /* moves the traverse in the negative direction */
           {
            sprintf(command,"C,I1M-%ld,R,C",(step*(-1)));
            wait=1-step/LOWSPEED;
           }

         if(step > 0)
   /* moves traverse in positive direction */
           {
            sprintf(command,"C,I1M%ld,R,C",step);
            wait=1+step/LOWSPEED;
           }

         ibwrt(trav,command,strlen(command));
         sleep(wait);
         sleep(10);
   /* you may have to play with the above sleep co"and. Essentially, it
```
gives the traverse time to finish its move before the next command is
issued. This isn't critical in this particular program, but in
something else – like a motion/data ac program, it may be. For

```
example, you will want the traverse to be done moving before data
collection begins */
        }
  /* these next few commands are just so the user can observe the
traverse movement at each point. if this code is incorporated into a
larger one, more than likely, these lines will be removed */
      printf("if everything looks OK press 1\n");
      scanf("%d",&flag);

      if(flag!=1)
       exit(0);
/*********************************************/
      xini = xcur[i];
      fflush(stdout);

  /* end of traverse movement code */


    }
   }
  }
```

C.3 A Simple Sampling Code in C

```
  /* This program collects hotwire data in raw form. */
  /* Run and programmed by: DAA */

  /*The command to make the thing run is "gcc –o {executable filename)
{codename} cib.o –lm. You must have the file "cib.o" in the same
directory as the source code. */

  /* The next two lines are library inclusions relating to the GPIB
card. Depending on the machine that is being used, either may be
appropriate. */

  #include<ugpib.h>
  /*#include"/usr/local/include/sys/ugpib.h"*/

  /* standard inclusions */
  #include<math.h>
  #include<stdio.h>
  #include<unistd.h>

  /* this defines "n" data points, you actually get n-1 useful points
and a marker point at the end of the array. The marker is a "0" */
  #define DATAPOINTS 65536

  /* beginning of Data Acq. */

 main()
 {
  int j;
```

```c
 int iotech,board,fluke;
/* gpib pointers to the iotech and interface board */
 FILE * calfile;
/* Where the calibration data is stored */
 char * calfilename;
/* The name of the calibration file */
 static short data[DATAPOINTS];
/* The waveform data, 256k data points */
 static double voltage[DATAPOINTS];
/* The voltage data, single channel */
 double gain=1.0;
  printf("Acquiring data...");
 calfilename="spectral.4";
/* output filename */
 calfile=fopen(calfilename,"a");
/* Open data file for writing */

 iotech=ibfind("dev1");
/* find the iotech */
 ibclr(iotech);
/* Clear the iotech */
 ibtmo(iotech,T1000s);
/* Set timeout to 30 seconds */
 ibwrt(iotech,"M4X",3);
/* Clear buffer overrun mask if set */
 ibwrt(iotech,"C1X",3);
/* Use channel 1 on iotech */
 ibwrt(iotech,"R0X",3);
/* +/-1 volts range */
 ibwrt(iotech,"G11X",4);
/* Binary transfer mode */
 ibwrt(iotech,"I5X",3);
/* sample rate (2000 Hz) */
 sleep(1);
/* Give iotech a chance to catch up */

/* Acquire Data from Iotech, binary mode */
 ibwrt(iotech,"N0X",3);
/* Put iotech in FIFO mode */
 ibwrt(iotech,"T0X",3);
/* Trigger on talk */
 sleep(1);

 printf("Acquiring data...");
 fflush(stdout);
 ibrd(iotech, (char *)data, 2*DATAPOINTS);
/* 2 bytes per data point, 1 channels, 256k data points */

 printf("done. (%d bytes collected)\007\n",ibcnt);

 fflush(stdout);
```

```
  for(j=1;j<=DATAPOINTS;j++)
    {

    voltage[j]=((2.0/gain)/60000.0)*data[j];
  /*the "2" is the voltage range, the "60000.0" is a conversion from
binary*/
    fprintf(calfile,"%lf \t\n",voltage[j]);
  /*write voltage into a datafile*/
    }
  fclose(calfile);
  }
```

C.4 Low Speed Hot-Wire Calibration Code in Matlab

```
  %This pertains to the hotwire calibration facility in lab 281. The
%user of this code must carefully follow these instructions to obtain
%proper results. This code pertains to the "chamber" of the
%calibration device as defined in Wilson's thesis (see Appendix B).

  %This script file will take excel hotwire calibration data from a
user %specified data file and perform the operations outlined is
Wilson's %thesis to convert measured temperature and pressure readings
to %velocity data. the only reason that Matlab has been used is
because %the governing equations for flow within the calibration
device
  %require finding roots of a 3rd order polynomial, 2 of the roots are
%incorrect the third root is the desired velocity. The difference
%between the desired velocity and the two false ones is obvious upon
  %inspection.




  TP = xlsread('Book3');
  %above command gets the data from excel. Make sure to format excel
%such that temperature sensor readings are in column 1 of the passed
%array and pressure readings are in column 2. (temp to the left of
%press.) Insert your excel filename between the single quotes.

  len = length(TP);
  %Determines the number of entries from the excel column vector.

  T = TP(1:len,1);
  %takes all the temperature readings and stores them in a column
vector

  P = TP(1:len,2);
  %takes all the pressure readings from TP and puts them in a pressure
column vector

  clear TP
  % clears out TP
```

```matlab
    %user defined constants
    P_atm = 97764.0;
    %the user should check this at calibration time
    gamma = 1.4;
    %specific heat ratio
    D_CH = .0256;
    %chamber diameter
    d_noz = .008128;
    %nozzle diameter
    R_air = 283;
    %metric gas constant for air
    RTD_coeff = .799178;
    %slope of the RTD calibration curve
    RTD_baseline = 200.49;
    %intercept of the RTD calibration curve
    %you must determine the voltage/temp relation between whatever type
of sensor you are using
    mu = 184.6*10^-7;
    %viscosity of air


    P_CH = 2 * P / (4.015*10^-3) + P_atm;

    %A column vector. The above line converts the directly read pressure
%measurement (in inches of water) to Pascals and adds on atmospheric.
    %Notice the factor of 2, this is because a U-tube manometer was
used.

    T_CH = (T - RTD_baseline)/RTD_coeff + 273.15;

    %A column vector. This converts from RTD readings to temperature in
%Kelvin

    for i = 1:len
    %if you get a divide by zero message on the front end, you may have
to %change the index


    rho_CH = P_CH(i)/(R_air*T_CH(i));
    %point by point determined constant

    sigma = (d_noz/D_CH)^2;
    %constant
    omega = (P_atm/P_CH(i))^(1/gamma);
    %point by point constant
    chi = rho_CH*D_CH/mu;
    %point by point constant


    alpha = 1.1518 * sigma * omega;
    beta = -4.4131*10^-6 * chi * sigma * omega;
```

```
    delta = 1.7252*10^-11 * chi^2 * sigma * omega;
    phi = 3.7937*10^-15 * chi^3 * sigma * omega;
    %point by point constants

    epsilon = ( ...
       (2 * (P_CH(i)-P_atm) * gamma * (    1 - (P_atm/P_CH(i)) ^ ((gamma-
1)/gamma)     ))...
    /...
    (  rho_CH * ( 1 - ( P_atm / P_CH(i) ) ^ (2/gamma) * (d_noz/D_CH)^4 )
* (gamma - 1) * (1 - (P_atm/P_CH(i)))  )...
    )...
    ^(1/2);
    %point by point determined constant


    polynomial = [phi*epsilon delta*epsilon (beta*epsilon-1)
alpha*epsilon];

    polyroots(i,1:3) = transpose(roots(polynomial));


    end


    dlmwrite('Data.xls',polyroots,'\t')
    %this is the output to an excel file named "Data". There will be 3
%columns in the output. Two of them will be obviously incorrect values
%of velocity, the third one is the one to keep.
```

C.5 The Oscillatory Hot-Wire Traverse Code in C

```
    /* This program is written to take velocity measurements in the disc
and tube spaces. Date: 04-12-2003. As arguments, it takes a list of
absolute positions. These should be presented as a column vector of
positions. The program will move the probe to the position values that
you specify. The program also asks for the slope and intercept of a
kings law calibration curve and the ambient temperature at calibration
time. These values are input at the command line */

    /* to run this code type gcc -o {executable filename} {code
filename} cib.o -lm at the command line. The file cib.o must be in the
same directory as the code */

    #include "/usr/local/include/sys/ugpib.h"
    /*#include<ugpib.h>*/
    /* select either of the above definitions depending on which machine
you are using */
    #include<math.h>
    #include<stdio.h>
    #include<unistd.h>
    #include<stdlib.h>
```

```
#define BUFSIZE 65550
#define STEPSIZE 400
#define LOWSPEED 1000

/* CHANGE AS NECESSARY */

#define NUM_LOCATION 73
/* count up the number of positions in the position file and stick
it in here */

/* CHANGE AS NECESSARY to account for rotational frequency*/

#define NUM_CYCLE 102
/* the number of cycles to be averaged */
#define NUM_POINT 1000
/*30 RPM -- change IOTech to I7X*/
/*#define NUM_POINT 857*/
/*70 RPM -- change IOTech to I6X*/

/* The number of points per one cycle, must be changed to
accommodate for rotational frequency. We adjust NUM_POINT/sampling
frequency such that it is identically equal to 1/rotational frequency.
For example, 30 rpm => .5 Hz rotational frequency => 1/rf = 2 ===
NUM_POINTS/sampling frequency */

main()

{
 int i,j,k,l;
 int flag = 0;
 int iotech1,iotech2;
 int trav,sequence;
 char command[20];
 FILE * fpposition;
 FILE * fpvel;
 FILE * fpdatafilename;

 /* traverse variables */
 double xcur[NUM_LOCATION];
 double xini = 0;
 long step, wait;
 double xstep;
 double xabs;

 double m,b;
/*m = slope, b = intercept */
 static double tdc_voltage;
 static short volt1[NUM_POINT],volt2[2*NUM_POINT];
 static double tdc[NUM_POINT],pulse[NUM_POINT];
 static double vel_volt[NUM_POINT];
 static double vel[NUM_POINT];
 static double sum_vel[NUM_POINT],ave_vel[NUM_LOCATION][NUM_POINT];
```

```c
 double gain=1.0;
/*must change as is necessary*/
 double Tsensor=250;
/*this may not be right depending on overheat ratio */
 double Tfluid;
/* amb. air temp measured before the run */
 double Tcalib;
/*temperature at calibration time*/

/* Create filename*/
 char filename[50];

/* Get the calibration constant for the hot-wire*/
 printf("enter the slope associated with the king's law calibration
curve.\n");
 scanf("%lf",&m);
 printf("enter the intercept associated with the king's law
calibration curve\n");
 scanf("%lf",&b);
 printf("enter the ambient temperature at calibration time\n");
 scanf("%lf",&Tcalib);
 printf("enter the current room ambient temperature\n");
 scanf("%lf",&Tfluid);

/* Initialize IOTECH1 for velocity */
 iotech1=ibfind("dev1");
/* change device number accordingly */
 ibclr(iotech1);
/* Clear the iotech */
 ibtmo(iotech1,T100s);
/* Set timeout to 100 seconds */
 ibwrt(iotech1,"M4X",3);
/* Clear buffer overrun mask if set */
 ibwrt(iotech1,"C1X",3);
/* Use channel 1 */
 ibwrt(iotech1,"R2X",3);
/* +/-5 volts range */
 ibwrt(iotech1,"G11X",4);
/* Binary transfer mode, little-endian */
 ibwrt(iotech1,"I7X",3);
/* sample rate 7 => 500 Hz */
 sleep(1);
/* Give iotech a chance to catch up */

 /*Initialize IOTECH2 for TDC and pulse*/
 iotech2=ibfind("dev14");
 ibclr(iotech2);
/* Clear the iotech */
 ibtmo(iotech2,T100s);
/* Set timeout to 100 seconds */
 ibwrt(iotech2,"M4X",3);
```

```c
   /* Clear buffer overrun mask if set */
    ibwrt(iotech2,"C1X",3);
   /* Use channels 1 */
    ibwrt(iotech2,"R2X",3);
   /* +/-5 volts range */
    ibwrt(iotech2,"G11X",4);
   /* Binary transfer mode, little-endian */
    ibwrt(iotech2,"I7X",3);
   /* sample rate */
    sleep(1);


    printf("move the traverse to zero displacement\n");
    printf("when this is the case, press 1\n");
    scanf("%d",&flag);
    if(flag!=1)
     exit(0);


   /* Initialize Traverse */
    trav=ibfind("dev3");
   /* change as is necessary */
    ibwrt(trav,"E,B",1);
    sprintf(command,"S1MLOWSPEED,");
    ibwrt(trav,command,strlen(command));


   /*CHANGE AS NECESSARY - this is the position file */

    fpposition=fopen("tubelocationfile","r");

   /*CHANGE AS NECESSARY - this is the position file */


    for(i=0;i<NUM_LOCATION;i++)
      {
       fscanf(fpposition,"%lf",&xcur[i]);
   /*this reads in the absolute position file update NUM_LOCATION to
match the file*/
       printf("%lf\n",xcur[i]);
      }

   for(i=0;i<NUM_LOCATION;i++)
      {
       /*move to ith point.*/

       xabs = xcur[i];
       xstep = xabs-xini;

       printf("moving from %lf to the new absolute position of %lf\n",
xini, xabs);
       printf("step distance = %lf\n",xstep);
```

```c
        if(fabs(xstep) >= 0.0001)
    /* this just tests if the step size is valid */
        {
         step = (long)(xstep*25.4*STEPSIZE);
    /* conversion to metric for the traverse */

         if(step < 0)
    /* moves the traverse in the negative direction */
          {
           sprintf(command,"C,I1M-%ld,R,C",(step*(-1)));
           wait=1-step/LOWSPEED;
          }

         if(step > 0)
    /* moves traverse in positive direction */
          {
           sprintf(command,"C,I1M%ld,R,C",step);
           wait=1+step/LOWSPEED;
          }

         ibwrt(trav,command,strlen(command));
         sleep(wait);
         sleep(10);
        }
        xini = xcur[i];
        fflush(stdout);


    /* Open a datafile for writing */
        fpdatafilename=fopen("datafilename","w");



    /* CHANGE AS NECESSARY - This is where the data is written to */

        fprintf(fpdatafilename,"/h/adolfson/research/osc_work/2.125-
30/tube/%lf\n",xcur[i]);

    /* CHANGE AS NECESSARY - This is where the data is written to */

        fclose(fpdatafilename);

        fpdatafilename=fopen("datafilename","r");
        fscanf(fpdatafilename,"%s",filename);
        printf("Data file name is %s \n",filename);
        fclose(fpdatafilename);

        fpvel=fopen(filename,"a");

        for(l=0;l<NUM_POINT;l++)
```

```c
      {
       sum_vel[l]=0.0;

      }

   /* Trigger IOTECH data acquisition*/
      ibwrt(iotech1,"N0X",3);
   /* Put iotech in FIFO mode */
      ibwrt(iotech1,"T0X",3);
   /* Trigger on TALK */
      ibwrt(iotech2,"N0X",3);
   /* Put iotech in FIFO mode */
      ibwrt(iotech2,"T0X",3);
   /* Trigger on TALK */
      sleep(1);

      for(j=0;j<NUM_CYCLE;j++)
      {

       printf(" the %d th cycle \n",j);


       printf("Acquiring data...\n");fflush(stdout);
       ibrd(iotech1,(char *)volt1,2*NUM_POINT);
       printf("done. (%d bytes collected by IOTECH
1)\007\n",ibcnt);fflush(stdout);
       ibrd(iotech2,(char *)volt2,2*NUM_POINT);
       printf("done. (%d bytes collected by IOTECH
2)\007\n",ibcnt);fflush(stdout);

       for(k=0;k<NUM_POINT;k++)
        {
         vel_volt[k]=((10.0/gain)/60000.0)*volt1[k];
         tdc[k]=volt2[k]*(10.0/60000);
        }
       for(k=0;k<NUM_POINT;k++)
        {
   /* this converts voltage to velocity */
           vel[k]=pow((b+m*vel_volt[k]*vel_volt[k]),2.29885);
         vel[k]=vel[k]*pow((Tsensor-Tcalib)/(Tsensor-Tfluid),0.5);
         fprintf(fpvel,"%lf\t%lf\n ",tdc[k],vel[k]);

        }

       printf("\n");
      }
      fprintf(fpvel,"\n");
      fclose(fpvel);
     }
    fclose(fpposition);
   }
```

C.6 A Reduction Code for Oscillatory Flow in C

```
   /* this code takes the data from The Oscillatory Hot-Wire Traverse
Code and ensemble averages it. Inputs to this code are the hot-wire
derived velocity data files from the aforementioned code and a list of
positions. It is best to number the velocity files to correspond with
the position files. The reason being is that when the code accepts the
list of positions, it reads and stores it from top to bottom. Thus,
when the code reads "position 1" from the position file, it goes
looking for a velocity output file with the name "position 1", when it
reads "position 2" it goes looking for a file of the same name, etc.
*/

   /* To run this code, type gcc -o {executable filename} {code
filename} -lm at the command line */

   /* standard inclusions */
   #include<math.h>
   #include<stdio.h>
   #include<stdlib.h>

   #define NUM_X 102000
   /* defined as 102 cycles*(sampling frequency*rotational period)*/
   #define NUM_CYCLE 80
   /* the number of cycles to be ensemble averaged. The code will read
from top to bottom until the number of cycles has been reached */
   #define NUM_FILE 73
   /* number of sampling locations in traverse */


   main()
   {
    int i,j,k,N,M,l;
   /*counter variables*/
    int initial,index;
    int Npoints;

    FILE * fpold;
   /* this is the raw hotwire-TDC sensor data */
    FILE * fpnewV;
   /* this is the velocity-crank angle output */
    FILE * fpRMS;
   /* this is the TI-crank angle output */
    FILE * fpVfilename;
   /* this will eventually be a pointer to a list of filenames in a
traverse */


    double data;
    double x1[NUM_X];
   /* an array of signals from the TDC sensor */
    double tdc[NUM_X];
```

```c
    double pulse[NUM_X];
    double Vel[NUM_X];
  /* an array of velocity signals */
    double f[NUM_X];
    double sumV,sumRMS;
  /*intermediate sums for average/TI calcualtions */
    double aveV[720],aveRMS[720];
  /* arrays of average values and TI's */
    double location[NUM_FILE];

    char datafilename[50];


    /****************************************************/

    fpnewV=fopen("80cycVelDataCooler8-9","a");
  /* this is the output velocity file */
    fpRMS=fopen("80cycVelRMSCooler8-9","a");
  /* this is the output TI file */

    for(i=0;i<720;i++)
      {
      fprintf(fpnewV,"%d\t",i);
  /* this makes 720 points in the output files i.e. half degrees */
      fprintf(fpRMS,"%d\t",i);
      }

    fprintf(fpnewV,"%d\n",i);
  /* puts a newline between the angle index and the velocity row */
    fprintf(fpRMS,"%d\n",i);


  /* This is where the list of positions is read in */

    fpVfilename=fopen("listofpositions","r");
     for(i=0;i<NUM_FILE;i++)
      {
       fscanf(fpVfilename,"%lf\n",&location[i]);
       printf("%lf\n", location[i]);
      }

    for(l=0;l<NUM_FILE;l++)
     {

      sprintf(datafilename,"%lf",location[l]);
      fpold=fopen(datafilename,"r");
      /*fpold=fopen("VelC0.000000","r");*/

      printf("The Data being processed was sampled at a distance of %lf
inches from the target impingement plate \n",location[l]);
      printf("Processing....,please wait!\n");
```

```c
for(i=0;i<NUM_X;i++)
{
 fscanf(fpold,"%lf\t%lf\n",&x1[i],&Vel[i]);
}

/*    printf("%lf\t%lf\t%lf\t%lf\n",x1[0],x2[0],x3[0],x4[0]);*/
/*fscanf(fpold,"%lf\t%lf\t%lf\%lf\n",&x1[i],&x2,&x3,&x4);*/

i=0;

while(x1[i]>0.5)
{
 i=i+1;
 /*fscanf(fpold,"%lf\t%lf\t%lf\%lf\n",&x1[i],&x2,&x3,&x4);*/
}

N=i;

/*printf("%d\t%lf\t%lf\n",N,x1[N],x2[N]);*/

index=0;

for(j=0;j<NUM_CYCLE;j++)
{
 Npoints=0;
 initial=index;


while((x1[index+N]<1&&x1[N+index+1]>1)||(x1[index+N]>1&&x1[N+index+1]>
1)||(x1[index+N]<1&&x1[N+index+1]<1))
      {
       tdc[index]=j;
       /*variableR[index]=x2[index+N];
          variableC[index]=x3[index+N];
          variableH[index]=x4[index+N];*/


/*printf("%lf\t%lf\t%lf\n",tdc[index],TempR[index],TempC[index]);*/
        index=index+1;
        Npoints=Npoints+1;

       }


     tdc[index]=j;
     /*variableR[index]=x2[index+N];
      variableC[index]=x3[index+N];
      variableH[index]=x4[index+N];*/
     Npoints=Npoints+1;
     index=index+1;

     /*printf("index is %d\n",index);
```

```c
      printf("Npoints is %d\n",Npoints);*/


  for(k=0;k<Npoints;k++)
   {
    if(((k+1)*720.0/Npoints-0.5)>floor((k+1)*720.0/Npoints))
       {
        pulse[k+initial]=floor((k+1)*720.0/Npoints)+1;
       }
     else
       pulse[k+initial]=floor((k+1)*720.0/Npoints);

   }


  fprintf(fpnewV,"%lf\t",location);

/* calculate ensemble averaged velocities */
  for(i=0;i<720;i++)
  {
   M=0;
   sumV=0.0;

   for(k=0;k<index;k++)
    {
     if(fabs(pulse[k]-(i+1))<0.1)
        {
         sumV=sumV+Vel[k+N];
         M=M+1;
        }
    }
   aveV[i]=sumV/M;
   fprintf(fpnewV,"%lf\t",aveV[i]);
  }
  /*Calculate TI levels*/

  fprintf(fpRMS,"%lf\t",location);

  for(k=0;k<index;k++)
  {
   for(i=0;i<720;i++)
    {
     if(fabs(pulse[k]-(i+1))<0.1)
        {
         f[k]=Vel[k+N]-aveV[i];
        }
    }
  }

  for(i=0;i<720;i++)
  {
   M=0;
```

```
      sumRMS=0.0;
      for(k=0;k<index;k++)
       {
        if(fabs(pulse[k]-(i+1))<0.1)
           {
            sumRMS=sumRMS+pow(f[k],2);
            M=M+1;
           }
       }
      aveRMS[i]=sqrt(sumRMS/(M-1))/aveV[i];
  /*this isn't RMS, it is TI*/
      fprintf(fpRMS,"%lf\t",aveRMS[i]);
    }

    fprintf(fpnewV,"\n");
    fprintf(fpRMS,"\n");
    fclose(fpold);


   }
 fclose(fpnewV);
 fclose(fpRMS);
 /*fclose(fpVfilename);*/
 }
```

C.7 A Fourier Transform Code with Power-Spectrum Plotting in Matlab

```
   %This code takes an array of sampled data from excel, performs a
%discreet Fourier transform on it and packages the result in terms of
%power and frequency. Also provided is a Matlab power/spectral plot.

   filename = input('enter your excel filename exactly as it appears
(without the .xls) : ','s');

   signal = xlsread(filename);

   %The above commands get the data from excel. Make sure to format
excel %such that input data is in column vector form. Insert your
excel %filename between the single quotes

   N = length(signal);
   %number of sample points for a N point DFT

   fs = input('enter the data sampling frequency (in Hz).\n');
   %this asks for and stores the sampling frequency.

   b = 1:N;
   % bins, necessary for DFT computation and power spectra plotting
   % looks like: b = [1 2 3 ... N]
   Ts = 1/fs;
   % sampling interval in seconds
   ts = Ts*(b-1);
   % discreet time points
```

```
% looks like: ts = Ts*[0 1 2 3 ...N-1]

%computation of FFT and power spectra
SIGNAL = fft(signal);
%DFT of x
pwr = SIGNAL.*conj(SIGNAL)/N;
%this computes the "power" of the signal
frs = (b-1)/N*fs;

%plot of the results

%this presents a space/time plot of the input signal.
subplot(2,1,1);
plot(ts, signal)
xlabel('Time, s')
ylabel('time domain signal')
grid on


%this presents a power/frequency plot
subplot(2,1,2);
loglog(frs, pwr);
grid on;
xlabel ('Frequency, Hz');
ylabel('Power');
```

```
    %this is a verification of Parseval's theorem. The theorem states
that %the sum square of the Fourier coefficients should equal the
average %value of the signal squared over the time length of the
sample. Here %is that check, for further details see any text on
Fourier analysis.
```

```
    disp('this is the verification of Parsevals theorem');
    format long
    [sum(pwr) norm(signal)^2]
    format
    disp('the above numbers should be identical up to machine accuracy,
if they do not then something is wrong and the results should be
discarded');
```

C.8 A 3-D Plotting Code in Matlab

```
    %%%%%%%%%this gets a matrix of values of crank angle and average
    %%%%%%%%%velocities or TI's. It looks like:
    %%%%%%%%%0 1 2 3 4 ...720
    %%%%%%%%%v1 v2 ...   v720
    %%%%%%%%%   ...
```

```
    %in short, this code will turn the results of the code "A Reduction
%Code for Oscillatory Flow in C" and make a pretty picture out of it.
%This particular code is specific to a tube profile, but following the
```

```
%comments, a user will have little difficulty switching to a disc
%profile.

   %geometrical constant - this is specific to the tube
   D_tube = 8.465;

   %this scans in the position file and figures out how many spatial
%positions there were
   filename = input('enter position filename exactly as it appears :
','s');
   posfile = dlmread(filename,'\t');
   clear filename;
   numpos=length(posfile);

   %here we take the tube or disc profile and apply the proper
normalizing %processes and, in the case of a disc profile, a position
shift (due to %the thickness of the probe). We also scan in the file
(or files in %the disc case) where data originates from.

     posfile = posfile+D_tube/2;
   %this makes the centerline the zero position (dia->rad)
     posfile = posfile/D_tube;
   %normalization r->r/D

   %this scans in the velocity - crank angle output file
     filename = input('enter velocity output filename exactly as it
appears : ','s');
     signal = dlmread(filename,'\t');
     clear filename;


   %this scans in the TI - crank angle output file
     filename = input('enter TI output filename exactly as it appears :
','s');
     TI_signal = dlmread(filename,'\t');
     clear filename;

   %manipulations on the velocity and TI matrices. Essentially, we
%remove the column corresponding to count = crank angle = 0 because it
%is garbage. we also strip off the 1->720 numbering sequence and keep
%in mind that as you step rightward in the matrix, you are increasing
%in index (or crank angle).
     vel_ca = signal(2:numpos+1,2:721);
     clear signal;
     maxvect = max(vel_ca);
     max_vel = max(maxvect);
     clear maxvect

     TI_ca = TI_signal(2:numpos+1,2:721);
     clear TI_signal;
     maxvect = max(TI_ca);
     max_TI = max(maxvect);
```

```
    clear maxvect


    %this chops off the ends of the data set to eliminate wall
conduction %effects and blowing through the access hole
    x = 12;
    chop_vel = vel_ca(2:numpos-x,1:720);
    position = posfile(2:numpos-x);
    crankangle = 0.5:0.5:360;
    maxvect = max(chop_vel);
    max_vel = max(maxvect);
    clear maxvect

    %this makes a surface plot of velocity vs. radial position and crank
%angle
    crankangle = 0.5:0.5:360;
    surf(crankangle,position,chop_vel)
    axis([0.5,360,min(posfile),max(posfile),0,max_vel])
    ylabel('r/D','FontSize',20)
    xlabel('\theta','FontSize',20)
    zlabel('||u||','FontSize',20)


    %this makes a TI contour map
    %[X,Y] = meshgrid(crankangle,position);
    %[C,h] = contour(X,Y,chop_TI);
    %h = clabel(C,h,'FontSize',14);
    %set(h,'BackgroundColor',[1 1 .6],'Edgecolor',[.7 .7 .7])
    %xlabel('\theta','FontSize',20)
    %ylabel('r/D','FontSize',20)
```

C.9 A Code to Determine Wall Shear Stress as a Function
of Crank Angle in an Oscillatory Flow in Matlab

```
    %given an array of velocity values like as delivered from the code
of %A3.6:
    %0 1 2 3 4 ...720
    %v1 v2 ...   v720
    %    ...

    %this program solves for wall shear stress and the error associated
%with it as well as plots the results

    %geometrical constant - change as necessary
    disc_spacing = 0.127; %5 inch

    %this scans in the position file and figures out how many spatial
%positions there were it also takes the positions (in inches) to
%meters.
    filename = input('enter position filename exactly as it appears :
','s');
    posfile = dlmread(filename,'\t');
```

```
posfile = 0.0254*posfile;
clear filename;
numpos=length(posfile);



%this scans in the velocity - crank angle output file
filename = input('enter velocity output filename exactly as it
appears : ','s');
signal = dlmread(filename,'\t');
clear filename;

%manipulations on the velocity matrix. Essentially, we remove the
%column corresponding to count = crank angle = 0 because it is
garbage.
%we also strip off the 1->720 numbering sequence and keep in mind
that %as you step rightward in the matrix, you are increasing in index
(or %crank angle).
    vel_ca = signal(2:numpos+1,2:721);
    clear signal;

%here we find the number of the index associated with the axial
%location x/S = 0.100
i=1;
    while (posfile(i)/disc_spacing)<0.1
        i=i+1;
    end

%now we shorten up the position file
posfile = posfile(1:i);

%now we eliminate far wall velocity data
vel_ca = vel_ca(1:i,1:720);

for j=1:720
%the following line finds the minimum velocity at each crank angle
    [C(j),I(j)]=min(vel_ca(1:i,j));
%now we take the spatial location of that minimum value and the next
5 %locations
    y(1:5,j) = posfile(I(j):I(j)+4);
%now we take the corresponding velocities
    u(1:5,j) = vel_ca(I(j):I(j)+4,j);
end

%Average velocity and positions
yavg = sum(y)/5;
uavg = sum(u)/5;

%place holders
Y(1:720,1:2) = 0;
U(1:720,1:2) = 0;
```

```
   %fixed origin and average velocity/position in two arrays to
facilitate %next step
   for i = 1:720
     Y(i,2) = yavg(i);
     U(i,2) = uavg(i);
   end

   %linear fit of average velocity to average position
   for i =1:720
     p(i,1:2) = polyfit(Y(i,1:2),U(i,1:2),1);
   end

   mu = 184.6*10^-7;      % units: N*s/m^2

   %computation of wall shear stress
   WSS = mu*p(1:720,1);
   theta = .5:.5:360;

   %now for the error check. Now that we have wall shear stress as a
%function of crank angle, we can recast our velocity on U+, Y+
%coordinates. That is, coordinates that are specific to the near-wall.
%Then, we take the converted velocity data and compare it to a line
(in %near wall coordinates) with a slope of 1. This should give us an
idea %of the error associated with the original line-slope
determination of %shear stress made above.

   %density
   rho = 1.1614;

   %shear velocity
   for i = 1:720
   vstar(i)=(WSS(i)/rho)^.5;
   end

   %viscosity
   nu = mu/rho;

   %conversion to u+ y+ co-ordinates
   for k = 1:720
     yplus(1:5,k) = y(1:5,k)*vstar(k)/nu;
     uplus(1:5,k) = u(1:5,k)/vstar(k);
   end




   %calculate deviation from linear fit
   for i = 1:720
     RSS(i) = (  ( (y(1,i)-u(1,i))^2 + (y(2,i)-u(2,i))^2 + (y(3,i)-
u(3,i))^2 + (y(4,i)-u(4,i))^2 ...
       + (y(5,i)-u(5,i))^2 ) / 4  )^.5;
   end
```

```
%%%%%%%%%%%%%%%%%%%%%%%%%%%%%%%%%%%%%%%%%%%%%%%%%%%%
subplot(2,1,1);
plot(theta,WSS)
xlabel('\theta [degrees]','FontSize',20)
ylabel('\tau_{wall} [N/m^2]','FontSize',20)
 axis([min(theta),max(theta),0,max(WSS)]);
 grid on

 subplot(2,1,2);
plot(theta, RSS)
    xlabel('\theta [degrees]','FontSize',20)
ylabel('RSS error','FontSize',20)
    axis([min(theta),max(theta),0,max(RSS)]);
    grid on
```

Appendix D—Supplemental DVD

A supplemental DVD is available for this report. The disc contains the data, code, figures and files that were necessary for the generation of this work. Also included is an electronic copy of this report. Each file will be explained such that future use will be as simple and straightforward as possible. The supplemental DVD can be obtained by contacting the NASA Center for Aerospace Information, 7121 Standard Drive, Hanover, Maryland 21076–1320, phone: 301–621–0390.

D.1 The "Unidirectional" Folder

The contents of this folder include the following:

1. A file titled "Summary_RE_17700_5_inch." This is a summary of the unidirectional case in which S = 5 in. (127 mm), Re = 17700. Presented in this file are ensemble average velocities across the tube (a single profile) and across the disc spaces (five profiles). Also presented are TI plots in the disc and tube spaces).
2. A file titled "Summary_RE_7600_2.125_inch." This is a summary of the unidirectional case in which S = 2.125 in. (54 mm), Re = 7600. Presented in this file are ensemble average velocities across the tube (a single profile) and across the disc spaces (five profiles). Also presented are TI plots in the disc and tube spaces).
3. A file titled "Summary_RE_7600_5_inch." This is a summary of the unidirectional case in which S = 5 in. (127 mm), Re = 7600. Presented in this file are ensemble average velocities across the tube (a single profile) and across the disc spaces (five profiles). Also presented are TI plots in the disc and tube spaces).
4. A file titled "Summary_RE_17700_2.125_inch." This is a summary of the unidirectional case in which S = 2.125 in. (54 mm), Re = 17700. Presented in this file are ensemble average velocities across the tube (a single profile) and across the disc spaces (five profiles). Also presented are TI plots in the disc and tube spaces).
5. A folder titled "Uni_flow_viz_pics." In this folder there are 4 files. These files are: A file titled "5high.jpg." This is a flow visualization result for the case Re = 17700, S = 5 in. (127 mm). A file titled "five_low.jpg." This is a flow visualization result for the case Re = 7600, S = 5 in. (127 mm). A file titled "twohigh.jpg." This is a flow visualization result for the case Re = 17700, S = 2.125 in. (127 mm). A file titled "twolow.jpg." This is a flow visualization result for the case Re = 7600, S = 2.125 in. (127 mm).
6. A folder titled "RE_17700_2.125_inch." In this folder, there are 10 files called "r1.jpg," "r4.jpg," "r5.jpg," "r7.jpg," "requals1.xls," "requals4.xls," "requals5.xls," "requals7.xls," "requals8.xls" and "tube_RE_17700_2.125_inch." The 5 jpg files are pictures of time and FFT traces for the radial locations r/D = 0.118, 0.473, 0.591, 0.827, and 0.945 (1, 4, 5, 7, and 8 in.). The Excel (Microsoft Corporation) file bearing the name "requals1.xls" is time-history data sets for the radial location r/D = 0.118 (r = 1 in.). Included in this Excel file is the raw voltage data that the anemometer recorded on the sheet "voltage," the converted velocity values and the ensemble averaged velocities and TI's on the sheet "velocity." Also provided in this file are plots of average velocity and TI. Finally there is a sheet called "spectral" in which there is a single, high frequency sample that was used for FFT purposes (for reference, this spectral sample can be processed with the code xlsfft.m, as described in appendix C section C.7). The other excel files are all similar in nature to the one that was just described. The exception is the file "tube_RE_17700_2.125_inch," in which there is a single profile in the tube space.
7. A folder titled "RE_17700_5_inch." The description of the contents of this folder is identical to that of number "6" above.
8. A folder titled "RE_7600_2.125_inch." The description of the contents of this folder is identical to that of number "6" above.

9. A folder titled "RE_7600_5_inch." The description of the contents of this folder is identical to that of number "6" above.

D.2 The "Oscillatory" Folder

The contents of this folder include the following:

1. A folder called "flow_movies." Within the flow_movies folder there are three Microsoft Power Point files called: "30_RPM_2.125_spacing.ppt," "30_RPM_5_spacing.ppt" and "70_RPM_2.125_spacing.ppt." These are "movies" of oscillatory flow visualization results compared to computational work done at CSU. The titles of the files are explanatory of the contents.
2. A folder called "2.125-30." This is a set of data for the operating condition $\omega = 30$ rpm, $S = 2.125$ in. This folder contains seven sub-folders called "ss1," "ss2," "ss3," "ss4," "ss5," "ss6," and "tube." All of these sub-folders contain similar information, so they will all be described at once. To begin, in each sub folder there will be an ASCII file that has to do with probe position. This file will be a column vector of probe sampling positions (more than ten locations and less than 100). All of the positions are in inches. Along with the position file there will be a collection of ASCII files with numerical titles. These titles correspond to the probe location at sampling time. Within these files are two column vectors, one of the columns is the velocity signal (as delivered from the anemometer) and the other column is a signal from the TDC indicator. This data is a continuous sample of the flow and the TDC indicator for 100 cycles. TDC is marked by a value near zero, away from TDC, the value is approximately 4. Also in each of these folders are two files called "pTI" and "pVel." This stands for "processed" *TI* or velocity. In other words, those files are the ensemble-averaged velocity and *TI* data for a entire cycle at each radial location. Using the code countV.c (as described in appendix C section 3.6), the position file and the collection of velocity/TDC signal files, the files pTI and pVel can be generated. The general layout of the output files is as follows:

$$
\begin{array}{cccccc}
 & position\,1 & position\,2 & ... & ... & ... & position\,n \\
0.5° & u(0.5°, positon\,1) & u(0.5°, positon\,2) & ... & ... & ... & u(0.5°, positon\,n) \\
1° & u(1°, positon\,1) & u(1°, positon\,2) & ... & ... & ... & u(1°, positon\,n) \\
... & ... & ... & ... & ... & ... & ... \\
... & ... & ... & ... & ... & ... & ... \\
... & ... & ... & ... & ... & ... & ... \\
360° & u(360°, positon\,1) & u(360°, positon\,2) & ... & ... & ... & u(360°, positon\,n)
\end{array}
$$

3. A folder called "2.125-70." The contents of this folder are identical in nature to that described in number 2. The difference is that the operating frequency was 70 rpm and the disc spacing was 2.125 in.
4. A folder called "5-30." The contents of this folder are identical in nature to that described in number 2. The difference is that the operating frequency was 30 rpm and the disc spacing was 5 in.

A couple of notes for the future user: The above data (e.g., pTI or pVel) can be plotted with the Matlab routine discthreed.m as described in appendix C section C.8.

D.3 The "Codes" Folder

In this folder are the following codes:

1) A C code called "stepper_program.c" as described in appendix C section C.2

2) A C code called "dc.c" – as described in appendix C section C.3
3) A Matlab code called "hotwire_chamber_calibration.m" as described in appendix C section C.4
4) A C code called "osc_hw_traverse.c" as described in appendix C section C.5
5) A C code called "countV.c" as described in appendix C section C.6
6) A Matlab code called "xlsfft.m" as described in appendix C section C.7
7) A Matlab code called "discthreed.m" as described in appendix C section C.8
8) A Matlab code called "oscwallss.m" as described in appendix C section C.9

There is also a file called "cib.o." This file is a collection of commands necessary for using an IEEE 488 bus/card with the above described programs. This file has to be included at the command line for proper compellation. For example, the correct syntax for running the code dc.c is as follows

gcc –o executable_filename dc.c cib.o –lm

D.4 The "Miscellaneous" Folder

This is a collection of figures and so forth that went into creating this report. We will not try to describe them all. If the reader is inclined to satisfy his or her curiosity then so be it.

REPORT DOCUMENTATION PAGE

Public reporting burden for this collection of information is estimated to average 1 hour per response, including the time for reviewing instructions, searching existing data sources, gathering and maintaining the data needed, and completing and reviewing the collection of information. Send comments regarding this burden estimate or any other aspect of this collection of information, including suggestions for reducing this burden, to Washington Headquarters Services, Directorate for Information Operations and Reports, 1215 Jefferson Davis Highway, Suite 1204, Arlington, VA 22202-4302, and to the Office of Management and Budget, Paperwork Reduction Project (0704-0188), Washington, DC 20503.

1. AGENCY USE ONLY (Leave blank)	2. REPORT DATE	3. REPORT TYPE AND DATES COVERED
	May 2006	Final Contractor Report

4. TITLE AND SUBTITLE

Validation of Multi-Dimensional Stirling Engine Design Codes: Measurements in the 90-Degree Turn Test Section

5. FUNDING NUMBERS

WBS–22–972–30–01
NAG3–2482

6. AUTHOR(S)

Terrence W. Simon and David Adolfson

7. PERFORMING ORGANIZATION NAME(S) AND ADDRESS(ES)

University of Minnesota
111 Church St. S.E.
Minneapolis, Minnesota 55455

8. PERFORMING ORGANIZATION REPORT NUMBER

E–15465

9. SPONSORING/MONITORING AGENCY NAME(S) AND ADDRESS(ES)

National Aeronautics and Space Administration
Washington, DC 20546–0001

10. SPONSORING/MONITORING AGENCY REPORT NUMBER

NASA CR—2006-214131

12a. DISTRIBUTION/AVAILABILITY STATEMENT

Unclassified - Unlimited
Subject Category: 20

Available electronically at http://gltrs.grc.nasa.gov

This publication is available from the NASA Center for AeroSpace Information, 301–621–0390.

12b. DISTRIBUTION CODE

13. ABSTRACT (Maximum 200 words)

The work to be presented herein was motivated largely by a desire to improve the understanding of oscillatory fluid mechanics inside a Stirling engine. To this end, a CFD project was undertaken at Cleveland State University with the goal of accurately predicting the fluid dynamics within an engine or engine component. Along with the CFD efforts, a code validation project was undertaken at the University of Minnesota. The material covered herein consists of four main parts. In section 1, an experimental investigation of a small aspect ratio impinging jet is discussed. Included in this discussion is a description of the test facilities and instrumentation. A presentation of the collected data is given and comments are made. Next, in section 2, a parallel experimental investigation is presented in which the same geometry as that of section 1 is used, but the flow conditions are changed from steady unidirectional flow to sinusoidally oscillating flow. In section 2, collected data are presented and comments are made. In section 3, a comparison is made between the results of sections 1 and 2, namely, sinusoidally oscillating flow results are compared to steady, unidirectional flow results from the same geometry. Finally, in section 4, a comparison is made between experimentally collected data (the main subject of this work) and CFD generated results. Furthermore, in appendix A, an introductory description of the primary measurement tool used in the experimental process—the hot wire anemometer—is given for the unfamiliar. The anemometer calibration procedure is described in appendix B. A portfolio of data reduction and data processing codes is provided in appendix C and lastly, a supplemental DVD and a roadmap of its contents is described in appendix D.

14. SUBJECT TERMS

Experimental oscillatory fluid mechanics; Experimental steady unidirectional fluid mechanics; Experimental and CFD comparisons

15. NUMBER OF PAGES

214

16. PRICE CODE

17. SECURITY CLASSIFICATION OF REPORT	18. SECURITY CLASSIFICATION OF THIS PAGE	19. SECURITY CLASSIFICATION OF ABSTRACT	20. LIMITATION OF ABSTRACT
Unclassified	Unclassified	Unclassified	